Hydrodynamic studies of the dual fluidized bed reactor systems for high temperature solid looping cycles

Von der Fakultät Energie-, Verfahrens- und Biotechnik der Universität Stuttgart

zur Erlangung der Würde eines Doktors der Ingenieurwissenschaften (Dr.-Ing.)

genehmigte Abhandlung

Vorgelegt von

Ajay Ramesh Bidwe

aus Pune, Indien

Hauptberichter:

Prof. Dr. techn. Günter Scheffknecht

Mitberichter:

Univ.Prof. Dipl.-Ing. Dr.techn. Markus Haider

Technische Universität Wien

Tag der mündlichen Prüfung:

21/06/2017

Institut für Feuerungs- und Kraftwerkstechnik der Universität Stuttgart

2017

Acknowledgements

Ajay R. Bidwe

Date: 19/10/2017

Dedicated to

To my father late Dr. Ramesh S. Bidwe, whose simplicity in life, dedication to the society as a physician and love for the nature keeps me inspired for every moment in life

&

To Dr. Ashok Marathe, who knows me more than myself.

You have a right to perform your actions, but you are not entitled to the fruits of the action. Never consider yourself cause of the results, and never refrain your duty.

(Bhagvad Geeta 2:47)

Table of contents

Nomenclature

Notations

Note: The notations related to hot test plant are denoted by the acute accent and for the cold model or general purpose without such accent. E.g. G_s represents cold model while $\acute{G}_s$ represents test plant.

Notation	Variant	Unit	Description
A		m²	area
	A_{CV}	m^2	area of cone valve opening
	A_{LS}		cross sectional area of loop seal, including supply section and recycle section of the loop seal
	$A_{riser\,i}$		cross sectional area of the riser i
	A_{stp}		cross sectional area of the standpipe
Ar		-	Archimedes number
D		m	diameter
	$D_{Ca\,bot}$	m	diameter of the carbonator wide bottom
	D_{stp}	m	diameter of the standpipe
d_p		µm	particle diameter
	$d_{p\,50}$	µm	mean particle diameter
d_p^*		-	dimensionless particle diameter
f	f_g, f_s		friction factor
g		m/s^2	gravitational acceleration
G_{s_i}		kg/m^{2}s	solid flux through riser i based on its cross section
G		kg/h	solid flow rate
G_{L_i}		kg/h	solid looping rate or flow rate of the solid particles between two fluidized beds via interlinking i
	$G_{L_{CV_i}}$	kg/h	solid looping rate from cone valve of CFB i
	$G_{L_{LV}}$	kg/h	solid looping rate through the L-valve
L		m	dimension / length of a Component
	$L_{1\,LS}$,	m	length of the loop seal
	$L_{2\,LS}$	m	width of the loop seal
H			height of the component of fluidized bed
	H_{exit}	m	height of the riser section above the exit of the riser

	H_{stp}	m	particle bed height in the standpipe
	H_{weir}	m	height of the recycle chamber of the loop seal
p		mbar	pressure
Δp_i		mbar	pressure drop in i
	$\Delta p_{CV\,i}$		pressure drop in cone valve of CFB i; measured between the loop of CFB i and return leg inlet of the other CFB
	$\Delta p_{LS\,i}$		pressure drop in the loop seal of CFB i; measured between the bottom of the loop seal and riser return leg inlet
	Δp_{acc}		pressure drop caused by the acceleration of the particles
	$\Delta p_{bed\,i}$		pressure drop in a bubbling fluidized bed
	$\Delta p_{cyc\,i}$		pressure drop in the cyclone of riser i; measured between the riser exit and cyclone bottom
	Δp_{fr}		pressure drop caused by the friction between gas-solid particles and solid-riser wall
	$\Delta p_{riser\,bot\,i}$		pressure drop in the bottom region of the riser i; between riser distributor and entry port from return leg
	$\Delta p_{riser\,top\,i}$		pressure drop in the top region of the riser i; between the riser exit and entry port from return leg
	Δp_{riser}		total pressure drop in the CFB riser i including bottom region and top region
	Δp_{static}		pressure drop caused by the weight of the particles
	$\Delta p_{stp\,i}$		pressure drop in the standpipe of CFB i; measured between the bottom of loop seal and cyclone bottom
T		°C, K	temperature
Mi		kg	solid Inventory in i
M_{To}		kg	total solid Inventory used in single loop circulating system or entire dual fluidized bed system
$M_{M\,i}$		g/mol	molar mass of the substance i
n_i		mol	number of moles of substance i
$\dot{n}_i$		mol/s	molar flow rate of i
$\tilde{R}$		J/mol.K	universal gas constant
Re		-	Reynold number

R_L		-	sorbent looping ratio
u		m/s	superficial velocity of
	u_{0_i}		riser i
	u_c, u_k		velocity related to turbulent regime
	u_g		gas in the packed bed
	u_s		solid particles in the packed bed
	$u_{0\,LS}$		loop seal
	$u_{0\,stp}$		standpipe
	u_{mf}		minimum fluidization velocity
	u_{mb}		minimum bubbling velocity
	u_{se}		minimum velocity of fast fluidization
	u_t		terminal velocity of the particle
u^*		-	dimensionless velocity
u_t^*		-	dimensionless terminal velocity of the particle
U		m/s	actual velocity considering particle voidage
	U_g		actual velocity of gas in a packed bed
	U_s		actual velocity of solid in packed bed
	U_{sl}		slip velocity between gas and solid in a packed bed
$\dot{V}_i$		m³/h	volumetric flow rate of gas supplied to riser i
	$\dot{V}_{LS}$	m³/h	aeration of loop seal
Δh		kJ/mol	heat of reaction
y_i			volume fraction of chemical compound i (gas phase)

Greek symbols

ε	-	voidage
ε_b	-	voidage in bubbling fluidized bed condition
ε_s	-	solid fraction
ρ_g	kg/m³	gas density
ρ_s	kg/m³	particle density
φ	-	sphericity of particles
$\emptyset$	mbar	pressure drop caused by energy dissipation
μ	Pa.s	dynamic viscosity
τ_{Ca}	s	carbonator space time

τ_R	s	particle residence time
γ	-	residence time ratio of light to heavy particles
σ	mbar	standard deviation of pressure
θ	s^{-1}	turnover ratio
ψ	-	fraction of friction and acceleration pressure drop from total riser pressure drop
ξ	-	aeration split or the fraction of the loop seal aeration flow entering supply side of the loop seal

Abbreviations

AR	Air reactor
ASR	Air staging ratio
ASU	Air separation unit
BFB	Bubbling fluidized bed
CaL	Calcium looping
CCS	Carbon capture and storage
CFB	Circulating fluidized bed
CFBC	Circulating fluidized bed combustor
CLC	Chemical looping combustion
DFB	Dual fluidized bed
FB	Fluidized bed
FCC	Fluid catalytic cracking
FR	Fuel reactor
HTSLC	High temperature solid looping cycle
PA	Primary air
PC	Pulverised coal
PSD	Particle size distribution
RT	Residence time
SA	Secondary air
SER	Sorption-enhanced reforming
TA	Tertiary air
TRL	Technology readiness level
TSI	Total solid inventory

Abstract

A high temperature solid looping cycle (HTSLC) is a type of chemical process carried out in twin reactor system. The hot solid particles are transferred from first reactor to second reactor and same particles are transferred back to the original reactor in the continuous and endless cyles. The purpose of the solid transfer is either to provide heat to carry out the desired reaction or to regenerate the particle reactivity. In some operations solid transport is required for both purposes. The calcium looping process, steam gasification process and chemical looping combustion are the examples of high temperature solid looping cycles. All these processes are well acknowledged for their potential in carbon capture development. Although these processes differ on the basis of chemistry, they require the use of same reactor system called dual fluidized bed (DFB) system.

These HTSLCs are currently under the demonstration phase at pilot scale. A 200 kW$_{th}$ test plant is built at University of Stuttgart to demonstrate calcium looping and sorption enhanced reforming process. This thesis presents hydrodynamic studies carried out on the cold model of the test plant. This study includes foundation of reactor schematic, proving feasibility of the schematic and suggesting improvements for the reactors. Various combinations of DFB systems are in use. A twin circulating fluidized bed (CFB) CFB-CFB combination is used to investigate calcium looping process (CaL mode). Two CFBs namely carbonator and regenerator are coupled with individual cone valve to facilitate solid transport between them. Within the same test plant another bubbling fluidized bed (BFB) and CFB combination is used for investigating Sorption-enhanced reforming process (SER mode). Based on the preliminary test plant design a cold model is built with a geometric ratio of cold/ hot as 1/ 2.5. The particles used in the study are as per the Glicksmann`s simplified scaling rules. These rules enable to extrapolate the results of cold model to predict the test plant performance. The results from cold model related to pressure drop, inventory and entrainment rates are important for extrapolation. Once the feasibility studies are carried out, the cold model is dedicated to detailed hydrodynamic studies.

In a CaL mode, two CFBs are interconnected with cone valves, a long term steady state operation is feasible in this schematic, with both cone valves delivering equal magnitude of solid flow rates. The dynamic pressure balance between the two CFB makes it possible. For CaL mode the predictions from extrapolation of cold model results show that most of the required boundary conditions are met in the test plant, i.e. pressure profiles, inventories and carbonator entrainment rates, except the regenerator entrainment rates. The modifications are suggested: a regenerator with hopper like bottom, loop seals with increased weir height and riser exit shape. Some of these suggested modifications upon testing again resulted in improved performance.

In SER mode cold model, a CFB (regenerator) and BFB (gasifier) are coupled with an L-valve and a loop seal situated at the bottom of BFB. The forethought DFB set up works in highly stable manner. The extrapolation of the cold model results show that most of the required boundary conditions are met in the test plant. The solid flow patterns and segregation tests in the gasifier confirmed the suitability of the gasifier design.

The standpipe and the loop seal stability is a crucial in a CFB as well as in a DFB operation. However, little is known about such an important part of the CFB system. The gas solid flow is studied in a CFB operation. It is found that, the amount of loop seal aeration influences the gas solid flow in loop seal and standpipe and entire riser hydrodynamics. The most of the loop seal aeration flow enters the recycle side of the loop seal and only up to 5-7 % is observed to enter the standpipe side of the loop seal. The slugging in standpipe is a common problem in small scale CFB risers. Selecting low solid downflow velocity can improve the slugging behavior in CFB standpipes. This study can help set proper guidelines for loop seal and standpipe design for HTSLC.

The accurate knowledge of particle inventory in a CFB riser is important in the case of HTSLC. Some process related parameters, such as space time, turnover ratio are dependent on the riser particle inventory. The pressure drop to inventory co-relation is normally used to calculate the particle inventory in a fluidized bed. However, in a CFB the pressure drop is significantly influenced by the friction and acceleration phenomenon. This phenomenon can cause error in inventory measurements and very little is known about the magnitude of the error. The experiments are performed in a small scale CFB unit to estimate the magnitude of the friction and acceleration pressure drop, by using quick closing valves method. The friction and acceleration pressure drop increases with increasing the riser velocity. However in turbulent regime, the riser contains more inventory than the pressure drop showing zero or negative influence of the friction and acceleration phenomenon. The core annulus flow structure in the CFB riser is supposed to cause this influence. Further studies to find accurate co-relations are required.

Kurzfassung

Der High Temperature Solid Looping Cycle (HTSLC) ist ein Prozess, der mit einer Zweibettwirbelschicht ausgeführt wird. Die heißen Feststoffpartikel werden vom ersten Reaktor in einen zweiten Reaktor überführt und umgekehrt. Das Ziel der Überführung der Feststoffpartikel ist die Bereitstellung der Wärme und der erforderlichen Prozessbedingungen, um die gewünschte Reaktion auszuführen. In einigen Verfahren ist der Feststofftransport für beide Ziele notwendig. Das Calzium-Looping-Verfahren, die Wasserdampfvergasung von Biomasse und der Chemical-Looping-Prozess sind Beispiele für HTSLC-Prozesse. Alle diese Verfahren können als CO_2-Abscheide-Verfahren eingestuft werden und basieren auf der Nutzung eines Zweibettwirbelschichtsystems.

Diese HTSLC-Prozesse werden gegenwärtig im Pilotmaßstab untersucht bzw. befinden sich im großtechnischen Einsatz. Eine 200 kW_{th} Pilotanlage ist an der Universität Stuttgart aufgebaut worden, um den Calzium-Looping- und den Sorptions-Enhanced-Reforming-Prozess zu untersuchen.

In Rahmen dieser Dissertation wurden fluiddynamische Studien in einem Kaltmodell einer Zweibettwirbelschichtanlage durchgeführt. In dieser Arbeit werden die Grundlagen des Reaktorprinzips, sowie das Erreichen der prozesstechnischen Zielwerte präsentiert. In einzelnen Fällen wurden Modifikationen vorgeschlagen, um die angestrebten Werte zu erreichen. Verschiedene Kombinationen wurden untersucht. Eine Kombination von zwei zirkulierenden Wirbelschichten wird für den Calzium-Looping-Prozess vorgeschlagen. Um den Feststoffkreislauf zwischen den Reaktoren zu steuern, werden sogenannte Spießventile eingesetzt. Für den Prozess der sorptionsunterstützten Reformierung wird eine Kombination aus stationärer Wirbelschicht und zirkulierender Wirbelschicht verwendet. Von einem vorläufigen Konzept für eine Pilotanlage ausgehend wurde ein im Maßstab 1:2,5 skaliertes Kaltmodell erstellt, an dem die Untersuchungen durchgeführt wurden. Die Skalierung erfolgte nach Glicksman. Die Ergebnisse aus dem Kaltmodell in Bezug auf Druckverlust, Partikelinventar und Umlaufrate können somit auf die realen Prozessbedingungen umgerechnet werden.

Für den Calzium-Looping-Fall zeigen die Ergebnisse, dass die wichtigsten erforderlichen Prozessbedingungen in der Pilotanlage erfüllt sind, wie z.B. Druckprofile und Partikelinventar. Die Feststoffumlaufrate war zunächst nicht ausreichend. Durch entsprechende Modifikationen konnte dieser Engpass überwunden werden.

Im Falle der sorptionsgestützten Reformierung konnten die prozesstechnischen Zielgrößen erreicht werden. Es konnte ferner die Eignung der Vergaserauslegung im Hinblick auf die interne Strömungsverteilung bestätigt werden.

Eine Schlüsselkomponente im Wirbelschichtsystem stellt der Siphon dar. Dieser dient zur Überwindung der Druckdifferenz bei der Feststoffrückführung in den Reaktorunterteil. Des Weiteren soll der Siphon die Gasatmosphären in den beiden Reaktoren sicher trennen. Der Verteilung der Fluidisierungsgasströme im Siphon kommt daher eine hohe Bedeutung zu. Des Weiteren ergibt sich eine erhebliche Abhängigkeit der Strömungsformen von der Fluidisierung.

Die genaue Kenntnis des Feststoffinventars in einer Wirbelschicht ist für den hier behandelten Prozess von großer Bedeutung. Üblicherweise wird die Druckdifferenz im Reaktor als Maß für das Feststoffinventar verwendet. Reibungs- und Beschleunigungsdruckverluste sowie weitere Strömungseffekte werden dabei naturgemäß vernachlässigt. Durch Auswiegen des Feststoffinventars war es möglich, diese Effekte zu quantifizieren. Dabei zeigte sich, dass neben den Reibungsdruckverlusten insbesondere durch die Feststoffströmung im Reaktor – nämlich eine Aufwärtsströmung des Feststoffes im Innenbereich und gleichzeitige Abwärtsströmung im Randbereich – sich signifikante Abweichungen ergeben.

1. Introduction

For more than a decade now the phenomenon of global warming is gaining more and more attention. The news channels have been busier in broadcasting news about the floods, droughts, hurricanes and changed weather patterns than before. Naturally the common people are asking why it is happening. Is it due to the global warming? The answer for these queries could be yes. Since the beginning of industrial revolution back in mid of 19th century, the atmospheric CO_2 concentration has raised from 290 ppm [1] to the 395 ppm [2] in the year 2012. The relation between global temperature raise and atmospheric CO_2 concentration raise is well discussed in the literature [3]. Studies show that the average surface temperature of the earth will increase by 1.5 to 4 °C till the year 2100 [4], furthermore this temperature change will cause some irreversible climate changes [4], such as melting of polar ice. This will cause a raise in global sea level and further raise in sea level will be caused by thermal expansion of the oceans. This may cause flooding of present landmass with the sea. Furthermore, changes in precipitation will be a major concern [5]. The frequency of hurricanes and destructive nature of precipitation will be increasing in multiple folds. In the areas where precipitation will be lowered longer dry periods are expected and lack of precipitation will bring severe changes in vegetation. Studies [4] show that the atmospheric CO_2 concentration will not reduce drastically even if the CO_2 emissions are ceased suddenly even now. Therefore, the climate change due to carbon dioxide emissions seems to be an unstoppable phenomenon. However, severity of the changes could be reduced if the measures are carried out well in time to prevent CO_2 emissions to atmosphere.

1.1. CO_2 capture technologies and High temperature solid looping cycles

The main root cause of the global warming problem are the CO_2 emissions resulting from the combustion of the fossil fuels. The fossil fuels (primarily coal, petroleum and natural gas) fulfill the majority of the energy demand, ca. 85% of the total while the rest is fulfilled through renewables, hydropower and nuclear energy [6]. The predicted trends show that there will be mere 10 % reduction in the fossil fuel dependency in the next 2 decades [6]. On the other hand the rapidly growing economies such as China, India and Brazil are showing rapid growth in energy demand and thereby increasing fossil fuel consumption. Therefore, energy demand and manmade CO_2 emissions are unlikely to reduce in future decades [6]. A zero emission (CO_2 emission) scenario should be a goal to prevent future catastrophic situations. This should not necessarily mean stop utilizing fossil fuels. A situation in present scenario means stop using electricity, stop using transport modes and stop industries.

Such a situation in present days is not preferable in present condition. A rational approach is to continue with fossil fuels and prevent CO_2 from releasing into atmosphere. This option is termed as the carbon capture and storage (CCS). However, this should be treated as a buy time strategy, unless we find more sustainable solutions in terms of energy consumption. In CCS the basic concept is to separate carbon either before or after the combustion, primarily in the form of concentrated CO_2 and then store it under the geological formations. The development of CCS is progressing separately in two sections: `Capture technologies´ and `Storage technologies´. This thesis primarily deals with the capture section of the CCS.

The CO_2 capture technologies are primarily classified into three categories, namely

- Pre-combustion
- Post-combustion
- Oxy-fuel technologies

The pre-combustion technologies use methods to remove the carbon from the fuels before a combustion step. A carbon-free fuel may be burned with normal air to generate energy. The reforming technologies and the gasification with carbon capture capabilities are included in the category of pre-combustion technologies. In post combustion technologies, the fuel is combusted using normal air firing methods before the capture. The flue gases are diverted into a separate CO_2 capture skid, where CO_2 is captured and concentrated CO_2 stream is generated. Processes such as amine scrubbing and calcium looping are the examples of post combustion capture process. In oxy-fuel technologies the fuel is combusted only with oxygen instead of air. Thus the flue gas stream produced is rich in CO_2. Table 1 gives a brief comparison of different carbon capture technologies currently in development. All capture technologies are currently under development and have reached various degrees of maturity level. Florin and Harris classified [7] various capture technologies as per their maturity or technology readiness level (TRL). Some TRL examples are shown in Table 1. To implement the pre-combustion and the oxy-fuel technologies either new plants should be built or significant modifications in the present plants are required to be made, while the post-combustion ones are the primary option for the retrofitting of the existing power plants. At institute of combustion and power plant technology, University of Stuttgart, significant research is focused on developing the carbon capture technologies. The technologies under development are amine scrubbing, oxy-fuel combustion, calcium looping, chemical looping combustion and sorption- enhanced reforming. Out of these processes the calcium looping, chemical looping combustion and the sorption- enhanced reforming are categorized as `High temperature solid looping cycle´(HTSLC). The HTSLC is a type of chemical reaction system in which the solid particles at high temperature (generally > 600°C) are transferred from first reactor to second reactor and second reactor to first reactor in a continuous loop. Typical
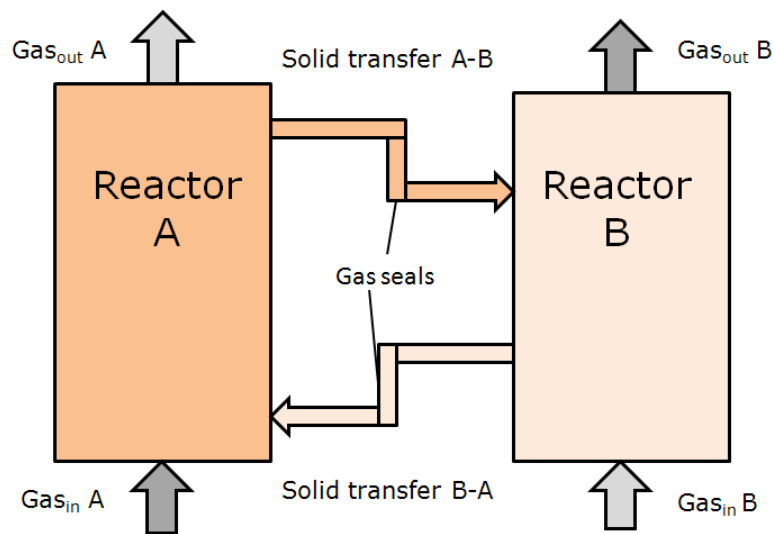
Figure 1 – A typical high temperature solid looping cycle process

HTSLC process is illustrated in Figure 1. In reactors, the gases are fed while the solid reactants are within the reactor. The product gases leave the reactors and solids are transported to the other reactor through a solid transfer system. The gas seals are usually employed to prevent mixing of the product gases from both the reactors. The purpose of transferring solid particles is either to supply reactive particles for the reaction, or to supply heat to support the reaction, or both. Such processes are under development for more than two decades. However, the term HTSLC is a recent and first cited by Anthony et al. [8]. HTSLC processes are mainly sub classified in 3 main processes.

- Steam gasification in dual fluidized bed systems
- Chemical looping combustion (CLC)
- Calcium looping or carbonate looping process (CaL)

These processes differ from each other on the basis of chemistry and the application, but are similar when compared to aspects like high temperature, two reactor systems and the transfer of solid particles. The gasification is a mechanism to produce the combustible gases from the solid or liquid fuels. Discovery of gasification dates back to 18th century [9] and is evolved over a period. The chemical looping combustion (CLC) is a novel technology for the combustion of fuels to generate electricity. The concept of CLC is founded back in 1953 by Lewis and Gilliland [10]. Calcium looping (CaL) is the most recently formulated among the three basic applications of HTSLC processes. It is being purely developed as an economic solution for the post combustion CO_2 capture.

Table 1 - Comparison of CaL with other CO_2 capture technologies

	Calcium looping	Amine scrubbing	Oxy-fuel combustion	Chemical looping combustion
Status	Under development, Demonstrated in pilot scales up to 1.7 MW_{th}.[11] Further scale up required	Commercial and most developed technology. Scale up for large scale plants is ongoing [12]	Demonstrated in pilot scale upto 40 MW_{th} [13]	Demonstrated in pilot scale up to 150 kW_{th} facilities. Significant research going on.
Technological readiness level (TRL) [7]	4-5 [7]	6 [7]	5 [7]	4 [7]
Efficiency penalty (without transport and compression)	6-7.2%% [14] 4.96%[15] 7.4-14.5%[16] 6.8%[17] 2.7-3.2%[18,19] 7.7-10.6% [20] 5.6% [21–23]	>6% [12] 7.8%[15] 7.7-10.3%[24]	6-8% [16] 5.85 %[15] 7.9-8.6%[24]	Gain in efficiency for gaseous fuels [25], 0.9-4 % for coal application [26]
CO_2 avoidance cost	8-37 \$/ton of CO_2 [16,21,27]	52-55 \$/ton of CO_2 [12]	16-44 \$/ton of CO_2 [16]	6-16 €/ton of CO_2
Features	Low with efficiency loss and cost, Can be integrated with cement plants, No need of desulfurization unit	Technology ready to use	Massive scale up potential, suitable for new power plants	None or low efficiency loss
Potential problems	Deactivation of sorbent, resulting in large make up flows, sorbent attrition	Energy consumption in solvent regeneration, Large requirements of solvents and disposal of waste solvents	Energy consumption in air separation unit	Process still immature, challenges for using a coal as a fuel

1.2. Calcium looping process

One of the rapidly developing post combustion capture technology under current investigation is the calcium looping (CaL) process. This process captures CO_2 using carbonation- regeneration reaction of calcium oxide. The reaction mechanism is known for a long time [28] and shown in Eq. (1).

$$CaO_{(s)} + CO_{2(g)} \leftrightarrows CaCO_{3(s)} \qquad \Delta h = \mp 170.5 \text{ kJ mol}^{-1} \qquad (1)$$
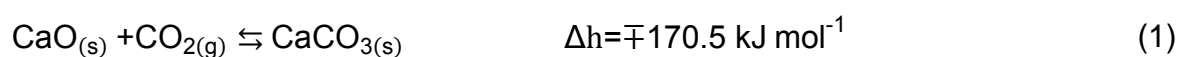
However, the present version to capture CO_2 from flue gases is first suggested by Shimizu et al. [29] in 1999. It is represented in a block diagram shown in Figure 2. The process requires the use of two reactors namely the carbonator and the regenerator. The carbonator is fed by the CO_2 loaded (10-15 vol %) flue gases. At suitable temperatures (600 – 700°C) in the carbonator CaO reacts with CO_2 contained in flue gases and $CaCO_3$ is formed (Eq.(1) forward reaction) and the heat is released. In the regenerator at higher temperatures (850 to 950°C) CaO is regenerated and CO_2 is released due to the endothermic backward reaction of Eq.(1). The heat supply is necessary in the regenerator to maintain higher temperature and the endothermic regeneration reaction. This required heat is provided by the oxy-fuel combustion of carbonaceous fuel such as coal or natural gas. The regenerated CaO is transferred back to the carbonator to be reused in the carbonation step. The obtained gas stream from regenerator is CO_2 rich, and after purifying is ready for the eventual sequestration.

1.2.1. Advantages, efficiency penalty and economics

The CaL offers clear advantages in terms of the efficiency loss and the economics over the rival CO_2 capture technologies. Table 1 compares the CaL with amine scrubbing and oxy-fuel combustion which are rival technologies for CO_2 capture. In
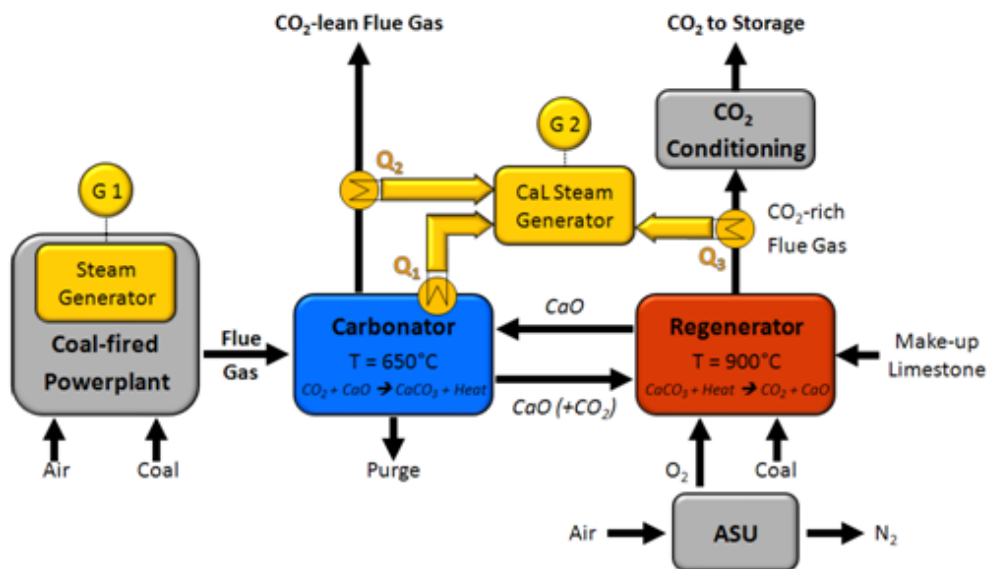
Figure 2 – Block diagram of the calcium looping process [52]

CaL process the use of high temperature and the fluidized bed (FB) enables heat from both the reactors to be utilized effectively in a steam cycle to generate electricity. The locations for heat recovery are mainly

- The exit streams of the carbonator and the regenerator
- Within the carbonator, where the temperature is required to be controlled due to the exothermic carbonation reaction and the sorbent coming from the regenerator.

Modeling and simulation studies [17] show that the electricity generated from the CaL process plant is significant and it is estimated that the total power output from the power plant is increased by ca. 45% (e.g. additional 481 MW_{el} from the flue gases of 1052 MW_{el} power plant [17]). In comparison, the amine scrubbing process, the most developed CO_2 capture process is a low temperature process (40°C-60°C); the heat input given in the solvent regeneration process is not utilizable in an efficient manner as in the CaL process. Therefore, efficiency loss in the amine scrubbing is higher than the CaL process. Thus, CaL offers a clear advantage over the amine scrubbing process. Efficiency loss also occurs in CaL process, mainly in the production of oxygen for oxy-fuel combustion in the regenerator. But total oxygen requirement is $1/3^{rd}$ of oxygen requirement of a pure oxy-fuel combustion plant of the same CO_2 capture capacity [17]. The CO_2 compression, transport and sequestration add some more efficiency loss. The efficiency penalty when compared to the other rival capture technologies is more than 12% (including compression) for amine scrubbing [12]. Various authors have calculated efficiency penalty for the oxy-fuel combustion, varying between 7.9% to 12.4% [16,24] (including compression), and oxy-fuel has always higher penalty compared to CaL [14–16].

Economics is a major advantage in favor of CaL process. Studies such as [16,21,27] have agreed over similar cost of CO_2 avoidance of around 15 $/ton of CO_2, while the cost of CO_2 avoidance for amine scrubbing and oxy-fuel combustion is 51-82 $/ton CO_2 [12] and 25 $/ton CO_2 [16] respectively. Some studies such as [16,27] suggest that CaL and oxy-fuel combustion have similar CO_2 avoidance costs, but the efficiency penalty gives CaL process an advantage.

1.2.2. Bottleneck issues of calcium looping

The CaL has some good advantages, but also has some inherent drawbacks. A major drawback is rapid loss of the sorbent reactivity. The limestone with its repetitive calcination carbonation cyclic process loses the reactivity quickly with increased cycle number [30]. Numerous factors are responsible for this loss, primarily formation of the carbonate layer and sintering of the particles which causes formation of a diffusion layer over the particle surface. Once, this diffusion layer is formed the carbonation reaction rate decreases [31], and only a minor fraction of the particle is available for a useful reaction rate. The loss of reactivity is highest in the initial cycles and decreases gradually after the initial cycles [30]. This observation is consistent with most of the natural limestone types [32]. After many cycles, the loss of reactivity stabilizes. Grasa and Abanades [33] have shown that the sorbent reactivity stabilizes at around 7-8%, called as the ´residual activity`.

To maintain enough sorbent reactivity of the overall bed, fresh sorbent flow should be introduced into the process system. Addition of fresh sorbent is called as the make-up flow. In practice, same quantity of the sorbent (mainly a less reactive) is

simultaneously removed from the system to maintain the material balance. The fresh sorbent has a high reactivity and thus its addition to already depleted sorbent improves the overall reactivity of the sorbent. Experimentally it is shown that the make-up flow has improved the overall bed reactivity [34]. However, introducing a fresh sorbent is related to additional heat demand in the regenerator [35,36], because the fresh sorbent should reach to a required temperature of 900°C and initial calcination also requires an additional heat.

Significant efforts are put into developing methods to enhance and retain the sorbent reactivity as well as preventing the decay of the sorbent. Most researchers [36–41] have confirmed the positive effects of hydration (i.e. exposing limestone in a steam environment). The hydration process causes cracks and fractures in the particle, this eases the diffusion of CO_2 inside the particles [37] and therefore sorbent reactivity is increased. However, these cracks may weaken the particle, therefore attrition behavior enhances and particles are no longer suitable for fluidized bed reactor system. Attrition is another bottleneck issue in the development of CaL process. Limestone naturally being soft material undergoes attrition quickly to a level difficult to restrict in a fluidized bed system. Therefore inventory loss from the fluidized bed reactor is a major concern [42]. However, various studies have implied that the attrition may not be a significant problem in the development of CaL [43].

Additional sorbent deactivation may occur, due to presence of the sulfur in the CaL. Sulfur with CaO forms calcium sulfate, which is a well-known (and desired) reaction in desulfurization process [9]. But formation of the calcium sulfate further decreases the fraction of sorbent useful for carbonation reaction. The influence of high concentration of CO_2 in regenerator is an important aspect but less studied. Limited studies [44,45] have shown that the regeneration reaction is kinetically slowed down with higher concentration of CO_2 in the regenerator and thereby affecting the CO_2 capture efficiency. Studies [44] indicate that the regenerator performance will be a key to successful implementation of the CaL process and therefore need further investigation.

1.2.3. Demonstrations

Ever since conceptualization, the development of CaL process has progressed steadily [29]. At initial stages, significant work related to micro scale studies in thermo-gravimetric analyzers [33,40,46] was performed. This work was fundamental in understanding sorbent behavior, and was key to show the process feasibility and basic design of the lab scale plants. The next steps involved proving process feasibility in small lab scale set ups. Several small lab scale set up were built and operated, namely 30 kW$_{th}$ INCAR-CSIC [47] in Spain, 75 kW$_{th}$ at CANMET in Canada at [42] and 10 kW$_{th}$ at University of Stuttgart [34,43,48] in Germany. These setups used electrically heated reactors. In these lab scale set ups the process is proven feasible on the basis of high CO_2 capture efficiency in carbonator (i.e. based on the difference between inlet and

outlet molar flow of CO_2 in carbonator). The INCAR-CSIC facility reported maximum capture efficiency of 90% [47], while CANMET facility and University of Stuttgart facility reported 96% [42] and 93% [43] respectively. Other successful pilot scale demonstrations are reported from Ohio state university, USA [38] and Tsinghua University, China [49] with very good success. The success at lab scale facilities gave a strong motive to demonstrate the process at a bigger scale or sub-pilot scale in real conditions. Till date three such sub-pilot scale plants for calcium looping process have been built and commissioned. These are 1.7 MW_{th} at La Pereda by ENDESA in Spain [11], 1 MW_{th} at TU Darmstadt Germany [50] and 200 kW_{th} at Universtiy of Stuttgart [51,52] described in the present work. Demonstration of these sub-pilot plants is reported as successful [11,50,52] and detailed scientific work is currently ongoing to address industrial concerns and gain further maturity level. At the present moment the CaL process is ready for higher pilot or demonstration scale (10-50 MW_{th}).

1.3. Sorption- enhanced reforming

Ever since the development of gasification technology back in 19th century, number of variants of gasification technology came to existence and flourished. Sorption- enhanced reforming (SER) is a latest variant among them. The gasification processes are categorized as autothermal gasification and allothermal gasification. In an autothermal gasification the necessary heat for endothermic gasification processes is provided by partial combustion of a solid fuel. If air used such process is called as an air fired gasification. A nitrogen content in the air causes dilution of the product gas, therefore product gas has a low calorific value. In allothermal gasification process, the heat required for the endothermic gasification is provided through an external heat carrier, therefore a direct contact of the product gas with air is avoided [53]. As a result, allothermal gasification processes generate a product gas with a higher calorific value. Most of the steam gasification processes as well as SER are categorized under the allothermal gasification processes. The SER is also a variant of steam gasification process, where steam gasification is coupled with the carbonation calcinations reaction of limestone shown in Eq. (1).

The block diagram of the SER process is well illustrated in Figure 3. The two reactors are called as the gasifier and the regenerator respectively. The process is very similar to the CaL process described in the previous section. In SER, the gasifier is equivalent to carbonator of the CaL. In gasifier the biomass is introduced in a fluidized bed of CaO. Pure steam is used as a gasification agent as well as fluidizing gas. The gasification reactions taking place are described in Table 2 [9,41]. The temperature range for gasification is kept between 600-700 °C, in this temperature range the CO_2 produced in the gasification process is absorbed by the reactive CaO present in the bed and forms $CaCO_3$ as per Eq. (1). The carbonation reaction benefits the gasification process in the following ways.
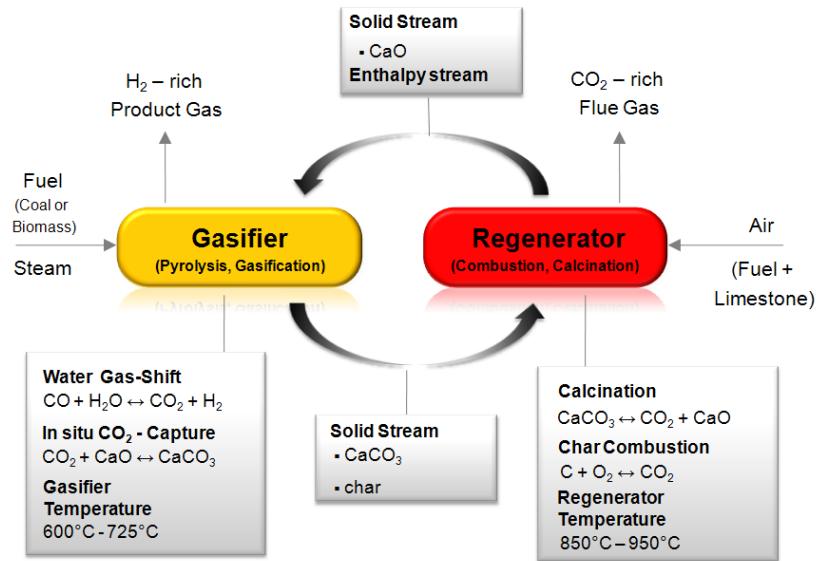
Figure 3 – Block diagram of SER process [66]

- The removal of CO_2 within the reaction zone causes shifting of the thermodynamic equilibrium of water-gas shift reaction (Table 2, Eq. (3)) to the production of H_2, thus resulting in increased levels of hydrogen.
- The heat released during carbonation reaction partially fulfills the heat requirement of the gasification process.
- The removal of CO_2 also enhances the calorific value of the product gas.

The formed $CaCO_3$ and the non-combusted char is then transported to the regenerator. In SER, the regenerator works in a similar way as in CaL process. At temperatures above 850°C, the CaO is regenerated from $CaCO_3$ as a reverse endothermic reaction of Eq. (1) and CO_2 is released. The necessary heat for the endothermic regeneration and increment of temperature is supplied by the combustion of char received from the gasifier. If necessary an additional fuel can be provided to the regenerator. The regenerated CaO at temperatures > 850°C is then recycled back to gasifier to fulfill the duty as sorbent as per Eq. (1) and heat supply to support the gasification reactions. The amount of CaO transferred between the beds is called as sorbent looping rate or sorbent flow rate.

Although biomass is costlier and lower in energy density than coal, it is considered as a primary fuel for SER process. This is mainly because the biomass has a large fraction of volatiles in its compositions (ca. 70%) compared to coal. These volatiles are converted to product gas quickly at temperature range of SER gasifier (600-750°C). On the other hand, coal with high char content will require temperature above 1000°C for quick gasification rates [54]. However coal with high volatile content can also be considered as a fuel in SER operations [41].

Table 2 - Important chemical reactions involved in the steam gasification of biomass [41]

Name of reaction	Chemical equation	Enthalpy Δh	Eq.
Biomass reforming	$C_nH_mO_p + (2n - p)H_2O \leftrightarrows nCO + \left(\frac{m}{2} + 2n - p\right)H_2$	–	(2)
Water-gas shift	$CO + H_2O \rightarrow CO_2 + H_2$	– 35.6	(3)
Methane reforming	$CH_4 + H_2O \rightarrow CO + 3H_2$	+224.8	(4)
Water-gas	$C + H_2O \rightarrow CO + H_2$	+135.8	(5)
Oxidation	$C + O_2 \rightarrow CO_2$	– 394.5	(6)
Oxidation	$C + 0.5O_2 \rightarrow CO$	– 111.5	(7)
Boudouard	$C + CO_2 \rightarrow 2CO$	+171.4	(8)
Methanation	$C + 2H_2 \rightarrow CH_4$	– 88.9	(9)

[a] Enthalpies at 923 K correspond to the likely operating temperature for biomass gasifier with CO_2 removal.

The primary fuel considered in SER is biomass which is a CO_2 neutral fuel. Therefore, regenerator should not be necessarily an oxy-fuel fired. An air fired regenerator would suffice in terms of CCS requirements. However if regenerator is equipped with an oxy-fuel combustion system, then SER will achieve net removal of CO_2 from the atmosphere [41]. Florin and Fennell [7] have categorized SER into a pre combustion capture technology with a low technology readiness level.

The process of SER is initially seeded by Curran et al. [55] in 1967 as a gasification process with CO_2 acceptor process. However only in recent decade the development has been expedited. Several small-scale projects have been cited proving enhancement of H_2 concentration in the product gas with the use of CaO as a bed material. Typically H_2 concentration raised to 55-80% [41,56–59] in SER process compared to normal steam gasification where H_2 concentration averages between 35-45% [60]. The large variation of the H_2 concentrations is justified by Florin and Harris [41], the use of different biomass types and different source of limestone are the main reasons. Corella et al. [61] mentioned that the reactor design, type of biomass and process conditions (pressure, temperature, bed material) affect the product gas concentration significantly.

1.3.1. Bottleneck issues

Since the sorbent used in SER is same as in CaL process therefore the bottleneck issues related to SER are same as discussed earlier in section 1.2.2, such as sorbent deactivation, attrition etc. However, the production of tar in SER process is an issue to be addressed separately.

Production of tars is inherent in gasification. The tars are condensable hydrocarbons resulting from complex cracking, pyrolysis reactions from the solid fuels. The tar production is considered problematic, since it causes blockages in process pipes and equipment and it makes product gas unsuitable for the use in generators. Temperature is the most influencing parameter for the tar production. Typically the tar production in gasification reduces with increase in gasification temperature [62,63]. Generally temperatures above 900°C are considered suitable for low tar production. But to facilitate carbonation reaction of limestone, gasification temperature in SER process is limited to 600-750°C. Therefore lot of tar related problems are anticipated in such low temperature gasification process. Contrary to general belief, according to Pfeiffer et al. [64] the temperature range of 600-700 °C is suitable for low tar production because in this temperature range the primary tar production is low and formation of tertiary tars is avoided. Poboss et al. [65] have studied the tar production in the SER conditions in University of Stuttgart 20 kW_{th} DFB facility; the tar production is found in the range of 8-40 g/kg fuel. The tar production decreases with increase in temperature and shows little increase at 750°C, due to the production of tertiary tars in this temperature range. The bed material also has significant impact on tar production. The facilities at TU Wien have reported the tar production between 4-8 $g/m^3_{(n)}$[1] of product gas generated [64], using catalytically active bed material for conventional steam gasification and 1-2 $g/m^3_{(n)}$ [1] for SER process [62]. According to Hawthorne et al. [66] bed material of TU Wien facility has much better tar cracking abilities. Therefore, it can be said the tar production in SER facilities can be controlled and may not pose critical problems at higher scales.

1.3.2. Demonstrations

Although SER process is shown feasible in small scale set ups, examples of higher scale demonstrations are few. The process has been demonstrated at a bench scale of 20 kW_{th} DFB (bench scale test plant) system [59] at University of Stuttgart. Product gas with H_2 concentration as high as 78% is observed in this 20 kW_{th} system [59]. More demonstration works of SER is carried out at TU Wien in a 100 kW_{th} DFB gasifier [62,64,67–69] using limestone as well as dolomite as bed material. The process is also demonstrated shortly in a pilot scale in 8 MW_{th} DFB pilot plant at Güssing, Austria [69].

1.4. Motivation

At University of Stuttgart, the development of HTSLC processes has been ongoing for a decade. Most of the work has been carried out for gasification and CaL process. Sorption-enhanced reforming (SER) is a variant of gasification mainly studied at University of Stuttgart. The research on CLC has started recently and is expected to

---

[1] (n) indicates volume at normalized condition i.e. 1.013 bar and 273.15 K

continue in the future. During the timeline of the present thesis several projects based on CaL, SER and CLC processes were executed at University of Stuttgart. These projects involved activities like economic and feasibility studies, parametric studies and demonstration projects. Some of the projects carried out during the timeline of the thesis (year 2008-2012) are enlisted in Table 3. The number of projects in Table 3 shows that significant research activity has been carried out at University of Stuttgart regarding the development of HTSLC. Projects such as C-3 capture, CATS, Brennflex and CLOCK were process feasibility projects. Within a scope of such feasibility projects, the process under study should be demonstrated in a bench scale or mini test scale experimental set up. The size or the capacity of the experimental set up is depending on the individual project objective. Before 2005, University of Stuttgart possessed just a couple of bubbling fluidized bed reactor systems, therefore to execute such feasibility projects required the fresh design and construction of the experimental set ups, i.e. the dual fluidized bed (DFB) systems.

Table 3 – List of projects involving HTSLC at University of Stuttgart during thesis duration

Sr No	Project name	Duration	Process
1	C-3 Capture*	2005-2008	CaL
2	CATS*	2008-2012	CaL
3	Brennflex*	2008-2011	SER
4	CLOCK*	2009-2012	CLC
5	CaOLING	2009-2012	CaL
6	CaLMOD*	2011-2014	CaL
7	SERGasII	2006-2009	SER
8	DLR@UniSt	2012-2012	SER
9	B t G	2009-2012	SER

*Projects involving hydrodynamic studies

The suitable reactor system for HTSLC processes is a dual fluidized bed (DFB) system. DFB system consists of two or more fluidized bed reactors with a solid transfer link between the reactors. The DFB reactor system provides the most comprehensive solution mainly because of two reasons: first the fluidized bed reactors are suitable reactors for gas solid reaction and secondly the solid transfer between the reactors can be achieved with little modification in the fluidized bed systems. The gaseous streams from both the fluidized beds are completely isolated. Chapter 2 will deal in more detail with the DFB systems.

Two aspects of the DFB system should be considered in the design of HTSLC process: process aspect and hydrodynamic aspects of the fluidized bed. Most of the present research regarding HTSLC is focused on the process aspect, i.e. the selection of appropriate particles, improving reactivity of the particles, understanding heat and mass transfer occurring during reactions, modeling and simulation of overall process

etc. However, limited research is focused on the hydrodynamic aspects. The main reason for this discrepancy may be due to the fact that the fluidization technology has evolved and continues to evolve separately and there exists a general belief that the expertise from the fluidization technology will always support the development of HTSLC processes. Another reason is the timeline of the HTSLC processes, so far the processes were under the scrutiny of their feasibility, therefore lot of efforts were made into the lab scale studies such as microscopic analyses and modeling- simulation studies. These processes are now becoming mature enough for the lab scale and pilot scale demonstrations. Therefore with more and more pilot scale studies the need for hydrodynamic studies will grow.

Designing a DFB system at University of Stuttgart is accomplished using proper chemical engineering practices. Most critical among these steps is a reactor design. The FB reactor design is a very complex affair. The designer should be aware of kinetics and hydrodynamics of the gas solid system. Several reactor modeling and simulation tools are available, but due to multiple assumptions taken while modeling and complex nature of the FB systems, the uncertainty about the design is high. For example, with the help of present models the fluidization regime, the pressure profile in a FB and gas solid conversion can be well predicted, but can deviate in practice to a significant extent. The predictions about the solid entrainment flux and operational stability are even more difficult, therefore relying heavily on such models is a big risk. However, to go ahead with the construction a sufficient degree of certainty is required. The cold flow models can provide much required certainty for the design and construction of the FB reactor system.

Cold flow model studies are exploited in the field of fluidization; they are best suited for doing basic studies in the fluidization. Furthermore, their use in generating correlations for mathematical models and validating models is very common [70]. For complex fluidized bed systems such as those used in this thesis, the cold model is a preferred way. At TU Wien in Austria, significant development in the DFB technology is carried out. Number of DFB systems ranging from 10 kW$_{th}$ to 8 MW$_{th}$ [53] have been constructed and operated, with the essential knowledge acquired in the cold model studies. The predictions from the cold model studies are found sufficiently accurate to the pilot plant studies [53]. Charitos et al. [71] at University of Stuttgart, have used the scaled cold model to validate the design of a 10 kW$_{th}$ CaL bench scale test plant. The experience gained during the cold model studies will not only help in designing the pilot plants but also be vital during the commissioning and operation of the plant. The practices developed for troubleshooting during the cold model studies will be indispensable during the operation of the plant. Furthermore, when the processes will be mature for commercial scale, the hydrodynamic studies carried out on the cold flow model and from built pilot plants will be helpful in improving the design of the future plants based on HTSLC.

1.5. Task and objective of the present work

1.5.1. Hydrodynamic feasibility of test plants for HTSLC through cold model studies

The primary objective of this thesis is to provide a support for finalizing the design of the multiple projects through cold flow model studies. The research methodology described in above paragraph is followed for the demonstration projects of Table 3. The cold model studies at University of Stuttgart are well practiced before [44,72], primarily for validating design of 10 kW$_{th}$ bench scale calcium looping facility. This thesis mainly involves the cold model studies related to CATS, Brennflex and CaLMod projects mentioned in Table 3. In the scope of these projects a 200 kW$_{th}$ dual fluidized bed test plant is built and operated. The main activities performed in the scope of this thesis are

- Formation of DFB concept
- Design and construction of cold model and performing cold model experiments
- Parametric study
- Suggestions to the test plant design
- Detailed hydrodynamic studies

The cold model is preliminary aimed at proving the feasibility of the DFB reactor system. Typical feasibility studies of a DFB system follows a sequence depicted in Figure 4. To begin with the cold model study, the main requirement is a basic design of the facility. This is comprised of the information regarding the

- Basic geometry of the FB (diameter, height, inlet location, exit location etc.)
- Operational conditions (temperature, pressure, gas composition, riser velocity, fluidization regimes)
- Particle properties (density, particle size distribution)

The scaling laws at this time come into the scene. The scaling laws were originally formulated by Glicksman [73–75] and later Horio [76]. They provided a useful tool to analyze the fluidization behavior in smaller scale and cold operating conditions. The scaling ratios generated from the scaling laws are a group of non-dimensional numbers. These non-dimensional numbers provide the basis for designing the cold model, performing experiments in cold conditions and comparing results of the cold model with the test plant. The detailed theory about scaling and practical use is elaborated in section 2.4. The cold model is designed, constructed and experiments are performed under scaled conditions. The results obtained are generally the riser pressure drops, solid fractions, riser entrainment rates, fluidization regimes and looping rates etc. These results are again extrapolated to the test plant conditions using scaling ratios. If the results match the test plant requirement then the basic design is finalized. Otherwise some changes in the basic design are suggested in terms of geometry,
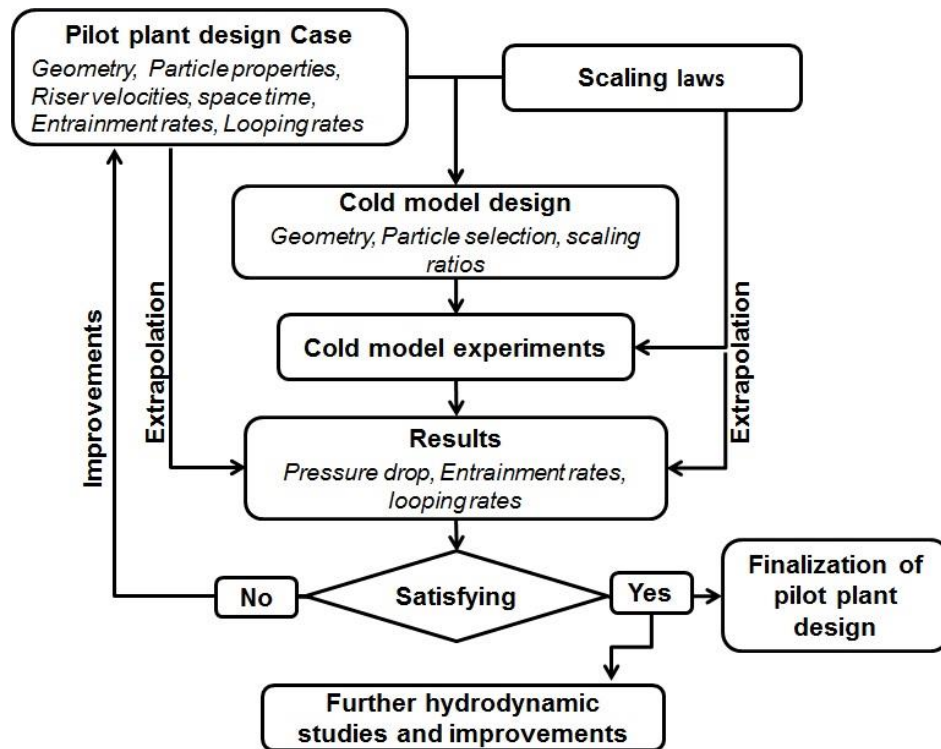
Figure 4- Typical feasibility study of a DFB system via cold model study sequence

operational conditions or particle selection. These changes may be tested again in the cold model (if possible) and if the changes bring satisfying results the facility design is then finalized.

In addition to the feasibility study the parametric study of the cold model is also an integral part of the research. In parametric studies, the influence of important operational parameters is tested especially to find out the operability of the DFB system, inventory distribution, effect on the solid entrainment flux and the solid looping rates etc.

1.5.2. Detailed hydrodynamic studies

The detailed hydrodynamic studies are carried out on different tasks. Over a period of time number of difficulties arose while operating DFB facilities. In order to solve such problems, it is necessary to understand the basics of the problem. Such understanding can only come through the detailed literature study or experimental study focusing on such problems. Some of the problems encountered in test operations are dealt in chapter 6 and 7 in detail.

1.5.3. Outline of the thesis

Before the manuscript of this thesis is formulated, the scientific work went through a peer review process and publications. In the course of this thesis author has published 7 papers as a lead author, where 3 papers are published in the journals and 4 papers in the conferences. The scientific content of these papers is used as the basis

of this thesis. Furthermore, the author has also contributed in as a co-author in 12 more publications including a chapter in a book, scientific content from these works is not used as a basis of this thesis but rather used as references. The list of publications is provided in the author's biodata.

The thesis is written in eight chapters and will follow a typical sequence of an experimental thesis. Introduction, state of the art, description of the experimental set up, description of experimental results and its analysis and followed by the summary. Chapter 2 is dedicated to the fluidization state of art, including fluidized bed hydrodynamics, dual fluidized bed systems and scaling laws. In chapter 3 detailed description of 200 kW_{th} DFB test plant is given. In addition, the description of the experimental set up is given and experimental methods are discussed. Chapter 4-7 are the core of the present thesis and present results and discussion of the experimental work done. Every chapter deals with the separate theme of investigation and summary of the chapter is presented at the end of the chapter. Chapter 4 and 5 are based on the hydrodynamic studies of the 200 kW_{th} DFB test plant at scaled cold conditions. Chapter 6 and 7 are about detailed hydrodynamic studies carried out in order to gain deeper understanding of the fluidized bed hydrodynamics, Chapter 6 is about the understanding of loop seal behavior and 7 is about estimation of friction pressure drop in a CFB riser. Chapter 8 finishes the thesis with outlook and some commentary about the future works.

2. State of the art - Fluidization

A fluid is clearly defined as a matter having ability to flow. Liquids and gases possess this ability while solids lack this ability. However, when fine solid particles come in contact with a liquid or a gas, these fine particles display fluid like behaviour i.e. ability to flow, they suspend and exert pressure, and when this phenomenon takes places in a closed volume this is termed as fluidization. In nature, a dust storm is an example of fluidization; mankind is using this phenomenon for commercial purpose since last century and continues to do so. This thesis is a small contribution to the ever evolving field of fluidization.

2.1. Commercial applications of fluidization and fluidized beds

The phenomenon of fluidization has a wide range of applications mainly related to the chemicals and process industry as well as the utility industry. Fritz Winkler from Germany patented and commissioned the first ever bubbling fluidized bed back in 1921 for the gasification of coal to produce water gas [9,77]. Since then the range of application of fluidized bed technologies continues to widen. The most common application is the process related to gas-solid catalytic reactions invented in 1940s. Fluidized beds offer many advantages and almost perfect conditions for such gas solid reactions compared to the other types of reactors. Therefore large numbers of fluidized beds as the catalytic reactors were built worldwide. The most famous applications is the fluidized catalytic cracking (FCC) process [78,79]. Other popular processes involving solid catalytic reactions are Fischer-Tropsch synthesis process [80], production of phthallic anhydride, acrylonitrilem, maleic anhydride, polypropylene etc. [79].

Another major commercial application of the fluidized beds is the combustion of solid fuels to generate heat or electricity through steam generation [9]. The combustion in fluidized beds offers many advantages over the pulverised coal (PC) firing technology [81]. The main advantage of the fluidized bed is fuel flexibility; a fluidized bed combustor can accept a wide range of fuel and fuel size compared to PC combustor [82]. Furthermore, a fluidized bed combustor is effective in pollutant emissions, mainly NO_x and SO_x emissions [81,83]. However, early fluidized bed combustors were limited in firing capacity of 250-300 MW_{el} compared to PC combustors, whose capacities are in scales of 800-1000 MW_{el} [84]. But recently, CFB combustors up to a capacity of 460 MW_{el} with supercritical steam parameters have been demonstrated [85]. Boiler manufacturers claim that firing capacity of CFB combustors will no longer be an issue and boilers up to the capacity of 800 MW_{el} can be built in future [86]. China is having the largest number of fluidized bed combustors units in the world [87]. Mineral processing is another process industry where fluidized

beds are used mainly for the purpose of roasting and calcination process [79,88]. In cement industry fluidized beds are preferred for pre calcination of limestone [89].

Above examples are those of large scale industries, in small scale process industry the fluidization is widely used for the purpose of mixing, drying, coating and granulation processes [79]. Medicine tablets are often coated in fluidized beds [90]. Fluidized bed dryers have a number of applications in the manufacture of milk powder, baby food, juices, dye pigments and chemicals [91]. The fertilizer industry effectively uses fluidized bed granulators for generating the desired product size [92]. These are some of the well-known applications of fluidized bed; among recent developments, HTSLC is a rapidly growing application, which combines the use of fluidized beds as gas-solid reactor and combustor.

2.2. Hydrodynamics of the fluidized beds

Hydrodynamics is a branch of fluid mechanics which deals with the motion of fluids. Solids are not fluids but in the fluidized bed conditions they are subjected to motion. Therefore, the term hydrodynamic is also applied to the fluidized bed. In a fluidized bed the solid particles display the fluid like properties in various ways.

- Static pressure in a fluidized bed at given level is equal to the weight of the solid per unit cross section above that level, non-fluidized bed doesn't display such static pressure.
- A denser object will sink into the bed and light object will float when it is fluidized. Without fluidization the objects will remain static.
- Solids can be drained from the nozzle of a fluidized bed like a stream of liquid, while in a non-fluidized bed such movement does not take place.

Compared to single phase fluids the flow in a fluidized bed is very complex due to the involvement of multiple phases and interaction between them, namely gas-solid, liquid-solid or gas-liquid-solid. This thesis will only deal with the gas-solid type of fluidization and all the discussions related to theory, experiments and results presented in this thesis are in accordance with the gas-solid fluidization.

2.2.1. Regimes of fluidization

The gas-solid interaction and its hydrodynamic behavior is fundamental to the science of fluidization. Change in a gas superficial velocity u_0 (volumetric flow rate of fluid divided by containers cross section) brings significant changes in gas-solid interaction and hydrodynamic properties; in fluidization these changes are called as ´regimes of fluidization`. Figure 5 illustrates different regimes of fluidization changing with increasing gas velocity. The particle bed is kept on a plenum and gas flow is introduced into the particle bed from below the plenum.

At very low gas velocity u_0, the gas travels only through the intra-particle gaps and no particle movement takes place. This regime is therefore called fixed bed or packed bed regime. Increasing gas velocity increases drag force on the particles and increases pressure drop (Δp) as shown in Figure 6. The pressure drop across the particle bed is predictable with the use of Ergun equation (see Eq.(10) [79]).

$$\Delta p = \left(\frac{150\mu(1-\varepsilon)^2 u_0}{(\varphi d_p)^2 \varepsilon^3} + \frac{1.75\rho_g(1-\varepsilon)u_0^2}{(\varphi d_p)\varepsilon^3} \right) H_{bed} \tag{10}$$

Where µ is the gas viscosity, ε is the voidage, φ is the particle sphericity, d_p is a mean particle diameter, ρ_g is the gas density and H_{bed} is the height of the particle bed.

Further increase in u_0 increases Δp, but at certain u_0 the drag force and buoyancy on the particles becomes equal to the weight of the particles. At this stage particles become fluidized and the bed shows ability to move or expand. The Δp does not increase any further with flow rate as shown in Figure 6. This condition is called minimum fluidization and the gas velocity at which this phenomenon occurs is called minimum fluidization velocity (u_{mf}). The term u_{mf} is of extreme significance in the field of fluidization. Several parameters, design values, scaling terms are often represented in terms of u_{mf} therefore accurate prediction is very important. The value of u_{mf} can be estimated experimentally or calculated using co-relations. Several empirical and semi-empirical co-relations are cited in the literature [79]. The most commonly used co-relation is given below in Eq. (11)

$$Re_{mf} = \frac{u_{mf} d_p \rho_g}{\mu} = [C_1{}^2 + C_2 Ar]^{0.5} - C_1 \tag{11}$$

Where Re_{mf} is Reynolds number at u_{mf}, $C_1 = 27.2$, $C_2 = 0.0408$ [93]. Ar is Archimedes number shown as Eq.(12).
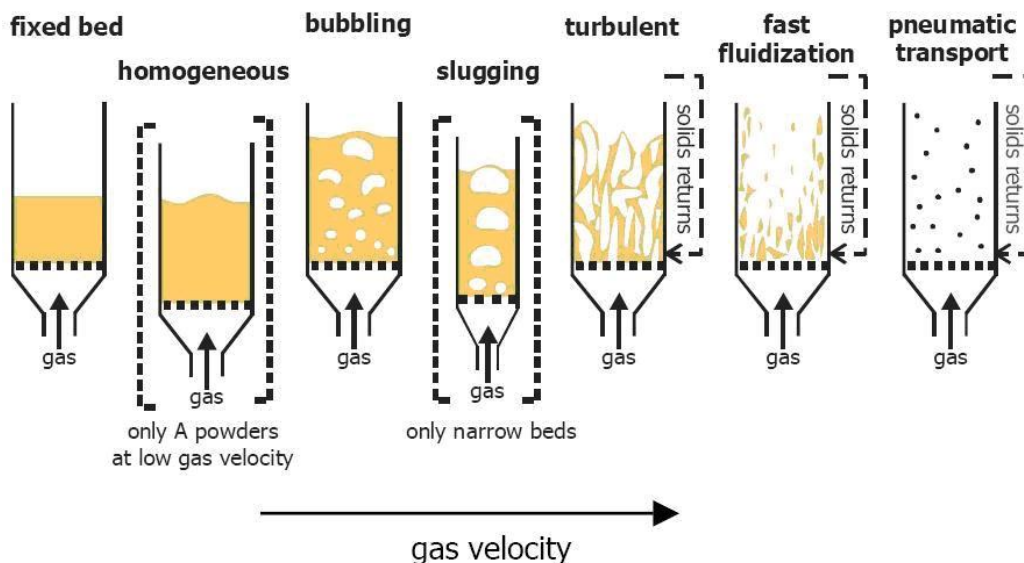
Figure 5 – Different regimes of fluidization observed with increasing gas velocity [196]
Note: A powders refer to Geldart A type powder
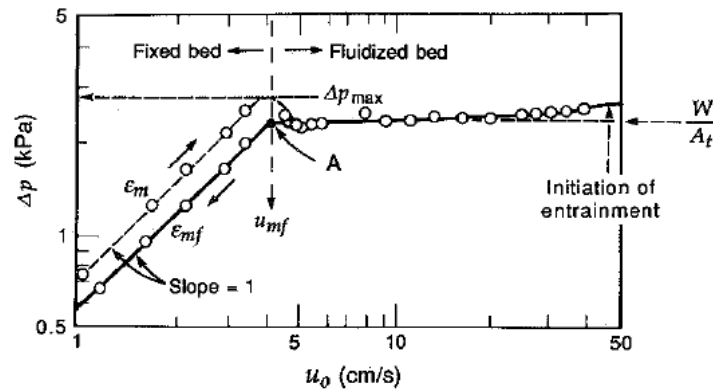
Figure 6 – Pressure drop vs velocity diagram in a particle bed [79]

$$Ar = \frac{\rho_g(\rho_s - \rho_g)g d_p^{\,3}}{\mu^2} \tag{12}$$

With further increase in the gas velocity above u_{mf}, the particle bed expands further and gas bubbles start to appear in the bed, giving appearance of a boiling liquid. This regime is called the bubbling regime and the velocity at which the first bubble occurs in the bed is called minimum bubbling velocity (u_{mb}). Respective co-relations of u_{mb} can be referred in the literature [94,95]. Further increase in u_0 above u_{mb} causes bigger gas bubbles to form. In narrow beds, these gas bubbles may become equivalent to the size of the container and cause further expansion of the bed. This regime is called slugging. Slugging is typical of small size beds, in larger beds the slugging regime may not occur since the bubbles do not become equivalent to the size of the container.

Further increase in u_0 causes the bed to expand even further and gradual change of regime from bubbling (or slugging) to turbulent takes place. The turbulent regime is marked with clear absence of bed surface unlike the packed bed or the bubbling bed. Rapid formation and coalescence of bubbles and particle entrainment out of bed is another main feature of this regime. The velocity at which particles are carried out of the bed is called as transport velocity denoted as u_t. Furthermore, the bed pressure is never constant but severely fluctuating. Therefore pressure drop is mainly represented as an average pressure drop. The magnitude of pressure fluctuations also change with increasing u_0: the magnitude of fluctuations reaches the maximum as shown in Figure 7 at gas velocity namely u_c [96,97]. Further increase in u_0 decreases fluctuations and fluctuations become stabilized at velocity u_k. The mathematical

Figure 7 – Pressure fluctuations variation in a fluidized bed with bed velocity

expressions for determining u_c and u_k are given in the literature [79] and are provided in Annex A. Despite of advances in the fluidization science, the exact nature of the turbulent regime is still debated, but generally it is accepted that the turbulent regime begins at u_c and ends at u_k [97]. This regime is preferred for the gas-solid reactions [98], mainly because this regime offers better gas-solid contact compared to bubbling and slugging regime.

With increased u_0 above turbulent regime, the distinction between bed and the freeboard disappears. Significant particle elutriation takes place and without the solid recirculation system the bed would become empty soon. This regime is called as the fast fluidization. This regime is a characteristic regime of the circulating fluidized bed (CFB) systems. However the fast fluidized regime is typically characterized with a dense particle concentration at the bottom of the bed and much leaner at the top. At even higher velocities, the entrainment is so significant that entire bed is very lean with particles, this regime is called the pneumatic transport. In the present thesis, the bubbling, the turbulent and the fast fluidized regimes are mainly under consideration.

The regime diagrams of fluidization have been in use for a long time, originally proposed by Reh [99]. The regime mapping has been made more easy by Prof. Grace [100] called as the Grace diagram is explained in detail in Annex A. The dimensionless particle diameter is plotted against the dimensionless superficial velocity and the position of the plot is compared with the indicated regimes on the diagram. At University of Stuttgart, Perez-Pulido [101] has developed a model to quickly identify the regime based on the Grace diagram.

Apart from the gas velocity, another main factor which is considered in hydrodynamics is a particle type. Geldart [102] has classified different particle types namely Geldart A, B, C & D particles. This classification is according to the fluidization behavior for particle size and density. The details of the classification and types are mentioned in Annex A. In the scope of the present thesis mainly Geldart B particles are used. Geldart B particles are sand like particles with particle size ranging from 40 µm-500 µm, furthermore for Geldart B particles minimum bubbling velocity and minimum fluidization velocity are nearly same (i.e. $u_{mb}=u_{mf}$) [103].

2.2.2. Bubbling and circulating fluidized bed

This section will discuss in detail about bubbling fluidized beds (BFB) and circulating fluidized beds (CFB), which are most commonly used types of fluidized bed reactors in HTSLC processes. The BFB operates in a typical bubbling regime and in a velocity range of 0.1 to 1 m/s (typical 0.5 m/s) for Geldart B particles. The particle bed is supported typically on a plenum or a distributor, the fluidizing gas is introduced in a wind box, which is an enclosed part below the distributor connected to a gas source. The gas distributor and wind box together ensure uniform distribution of the gas in a BFB. A BFB reactor is typically divided in a particle bed or bubbling bed zone and a

freeboard zone. The BFB has a very distinct surface, and the solid fraction (ε_s) is in the range of 0.3-0.5 depending on the gas velocity. The freeboard zone is almost devoid of solid fraction, only a few elutriating particles are observed here. The pressure drop of the bubbling bed (Δp_{bed}) is proportional to the weight of the particles or solid inventory (M) in the fluidized bed, calculated as Eq. (13)

$$\Delta p_{bed} = (1 - \varepsilon)\rho_s g H_{bed} = \varepsilon_s \rho_s g h_{bed} = \frac{Mg}{A} \tag{13}$$

Where, H_{bed} is the height of the particle bed in BFB, and A is area of the fluidized bed cross section (bubbling bed in this case). The pressure drop from suspended elutriating particles is negligible. The solid fraction ε_s, is related to voidage ε by Eq. (14).

$$\varepsilon_s = 1 - \varepsilon \tag{14}$$

In a BFB, the particle entrainment out of the bed is low, or none if free board zone is sufficiently long. Only very fine particles leave the bed, this is called as elutriation. The solid recirculation system is optional to the BFB, since the solid inventory leaving the system from elutriation is very low. The bed cross section in the freeboard zone is often made wider to ensure lower elutriation. The gas-solid flow in a bubbling fluidized bed is relatively simple. The average solid fraction of the particle bed is constant over the particle bed (h_{bed}) height. The particle bed is divided in two phases, a bubble phase and an emulsion phase. It is assumed that within the emulsion phase the gas travels at the minimum fluidization conditions, while the excess gas flow travels through the bubbles [79]. The gas in the bubble phase makes hardly any contact with the surrounding particles. Only the fraction of gas near the periphery of the bubble and gas in the emulsion phase can make sufficient contact. Several models for the gas solid flow in the BFB are proposed. Kunii-Levenspiel model [79] is most widely used model amongst them. Due to the poor gas-solid contact, BFB reactors are not the most ideal reactors for the gas-solid reactions, however they are suitable for processes in which the longer particle residence time is required, such as gasification. Nevertheless, simplicity of operation make them preferred FB reactor system in general.

A typical circulating fluidized bed (CFB) system is shown in Figure 8. A CFB system consists of riser and solid recirculation system. Riser is a long cylindrical part where particles flow upwards. Similar to a BFB the gas flow is introduced in a windbox, the gas distributor ensures equal distribution of the gas. The solid recirculation system is a vital part of a CFB system, consisting of gas solid separator e.g. a cyclone, a downcomer or standpipe and a non-mechanical valve e.g. loop seal, L-valve or J-valve. Recirculation system ensures continuous supply of the solid particles back to the riser, without the solid circulation system the riser would be empty within minutes.

Contrary to BFB, no distinct bed surface exists in a CFB and particles are distributed all over the riser. However, the solid distribution is not uniform in axial as well as in radial direction [104]. As shown in Figure 8, the bottom zone consists of higher concentration of particles or solid fraction (ε_s), this zone is called as dense bed
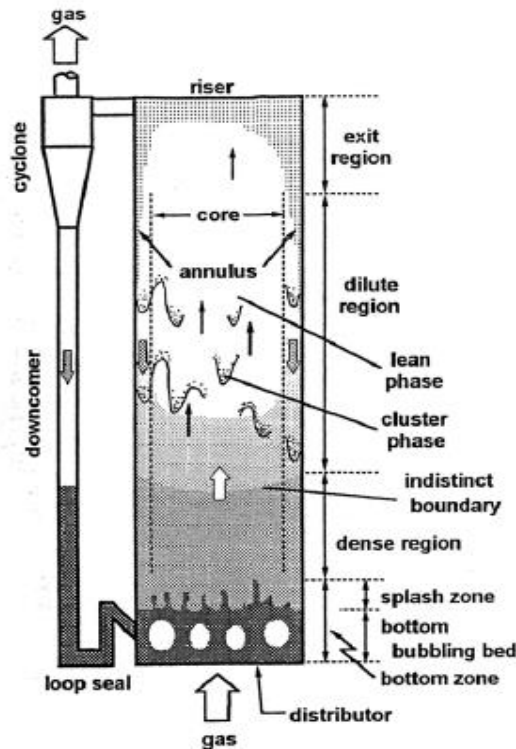
Figure 8 – A typical circulating fluidized bed CFB [100]

zone [105]. In most of the length of a riser the solid fraction is very low, this zone is called as lean zone or developed zone. Some works [106] have stated that there exists a region called transient region, in which solid fraction in the riser gradually decreases from the dense zone to the lean zone. This zone is also mentioned as acceleration zone [106]. In some risers it is observed that the solid fraction near the exit increases slightly [107,108], some particles in the exit region are recycled back into the riser instead of entraining out of the riser. Such recycling of particles causes increased solid fraction at the exit and the phenomenon is called as exit effects [107]. In radial direction, the solid fraction in the center of the riser is less compared to the wall region shown in Figure 8. The particles flow typically in a core annulus structure [109]. In the core zone with lower solid fraction particles travel upwards, while in the annular region near to the wall the particles with higher solid fraction, travel downwards. There is constant exchange of particles between core and annular region. Numerous authors [105,107,110–113] have modeled this complex gas solid flow in CFBs. More advancements are expected in this research area of fluidization in the near future.

2.2.3. Pressure drop in a CFB riser

The pressure drop in the CFB can be measured from Eq.(13) or the average solid fraction from a known pressure drop can be measured, but main problem with Eq.(13) in applying to a CFB riser, is that the solid fraction (ε_s) in a CFB riser changes significantly over the height of the CFB riser. Therefore Eq.(13) can only be applied to a CFB riser with an integral and ε_s as a function of riser height. Apart from the weight

of the particles, additional pressure drop is caused by the friction between gas and solid, solid and wall and the acceleration of the particles. Thus total pressure drop in a CFB system can be formulated as in Eq. (15) [107].

$$\left(\frac{dp}{dH}\right)_{total} = \left(\frac{dp}{dH}\right)_{static} + \left(\frac{dp}{dH}\right)_{acc} + \left(\frac{dp}{dH}\right)_{fr\,g} + \left(\frac{dp}{dH}\right)_{fr\,s} + \emptyset \qquad (15)$$

Where $\left(\frac{dp}{dH}\right)_{static}$ is the static pressure drop due to the weight of the particles, $\left(\frac{dp}{dH}\right)_{acc}$ is the pressure drop due to the acceleration of the particles, $\left(\frac{dp}{dH}\right)_{fr\,g}$ is the pressure drop due to the friction between gas and particles and $\left(\frac{dp}{dH}\right)_{fr\,s}$ is the pressure drop due to the friction between solid particles and wall of the riser. $\emptyset$ is an additional pressure drop caused by the energy dissipation in dense region of the riser, suggested by Zhu & You [114]. The individual pressure drops can be calculated using the Eq. (16) to (19)[107,115,116].

$$\left(\frac{dp}{dH}\right)_{static} = \rho_g g\,\varepsilon \,+\, \rho_s g\,(1-\varepsilon) \qquad (16)$$

$$\left(\frac{dp}{dH}\right)_{acc} = \frac{d}{dH}\left(\rho_g g\,\varepsilon U_g{}^2 + \rho_s\,(1-\varepsilon)U_s{}^2\right) \qquad (17)$$

$$\left(\frac{dp}{dH}\right)_{fr\,g} = \frac{2f_g \rho_g\,\varepsilon\,U_g{}^2}{D} \qquad (18)$$

$$\left(\frac{dp}{dH}\right)_{fr\,s} = \frac{2f_s \rho_s\,(1-\varepsilon)U_s{}^2}{D} \qquad (19)$$

Eq. (16) is similar to Eq.(13) with an addition of weight of the gas ($\rho_g g\,\varepsilon$), the static pressure drop of gases is minuscule therefore mostly neglected. In Eq. (18) and Eq. (19) f_s and f_g are solid and gas friction factors and D is riser diameter. Rautiainen et al. [115,117] have presented a detailed study about the friction factors.

Several experimental and modeling works have confirmed that the pressure drop due to friction and acceleration may be significant. However, the information is very scarce. The experimental works like [118,119] have confirmed the influence of friction and acceleration in a CFB. These works show that the actual solid fraction (obtained from optical fiber probes) of the particles in a CFB is lower than the apparent solid fraction (obtained from Eq.(13)). The magnitude of friction pressure drop based on the difference between the actual to apparent suspension density is found in the range of 20-40% [120]. Pugsley & Berruti [107] found that their model is close to the experimental results only when the acceleration and friction terms (Eq. (17) to Eq. (19)) were included in addition to the static head (Eq. (16)) term in the model. Thus, pressure drop due to friction and acceleration occurs and it could be significant. However, the magnitude of frictional and acceleration losses reported in literature shows significant variation, but most of these works agree over the significant acceleration pressure drop

in the acceleration zone but disagrees over the losses in other zones of the riser [107]. Qi et al. [116] found that the friction pressure drop in the upper dilute region is significant and gas velocity plays an important role in the extent of friction pressure drop in a riser. In the scope of this thesis efforts were made to determine the magnitude of the friction and acceleration pressure drop for calcium looping process. Chapter 7 deals with the topic in detail.

2.2.4. Solid entrainment in a CFB

The solid particle flow leaving from riser exit is called entrainment or solid circulation. It is generally represented as riser solid flux (G_s) in kg/m²s, which is solid circulation rate (G) in kg/s divided by the area of the riser. Solid circulation from CFB may be significant. Based on the circulation rates the CFB risers are classified as high flux CFB riser and low flux CFB risers [121]. The high flux CFB risers have typical G_s above 200 kg/m²s and are widely used as FCC risers, with Geldart A particles. The high flux or low flux depends primarily on the type of particle, solid feeding device and the operational velocity [121]. Table 4 shows the difference between high flux and low flux CFB risers.

Table 4 – High flux and low flux CFB risers

	High flux CFB risers	Low flux CFB risers
Solid flux	200-1200 kg/m²s	5-200 kg/m²s
Velocity	6 – 28 m/s	2-8 m/s
Particle type	Typically Geldart A also with B with suitable velocity and solid feeding	Mainly with Geldart B
ε_s developed zone	3% to 12% [121]	0 to 2% [9,121]
Solid residence time	Very low	High
Solid feeding	Orifice, mechanical feeder, L-valve	Non mechanical valve e.g. loop seal,
Standpipe diameter	More than D_{riser}	Smaller or equal to D_{riser}
Example	FCC risers	CFB combustors

Mathematically riser entrainment flux is expressed as Eq. (20) [122].

$$G_s = (1 - \varepsilon_{exit}) \, \rho_s \, (u_0 - u_t) \tag{20}$$

where ε_{exit} is the voidage value of exit region of the riser. u_t is called terminal velocity, the gas velocity above which the particles begin to leave the riser in the form of solid circulation. For HTSLC processes, the solid entrainment rates provide the reactant flow and heat flow to carry out necessary reactions of HTSLC. The riser entrainment requirements for different HTSLC processes are shown in the following Table 5. These calculations are based on simple mass and energy balance calculations. It is clear from the Table 5 that for HTSLC the entrainment requirements are well below 200 kg/m²s. Therefore low flux CFB risers are typically required for the HTSLC processes, except steam gasification, where due to the low temperature difference between the gasifier and combustor and strong endothermic reaction the required entrainment rates may

exceed 300 kg/m²s [123]. Guan et al. [124,125] have proposed a design with a moving bed in the return leg to enhance the solid flux. Recently University of Stuttgart proposed a preliminary concept of high flux triple fluidized bed system for a steam gasification process [126]. However, for most of the HTSLC processes the CFB system similar to CFB combustor is appropriate.

Table 5 : CFB entrainment rates required for HTSLC processes

Sr No	Process	ΔT between two FB °C	G_s kg/m²s	Ref
1	CaL	250	10-20	[71]
2	CLC	50	30 – 80[a]	[127]
3	SER	200 – 250	3-12	This work
4	Steam gasification	50	>300	[123]
	a- For 100% MeO content			

2.2.5. Solid recirculation system

As discussed earlier, due to significant entrainment of particles in a CFB the inventory in a riser would empty within a matter of minutes. A solid recirculation system ensures the return of the entrained particles back into the CFB riser without affecting the gas-solid flow direction in the CFB. The particles are separated from gases in the cyclone and they travel through a downcomer or standpipe to solid recirculation device. Various types of mechanical such as cone valve, or non-mechanical valves are used as solid recirculation device like loop seal, L-valve or J-valve. In high temperature application like combustors or in HTSLC processes the non-mechanical valves are preferred since they don't have moving parts. The application of L-valve, loop seal and cone valve are under consideration in the present work.

The L-valves are widely used as non-mechanical valves especially in high flux CFB risers. The main advantage of L-valve is its ability to generate significantly higher circulation rates [128] and control of solid circulation rates. Secondly it requires less aeration compared to other non-mechanical valves. As shown in Figure 12 the L-valve is a L-shaped device. The vertical arm of the L-valve also acts as a downcomer, and is usually connected to the cyclone. The aeration port is usually provided on the vertical arm and slightly above the horizontal arm level as shown in Figure 12. The preferred location of aeration is 1.5 D [129] from the bottom of the L-valve. When the port is aerated the solid flow is initiated through the L-valve. The solid flow is proportional to the aeration rates [129–131]. The flow through the L-valve is widely studied and the precise solid flow with aeration rate can be predicted using the models from Arena [130], Smolders [129] and Geldart [131]. The solid downflow in the vertical arm of the L-valve is necessarily a fixed bed flow. The solid flow in the horizontal section is complex, the upper surface is more fluid like where solid particles flow in pulses, the lower part of horizontal section is somewhat like dead zone with little particle movement. The effectiveness of L-valves is limited in case of coarser particles.

Loop seals are also widely used in CFB, mainly in low flux CFB risers like CFB combustors. They provide an excellent pressure seal between the high pressure side of CFB bottom and low pressure cyclone side. However loop seals are less known for their control of solid flow but are considered as pass through device. Some useful information on standpipe and loop seal systems can be referred in books on fluidization [9,79,109]. Basu and co-workers provide a very useful insight of loop seal operation [132,133] and most importantly provide useful guidelines for designing a loop seal and standpipe systems in this work [9].

The typical loop seal standpipe arrangement is shown Figure 9. The loop seal itself consists of two sections, the supply section and the recycle section. The supply section is fed with a particle flow from the riser cyclone. The standpipe is between the cyclone bottom and top of supply section of the loop seal. The recycle section is next to the supply section and shorter. The particle height in the recycle chamber is fixed, this height is often referred as weir height. The pipe after weir overflow is called return leg (CFB system). It connects loop seal with the riser or the transfer leg (DFB system) connecting the other reactor. In a CFB operation the loop seal works when it is fluidized at the bottom. If the aeration and the particle height in the standpipe is enough to generate pressure higher than the riser, the particles in the recycle chamber are pushed into the riser. In a CFB system the bottom of the loop seal is the highest pressure point in the system. The fluidization in the loop seals may be given separately in both sections of the loop seal or may be together in both sections. Some loop seals also employ additional side aeration on the supply side [134]. The solid downflow, within the standpipe and loop seal (supply section) occurs in three modes as explained by Knowlton [109]. The dilute mode occurs above particle bed height, when particles rain down from cyclone. Below the particle height level solid flows in bubbling fluidized mode or moving bed mode. The regime in the recycle side of the loop seal is necessarily a bubbling.
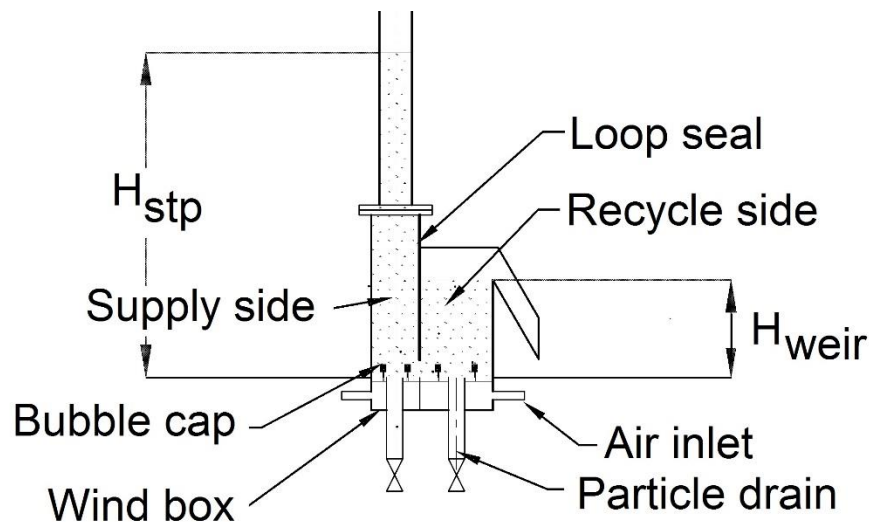
Figure 9 – Typical standpipe loop seal arrangement

In a moving bed condition the pressure drop in the standpipe or supply side of the loop seal can be estimated using the equation shown below in Eq. (21) [133].

$$\Delta p_{stp} = \left(\frac{\Delta p}{dH}\right)_{stp} H_{stp} = \left(\frac{150\mu(1-\varepsilon)^2}{(\varphi d_p)^2 \varepsilon^3}|U_{sl\,stp}| + \frac{1.75\rho_g(1-\varepsilon)}{(\varphi d_p)\varepsilon^3}|U_{sl\,stp}|^2\right) H_{stp} \tag{21}$$

Eq. (21) is a modified Ergun equation (Eq. (10)), the slip velocity $(U_{sl\,stp})$, is the relative velocity between gas and solid within the standpipe and is defined by Eq. (22).

$$U_{sl\,stp} = U_{s\,stp} - U_{g\,stp} \tag{22}$$

where $U_{s\,stp}$ and $U_{g\,stp}$ are the real velocity of gas and solid in the standpipe respectively. For solid flow downward flow is assigned a positive sign while for gases the downward flow is assigned a negative value.

The pressure drop in the recycle side of the chamber and bubbling mode standpipe can be estimated using Eq. (13). A moving bed or bubbling standpipe is common in CFB applications and is considered to be stable. However, in small scale facilities, slugging may occur as a result of small scale standpipe diameter and is threatening operational stability. Despite of simplicity and easy operation the loop seals and standpipes are little understood [103]. Little information and design data are available in comparison to other aspects of fluidization. Some thumb rules for design are provided by Basu [9] but these rules may not be suitable in every application. During past experimental campaigns on DFB systems of University of Stuttgart, an instability [44,71] in the standpipe and loop seals lead to frequent halting of operation. Therefore the design thumb rules of Basu [9] are questioned.

2.3. Dual fluidized bed systems

The dual fluidized bed (DFB) reactor system is a preferred reactor system for the HTSLC processes. A DFB system is a combination of two fluidized bed reactor systems with an interlinking for solid transport between the two fluidized beds. The DFB system offers a convenient transport of the solid reactants from one reactor to the other without mixing the gases between the two reactors. Figure 10 shows a typical example of DFB system. Theoretically FCC systems also use a DFB system, and are in use since the 1940`s. Every catalytic reaction with catalyst regeneration is carried out in a DFB system. As per Corella et al. [60] the DFB systems of FCC reactors or catalytic reaction system typically use the CFB as one reactor and downcomer-seal pot arrangement as the second reactor, while the gasification DFB or HTSLC DFB require a separate FB reactor for different reaction steps. Table 6 shows the number of DFB facilities all over the world currently under operation for different HTSLC processes.

A classification of DFB systems is not reported in the literature; however DFB classification is suggested in this work based on the type of FB reactors used and the
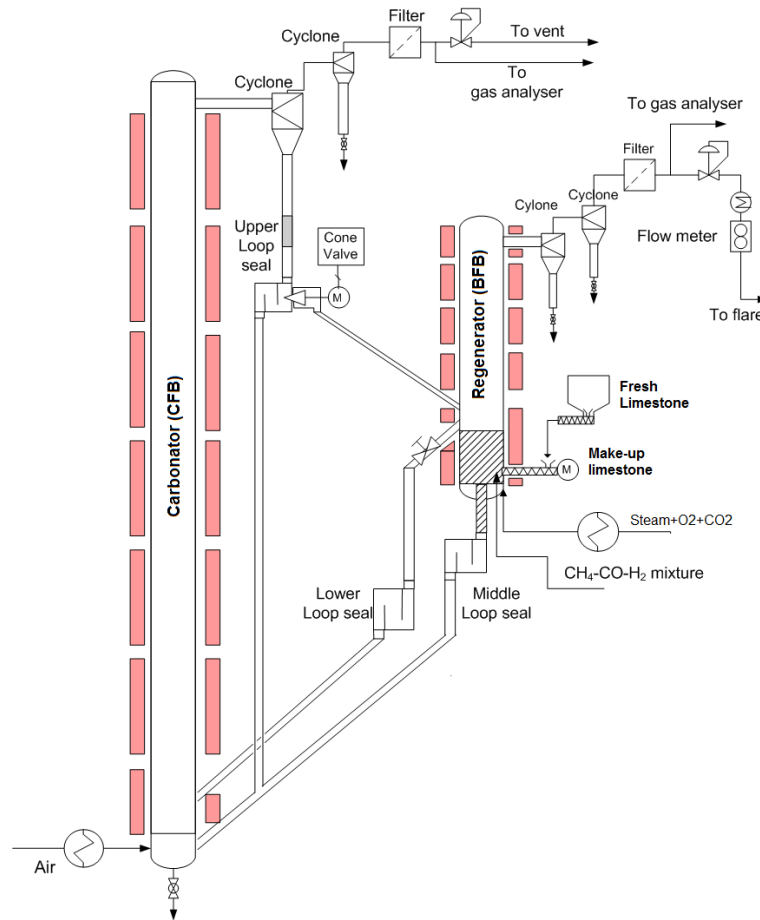
Figure 10 – 10 kW$_{th}$ electrically heated bench scale test plant facility at University of Stuttgart, (DIVA-ELWIRA)

type of interlinking used. Three combinations of FB reactors are possible in DFB systems and are shown in Figure 11.

- BFB – BFB
- BFB – CFB or CFB – BFB
- CFB – CFB

In BFB-BFB type system both reactors are operating in a bubbling regime or may be operable in a turbulent regime. BFB-BFB systems are easy to operate and are suitable for small scale or a lab scale installation or where the use of BFB reactors is required. Since BFB do not generate large enough solid entrainment, the solid transfer between the two beds is achieved with the help of pneumatic transport or with the use of an extra CFB riser.

BFB-CFB type is the most widely used DFB system, suitable for small to large scale systems. The CFB risers act simultaneously as reactor and generate solid circulation required for solid looping. The solid transport from BFB to CFB is generally under gravity with a loop seal (in between) to prevent gas mixing. It is also a preferred combination for steam gasification system, where BFB is gasifier and CFB is combustor [60]. The largest DFB system based on this type is 8 MW$_{th}$ in Güssing, Austria [69]. The CFB-CFB type is the preferred choice for large and commercial scale installations due to the inherent advantages offered by the CFB. Till date the largest

29
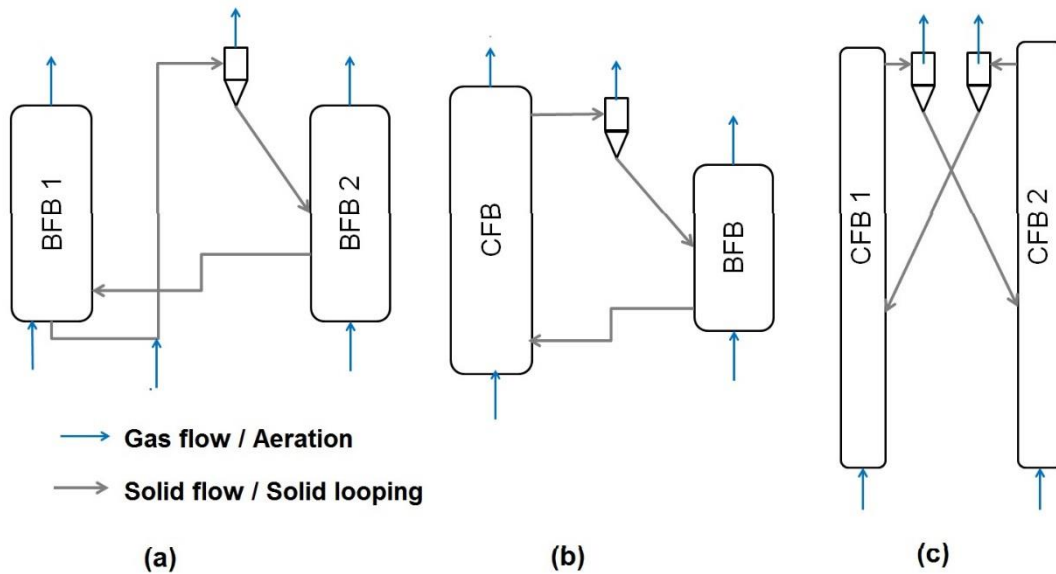
Figure 11 – Types of DFB system based on the combination of fluidized beds (a) BFB - BFB (b) BFB – CFB (c) CFB - CFB

installation for CFB-CFB type is 1.7 MW_{th} CaL pilot plant at La-Pereda. Compared to other two types of DFB systems the operation of this system could be challenging. Two approaches are used presently to carry out solid looping. In the first approach both CFB operate independently, with a diversion (complete or partially) of solid flow from both the loop seals takes place. This approach is used in the present work, as well as at INCAR-CSIC [47], TU Darmstadt [50,135] and La-Pereda unit [11]. In the second approach as used by TU Wien [136], both the CFBs are interlinked at the bottom via loop seal and solid circulation generated from one of the CFB is transported to the neighboring CFB.

The interlinking of the fluidized bed is very important in DFB systems; its primary function is to transport solid particles from one fluidized bed to other, without mixing the gases between them, or in other words solid looping between them. The solid flow rate between the reactors is called as the ´solid looping rate` denoted as ´$G_{L_i}$`, where i is the type of interlinking used. Several types of interlinking are in use namely loop seals, double exit loop seals with a mechanical valve, L-valve, pneumatic transport and mechanical conveyor. Figure 12 shows the schematics of different types of interlinking applied in various DFB facilities across the world.

Loop seals are commonly used in single loop CFB systems and also most commonly used for interlinking between the two fluidized beds [47,53,137–140], for DFB applications the supply side of the loop seal receives the particles from FB1 and recycle side of the loop seal is directed towards FB2. The main advantage of loop seal is that there are no mechanical or moving parts; it is simple in construction and operation; and mainly provides a very good pressure sealing between the reactors.

Table 6- DFB facilities across the world

Sr	Location	Process	Size	Type and interlinking	Ref
1	University of Stuttgart	CaL, SER, CLC	10 kW$_{th}$	CFB- BFB Double exit loop seal and cone valve	[34,43,63,141]
		CaL SER	200 kW$_{th}$	CFB-CFB (Car- Reg) CFB-BFB (Ga- Comb) Cone valve, L-valve	This work
2	SPE-TUHH, Hamburg	CLC		CFB-BFB, (AR- FR) Loop seal	[142]
3	Güssing, Austria	Gasification SER	8 MW$_{th}$	BFB – CFB (Ga- Comb) Loop seals	[69]
4	TU Wien, Austria	CLC	120 kW$_{th}$	CFB- CFB (AR – FR) Loop seals	[136]
		Gasification SER	100 kW$_{th}$	BFB-CFB (Ga- Comb) Loop seals	[53,62]
6	TU Darmstadt, Germany	CaL and CLC	1 MW$_{th}$	CFB – CFB (Car- Reg and AR- FR)	[50,135]
7	La Pereda, Spain	CaL	1.7 MW$_{th}$	CFB- CFB (Car- Reg) Double exit loop seal	[11]
8	Chalmers, Sweden	CLC	10 kW$_{th}$	CFB- BFB (AR – FR)	[138]
		CLC (coal)	100 kW$_{th}$	CFB-BFB (AR-FR) Loop seals	[143]
11	ICB-CSIC, Spain	CLC	0.5 kW$_{th}$	BFB-BFB (AR-FR)	[144]
		Gasification CLC	10 kW$_{th}$	BFB-BFB (AR-FR)	
12	INCAR circe Oviedo, Spain	CaL	30 kW$_{th}$	CFB- CFB (Car-Reg) Loop seals	[47]
13	CANMET, Canada	CaL	75 kW$_{th}$	CFB – BFB (Car-Reg) Loop seals	[42]
14	Ohio State University, USA	CaL	25 kW$_{th}$	Interconnected Moving bed-Entrained bed	[38]
15	IFP-Total, France	CLC	10 kW$_{th}$	BFB – BFB (AR-FR) Pneumatic transport	[145]
16	Dalhousie University, Halifax	SER	0.2 kg/h	CFB-BFB (Ga- Comb)	[67]
17	Southeast University, China	CLC, Gasification	10 kW$_{th}$	CFB-spouted bed	[146]
18	KITECH Cheonan, South Korea	Gasification	200 kW$_{th}$	BFB – CFB (Ga- Comb) Loop seals	[137]
19	Cranefield, UK	CLC, CaL	25 kW$_{th}$	CFB-BFB (Car- Reg)	[53]

AR: Air reactor, Car: carbonator, Comb: combuster, FR: Fuel reactor, Ga: Gasifier, Reg: Regenerator
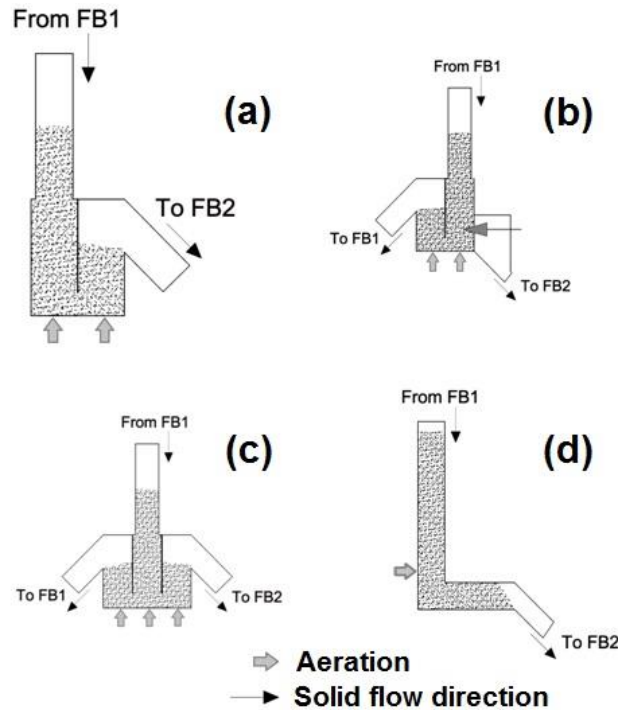
Figure 12 – Types of interlinking (a) loop seal (b) loop seal with cone valve (c) double exit loop seal (d) L-valve

However, there are few disadvantages of using loop seals in a DFB system.

- Loop seals offer no or very little control over global circulation rate, the control of global circulation rates should be initiated by other means
- No internal circulation with FB1
- Sealing is ineffective in highly fluctuating FB operation
- The aeration requirement is high therefore may become source of dilution (in small scale units) for product gases in FB2.

The double exit loop seal with a mechanical valve (Figure 12b) is an effective solution to deal with the disadvantages of the loop seal. This type of interlinking consists of a normal CFB loop seal for FB1 with a small variable orifice (valve e.g. cone valve) on the supply side of the loop seal to facilitate particle flow to the FB2 as shown in Figure 12b. In industry this configuration is used in FB combustors for solid supply to external heat exchangers [147]. University of Stuttgart has been using this type of interlinking [34,43,52,59,71,72] and aims to develop it further.

The cone valve can control the solid flow rate precisely. Cone valve characteristics are studied in [71] whereas Eq. (23) shows that the cone valve flow rate is linear to the pressure drop across the valve [71] while some other studies show it as a square root of the pressure drop [148].

$$G_{L_{CV}} = k \, A_{CV} \Delta p_{CV}^n \text{ (where n = 1 [71], n = 0.5 [148])} \tag{23}$$

Unlike an L-valve and a loop seal the cone valve is a type of mechanical valve and commonly used in CFB combustors for the application of external heat exchangers. L-valves are commonly used in single loop CFB systems. L-valves in DFB application are seldom but recently cited [149,150]. The application of L-valves in DFB systems has a considerable potential mainly because

- they allow very precise and repeatable control of solid looping rates
- they require less aeration therefore less dilution of the product gases

The use of high superficial gas velocity ($u_0 > 10$ m/s) namely in pneumatic transport regime as a means of solid conveying is common in process industry. A similar principle is used in DFB application as a means of interlinking. This mechanism is suitable for BFB-BFB units where fluidized beds cannot generate enough global circulation rates due to lower superficial velocities [42,49,149,151]. Screw conveyors are widely used for solid conveying and are primarily used in fluidized beds for feeding fuel and bed material. However screw conveyors as a means of interlinking are rare and cited only at 1 MW$_{th}$ DFB facility at Darmstadt [50].

The concept of double exit loop seal (Figure 12c) is inspired from the multiple exit loop seals used in FBCs to ensure uniform distribution of recycled particles. For DFB application this type of interlinking is cited in the literature [136] interestingly at La-Pereda CaL DFB facility in Spain [11,152]. The two exits in the loop seal are basically to facilitate global circulation and internal circulation without the application of moving parts. However, the success of this configuration is questionable, because in practice the pressure between two fluidized beds is different unlike FBC where multiple exits enter in the same FB. The control of global circulation rates will be a major concern in such configuration.

2.4. Scaling theory and cold model studies

Cold model studies are widely used to study the fluidization and support the design of complex fluidized bed systems [153,154] as used in present study. Cold models studies may be scaled or non-scaled ones. The scaled ones are mainly based on the application of scaling relationships developed by Glicksman [74,155] and Horio [76]. Simplified scaling relationships [155] shown in Eq. (24) are a set of dimensionless numbers.

$$\frac{u_o^2}{gL}, \frac{\rho_s}{\rho_g}, \frac{u_o}{u_{mf}}, \frac{L_1}{L_2}, \frac{G_s}{\rho_s u_o}, \frac{\Delta p_{riser}}{\rho_s g D_{riser}}, \phi, PSD \tag{24}$$

These dimensionless numbers provide an opportunity to imitate the high pressure and temperature fluidization conditions; at ambient conditions in transparent containers. This facilitates hydrodynamic studies, such as understanding fluidization behavior, gas-solid flow patterns, fluidization regime, pressure profiles and entrainment

$$\frac{u_o^2}{gL},$$

$$\frac{\rho_s}{\rho_g},$$

$$\frac{u_o}{u_{mf}},$$

$$\frac{L_1}{L_2},$$

$$\frac{G_s}{\rho_s u_o},$$

$$\frac{\Delta p_{riser}}{\rho_s g D_{riser}},$$

$$\phi, PSD$$

DFB Geometry

Particles

Particle size

Operational velocities

Entrainment flux and rates extrapolation

Pressure, inventory and solid fraction extrapolation
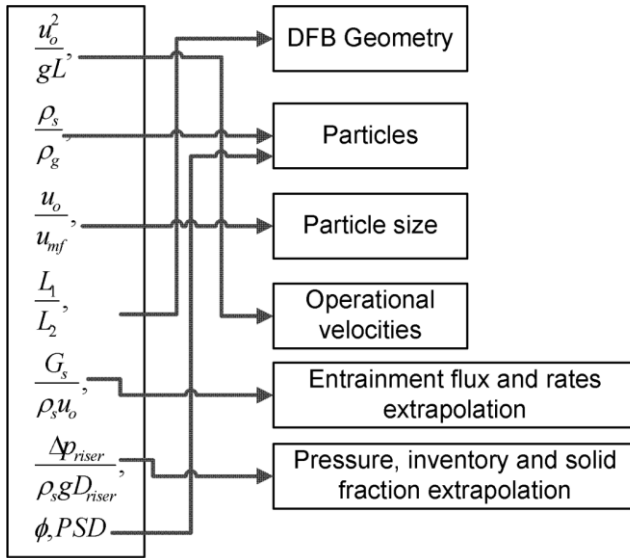
Figure 13-Application of scaling laws for the cold model design and extrapolation of results

flux measurements, which otherwise is difficult in an enclosed high temperature-pressure fluidized bed system.

Figure 4 shows the general methodology for the cold model studies, primarily inspired from Kehlenbeck [156]. To begin the work for designing the cold model we need a basic pilot plant design, the geometry of the pilot plant, the particles to be used, the required inventories and the entrainment rates. The cold model is designed from the application of scaling laws, which primarily means matching the dimensionless numbers of the Eq. (24) of hot test plant and cold model at ambient conditions. It is important to note that since this thesis is primarily comparing between hot or real scale test plant and a cold model, therefore the same notations and abbreviations are used. However, all the notations and abbreviations related to the test plant are denoted by an ´Acute´ accent. (e.g. $ú_0, Ĺ, Ḋ, Ǵ_s$ etc.), while the notations and abbreviations related to cold model are without such accent (e.g. u_0, L, G_s etc.).

The cold model design follows the following steps shown in Figure 13. Initially the geometry of the cold model is finalized, the length (L_1) and the diameter (L_2) are the major dimensions. The geometry number $\left(\frac{L_1}{L_2}\right)$ of Eq. (24) for the cold model and test plant should be matched. Thus

$$\left(\frac{Ĺ}{Ḋ}\right) = \left(\frac{L}{D}\right) \tag{25}$$

In practice, a geometric ratio ($Ḋ/D$) is selected and the dimensions of the cold model are finalized using the test plant dimensions. Choosing a suitable geometric ratio is important because the cold model should be small enough to facilitate ease of construction and operation of the set up. Secondly it shouldn't be too small so that the wall effects do not play a significant role in hydrodynamics of the fluidized bed [73]. To select the density of the particles required in the cold model the density $\left(\frac{\rho_s}{\rho_g}\right)$ ratio of Eq. (24) is used as

$$\left(\frac{ṕ_s}{ṕ_g}\right) = \left(\frac{\rho_s}{\rho_g}\right) \tag{26}$$

The particle size is chosen in such a way that the fluidization number $\left(\frac{u_0}{u_{mf}}\right)$ is constant for cold model and test plant, since u_{mf} is a function of particle size (see Eq. ((11)). For the selection of scaled velocity for the cold model operation the Froude number $\left(\frac{u_0^2}{gL}\right)$ is used. The scaling relation of operational velocity between the cold model and test plant is thus

$$\frac{\acute{u}_0}{u_0} = \sqrt{\frac{\acute{L}}{L}} \tag{27}$$

During cold model experiments the entrainment flux and pressure drop in various parts of the riser are primarily measured. The extrapolation of entrainment flux and pressure drops can be extrapolated to the test plant using the following relations. The extrapolated pressure drop can be converted to weight and solid fraction using the Eq. (13) and calculations of space time and looping ratio can follow.

$$\frac{\acute{G}_s}{G_s} = \frac{\rho_s \acute{u}_0}{\rho_s u_0} \tag{28}$$

$$\frac{\acute{\Delta p}}{\Delta p} = \frac{\rho_s \acute{D}}{\rho_s D} \tag{29}$$

Numbers of DFB cold model studies have been reported recently. Cold model studies for Chemical looping combustion and DFB gasification processes are more in number. Table 7 shows the overview of the DFB cold model studies worldwide.

It is a well known fact that the scaled cold model studies have considerable limitations, therefore the design of larger facilities based on the scaled cold model studies should take sufficient information from the cold model studies and integrate with prior experience and engineering judgement [157]. A major well known limitation is the inability to match all the scaling ratios exactly. To find exactly matching particles with exact PSD is an extremely difficult task. Also the construction of exactly similar components at lower scale in glass or plastic becomes difficult. Furthermore the Geldart classification of the scaled particles should be the same as the test scale particles [103]. In the present work a major limitation of scaled cold model studies is foreseen as the reaction. The carbonation reaction will absorb a major fraction (ca. 10-15 vol%) of gases in carbonator and in the regenerator extra gas flow will be generated (Ca. 20-30 vol%). This fact will affect the riser hydrodynamics to a large extent and in cold model studies it is impossible to create such an effect. Furthermore intra particle forces and electrostatics have an influence on the FB hydrodynamics and are unaccounted in the scaling laws [73]. Nevertheless the scaled cold model studies or in general cold model studies have been used to reduce the uncertainty of the pilot plant designs. Hofbauer et al. [53] mentioned that the predictions of the cold model studies proved sufficiently accurate for the pilot plant. Therefore the outcome of this work will

Table 7 – List of DFB cold model studies performed across the world

Sr No	Location	Process	Size/Scale●	Details	Ref
1	University of Stuttgart	CaL, SER CLC	10 kW$_{th}$	CFB- BFB loop seal and cone valve	[71,72,141]
2	Tsinghua University, Beijing China	CaL	-	BFB – BFB Pneumatic transport	[49]
3	TU Wien	Gasification	100 kW$_{th}$	CFB-BFB	[53,156,158]
4	IIS, Tokyo University Japan	Gasification	-	CFB-Downcomer-Standpipe High flux concept	[124]
5	KITech, Korea	Gasification	-	CFB-BFB	[159]
6	CMERI, Durgapur India	Gasification	-	CFB- BFB L-valve	[150]
7	Italy	Gasification	-	CFB- BFB	[160]
8	Norway	CLC	-	CFB –CFB Double exit loop seal	[152,161]
9	IET, TU Hamburg	CLC	-	CFB- BFB Two staged BFB	[162]
10	WKU, USA	CLC	10 kW$_{th}$	CFB-BFB	[163]
11	VTI, Moscow	CLC	-	CFB-CFB	[164]
12	Chalmers, Sweden	CLC	-	CFB- BFB	[122]
13	IFP, Lyon [149]	CLC	-	BFB – BFB Pneumatic transport	[149,165,166]
14	TU Wien	CLC	120 kW$_{th}$	CFB-CFB	[140]
15	KIER, Daejeon Korea	HTSLC	-	BFB- BFB	[151]

● This value mentions the firing capacity of the test plant or pilot plant for which the cold model is built

- No information of the size or scale available

be crucial in further design and operation of the 200 kW$_{th}$ test plant at University of Stuttgart.

3. Conceptual design of the 200 kW$_{th}$ DFB test plant and experimental-cold model set up

After successful demonstration of the calcium looping (CaL) process [34,43] and the sorption-enhanced reforming (SER) process [59] in the 10 kW$_{th}$ bench scale test plant at University of Stuttgart, the main task is to demonstrate both the processes at a larger scale. The 10 kW$_{th}$ bench scale set up consists of an electrically heated reactor system, the required heating of the reactors and the sorbents is provided by the external electrical heating system. But in actual industrial scale if the process needs to be scaled up, then the electrical heating systems are not at all practical. The sorbents will be required to heat with the help of combustion of fuels. Therefore at higher scales the chemistry of the process will be different than the electrical heated system and will show its influence on the process. Therefore, before the large commercial scale projects are taken up, it is necessary to study the above mentioned aspects of the process and preferably in a set up similar to the industrial scale system.

A test plant of 200 kW$_{th}$ capacity will provide a good platform to demonstrate and study the CaL and SER process in process conditions similar to an industrial scale. The capacity of 200 kW$_{th}$[2] is selected based on the space availability and the structural capacity of the laboratory building. Both CaL and SER processes are to be demonstrated within a single test plant. The main tasks performed in the scope of this thesis are limited to the formation of the DFB concept and to validate the DFB concept using the hydrodynamically scaled cold model experiments.

3.1. Block diagram of the 200 kW$_{th}$ test plant

Figure 14 shows the block diagram of the 200 kW$_{th}$ test plant at University of Stuttgart. The plant consists of 3 reactors namely gasifier, carbonator and regenerator; namely reactor R1, R2 and R3 respectively. The test plant is primarily designed to operate in 3 modes
   a. Calcium looping mode (CaL mode)
   b. Sorption- enhanced reforming mode (SER mode)
   c. Oxy-fuel mode
This thesis will discuss only the CaL mode and SER mode.

---

[2] The fluidized bed capacities especially those used for the purpose of combustion are mostly represented in terms of the fuel firing capacity. 200 kW$_{th}$ is an average firing capacity of the 3 reactors used in the test plant.
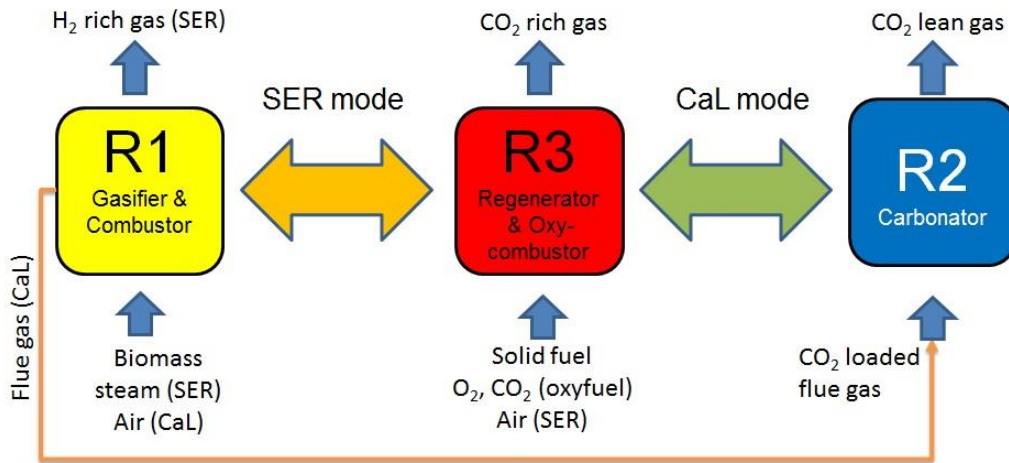
Figure 14 – Operation modes of 200 kW$_{th}$ test plant at University of Stuttgart

In the CaL mode, R2 will be operated as a carbonator, where carbonation reaction will take place and the R3 will act as a regenerator, where regeneration reaction will take place. In R3, the required heat will be produced from the combustion of solid fuels. Sorbent or solid looping will take place between R2 and R3 via interlinking. Additionally in CaL mode the R1 will be operated as a combustor to generate the flue gas which will enter the carbonator. Various types of solid fuels ranging from biomass to coal will be combusted to test the influence of fuel type on the calcium looping process. The carbonator can also be fed with an artificial mixture of flue gases.

In SER mode, reactor R1 will act as a gasifier, where hydrogen rich product gas will be generated. Reactor R3 will act as a regenerator. Here heat required for gasification and sorbent regeneration will be produced by combustion of the solid fuels. The solid looping in SER mode will take place by R1 to R3 interlinking. Reactor R3 in all aspects is a common reactor in CaL mode and in SER mode, with same purpose and same capacity. Therefore the hydrodynamic studies related to R3 regenerator are applicable for CaL mode as well as SER mode. Next sections will discuss in detail about the reactor selection, interlinking methods and process flow of CaL mode and SER mode respectively.

3.2. Reactor selection and interlinking mechanism

In previous section, the function of each reactor is described, the selection of reactor type is based on individual function as a reactor.

Reactor R1 is a gasifier in SER; a gasifier reactor should provide following.
- Provide an ample residence time for the fuel particles, since the steam gasification at the desired process conditions (i.e. 600-700 °C and atmospheric pressure) is a kinetically very slow reaction [54].

- Provide a very good contact between the gasification agent, product gas with the sorbent bed material, in order to facilitate the required gasification and reforming reactions. [160]

A suitable type of fluidized bed which would satisfy above criteria is a bubbling fluidized bed (BFB) or a turbulent fluidized bed (TFB). A BFB can offer high residence time for the fuel particles; but a turbulent fluidized bed has a better gas-solid contact efficiency than a BFB. Therefore reactor type selected for R1 is BFB reactor with some TFB features to improve gas solid contact. A BFB with a conical bottom is a preferred choice. The conical bottom will generate higher velocity at the bottom of the fluidized bed, therefore creating velocity patterns close to TFB conditions. The rest of the bed will have BFB velocity patterns, therefore unnecessary particle elutriation will be avoided. DFB biomass gasifiers working at TU Wien have also employed similar type of BFB having a conical shape [53].

Reactor R2 has the function of carbonator only in CaL mode. Previously at IFK, University of Stuttgart, carbonator has been demonstrated as a BFB reactor [43] and also as a CFB reactor [34]. However, contact efficiency of gas solid particles is much better in a CFB reactor than a BFB, the gases can bypass the solid reactants without reaction through bubbles. Rodriguez et al. [167] compiled the results from various facilities including the 10 kW$_{th}$ University of Stuttgart facility, and concluded that the CFB carbonator is kinetically more effective than the BFB reactor. Furthermore, a CFB will require less area than a BFB reactor for a same flue gas load, therefore considering all above aspects, R2 is selected as a CFB reactor.

Reactor R3 has the function of a regenerator in both CaL and SER mode. The required heat for the reverse endothermic reaction of Eq. (1) is generated by the combustion of carbonaceous fuels. A CFB is well proven commercially for its application as a combustor for a wide range of fuels [9]. Therefore the regenerator is selected as a CFB reactor. The requirement of oxy-fuel mode also indicates the need of a CFB reactor. At IFK in 10 kW$_{th}$ bench scale plant the regenerator operation in a CFB mode has been examined and found successful [43,59]. INCAR CSIC facility in Spain also operates regenerator in a CFB mode [167].

In CFB combustion process it is common practice to introduce the air in stages. This is done in order to improve the combustion quality and reduce NOx formation by avoiding high temperature spots in the bottom zone [82,168]. Similar to air staging in CFB combustors, air staging in the regenerator reactor is also required and its hydrodynamic and process implications need to be tested.

Thus the 200 kW$_{th}$ test plant in CaL mode will have a CFB (R2)-CFB (R3) type DFB system. The SER mode will have BFB (R1)-CFB (R3) type DFB system. The schematic of test plant set up in CaL mode and SER mode are shown in Figure 15 and Figure 16 respectively. The details of all three reactors including basic dimensions of the reactors are compiled in Table 8. The task of sizing the reactors is not covered in

Table 8 – Details of the 200 kW$_{th}$ test plant

	Unit	Gasifier R1	Carbonator R2	Regenerator R3
Diameter	m	0.35[a]	0.23[a]	0.17[a]
		0.33[f]	0.22[f]	0.21[f]
Height	m	6[a,f]	10[a,f]	10[a,f]
Firing capacity	kW$_{th}$	200	170-230	200-330
Operational velocity	m/s	0.5-1 (Gasification)	4-6	4-6
		1-2 (Combustion)		
Regime	-	Bubbling/Turbulent	Fast	Fast
Entrainment flux			5-25	10-40
Solid inventory	kg	30-50	30-50	10-15
Solid fuel		Wood pellets	None	Wood pellets
				Coal

a- Preliminary dimensions considered for cold model study
f- Final dimensions

the scope of this work. For methodology of fluidized bed sizing of CaL process and SER, refer the following literature from Hawthorne and co-workers [51,66].

3.2.1. The interlinking mechanisms in CaL and SER mode

For 200 kW$_{th}$ test plant at University of Stuttgart, two separate interlinking methods are used for CaL mode and SER mode. The CaL mode consists of two CFB's, a novel way of interlinking with two cone valves is proposed here. University of Stuttgart has previous experience with the application of cone valve in 10 kW$_{th}$ bench scale plant. University of Stuttgart would like to test the application at 200 kW$_{th}$ test plant at higher scale before being implemented at higher scale. Each CFB of carbonator and regenerator will have own cone valves which will deliver solid flow into the opposite CFB. Thus control of the solid looping rates between the beds is effectively accomplished with a cone valves, while the internal circulation in an individual CFB loop will also be in operation.

In SER mode, the interlinking is achieved with the help of an L-valve (between the regenerator and gasifier) and a gasifier loop seal (between gasifier and regenerator). L-valve requires fluidization air in the range of 0-10 liters per minute. The fluidization requirement is calculated using the L-valve aeration models from Arena and Smolders [129,130]. During test plant operation, the aeration values were found in accordance with the models. Thus, the dilution of product gas resulting from the L-valve will be a minimum, however in real scale test plant this aspect is of least worry since aeration can be provided in the form of steam, but in present case the use of steam is avoided to simplify data analysis process. The gasifier loop seal connects the link between the gasifier and the regenerator as shown in Figure 16.

3.2.2. Gas solid process flow in CaL mode

The schematic of 200 kW$_{th}$ test plant at University of Stuttgart of CaL mode is shown in Figure 15. The flue gases are either generated in combustor (R1) and are fed to the carbonator (R2) through a blower or the synthetic mixture of the flue gas (from CO_2-N_2 tanks and using gas mixers) is fed to the carbonator. In the carbonator the CO_2 is absorbed by an active CaO at temperature of 600 to 700°C to form $CaCO_3$. The CO_2 lean flue gases and the formed $CaCO_3$ leave the carbonator and enter the cyclone (cyc_{Ca}), where gas solid separation takes place very effectively. The gases leave the cyclone from the top exit while the solid $CaCO_3$ particles drop into the standpipe (stp_{Ca}). The solid flow rate of $CaCO_3$ particles falling in standpipe of carbonator is called as entrainment rate ($\acute{G}_{Ca}$) in kg/h or entrainment flux ($\acute{G}_{sCa}$) in kg/m²s. Part of this entrainment is sent to the regenerator via the cone valve (CV_{ca}).

Figure 15 – Schematic of CFB-CFB DFB system for CaL mode

This is called solid looping rate ($\acute{G}_{L\,CV\,Ca}$) and the remaining entrainment ($\acute{G}_{Ca} - \acute{G}_{L_{CV\,Ca}}$) is recirculated to the carbonator through the internal loop seal of carbonator (LS_{Ca}).

In the regenerator, within the temperature range of 850 to 950 °C, CaO will be regenerated from $CaCO_3$ and gaseous CO_2 will be released. The fluidization medium is oxygen mixed with recycled flue gas. The required heat for endothermic regeneration reaction is supplied by the oxy-fuel combustion of a solid fuel, i.e. coal. To improve the combustion and avoid temperature hot spots the oxygen is applied in stages, similar to air staging in a CFB boiler through primary air (PA), secondary air (SA) and tertiary air (TA) nozzles respectively. The gaseous stream in regenerator will be a CO_2-rich stream, due to oxy-fuel combustion and CO_2 release from regeneration reaction of Eq. (1). This CO_2 rich gas stream and the formed CaO leaves the reactor and gas solid separation takes place in the cyclone (cyc_{Re}). The gases leave the cyclone from top exit and the regenerated CaO falls into the standpipe of regenerator (stp_{Re}) at an entrainment rate ($\acute{G}_{Re}$) in kg/h. From the regenerators cone valve (CV_{Re}) the required CaO is supplied to the carbonator as a solid looping rate ($\acute{G}_{L_{CV\,Re}}$) and the remaining entrainment ($\acute{G}_{Re} - \acute{G}_{L_{CV\,Re}}$) is internally circulated within the regenerator through the internal loop seal (LS_{Re}). The discharge from the cone valves falls into the opposite CFB's return leg.

It is important to note that the solid looping rates from both the cone valves should be of similar magnitude ($\acute{G}_{L\,CV\,Ca} = \acute{G}_{L\,CV\,Re}$), without similar flowrates, the DFB system will be unsteady.

The gases from both reactors pass through an additional cyclone. This cyclone captures particles which accidently escape the first cyclone due to disturbances in the loop seal. Gases then pass through the coolers and bag house filters before venting to atmosphere via ID fan. A part of the cooled gas stream from the regenerator is recycled back to the regenerator to ensure proper oxy-fuel conditions (i.e. fuel, oxygen 20-25 vol% dry, carbon dioxide 70-75 vol% dry) in the regenerator.

3.2.3. Gas solid process flow in SER mode

The schematic of the 200 kW$_{th}$ test plant at University of Stuttgart of SER mode is shown in Figure 16. The SER mode operates with gasifier (R1) and regenerator (R3). In test plant operation the gasifier consists of a limestone bed fluidized with pure steam through spargers, the fuel such as biomass/lignite is inserted within the limestone bed in the conical section of the gasifier. The product gas from gasification process comes in contact with the bed and CO_2 is absorbed as per Eq. (1) The H_2 enriched product gas leaves the gasifier from top exit. Since bubbling fluidization regime is maintained in the gasifier, the solid entrainment from the gasifier is not expected. When gasifier loop seal is fluidized, the formed $CaCO_3$ and non-gasified char from the gasifier is transported to the regenerator.
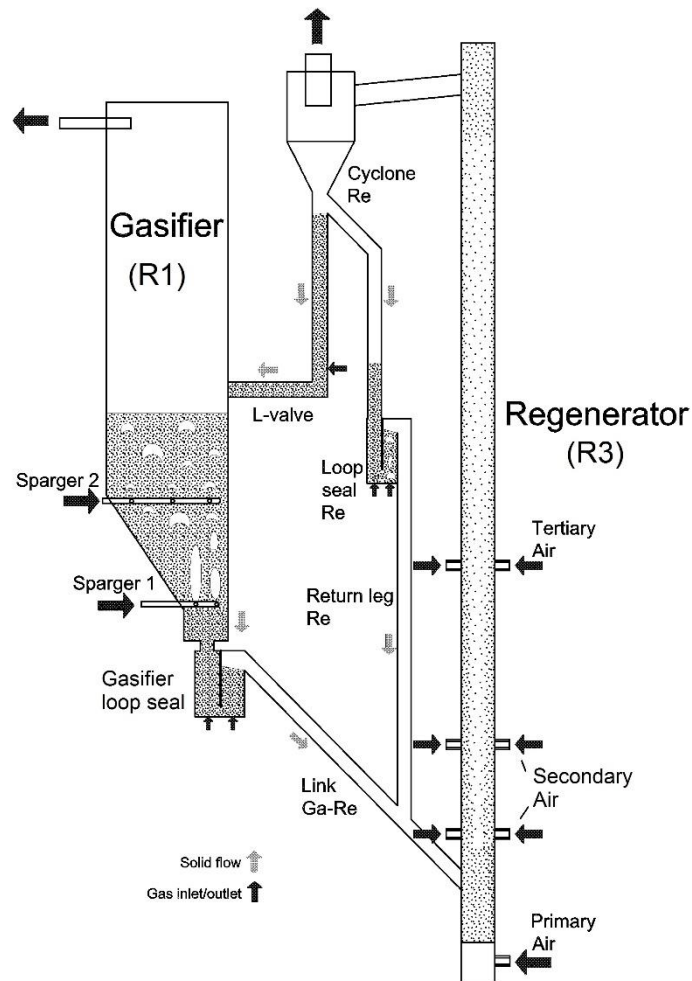
Figure 16 - Schematic of CFB-BFB DFB system for SER mode

The regenerator is an air fired or oxy-fuel type CFB combustor, the function of the regenerator is the same as explained in the previous section, except the fuel for combustion will be received from gasifier as non-gasified char. The required heat for regeneration of sorbent and to maintain temperature above 850°C is generated by the combustion of this non-gasified char from gasifier, and if necessary extra fuel may be added to maintain the required heat balance. The fluidizing regime is maintained in fast fluidization regime. At such conditions, the formed CaO is entrained out of the regenerator and falls in the L-valve pipe after gas solid separation in cyclone. The part of entrainment ($\acute{G}_{Re}$) is diverted to the gasifier as a solid looping rate through the L-valve $\acute{G}_{L_{LV}}$, and the remaining entrainment ($\acute{G}_{Re} - \acute{G}_{L_{LV}}$) is re-circulated back to the regenerator through standpipe- loop seal- return leg arrangement of the regenerator as shown in Figure 16. The discharge of the L-valve is given in the freeboard of the gasifier. The amount of aeration in the L-valve controls the sorbent looping rate in the DFB system.

The gases leaving the gasifier and the regenerator are analyzed in separate gas analyzers. The product gases from gasifier are burned off, since the product gas

quantity is small and the purpose of the test plant is to demonstrate the process not to sell the product gas. The flue gases from gasifier and regenerator are cooled and filtered before venting off.

3.2.4. Additional design features

Certain design features were considered for the test plant which may improve the performance of the process. The design features which are considered in the preliminary design of the plant are as listed as follows.

- Conical bottom shape for the BFB gasifier
- The carbonator with a wide diameter bottom
- Air/oxidant staging in the regenerator

The gasifier shape and particle movement has an influence on the fuel conversion efficiency in the gasifier. Studies [169] suggest that the light char particles have a tendency of segregating in the upper layers of the fluidized bed. The gasifier is designed in such a way that the bed material exits from the bottom of the gasifier, via the loop seal to the regenerator. The floating char will be prevented from making quick exit to the regenerator, thus char residence time in the gasifier will be improved. Furthermore, introducing solid fuel in the middle of the bed can provide more contact of fuel and reacting gases with the bed material. The gasifier is also designed as an inclined surface at the bottom as shown in Figure 16. This inclined surface is inspired from the works of Hofbauer et al [53] and Foscolo et al. [160]. Foscolo studied the inclined surface gasifier in a cold model and showed that the inclined surface helps create the solid circulation pattern as per Kuramoto et al. [170]. Foscolo et al. [160] also showed that the fuel residence time is improved when fuel is introduced in the conical section on the slant side.

The wide bottom of the carbonator as shown in Figure 15 is a novelty in a reactor design. The wide bottom CFB has been cited for the use of biomass flash pyrolysis [171] and chemical looping combustion [138]. Previously at University of Stuttgart, Korovesis [172] showed the successful application of the wide bottom in a cold model. The wide bottom provides the advantage of an increased particle residence time. The wider diameter at the bottom would create a lower superficial velocity zone matching turbulent regime condition, which is suitable contact condition for carbonation reaction. Furthermore, due to the larger area the reactor would contain larger inventory compared to a uniform diameter riser. The increased space time due to more inventory in the riser may prove crucial to achieve high rates of CO$_2$ capture in the carbonator. For the initial design, a wide bottom diameter ($D_{Ca\,bot}$) is chosen around 1.4 times the diameter of the riser above (D_{Ca}). The diameter is selected in such a way that the velocity in the bottom zone would be always more than the particle terminal velocity (u_t) even for the lowest operational velocity to ensure generation of the entrainment rates ($G_{s\,Ca}$).

Testing of these features in the cold model would certainly clear the hydrodynamic aspects of these design features, give prior experience and ultimately help in improving the final design of the test plant.

3.3. Experimental – Cold model set up

3.3.1. Cold model design and description

The cold model experimental set up which is the core theme of this thesis is based on the Glicksmann scaling laws. The theoretical and application aspects of the fluidized bed scaling are covered in section 2.4. To design a cold model, some basic design data of the plant to be scaled (200 kW$_{th}$ test plant) is necessary. First step is the geometric design of the cold model. The preliminary dimensions of the test plant are shown in Table 8. The geometric ratio of the cold model: Test plant is chosen as 1:2.5. Among geometric ratios from 1 to 4, a 2.5 times smaller cold model is found to be an optimum ratio. The dimensions of the cold model are given in Table 9. The riser, standpipe and loop seal are designed with a geometric ratio of 1:2.5, while cyclones are designed independently using guidelines from Perry's Handbook [173]. All three FB units of the cold model are made up of transparent plexi-glass as a common practice in the construction of cold models and they are mounted on neatly designed aluminum profiles. The aluminum frame is divided in 3 compartments as shown in Figure 17. The first compartment on the left is where R1 is installed. R3 (regenerator) is installed in the middle compartment and R2 on the right. The R3 is placed in the middle because it has to facilitate the solid looping to R1 and R2 via separate interlinking mechanism i.e. cone valve in CaL mode and L-valve in SER mode. The construction of the test plant also followed the same positioning of the reactors, cyclones, loop seals, cone valve and L-valve of

Figure 17 – Cold model set up with the aluminum frame work.

R1, R3 and R2 respectively as positioned in the cold model.

The interlinking required as per CaL mode and SER mode are carried out as shown in Figure 15 and Figure 16 respectively. To achieve this the R3 solid recirculation system is designed as shown in Figure 16. As shown in Figure 16, the L-valve is situated directly below the R3 cyclone and the overflow of the L-valve is directed to the standpipe loop seal of R3. The cone valve is installed on the supply side of the loop seal and its discharge is directed to R2. This configuration was earlier proposed by Nikolopoulous [174] at University of Stuttgart.

Table 9 – Dimensions of the cold model

		Unit	R1	R2	R3
Riser					
	Diameter		140	92/140[a]	69
	Height	mm	2500	4000	4000
	Exit		T shaped	T shaped	T shaped
	H_{exit}[b]		-	90	200
Cyclone			-		
	Barrel diameter			120	92
	Height	mm		530	370
Standpipe					
	Diameter	mm	-	40	30
	Height			1000	1000
Loop seal			(Gasifier LS)		
	Length breadth		70 x 35	95 x 45	85 x 35
	height	mm	150	300	200
	Weir height		70	40-200	30-150
	Weir type		Fixed	Variable	variable

[a] Wide bottom diameter

[b] Height of the riser section above the riser exit

The final cold model schematic of CaL mode and SER mode are shown in Chapter 4 and Chapter 5 respectively. A major deviation in cold model from test plant design is the absence of any downstream components, such as control valves, filters, coolers and ID fans.

3.3.2. Measurement methods and data acquisition

The experimental methods in the field of fluidization are well developed. The methods applied in the present thesis are routine methods inspired from Louge [175]. The main measurements carried out during the experiment are:

a. Gas / air flow

b. Pressure at the various locations

c. Riser entrainment rates

d. Solid looping rates i.e. cone valve or L-valve flow rates

The details of the air flows required in the three fluidized beds are given in Annexe B. To summarize, the air flow to the risers R2 and R3 is supplied from a blower, while the loop seals aeration and BFB R1 is supplied by compressed air network. All the flows except the CO_2 flow are monitored and controlled manually with the rotameter. The detailed piping and instrumentation diagram, drawings and photos of the cold model can also be referred in Annexe B. The pressure measurement at various locations in the DFB system is very important. The pressure measurements will enable us to determine the pressure profile and fluctuations in the fluidized bed,
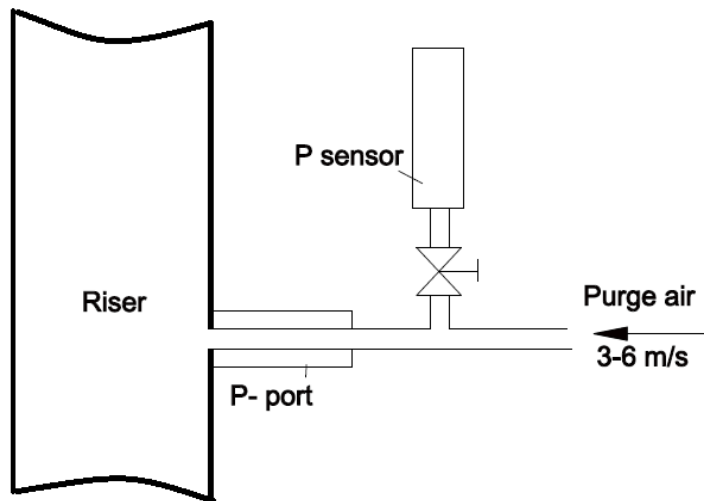
solid suspension and riser inventory determination. The differential pressure transmitters and normal pressure transmitters are used for measuring pressure. Differential pressure transmitters give a direct value of the pressure drop (Δp) between the two pressure ports or sections in the fluidized bed. When a normal pressure transmitter is used, the pressure value is relative to the atmospheric pressure.

Figure 18 – Purging arrangement for preventing blocking of pressure ports

During the fluidized bed operation the pressure port often got blocked with particles and accurate reading became difficult. To tackle this problem several methods are used such as the use of filter wool. However continuous purging of air is found to be the most effective method to avoid blocking of pressure port. Figure 18 shows the schematic of air purging at pressure port. The extra air input into the riser may affect the hydrodynamics of the system. The pressure measurements are continuously recorded using a LabView® program as a data acquisition system at a frequency of 1 Hz. The Δp between the two sections is calculated by using the difference of pressure values. The solid fraction (ε_s) between the two pressure measuring ports is calculated using Eq. (13) and the Δp values.

The measurement of riser entrainment rates (G) or entrainment flux (G_s) and solid looping rates from cone valve or L-valve are explained in next section.

3.3.3. Experimental procedure

In the scope of the present work, using a single standard experimental procedure for the entire scope of the thesis is not possible. The experimental procedures used in this work are broadly classified into three categories, mainly

1. Single loop CFB experiments
2. Dual loop or DFB experiments: these are the ones mainly used for CaL mode and SER mode experiments.
3. Special experiments: these experimental procedures are explained further in the manuscript. These special experiments are mixing and segregation experiments in BFB (see Chapter 5) and estimation of friction and acceleration magnitude in a CFB riser (see Chapter 7).

Single loop CFB experiments are performed on a single CFB. These experiments are mainly performed to evaluate the performance of a CFB, without the influence of the other fluidized bed of the DFB. The experimental procedure described here is used for majority of the experiments. At the beginning of an experiment, the solid particles from entire system are emptied and no gas flows are used. The selected solid inventory is weighed and termed as total solid inventory (M_{To}). This total solid inventory, M_{To} is poured into the standpipes of a CFB. Once the solid inventory is set, the air flow is introduced into the CFB as primary air at a given riser superficial velocity. Next first step is to initiate solid circulation in a CFB. For this the loop seal of the CFB in operation is steadily supplied with the air, the solid flow initiates from the loop seals and over the weir solid particles drop into the riser, the riser with enough transport velocity carries the particles out of the riser and these particles are separated from the gas flow into the cyclones and particles fall back into the standpipe. Thus solid circulation is initiated. The loop seal aeration is adjusted for a trouble free operation. Since the solid flow from the loop seal- standpipe is initiated the pressure in the riser is increased and visually the riser is now full of solid particles. Over the data acquisition system the pressure in the riser can be monitored. In few minutes of operation, the pressure in the riser, cyclone and standpipe gets stabilized. The period after stabilization of the pressure profile, can be considered as steady state. During steady state, the average pressure drop of the riser is constant over a period of time, the pressure fluctuations are also uniform and the height of particles in the standpipe is very stable. The steady state is determined when the average total riser pressure drop remains constant with uniform fluctuations for a period of more than 10 minutes. The time remains is recorded for a steady state.

The riser entrainment rates are measured mainly using the discontinuous method. The loop seal aeration is stopped for certain span of time, the stoppage in the loop seal aeration stops material flow from loop seal to riser, therefore solid flow coming from the riser is accumulated in the standpipe (ΔH_{stp}).The time required to accumulate certain height (Δt) in the standpipe is noted and then based on the bulk density ($\rho_{s\,bulk}$) of the particles the entrainment flux rates are calculated using the formula below in Eq. (30).

$$G_s = \frac{\frac{A_{stp}.\Delta H_{stp}.\rho_{s\,bulk}}{\Delta t}}{A_{riser}} \tag{30}$$

The loop seal aeration is resumed once the height and time is noted. However, with this method one should be careful, that the time span of accumulation should not extend to an extent that it affects the riser hydrodynamics, causing the errors in the measurements. Therefore, the time span should be as small as possible. In our experience 3-10 s is an optimum time span for measurements. Readings less than 1 second are not considered because of significant errors involved. The measurements are generally taken at the end of steady state. Minimum three such readings are taken for every steady state with a gap of at least 3 minutes to allow the system to regain the original hydrodynamic state, i.e. original mean pressure drop and fluctuations. Sometimes it used to happen that after taking the entrainment rate reading the system may not regain original pressure drop after 3 minutes. In such cases more waiting time is considered till the original hydrodynamics is reached or the entire experiment is discarded. It is observed that loop seal aeration patterns get disturbed in such discontinuous methods and causes irregularities in achieving the original hydrodynamics in the riser.

The dual loop or DFB experiments are similar to single loop experiments, except the use of two fluidized beds coupled with each other. In CaL mode two CFB's R2 and R3 are fed with total solid inventory (M_{To}), initially two CFBs are operated as single loop CFB system without coupling with cone valve. Once the CFB's appear steady on the computer screen, cone valves from both CFB's are opened. Once the cone valves are opened, the solid inventory is redistributed again within R2 and R3, and within few minutes, the DFB operation is stabilized. The stable steady DFB operation is identified just as single loop CFB system, i.e. steady pressure drops, uniform fluctuations and steady particle height in both CFB's. If the steady situation persists for more than 10 minutes, the timings are noted for steady state pressure measurement data. Once these 10 minutes are over, the riser entrainment fluxes are measured as explained earlier in single loop CFB experiments (one CFB at a time) and cone valve flow rates are measured after that. To measure the cone valve flow rate, the solid flow from the cone valve is diverted into the sampling port shown in Figure 19 for certain time and the diverted solid inventory is removed and weighed. After weighing the removed inventory is given back to the respective risers.

SER mode is operated with BFB R1 and CFB R3. Initially, the total solid inventory is weighed and distributed into the R3 standpipe, L-valve and R1 BFB. To operate at first, the R3 is operated in a single loop CFB operation, and R1 is only fluidized through spargers. The aeration in the L-valve and gasifier loop seal of R3 is not initiated. Once the R3 single loop CFB operation becomes steady, the aeration in the gasifier loop seal of R1 is initiated and immediately the L-valve aeration is also applied. This step initiates the solid flow circulation between R1 and R3 making the system coupled. The redistribution of solid inventory takes some time the pressure profile of the entire DFB system is stabilized. In SER mode the steady state is considered when the pressure profile of R3 is uniform and the particle bed height in R1 and standpipe of R3 remains

constant. If steady situation persists for more than 10 minutes, the timings are noted for steady state pressure measurement data. Once these 10 minutes are over, the riser entrainment fluxes are measured as explained earlier in single loop CFB experiments and L-valve flow rates are measured after that. To measure the L-valve flow rate, a measuring cup is installed in the R1, near the exit of L-valve as shown in Figure 19b. The flow from the L-valve is directly trapped into the measuring cup and time required to fill the cup is recorded. The inventory trapped in the cup is immediately released into the R1 bed.
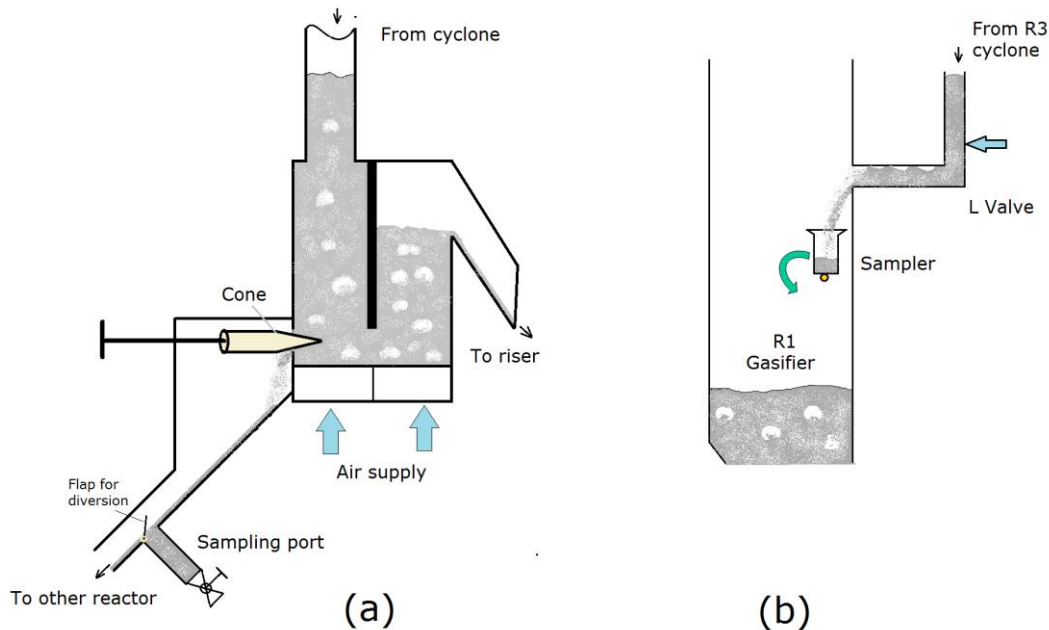

Figure 19- Solid looping rate measurement schematic a) Cone valve in CaL mode set up b) L-valve flow measurement in SER mode set up

3.3.4. Particle selection and the hydrodynamic scaling

The selection of appropriate particles in scaled hydrodynamic studies is an important step. The particle selection is mainly driven by the density ratio and velocity ratio in the simplified scaling ratios mentioned in Eq. (24). Separate particles are required for the CaL mode and SER mode experiments due to variation in the densities.

For CaL mode studies, previous used particles were considered at first. During scaled studies of 10 kW$_{th}$ bench scale test plant DFB system at University of Stuttgart [71,72] Zirconium dioxide particles with a density of 5700 kg/m³ were used. Since these particles were specially manufactured their cost is very high (ca. 500 €/kg). Therefore for a bigger scaled cold model of this work, other economically feasible particles were required to be found. After a brief search, iron oxide particles with a particle density of 5100 kg/m³ with a PSD of 100-200 µm were selected. The details of the densities of gas and particles are given in Table 10. It is important to note that the gas density in regenerator is different compared to carbonator due to higher temperature and CO$_2$

Table 10 – Details of the particles used in the experiments

Parameter	Unit	Test plant	Cold model	Test plant	Cold model
CaL mode		**Carbonator**		**Regenerator**	
T	°C	600-700	20	850-950	20
ρ_s	kg/m³	1800	5170	1800	5170
ρ_g	kg/m³	0.39	1.18	0.44	1.26
d_p	µm	300-500	100-200	300-500	100-200
SER mode		**Gasifier**		**Regenerator**	
T	°C	600-700	20	850-950	20
ρ_s	kg/m³	2000	7800	1800	5170
ρ_g	kg/m³	0.23	0.9	0.35	1.18
d_p	µm	300-500	100-200	300-500	100-200

content. Therefore, to match the density ratio in the regenerator with the same particles, gas density is adjusted using mixture of air and CO_2.

For SER mode, the gas-particle density ratio of gasifier and regenerator is different. But in the SER mode the difference is large and matching the ratio for both reactors is not possible using the variation in the gas densities. The steel powder with a density of 7800 kg/m³ has a density ratio with air is close to the gasifier conditions, but these particles do not offer scaled conditions for regenerator operation. To proceed further with this limitation, the experiments the DFB experiments of SER mode were conducted with steel particles, and the results of scaling related to regenerator are analyzed from CaL mode experiments in which regenerator is operated with iron oxide particles. On the other hand, results of scaling related to gasifier are analyzed from steel powder particles experiments.

With the knowledge of particles and geometry of the cold model and test plant the scaling ratios can be derived as explained in section 2.4. The scaling ratios are very useful in extrapolating cold model results to the test plant and determine the feasibility. The pressure drop, riser inventory and entrainment rates are identified as important parameter for extrapolation. Table 12 in chapter 4 and Table 15 in chapter 5 show the scaling ratios for CaL mode and SER mode which are used for the extrapolation of the cold model results.

4. Hydrodynamic studies of the cold model of the 200 kW$_{th}$ CFB-CFB test plant for the CaL process.

This chapter will discuss the hydrodynamic studies of the CFB-CFB test plant for calcium looping (CaL) process using the scaled cold model. A part of the work presented in this chapter is published in [176,177].

4.1. Objectives of the cold model study

One of the main aim of the 200 kW$_{th}$ test plant is to demonstrate the calcium looping process (CaL) with satisfactory CO_2 capture levels, however unless the DFB test plant is hydrodynamically stable, this aim of achieving satisfactory CO_2 capture is difficult. The cold model provides a platform to investigate the necessary hydrodynamic stability of the DFB system before the test plant is constructed. The CaL mode DFB test plant is the combination of R2 and R3 which are both CFBs interlinked by the use of two separate cone valves, as shown in Figure 15. The first objective of the cold model study is to prove the feasibility of the solid looping mechanism discussed earlier in section 3.2.2 (page 42), which requires an equal magnitude of solid flow from both cone valves in order to achieve a long term hydrodynamic steady state. In addition to the long term steady state (hydrodynamic stability) it is also necessary to examine, if the required boundary conditions of the 200 kW$_{th}$ CaL test plant are met in stable hydrodynamic conditions. Fulfilling boundary conditions is a key to achieve the required levels of CO_2 capture. In the next section the required boundary conditions are described in detail. Here the methodology described in section 1.5.1 (page 14) and section 3.3 (page 45) about the scaling of fluidized bed systems will be applied. If a certain boundary condition is not met in the cold model studies, modifications in the design for the 200 kW$_{th}$ test plant or changes in the operational conditions are suggested and if necessary these changes are tested again in the cold model. Furthermore, the operational experience gained from the cold model experiments will be crucial during the commissioning and the operation of the test plant. To gain this experience a parametric study is conducted where influence of various parameters on the DFB system is investigated.

4.2. Process and operational boundary conditions

The CO_2 capture efficiency is influenced by several factors as studied by Charitos et al. [43], namely carbonator space time ($\acute{t}_{Ca}$), sorbent looping ratio ($\acute{R}_L$), gas solid contact in carbonator, carbonator temperature ($\acute{T}_{Ca}$), CO_2 partial pressure, fresh limestone make up and sorbent reactivity. The carbonator space time ($\acute{t}_{Ca}$) is defined

as the ratio of moles of CaO present in the carbonator ($\acute{n}_{Ca}$) to the molar flow rate of CO_2 ($\acute{n}_{CO_2}$) entering the carbonator and shown in Eq. (31).

$$\acute{\tau}_{Ca} = \frac{\acute{n}_{Ca}}{\acute{n}_{CO_2}} \tag{31}$$

Assuming the carbonator inventory is pure CaO, implies;

$$\acute{n}_{Ca} = \frac{\acute{M}_{Ca}}{M_{M\ CaO}} \tag{32}$$

Where $M_{M\ CaO}$ is the molecular weight of the CaO. Thus $\acute{\tau}_{Ca}$ is directly proportional to the carbonator inventory ($\acute{M}_{Ca}$). The sorbent looping ratio ($\acute{R}_L$) is defined as per Eq. (33) as the ratio of molar flow rate of CaO ($\acute{n}_{CaO}$) entering the carbonator from regenerator to the molar flow of CO_2 ($\acute{n}_{CO_2}$) entering carbonator. $\acute{n}_{CaO}$ is also called as sorbent flow rate.

$$\acute{R}_L = \frac{\acute{n}_{CaO}}{\acute{n}_{CO_2}} \tag{33}$$

The carbonator velocity $\acute{u}_{0\ Ca}$ and $\acute{n}_{CO_2}$ are also correlated.

$$\acute{n}_{CO_2} = \frac{\acute{p}_{Ca}\acute{u}_{0\ Ca}\acute{A}_{Ca}}{\tilde{R}\ \acute{T}_{Ca}}y_{CO_2} \tag{34}$$

Where $\acute{p}_{Ca}$ the absolute pressure in the carbonator is, $\acute{A}_{Ca}$ is the carbonator cross section, $\tilde{R}$ is the universal gas constant, $\acute{T}_{Ca}$ is the carbonator temperature and y_{CO_2} is the concentration of CO_2 at the carbonator inlet.

Experimental studies [34,43] have demonstrated a direct relation of $\acute{\tau}_{Ca}$ and $\acute{R}_L$, with the CO_2 capture efficiency. Further studies have been made to define the space time and the sorbent looping ratio by taking the reactivity of the limestone into consideration [34,43], namely the active space time and the active solid looping ratio respectively. However, in this work, only the old definition of space time (Eq. (31)) and sorbent looping ratio (Eq. (33)) is considered. Table 11 shows the required values of these parameters to achieve in a process called as the process boundary conditions.

Table 11- Process boundary conditions CaL in 200 kW$_{th}$ test plant [43,178]

Parameter	Symbol	Unit	Value
Riser superficial velocity	$\acute{u}_{0\ Ca}$, $\acute{u}_{0\ Re}$	m/s	4-6
Carbonator space time	$\acute{\tau}_{Ca}$	min	>20
Sorbent looping ratio	$\acute{R}_L$	-	4-14
Carbonator solid fraction	ε_s	-	higher than CFBC[a]
Regenerator solid fraction	ε_s	-	equivalent to CFBC[a]

a – refer Table 13 for values

The operational boundary conditions delineate the minimum and maximum values of the operational parameters in an actual plant. Table 11 shows the required process boundary conditions [43,178] for the CaL process in order to achieve high CO_2 capture efficiency. The riser velocity (u_0), space time (τ), sorbent looping ratio (R_L) and gas solid contacting can be investigated in a cold model, if the desired boundary conditions can be achieved or not. As per Eq. (32), $\acute{\tau}_{Ca}$ is directly related to the riser inventory of carbonator; and the riser pressure drop ($\Delta\acute{p}$) and riser inventory ($\acute{M}_{Ca}$) are co-related with Eq. (13). Therefore Δp becomes the calculation source of space time. The solid looping rate from cone valve of regenerator ($\acute{G}_{L_{CV\,Re}}$) is none other than sorbent flow rate $\acute{n}_{CaO}$, (assuming material as fully calcined and pure CaO).

$$\acute{n}_{CaO} = \frac{\acute{G}_{L\,CV\,Re}}{M_{M\,CaO}} \tag{35}$$

However, the cone valve receives solid flow originally generated from the riser as a riser entrainment flux ($\acute{G}_s$) in kg/m²s or entrainment rates ($\acute{G}$) in kg/h. Therefore, a riser entrainment rate should be greater than cone valve flow rate ($\acute{G}_i > \acute{G}_{L_{CV\,i}}$). Therefore sorbent looping ratio as process boundary condition is used as a source for determining the operational boundary condition for cone valve flow rate ($\acute{G}_{L_{CV\,i}}$) and the riser entrainment rate ($\acute{G}_s$). The gas contacting is relatively undefined, but Charitos et al. [71] have proposed that the carbonator should exhibit higher solid fraction values (ε_s) compared to circulating fluidized bed combustor (CFBC).

Table 12 shows the required values of $\acute{W}_{Ca}$, $\acute{G}_s$, $\acute{G}_{L_{CV}}$ for 200 kW$_{th}$ test plant based on the process boundary conditions set in Table 11. The values of test plant are calculated using the Eq. (31) to (34) and Eq. (13) for the range of riser velocity and maximum CO_2 concentration of 15 volume %. The respective scaled values (for cold model) of u_0, G_s, Δp and W_{Ca} are calculated using the scaling ratios explained earlier in section 3.3.4 (page 50), these values are also shown in Table 12.

Compared to the carbonator the operational boundary conditions related to regenerator are relatively less discussed in the literature. The sizing of the regenerator is dependent on the heat requirement for the regenerator reaction, i.e. to heat up sorbent to higher temperature and support endothermic regeneration reaction. Therefore regenerator should be designed accordingly to combust enough of solid fuel

Table 12 - Operational boundary conditions of the test plant and cold model

Parameter	Unit	Carbonator		Regenerator		Ratio
		Test plant´	Cold model	Test plant´	Cold model	
u_0	m/s	4-6	2.5-4	4-6	2.5-4	1.57
$G_{s\,i}$	kg/m²s	5-25	10-45	10-40	15-70	0.55
G_i	kg/h	>1200	>350	>1200	>350	3.41
$G_{L_{CV}}$	kg/h	350-1200		350-1200		
Δp_i	mbar	70-100	80 - 115	60-80	69-92	0.87
M_{Ca}	kg	30-50	5.5 - 9			5.43

with the mentioned riser velocity in Table 11. Secondly regenerator should generate enough entrainment flux $G'_{s\,Re}$ to satisfy the required solid looping rate from cone valve $\acute{G}_{LCV\,Re}$ or the sorbent flow rate ($\acute{n}_{CaO}$). The required values of $u'_{0\,Re}$, $G'_{s\,Re}$, $\acute{G}_{LCV\,Re}$ are mentioned in Table 12.

4.3. Pressure balance analysis

The pressure balance studies are integral part of the hydrodynamic studies [71,179]. The pressure balance analysis is very useful in understanding the operation of a fluidized bed system. The pressure balance analysis presented here is applicable to the test plant as well as the cold model. For CaL mode DFB set up the pressure balance terms are shown in Figure 20, there are two clear distinct pressure balance loops. The first loop is a normal CFB loop, riser – cyclone – standpipe – loop seal – return leg – riser. The pressure balance for this loop can be described as per in Eq. (36) and Eq. (37) for carbonator and regenerator CFB respectively. This loop is similar to many other works on CFB loop [71,108,132,180].

$$\Delta p_{stp\,Ca} = \Delta p_{LS\,Ca} + \Delta p_{\,riser\,top\,Ca} + \Delta p_{cyc\,Ca} \tag{36}$$

$$\Delta p_{stp\,Re} = \Delta p_{LS\,Re} + \Delta p_{\,riser\,top\,Re} + \Delta p_{cyc\,Re} \tag{37}$$

Where, $\Delta p_{stp\,i}$ is a standpipe pressure drop, measured from the bottom of the loop seal till the bottom of the cyclone of the respective CFB i. $\Delta p_{LS\,i}$, is called as the loop seal pressure drop, measured between the bottom of loop seal and the entrance of return leg into riser of own CFB. $\Delta p_{riser\,top\,i}$ is the pressure drop in the riser i above the entrance of return leg into the riser i till the top of same riser as shown in Figure 20. The pressure drop between the distributor and the return leg entrance $\Delta p_{riser\,bot\,i}$ does not appear in the pressure balance, since the terms self-cancels. The total pressure drop in the riser $\Delta p_{riser\,i}$ is the sum of riser bottom pressure drop and riser top pressure drop as per Eq. (38)

$$\Delta p_{\,riser\,i} = \Delta p_{\,riser\,bot\,i} + \Delta p_{\,riser\,top\,i} \tag{38}$$

Furthermore, $\Delta p_{cyc\,i}$ is a cyclone pressure drop measured between the riser exit to the cyclone bottom.

The second loop in this DFB system links both CFBs. This loop can be traced as standpipe (Ca) - cone valve (Ca) - riser top (Re) - cyclone (Re) in case of carbonator to regenerator link and vice versa for regenerator to carbonator link i.e. standpipe (Re) - cone valve (Re) - riser top (Ca) - cyclone (Ca). Pressure balance for this loop can be described as follows in Eq. (39) and (40) for carbonator to regenerator and regenerator to carbonator link respectively.

$$p_{Ca} + \Delta p_{stp\ Ca} = \Delta p_{CV\ Ca} + \Delta p_{riser\ top\ Re} + \Delta p_{cyc\ Re} + p_{Re} \qquad (39)$$

$$p_{Re} + \Delta p_{stp\ Re} = \Delta p_{CV\ Re} + \Delta p_{riser\ top\ Ca} + \Delta p_{cyc\ Ca} + p_{Ca} \qquad (40)$$

Where, p_{Ca} and p_{Re} are the absolute pressures of the carbonator and the regenerator cyclone exit respectively. Thus, from Eq. (39) and (40) it is implied that the cone valve pressure drop Δp_{CVi} is the difference between the exit pressure drops between the two reactors and the difference between the standpipe pressure drop Δp_{stpi} and the sum of the pressure drops in the riser top and the cyclone of the other reactor.

Figure 21 shows the typical axial pressure map of CaL mode set up, where the pressure terms of Eq. (36) to Eq. (40) are shown with respect to height above the distributor of both risers. In the cold model, both CFB exits do not have a pressure regulating valve, therefore the exit pressures of both CFB´s are atmospheric and are nearly equal. However, in actual test plant, exit pressures are controlled by the control valves and it is observed that they play a major role in influencing the hydrodynamics
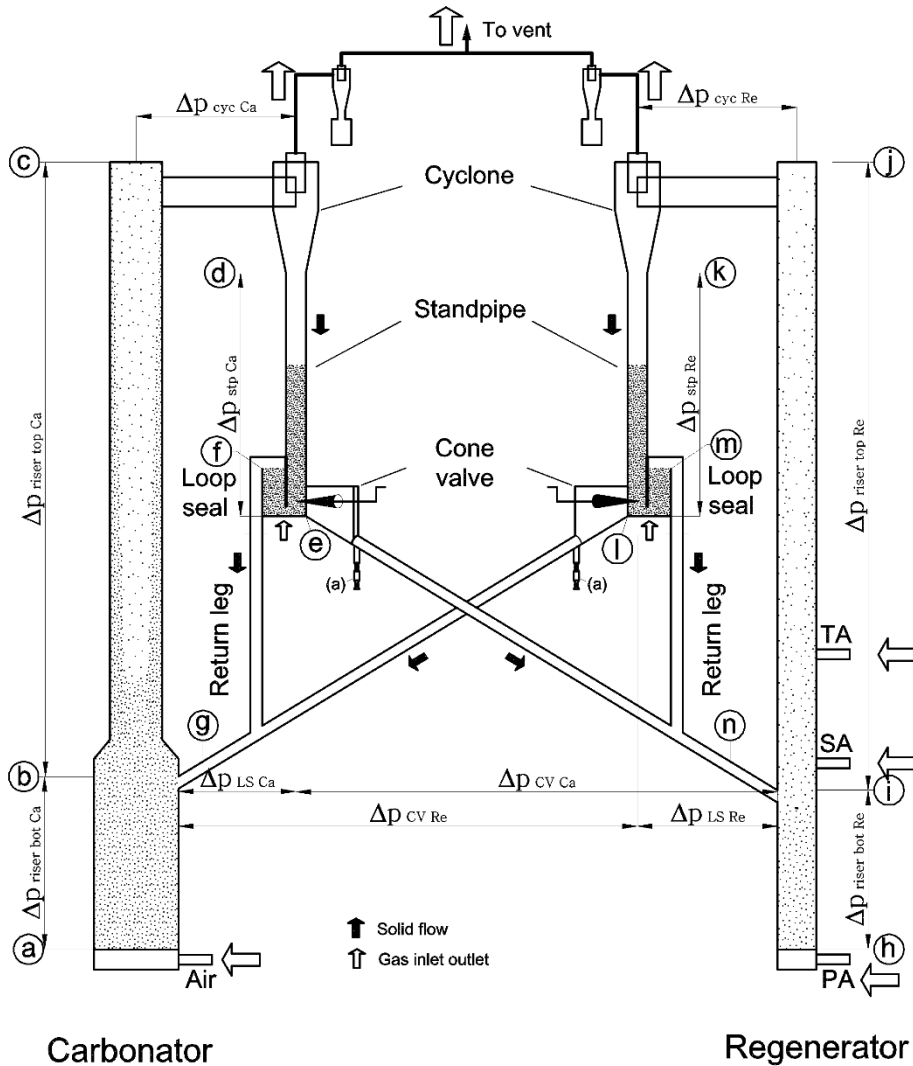

Figure 20- Scheme of the CFB – CFB CaL mode cold model set up and pressure balance terms
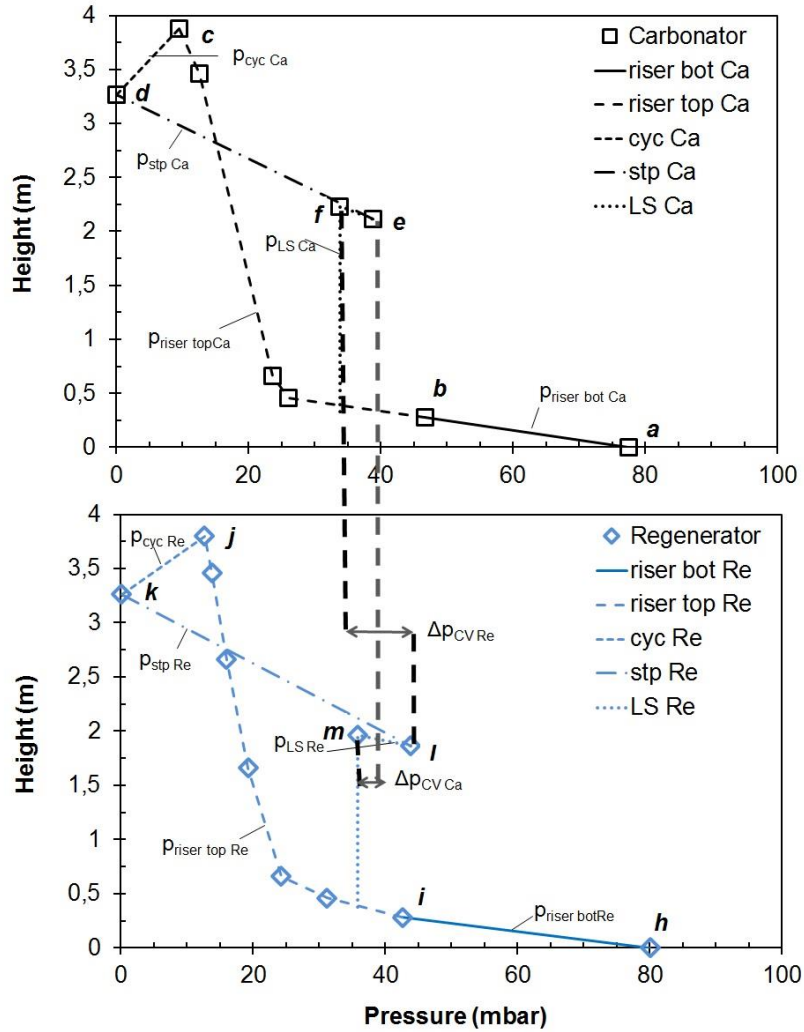
Figure 21 - Pressure map of cold model DFB system in a dual operation mode ($u_{0\ Re}$=3.5 m/s, ASR PA:SA:TA% 70:24:6%, $u_{0\ Re}$=3.5 m/s , $A_{CV\ Ca} = A_{CV\ Re}$ = 79 mm²). Refer Figure 20 for the profile points: a-f carbonator, h-m regenerator

of the entire DFB system. The pressure balance gives an idea how a DFB system will function. Eq. (36) and (37) show that the internal changes in $\Delta p_{\,riser\ top}$, Δp_{cyc} and Δp_{LS} will be affecting the $\Delta p_{\,stp}$ in the internal CFB loop. While Eq. (39), (40) shows that the change in $\Delta p_{\,riser\ top}$ of a CFB will affect the $\Delta p_{\,stp}$ of the other CFB. Analyzing Eq. (39), (40) and (23) it is understood that in order to ensure mass flow through the cone valve, the standpipe should have enough pressure to overcome the pressure drop in the other reactor. Thus any changes in the parameters in any of the CFB will affect the hydrodynamics in both the CFBs and the cone valve flow rate.

4.4. Results and discussions

The details of the experimental set up, experimental procedure and data analysis methods are explained earlier in Section 3.3 (page 45-50). The results are analysed and presented in this section.

4.4.1. Solid looping between the two CFBs

A preliminary aim of this study is to prove the feasibility of the solid looping mechanism. In Figure 22 the solid looping rate from the cone valve ($G_{L_{CV}}$) measured separately at the carbonator and the regenerator is shown as a point irrespective of operational conditions in both CFB's. Number of experiments at various riser velocities, total solid inventories (M_{To}), cone valve openings consistently show that solid looping rates from both CFB`s cone valves are nearly equal. Apparently the dynamic pressure balance of the DFB system helps equalizing the flow rate coming from both cone valves. Furthermore, long term steady states have been observed with uniform pressure profiles in both CFBs and uniform solid looping rates. This shows that the DFB system of two CFBs coupled with two cone valves is feasible. Figure 22 also shows that the solid looping rates can be controlled in a wide range from 3 kg/h up to 250 kg/h using a cone valve. Direct application of the scaling ratio to the solid looping rate is invalid, but for simplicity if we assume the scaling ratio of riser entrainment rate for cold model cone valve flow rate, then the 0-250 kg/h in cold model is scaled as 0-800 kg/h in the test plant (see Table 12). This is shown as a secondary y axis in Figure 22 using the scaling ratio. As per Table 12 the required solid looping rates are in the range of 350-1200 kg/h. Therefore it can be concluded that the minimum required solid looping rates have been achieved in the cold model, but maximum required solid looping rate is not achieved. In next sections the reasons for this shortage of solid looping rates are understood and the modifications for test plant are suggested.
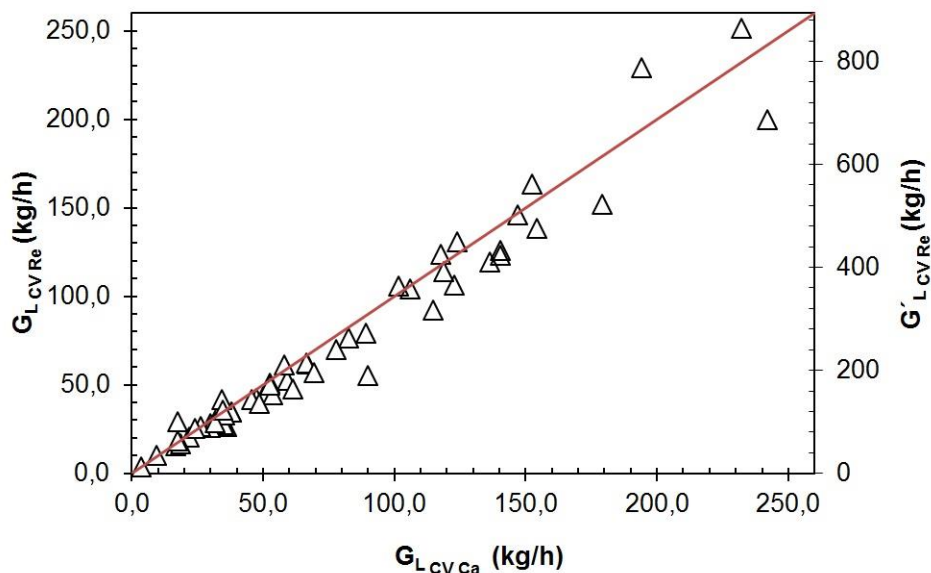

Figure 22 – Solid looping rate from cone valve measured at carbonator and regenerator cone valve in DFB cold model operation irrespective of operational conditions. Secondary Y axis shows the scaled looping ratio assuming scaling ratio in Table 12

4.4.2. Riser pressure profiles, inventories and entrainment rates

4.4.2.1.   Carbonator

A typical riser axial pressure profile and corresponding solid fraction profile of the carbonator is shown in Figure 23. The pressure is shown relative to the pressure at the exit of the riser. The pressure profile shown in Figure 23 is a representative one and subjected to change with change in operational parameters such as riser velocity, total solid inventory etc. The difference of pressure values between two measurement points is the pressure drop, the pressure value at bottom of the riser (height = 0 m) is the value of total pressure drop in the riser ($\Delta p_{riser\,Ca}$). Using pressure drop values between two points and using Eq. (13), the solid fraction (ε_s or 1-ε) is calculated. The solid fraction between two pressure points is assumed constant, therefore the solid fraction value is indicated at the middle of two pressure points. As seen in Figure 23 the carbonator is clearly divided in two zones, a dashed line marks the level at which the riser diameter changes from wide bottom ($D_{Ca\,bot}$=140 mm) to 92 mm. The wide bottom zone shows explicitly high pressure drop and high solid fraction. In Figure 23 the solid fraction in bottom zone is high as 0.25, which is considerably higher than the solid fraction in a normal CFB and resembles the solid fraction in a turbulent bed. Wide bottom geometry creates a low velocity zone of turbulent regime in the bottom region, therefore turbulent fluidized bed conditions are created in this zone. Above 0.4 m level where diameter is 92 mm, the gas velocity is higher; the solid fraction shows drastic reduction to a very low value of 0.01. The visual observation confirms a core-annulus structure in this zone. The exit region shows slightly increased solid fraction, showing signs of exit effect [108]. The abrupt T-shaped exit creates slight solid back mixing in the riser exit region and increases the solid fraction. The solid fraction values recorded in different sections of the carbonator are compared with the solid fractions of a normal
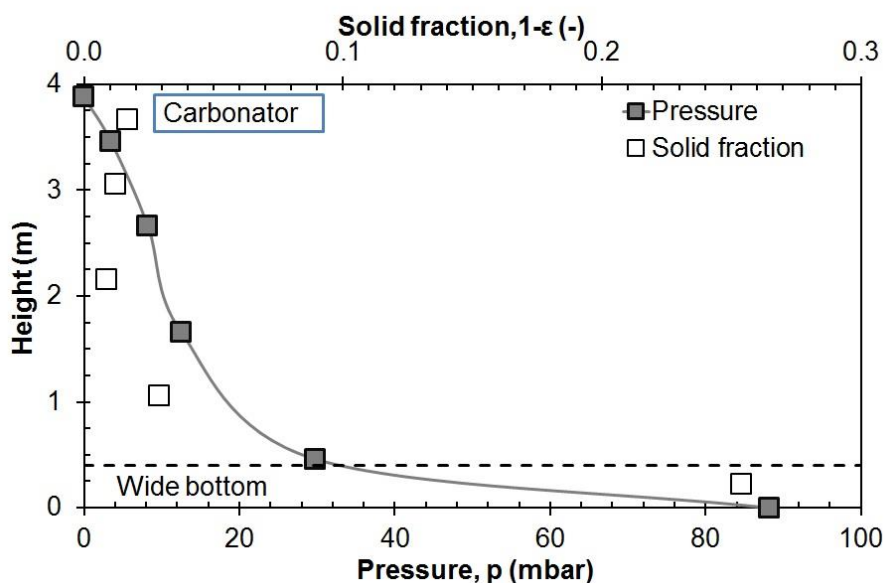

Figure 23 - Typical carbonator pressure profile and solid fraction ($1 - \varepsilon$) profile

Table 13 - Solid fraction (ε_s) values of the hydrodynamic regions of the CFB carbonator and the CFB combustor

	Dense bottom zone	Lean core annulus region	Exit region
Carbonator in this study	0.15-0.32	0.005-0.02	0.01-0.02
Carbonator Charitos et al.[71]	0.1-0.22	0.01-0.025	0.01-0.07
CFB combustor [71]	<0.2	< 0.01	

CFB combustor (CFBC) and CFB carbonator used by Charitos et al. [71] (see Table 13). The carbonator in this study clearly displays much denser bottom zone compared to other carbonator and CFBC. Contrarily the upper lean region and exit region solid fractions are recorded lower than by [71] but are higher or equivalent to CFBC. Therefore for a carbonator the solid fraction profile is satisfactory. In other work [34] it is shown that the significant portion of CO_2 capture takes place in bottom dense zone of a CFB. Several other works have also implied that the gas solid contacting in a turbulent bed is very good [181]. Therefore such design with wide bottom riser may be suitable for carbonator.

Carbonator riser inventory (M_{Ca}) calculated for pressure profile shown in Figure 23 using Eq. (13) equals 11.8 kg. This includes both bottom dense and top lean region. Using the scaling ratio from Table 12, the carbonator inventory in the test plant ($\hat{M}_{Ca}$) will be 64 kg, much higher than the required as shown in Table 12. The cold model shows that the required solid inventory in the carbonator is met. In case without wide bottom diameter, for the same cold model carbonator total pressure drop, M_{Ca} would have been 5.6 kg; ($\hat{M}_{Ca}$=32.4 kg). Therefore a wide bottom design may prove to be an advantage.
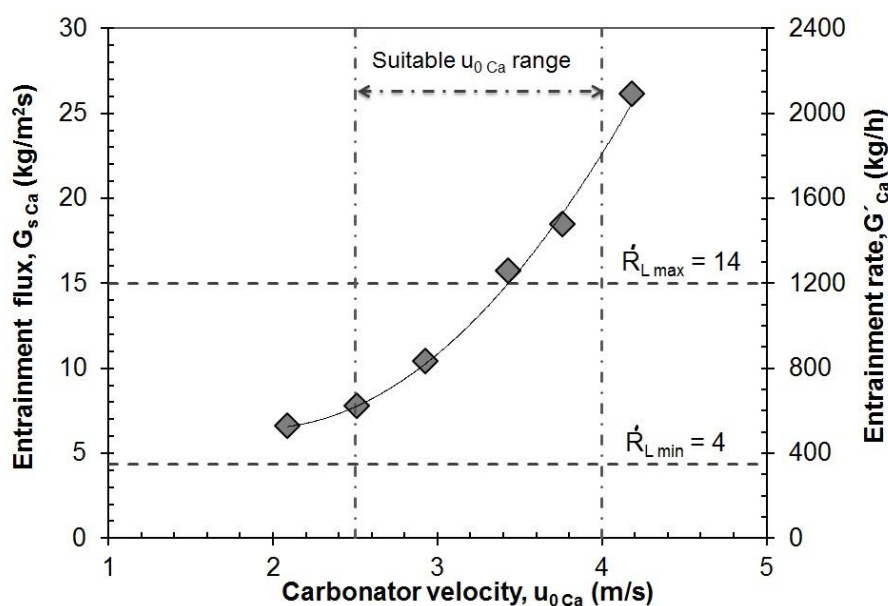

Figure 24 - Carbonator entrainment flux ($G_{s\,Ca}$) variation with carbonator velocity $u_{0\,Ca}$. (Particles iron oxide, d_{p50}=166 μm)

The carbonator solid entrainment flux ($G_{s\,Ca}$) against carbonator velocity ($u_{0\,Ca}$) in a single loop operation is shown in Figure 24. $u_{0\,Ca}$ is corresponding to the velocity in the top region diameter (92 mm) of the riser. As seen entrainment flux $G_{s\,Ca}$ clearly increases with increase in $u_{0\,Ca}$ with an exponential growth function. Such trends are common in a loop seal operated CFB riser [71,104,140]. The test plant entrainment rate $\acute{G}_{Ca}$ in kg/h is shown as secondary axis; by using the scaling ratio in Table 12. The entrainment rates corresponding to sorbent looping ratio ($\acute{R}_L$) of 14 is equal to 1200 kg/h, which is achieved at test plant carbonator velocity ($\acute{u}_{0\,Ca}$) of 5.3 m/s. Thus, the entrainment rates from carbonator are also found to be within the required range.

4.4.2.2. Regenerator

The air or oxidant staging is a vital factor which influences the pressure and solid fraction profile of the regenerator. In air staging operation the total volumetric flow rate ($\dot{V}_{Re}$) to the regenerator is divided in primary air (PA), secondary air (SA) and tertiary air (TA). The air staging ratio (ASR) here is denoted as the fraction of $\dot{V}_{Re}$ given in PA, SA and TA nozzles respectively. e.g. ASR 70:24:6 in Figure 25 represents 70% of $\dot{V}_{Re}$ in the PA nozzle, 24% in the SA nozzle and remaining 6% in the TA nozzle respectively. In without air staging operation, $\dot{V}_{Re}$ is given only through the PA nozzle. The regenerator velocity $u_{0\,Re}$ corresponds to $\dot{V}_{Re}$. Figure 25 shows the pressure profile and solid fraction profile of the regenerator with and without air staging operation. The solid fraction is measured using the pressure drop between the two pressure points as explained earlier (Page 59). In an air staged operation, at the bottom of regenerator (part of regenerator below SA nozzle) significant pressure drop and high solid fraction (0.1 to 0.27) is observed. The part above the SA nozzle can be called a lean zone, since a low pressure drop and a low solid fraction (average 0.011) is observed. The
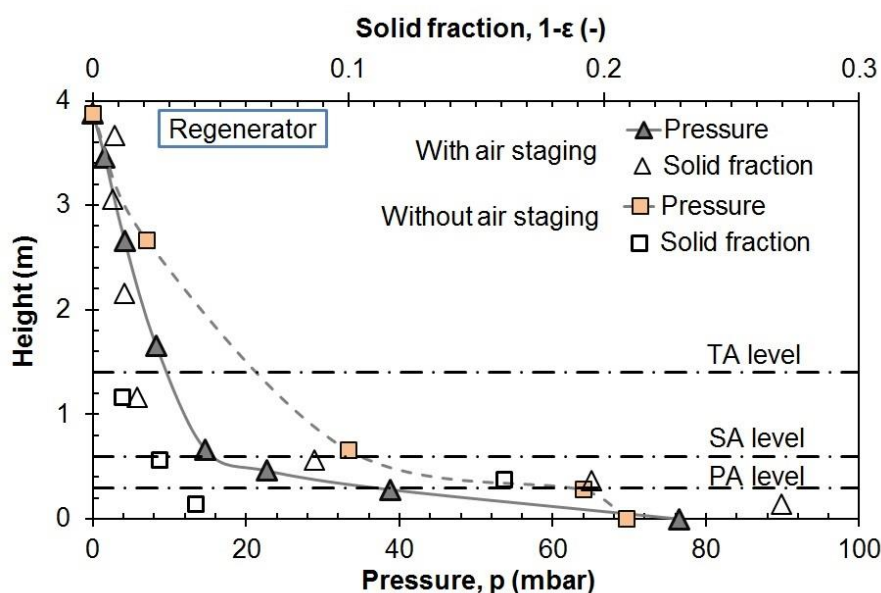

Figure 25 - Typical regenerator pressure and solid fraction (ε_s) profile, with and without air staging (Conditions: u$_{0\,Re}$ = 3.7 m/s, ASR 70:24:6% in air staging experiment).

dense zone at the bottom occurs due to the air staging, the gas velocity in the bottom zone is low therefore the turbulent conditions are created. Additionally as per Ersoy et al. [168] the insertion of secondary air causes further densification of the bottom zone. Without air staging, for the same $u_{0\,Re}$ and slightly lower total pressure drop value, the pressure profile is different. The pressure profile resembles an S- shape curve. The bottom zone is comparatively leaner (0.05-0.17), but the pressure drop and solid fraction in the upper lean region is higher compared to air staged operation.

The regenerator entrainment flux ($G_{s\,Re}$) against the regenerator superficial velocity ($u_{0\,Re}$) in a single loop operation is shown in Figure 26. The $u_{0\,Re}$ corresponds to $\dot{V}_{Re}$. As seen in Figure 26, $G_{s\,Re}$ is maximum without air staging. Entrainment flux clearly decreases with the application of air staging in comparison to without air staging. The increase in PA fraction increases the entrainment flux. This observation is consistent with the literature [140,154]. The test plant entrainment rate $\acute{G}_{Re}$ in kg/h is shown as secondary axis; by using the scaling ratio in Table 12. The entrainment rates corresponding to sorbent looping ratio ($\acute{R}_L$) of 14 is equal to 1200 kg/h, would be achieved at test plant regenerator velocity $\acute{u}_{0\,Re}$ = 6.7 m/s, and at cold model $u_{0\,Re}$=4.3 m/s without oxidant staging. This operating velocity is higher than the normal range of operating velocity and furthermore the air staging effect will reduce entrainment rates even more. In short the regenerator cannot generate enough entrainment flux to fulfill the required solid looping rates of up to 1200 kg/h (R_L = 14), but can fulfill partially up to 800 kg/h. This observation is the main reason why the solid looping rates reported in section 4.4.1 are limited to a value, and a simple conclusion can be made that the regenerator requires modifications in the design.
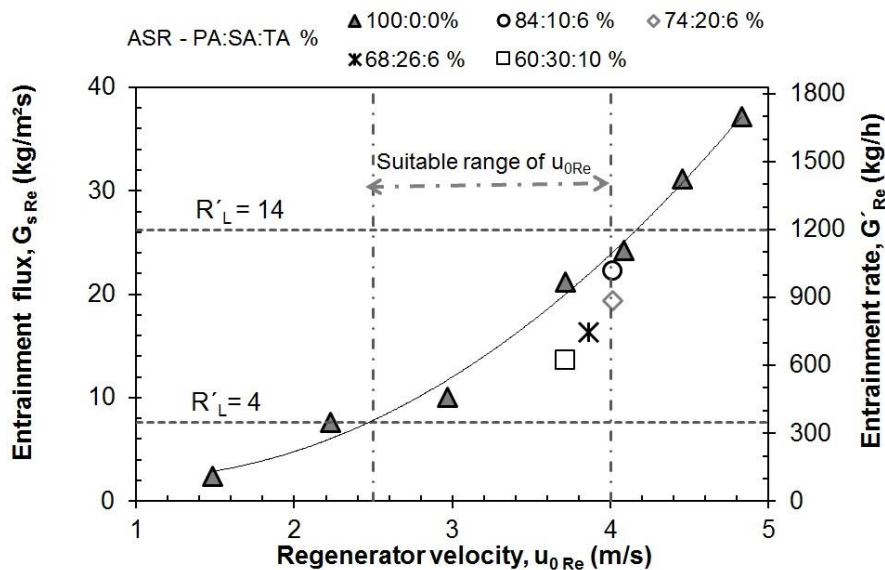

Figure 26 - Regenerator entrainment flux variation with and without air staging and riser velocity. Particles iron oxide, dp$_{50}$ = 166 µm

4.4.2.3.   **Fluctuations analysis**

Understanding the pressure fluctuations in a CFB operation is important as it helps identifying regimes. Pressure fluctuations in a CFB are represented in various ways, in this work the pressure fluctuations are quantified by the ratio of standard deviation of riser total pressure drop ($\sigma(\Delta p_{riser\ i})$) and riser total pressure drop $\Delta p_{riser\ i}$.

Figure 27 shows the variation of $\frac{\sigma(\Delta p_{riser\ Ca})}{\Delta p_{riser\ Ca}}$ in the carbonator against the carbonator velocity ($u_{0\ Ca}$). As seen, $\frac{\sigma(\Delta p_{riser\ Ca})}{\Delta p_{riser\ Ca}}$ reduce substantially with increase in $u_{0\ Ca}$ and becomes stable around 5% at 3.7 m/s.
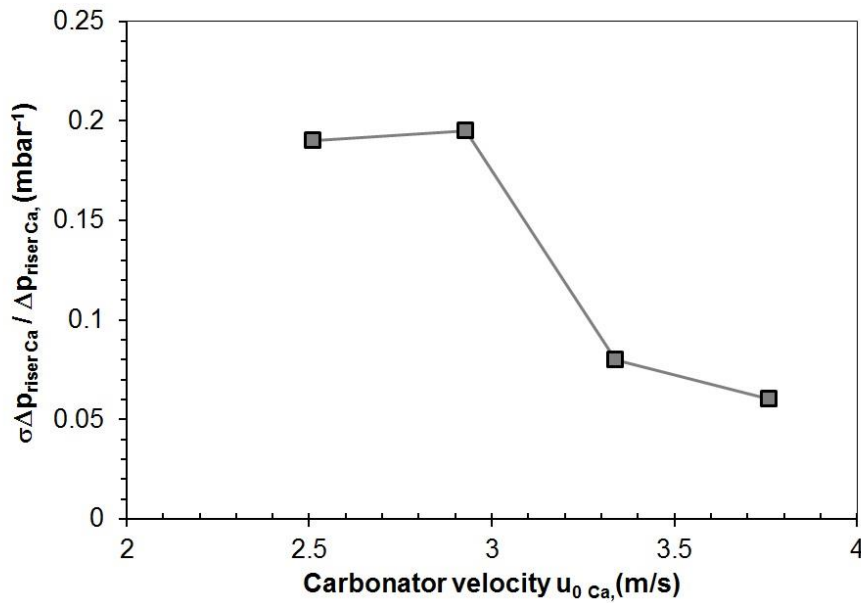

Figure 27- Carbonator's pressure fluctuations at different carbonator superficial velocities

The riser pressure fluctuations are widely used in qualitative identification of fluidization regimes. As discussed in section 2.2.1 and Figure 7, the pressure fluctuations in a riser follow a typical variation with change in riser velocity. It reaches a maximum at a velocity namely u_c and then steadily reduces and stabilizes at around certain value at velocity namely u_k. As discussed earlier, it is generally accepted that the turbulent regime begins at u_c and ends at u_k. Above u_k the regime is mainly fast fluidized regime. Thus up to 3.7 m/s the fluidization regime is mainly turbulent regime and above 3.7 m/s is fast fluidization regime. The experiments are not carried out to reveal the exact value of u_c.

In the regenerator, the variation of pressure fluctuations with riser velocity shows a similar trend as in carbonator only for the without air staging case. The pressure fluctuation behaviour changes significantly with the application of the air staging. Figure 28 shows the variation of the pressure fluctuation with various staging ratios, for a constant regenerator velocity ($u_{0\ Re}$). As seen in Figure 28, with a decrease in PA fraction, the pressure fluctuations increase rapidly; for PA flow of 50% of total VFR,
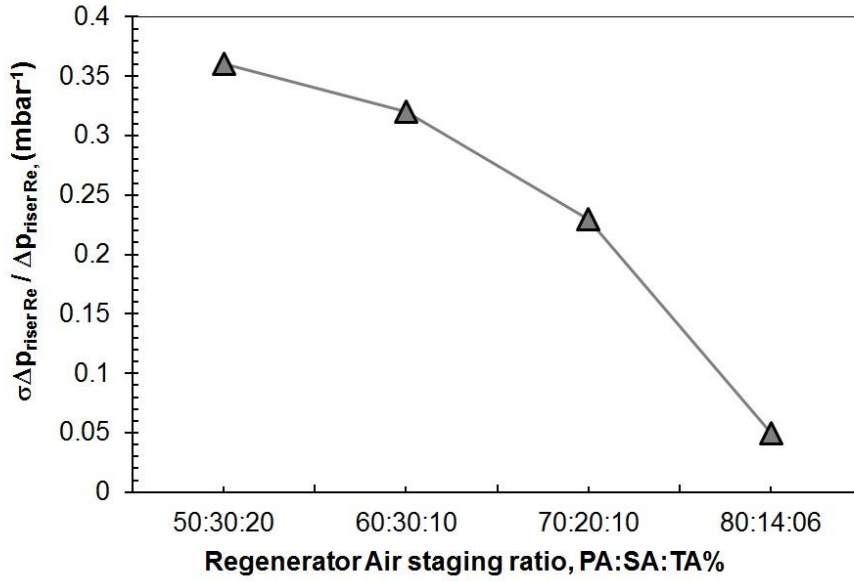
Figure 28- Regenerator's pressure fluctuations variation with change in air staging ratio

$\frac{\sigma(\Delta p_{riser\,Re})}{\Delta p_{riser\,Re}}$ is observed as high as 35%, and for PA flow of 80% of total $\dot{V}_{Re}$ for the same $u_{0\,Re}$, the $\frac{\sigma(\Delta p_{riser\,Re})}{\Delta p_{riser\,Re}}$ is observed as low as 5%. The increase of pressure fluctuations is a problem for the stability of the loop seal since it was observed that at high fluctuations gas escapes frequently through the cone valve. From these observations it is advised to operate the regenerator with PA with at least 70% $\dot{V}_{Re}$.

4.4.3. Solid flow diversion through cone valve and cone valve characterization

The solid looping rate from cone valve ($G_{L_{CV}i}$) cannot exceed riser entrainment rates (G_i). However, it is interesting to find out what fraction of the riser entrainment a cone valve can divert as a solid looping rate. The fraction of riser entrainment rate
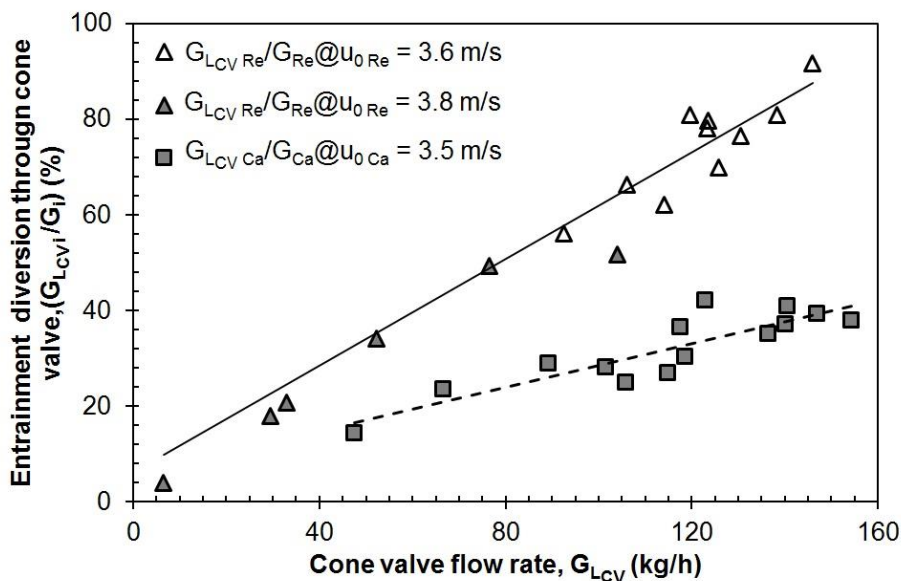

Figure 29 - Fraction of riser entrainment diverted through cone valve

diverted in the cone valve $\left(G_{L_{CV}\,i}/G_i\right)$ against the $G_{L_{CV}i}$ rate of the respective CFB is plotted in Figure 29. The riser velocity in this set of data points is constant and recorded entrainment flux is within a close range. Figure 29 implies that for the same $G_{L_{CV}}$ the fraction of solid flow diversion in regenerator cone valve is higher than the carbonator cone valve. The cone valve flow reached a maximum limit of ca. 150 kg/h because the solid flow diversion in regenerator cone valve reached close to a maximum limit and the diversion was as high as 80-90%. In the same situation the carbonator cone valve had diverted only 40% of G_{Ca}. Following conclusions can be made from this observation.

    a. The maximum solid looping rate which such a DFB system can offer is determined by the riser with lower entrainment rates, which in the present case is regenerator. It also implies the need to improve regenerator entrainment rates.

    b. Cone valves can divert a significant fraction of the entrainment rate they receive from the cyclone. In the present case, this fraction is observed as high as 90%.

Figure 30 shows the cone valve flow rates $G_{L_{CV}}$ against the product of cone valve opening and square root of the pressure drop across the cone valve ($A_{CV}.\sqrt{\Delta p_{CV}}$). The data points are taken from both cone valves. The data of Figure 30 is fitted with the equation.

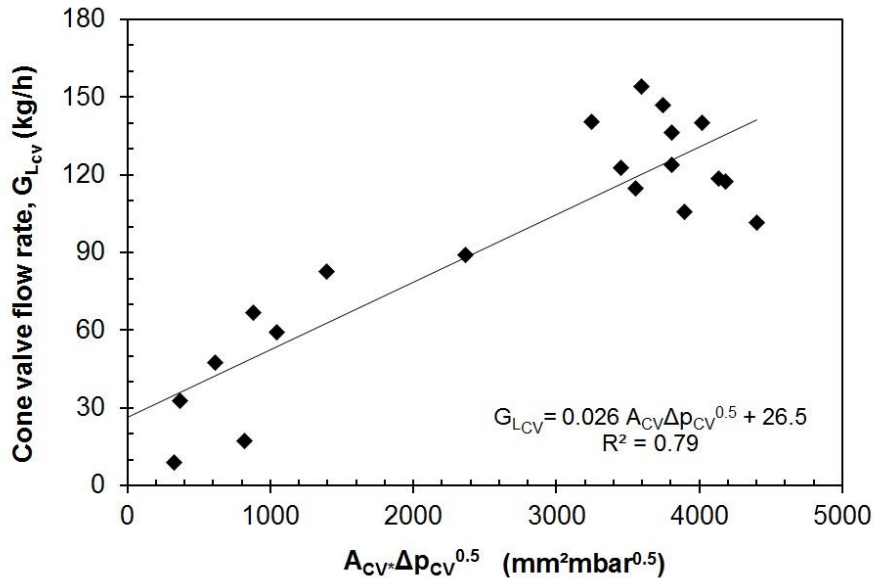$$G_{L_{CV}} = 0.026\, A_{CV}\, \sqrt{\Delta p_{CV}} + 26.47 \qquad (41)$$

Figure 30 -The cone valve equation, solid looping rate from cone valve against the product of area of the cone valve and square root of the pressure drop. Data points from both cone valves.

The cone valve equation found in this work Eq. (41) shows a satisfactory fit and is in agreement with the literature [148].

4.4.4. Influence of operational parameters in DFB operation

The parameter variation experiments are performed in order to study the influence of various parameters on the hydrodynamics of the DFB system.

4.4.4.1. Carbonator velocity

The effect of change in carbonator velocity ($u_{0\,Ca}$) on the pressure profile in both CFB`s is shown in Figure 31. In this set of experiments the regenerator velocity $u_{0\,Re}$, regenerator air staging ratio (ASR), total solid inventory (M_{To}) and cone valve openings ($A_{CV\,Ca}$, $A_{CV\,Re}$) are kept constant. As observed in Figure 31, the change in $u_{0\,Ca}$ brought changes in pressure profiles of both the risers. The increment in $u_{0\,Ca}$ causes decrease in $\Delta p_{riser\,Ca}$ in the carbonator and subsequent increase in $\Delta p_{riser\,Re}$. This indicates transfer of solid inventory from carbonator to regenerator. Increasing $u_{0\,Ca}$ reduces solid fraction (ε_s) in the bottom dense zone of carbonator and same time increases solid fraction in the top lean region of the carbonator, this behavior is common in a CFB [104]. However, the reduction in solid fraction is limited and does not reduce to the
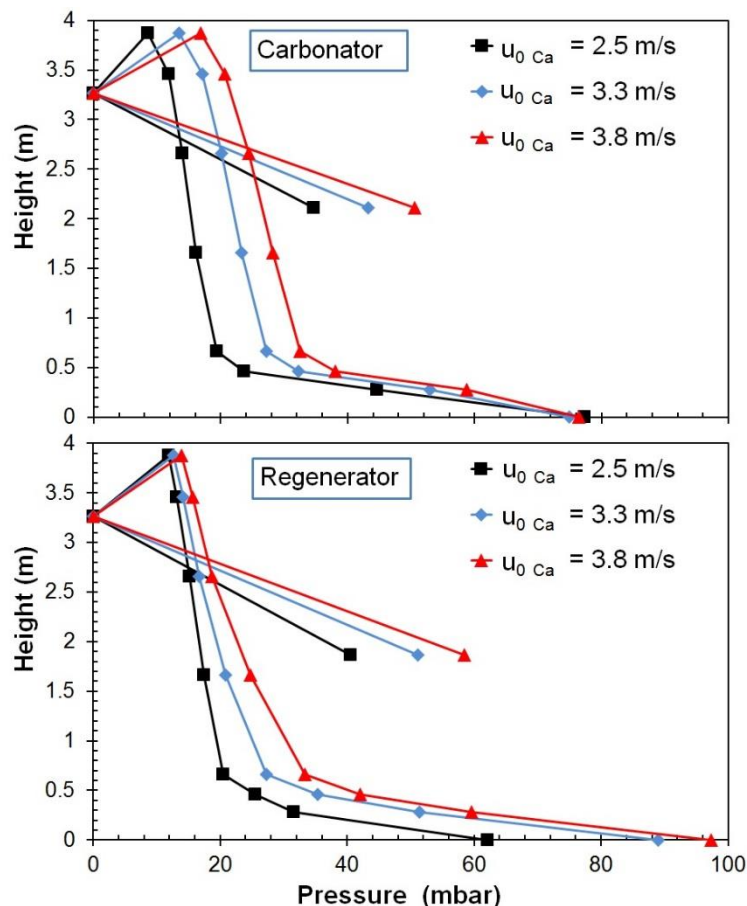

Figure 31- Effect of variation in carbonator velocity (u₀ Ca) on the pressure profile of both risers (Conditions: M_{To} = 10 kg, $u_{0\,Re}$ = 3.7 m/s, ASR PA: SA: TA %= 60:30:10 % $A_{CV\,Ca}$ = $A_{CV\,Re}$ = 79 mm²)

extent that carbonator bottom zone becomes lean: in comparison the risers with uniform diameter may become lean (ε_s<0.05) in the bottom zone with increase in the riser velocity [104]. This is an additional advantage of the wide bottom geometry.

The increment in $u_{0\,Ca}$ increases $\Delta p_{\,riser\,top\,Ca}$ and $\Delta p_{\,cyc\,Ca}$, therefore in response $\Delta p_{stp\,Ca}$ also increases as per Eq. (36). Since the DFB is interlinked, the increased $\Delta p_{stp\,Ca}$ tries to balance with the $\Delta p_{\,riser\,top\,Re}$ by inventory transfer. The pressure profile in the regenerator shows the pressure increment in the bottom dense zone. The pressure profile in the top lean region of regenerator especially above 2 m is nearly unchanged. Since, $u_{0\,Re}$ and the regenerator ASR are constant, the solid inventory transfer from carbonator has the same effect as the addition of the solid inventory to the CFB at constant velocity. Vice versa, when the $u_{0\,Re}$ is increased or if the fraction of PA in air staging is increased the solid inventory transfer is observed from regenerator to carbonator [177]. Variation in $u_{0\,Ca}$ also affects the solid looping rate from cone valve as shown in Figure 34a. The solid looping rate from cone valve decreases when carbonator velocity is increased from 2.5 m/s to 2.9 m/s. Further increase in carbonator velocity up to 3.76 m/s increased the cone valve solid looping rates. The pressure balance equations may clarify this variation in the solid looping rates but no definite trend is observed.

4.4.4.2.   Influence of total solid inventory of entire DFB system

The effect of increased total solid inventory (M_{To}) in the DFB system is shown in Figure 32. In this set of experiments the operational parameters such as both riser velocities, regenerator ASR and cone valve openings of both CFBs are kept equal and constant. In every experimental run a known quantity of solid inventory is added to the standpipe and pressure readings are taken after system is steady. As seen in Figure 32, the increment in M_{To} increases the pressure drop in both risers. The pressure drop and solid fraction is increased mainly in the bottom dense zone of the riser. The inventory is distributed in such a way that most of the added inventory accumulates in the bottom of the carbonator. The solid fraction in the top lean region and exit region of both risers does not show significant variation. The cone valve flow rates are also affected by the increment in M_{To} as shown in Figure 34b. Initial increment in M_{To} increases $G_{L_{CV}}$ and further increment in M_{To} decreases $G_{L_{CV}}$. Although, cone valve openings $A_{CV\,Ca}$, $A_{CV\,Re}$ are kept constant, M_{To} increment varies the pressure balance values and as per Eq. (37) (40) and (41) therefore the changes in $G_{L_{CV}Ca}$ and $G_{L_{CV}Re}$ are observed. However comparing Figure 34a and Figure 34b the trend of cone valve flow variation is not clear, when riser velocity is changed or M_{To} is changed.
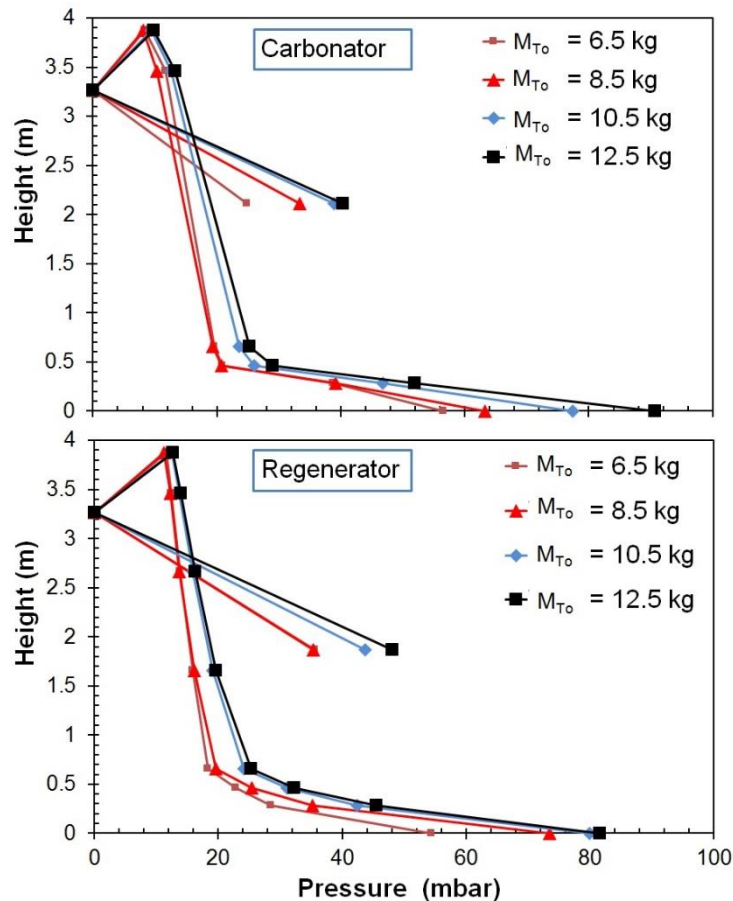
Figure 32 - Effect variation of total solid inventory M_{To} on the pressure profile of both risers (Conditions: $u_{0\,Ca}$ = 2.9 m/s, $u_{0\,Re}$ = 3.6 m/s, ASR PA: SA: TA %= 60:30:10 %, $A_{CV\,Ca}$ = $A_{CV\,Re}$ = 30 mm²)

4.4.4.3. Cone valve openings

Figure 33 shows the effect of cone valve opening on the pressure profiles of both risers. In this set of experiments, only the cone valve opening is increased stepwise in each experimental run, while both riser velocities, regenerator ASR, M_{To} are kept constant. Both cone valves are opened in equal size in a given experimental run i.e. $A_{CV\,Ca}$= $A_{CV\,Re}$ denoted as A_{CV} in Figure 33. As seen the pressure profile only changes when cone valve opening is changed from 3 mm² to 10 mm². At 3 mm² opening, the opening is not large enough for solid transport between the reactors and both risers are virtually not in coupled mode. When opening is increased to 10 mm² the sufficient solid transport between the CFB´s takes place and pressure profiles are adjusted according to pressure balance. Further increment in cone valve opening shows no change in pressure profile of both carbonator and regenerator. Thus no major inventory shift or distribution of inventory is observed when both cone valves are opened at same values. The effect of increased cone valve opening on the cone valve flow rate is shown in Figure 34c. The cone valve flow rate clearly increases with increase in cone valve opening, since pressure profiles were constant and standpipe pressures were also constant. Figure 34c indicates that the cone valve opening plays a major role in
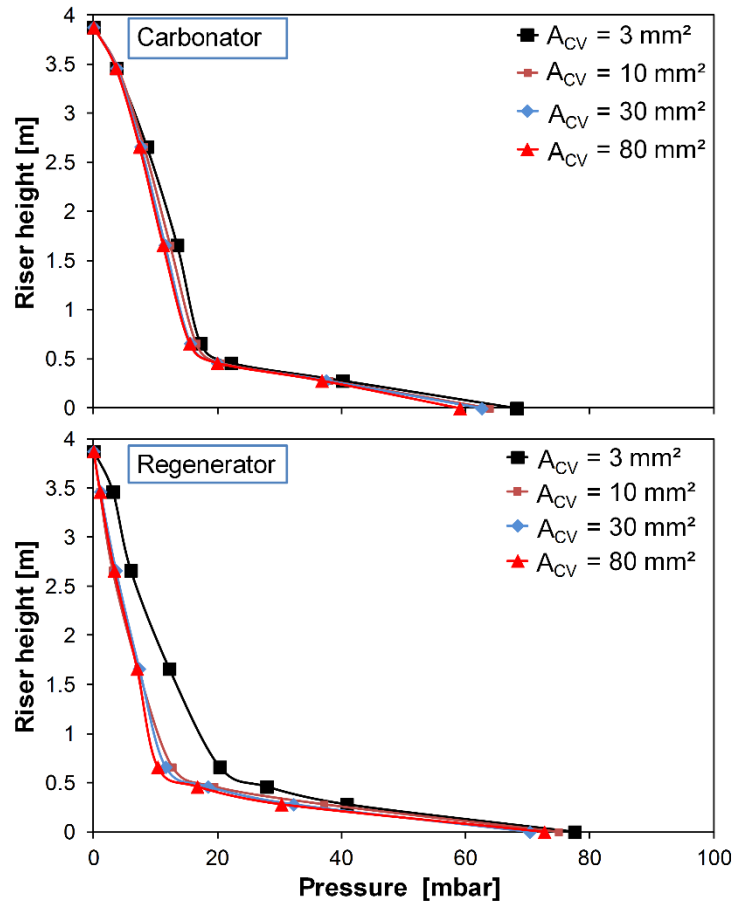
Figure 33 - Effect of cone valve opening in the dual mode on pressure profile of both risers (Conditions: M_{To}= 10 kg, $u_{0\,Ca}$ = 2.9 m/s, $u_{0\,Re}$= 3.71, ASR PA: SA: TA %= 60:30:10 %,)

controlling cone valve flow rates. In comparison to solid inventory variation or riser velocity variation shown in Figure 34a and Figure 34b respectively, the cone valve flow variation with cone valve opening variation is more predictable. i.e. flow will increase with opening of the valve and decrease with closing of the valve. The observation mentioned in this section is important from operators point of view, because in test plant operation, the operators may change the cone valve opening without affecting the pressure profile of the risers.

4.4.5. Factors affecting steady operation

Long term steady state operation is one of the features of this DFB cold model used in this study. However, in some operational conditions the DFB operation becomes unsteady. In a typical steady DFB operation the pressure profiles in both CFB´s are steady, whenever an operational parameter is changed next steady state is achieved smoothly with a transient state in between. In a transient state the pressure profile of both CFBs change as per the new pressure balance values and the inventory transfer and changes in cone valve flow rate take place. Such changes in pressure profile and cone valve flow rates are shown in Figure 31 to Figure 34. However in an unsteady operation the transient state lasts longer than usual. As a result one of the CFB loses a large fraction of its inventory to the other CFB without receiving much
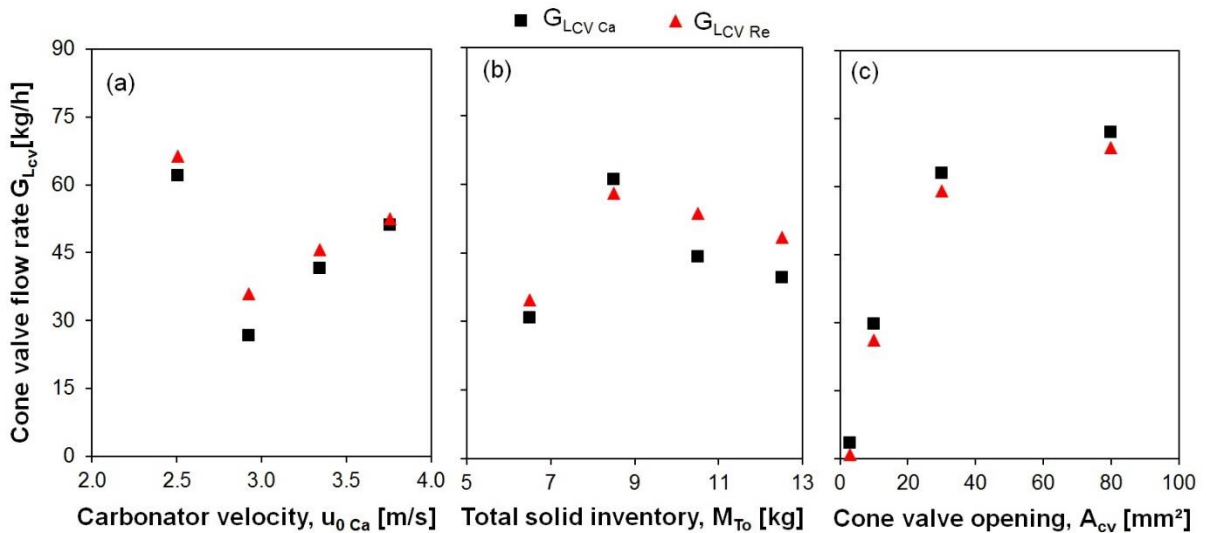
Figure 34 - Effect of the parameter variation on the cone valve flow rate in dual mode a. variation in carbonator velocity; b. variation in total solid inventory; c. Variation in cone valve opening (For conditions see Figure 31 to Figure 33)

inventory from the other CFB. A situation could arise that one CFB is entirely empty and other is full of solid inventory. The cone valve flow rates also do not equalize in such situation. Thus the DFB system struggles to gain steady state operation. Since one CFB receives large fraction of M_{To} and other CFB almost empties, the phenomenon of slugging and choking makes the CFB operation futile. Therefore, such an unsteady state in DFB operation is undesirable.

An unsteady DFB operation occurs when the operational parameters especially the riser velocity and the cone valve openings in both CFB`s are set with a large difference. Typically when the riser velocity in one CFB is set above 4 m/s and the riser velocity in other CFB is set at lower velocity of 2 m/s or less. The CFB with a higher riser velocity loses inventory while the low velocity CFB gains the inventory. When the cone valve opening in one CFB is set at 100% and if other is set mere at 15%, such unsteady state happens. In this situation the CFB with larger cone valve opening loses its inventory and the other CFB with a smaller cone valve opening gains the inventory. Similarly if the difference between exit pressures of CFB´s is high, such an unsteady situation may occur. The cold model is not equipped with a pressure regulating valve on the exit to observe this effect, but this observation is confirmed during the operation of the test plant [182]. This observation indicates that the operational conditions i.e. riser velocities, cone valve openings and CFB exit pressures in both CFB`s should be selected in close range without a large difference.

4.5. Design improvements and suggested alterations

4.5.1. Regenerator geometry

From the results discussed so far it is clear that the required solid looping rates may not be achieved in the test plant operation with planned preliminary design. The low entrainment rates from regenerator (G_{Re}) are identified as bottleneck due to its smaller riser cross section in comparison to carbonator. The effect of air staging is causing further reduction. To deal with the influence of air staging on the entrainment flux, the hopper like bottom is proposed for regenerator bottom. Such a geometry is common in industrial CFBC [9]. It can help to maintain higher velocities through PA nozzle than uniform cross section riser. With the suggested changes the test plant is constructed. The details of the final geometry can be referred in the Annexe B, Figure A 10. The riser at the bottom is 110 mm in diameter while near the exit is designed as 210 mm (from originally planned 170 mm) in diameter with stepwise increments. This stepwise increment is also deliberately created to nullify any velocity raise due to the CO$_2$ release from regeneration reaction. Initial results have shown that the entrainment rates from regenerator were satisfactory and the cone valve flow rates ($\acute{G}_{CVRe}$) up to 2500 kg/h were achieved during commissioning of the test plant [182].

4.5.2. Influence of the riser height above the riser exit

Apart from the application of hopper like bottom to the regenerator a review of design of the riser exit is also suggested. Both carbonator and the regenerator have abrupt (T shaped) exits shown in Figure 15. The dimensions of the riser exit are given in Table 9. Such a ´T Type` exit increases particle recirculation in the exit region, so called exit effects [108]. The shape of exit can influence the riser entrainment to a significant extent as suggested by Gupta et al. [108]. To choose a suitable type or modification in the exit shape, the single loop experiments are performed on the regenerator with T shaped exit by varying the riser length above the exit (H_{exit}). Four different lengths are selected; 0 mm, 50 mm, 100 mm and 200 mm. The 200 mm is the maximum length available in the cold model and the results presented in the section 4.4.2.2 are from H_{exit}=200 mm. To reduce the H_{exit} the volume in the length above exit is blinded at selected distances. The possibility of using smooth bend exit is also tested in these experiments, because smooth bend type exit is known to have highest possible entrainment rates. For testing smooth bend type exit, the entire T shaped exit assembly is replaced with a smooth bend named C-shaped exit. The experimental procedure of single loop CFB experiments is explained in section 3.3.3. Only the entrainment rates are compared here in this section.

Figure 35 compares the regenerator entrainment flux ($G_{s\,Re}$) against regenerator velocity ($u_{0\,Re}$) at various heights above the exit (H_{exit}) with C shaped exit. The results are also compared with the required circulation rates at scaled conditions. As observed
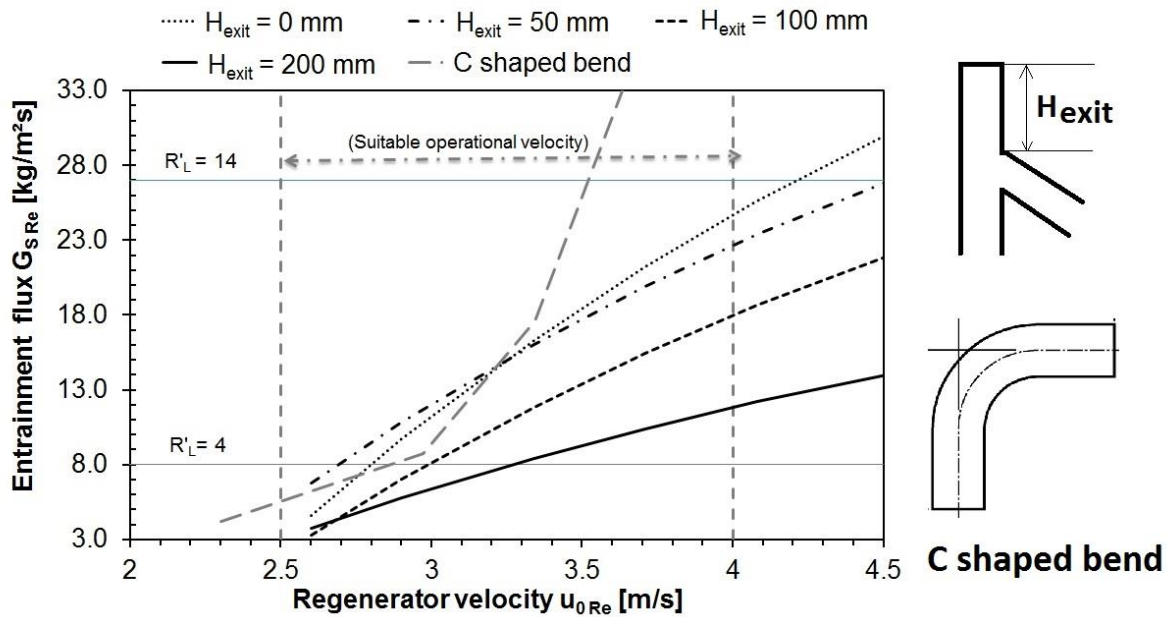
Figure 35 – Influence of the riser height above exit of the riser on the riser entrainment flux and comparison with a c shaped bend type exit.

in Figure 35, the riser entrainment rates are significantly affected by the type of exit. The T shaped abrupt exit produces lower entrainment rates compared to C shaped exit. In the case of T shaped exit the height of riser above the exit also affects the entrainment rates to a significant degree. The increase in the height (H_{exit}) decreases the entrainment rates. For the length of 0 mm or 50 mm the circulation rates are maximum in the case of T shaped exit. These results are in agreement with the prediction of Lackermeier and Werther [183]. For calcium looping process the C shaped exit may produce the entrainment rates high enough to satisfy the required solid looping rates, while T shape exit may struggle within the required velocity range. However, due to the need of combustion process in the regenerator the smooth bend exit is not suggested, because the entrainment rates will be significant and that will cause a low burnout of the solid fuels, which is undesirable. Therefore it is suggested to continue with a T shaped exit with a minimum possible height above the exit.

4.5.3. Influence of the loop seal depth and cone valve performance

The preliminary design had a major drawback of limited solid looping rate. As per Eq. (41) to increase solid looping rate from cone valve, the pressure drop across the cone valve and-or cone valve opening should be increased. The pressure drop across the cone valve as per Eq. (39) and (40) is increased when the standpipe pressure drop is increased. An innovative approach is selected to increase pressure drop in the loop seal, i.e. to increase the weir height or the height of recycle side of the loop seal (see section 2.2.5 for loop seal construction) of the loop seal.

Very little is known about the design of the loop seal, therefore to find out the suitable weir height or recycle chamber depth, special loop seals are constructed for

both CFB's. These specially constructed loop seals have uniform cross section and only the weir height is variable using a movable slide as shown in Figure 36. The dimensions of the supply chamber are kept fixed. With the movable slides the influence of the weir depth can be investigated. The experiments are performed in DFB operation as explained in experimental section.
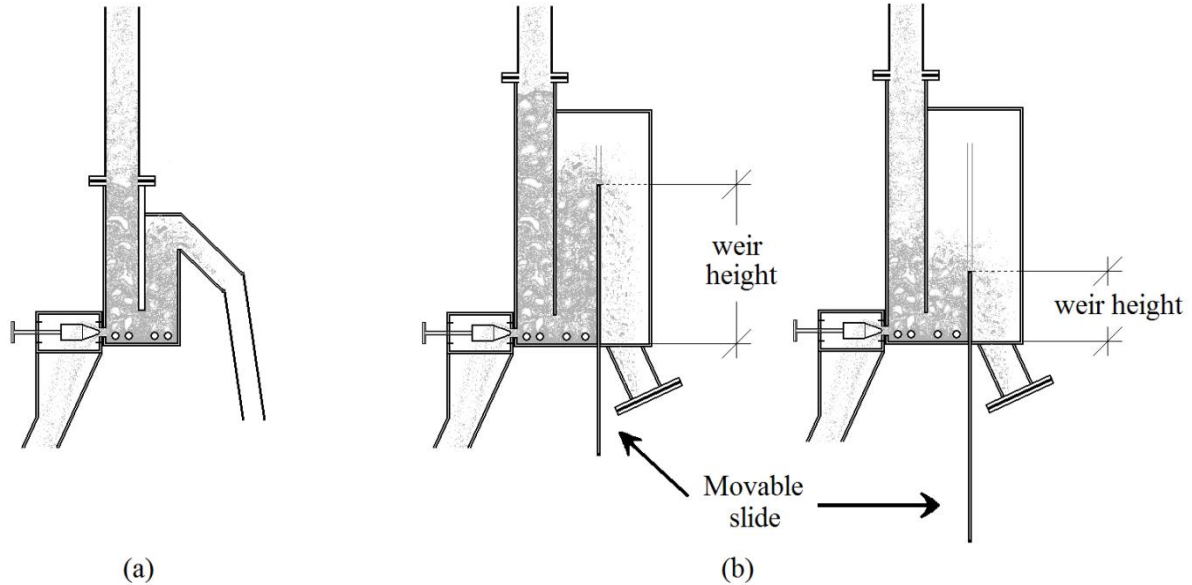

Figure 36 - Loop seal configuration with a fixed (a) and modifiable (b) recycle chamber depth

Figure 37 shows the influence of loop seal weir height on the standpipe ($\Delta p_{stp\ Re}$) and loop seal pressure drop ($\Delta p_{LS\ Re}$) and the corresponding solid looping rate from cone valve ($G_{L_{CV}\ Re}$). Only the regenerator results are shown here. Similar observation is confirmed for carbonator loop seal. In this set of experiments the following operational parameters are kept constant: riser velocity in both CFBs, ASR in regenerator and cone valve openings in both CFBs. Total solid inventory (M_{T_o}) in this set of experiments is varied because with increasing weir height in the loop seal the solid inventory required in the loop seals also increased. Therefore, M_{T_o} is adjusted in order to achieve a constant pressure drop in both CFB's. However maintaining exact total pressure drop in both CFB's is difficult in all experiments but manageable within a close range. The total pressure drop in regenerator is recorded between 65-73 mbar, while for carbonator recorded between 32 to 45 mbar. The loop seal operation for increased recycle chamber depth is performed with loop seal fluidization velocity in the range of 3-6 u_{mf}, it is the suitable range of operation for loop seal fluidization (see chapter 6). As seen in Figure 37, the increasing weir height clearly increases the solid looping rate from cone valve. Visual observation shows that the bed height in the standpipe is also increased with every step increase in the weir height. With increased bed height of the particles in the standpipe the pressure drop in the standpipe is increased and since the riser pressure drop in the opposite reactor was constant the pressure drop across the cone valve is also increased. Therefore such increment in the standpipe creates increment in the solid looping rate from cone valve too. The solid
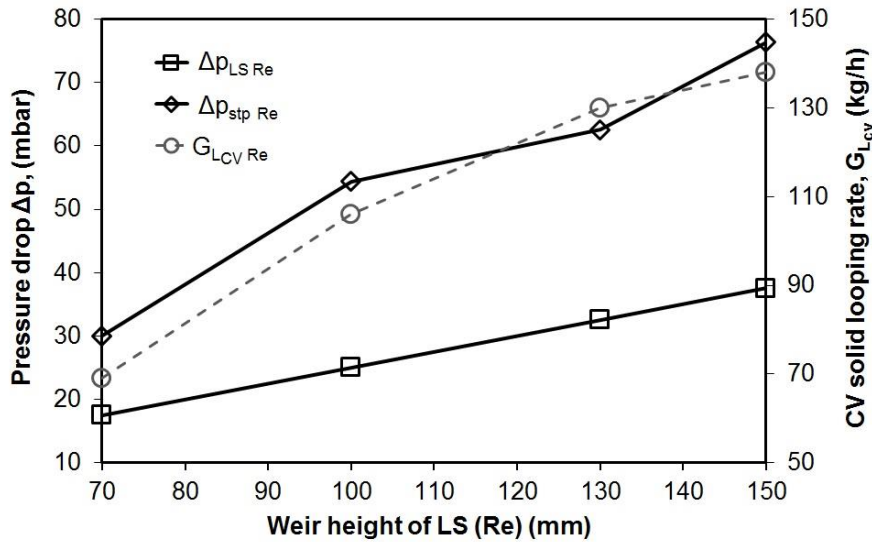
Figure 37- Effect of regenerator loop seal recycle chamber depth of CFB on the standpipe pressure drop and cone valve flow rate of regenerator. ($u_{0\ Re}$=3.5 m/s, ASR PA:SA:TA% 70:24:6%, $u_{0\ Ca}$=3.5 m/s , $\Delta p_{riser\ Re}$ = 65-73 mbar, $\Delta p_{riser\ Ca}$= 33-45 mbar $A_{CV\ Ca}$= $A_{CV\ Re}$= 79 mm²)

looping flow rates from cone valve above 70 kg/h shown in Figure 22 are achieved with increased loop seal weir depth.

Regarding the loop seal operation, increment in the recycle chamber depth did not show any signs of difficulty in the operation or need to change the quantity of loop seal aeration. Detailed studies of the loop seal operation are reported in chapter 6.

4.5.4. Diameter of carbonator bottom ($D_{Ca\ bot}$)

The influence of the carbonator's wide bottom has been discussed earlier in section 4.4.2. However, the hydrodynamics of the wider diameter riser has been less studied in the literature and the influence on the riser circulation rates are less known. From Figure 26 it is well understood that the primary velocity is a main driver of riser entrainment rate. Due to lower velocity in the wide diameter region for a wider diameter riser, the riser entrainment rates are expected to be affected. Therefore to study the exact influence, the bottom diameter of carbonator ($D_{Ca\ bot}$) is varied and single loop CFB experiments are performed on R2 cold model. Two separate riser bottoms are constructed for R2 cold model, namely 110 mm and 92 mm of the same length as 140 mm bottom. The single loop CFB experiments are performed as explained earlier in experimental section 3.3.3. The results are investigated for carbonator pressure profile and carbonator entrainment rates.

In Figure 38 the carbonator pressure profile is shown for constant total solid inventory (single loop CFB) of 10 kg and constant carbonator velocity of 2.9 m/s. As seen for a wider diameter of 140 mm the total pressure drop in the riser is less than the uniform diameter riser of 92 mm. This is reasonable due to larger area available in riser with wide bottom and as per Eq. (13) the pressure drop will be lower for wider bottom. But the solid fraction in the lean region is lower for wider bottom compared to
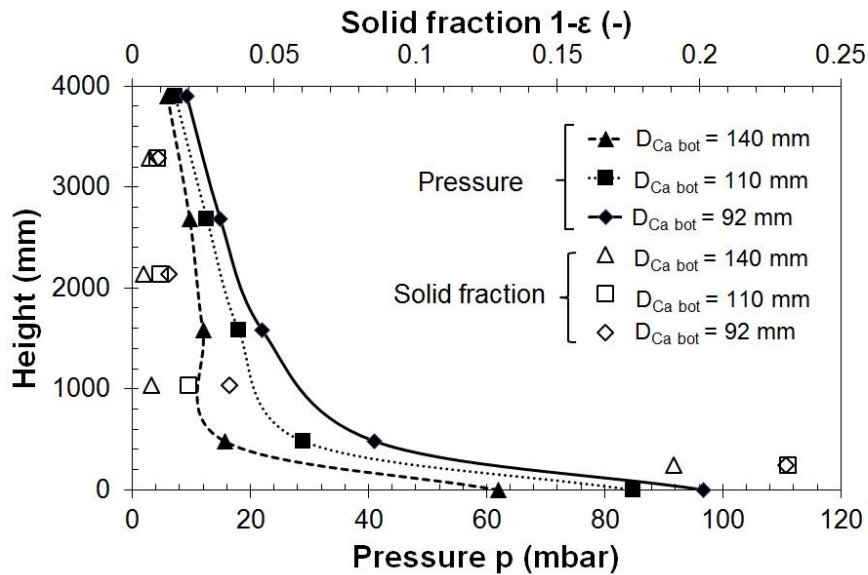
Figure 38- Pressure profile variation over the height of the riser for various carbonator bottom diameters. Single loop M_{To}= 10 kg, $u_{0\,Ca}$= 2.9 m/s

uniform diameter riser. It is also important to notice that the pressure drop and solid fraction in the exit region do not differ much with the diameter of the bottom section rather it is dependent more on the riser superficial velocity.

The carbonator entrainment rates $G_{s_{Ca}}$ for different bottom diameters are shown in Figure 39. The trend for 140 mm diameter in comparison with 110 mm and 92 mm shows lower entrainment rates. The variation of entrainment flux trend between 110 mm and 92 mm is not conclusive. However, comparing between 92 mm and 140 mm it shows that the wide bottom can affect the riser entrainment rates. Compared to uniform diameter riser the $G_{s_{Ca}}$ rates are lowered by 5-7% for wider diameter of 140 mm. When the $G_{s_{Ca}}$ values are compared with the required solid looping rates values the uniform diameter riser shows better performance.

In Figure 40 the carbonator inventory (M_{Ca}) is calculated for the riser pressure profiles of Figure 38, using Eq. (13). Since the area of wide bottom and the riser are different for 110 mm and 140 mm case, the pressure drop for two sections (wide bottom and riser) are measured separately and riser inventory is calculated for respective riser areas. The sum of two sections is then M_{Ca}. It is clear from Figure 40 that the M_{Ca} hold by the riser increases with the wide bottom

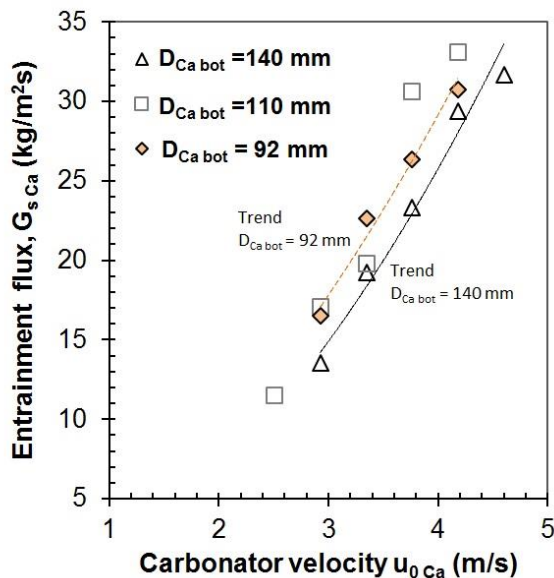**Figure 39 – Influence of the carbonator's bottom diameter on the riser circulation rate, M_{To}= 12 kg, dp_{50}= 141 μm**
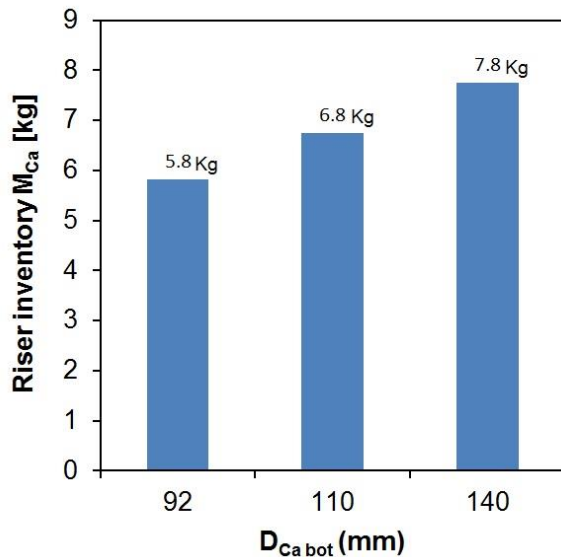
Figure 40 – Calculated riser inventory from Eq. (13) for pressure profile of Figure 38

diameter and is maximum for 140 mm. In section 4.4.2 it is shown that the riser with wide bottom has an advantage in achieving suitable operational boundary conditions. If compared with the riser entrainment rates, the wide bottom influences the riser entrainment slightly but offers a large solid inventory for increased space time. To conclude from these observations made in this section, the wide bottom design of carbonator is validated.

4.6. Summary

The hydrodynamic investigation of the 200 kW$_{th}$ calcium looping test plant was carried out in a geometrically and hydrodynamically scaled cold model. The novel CFB-CFB type dual fluidized bed system is used with two separate cone valves. Cone valves are used as an interlinking between the two CFBs. Achieving steady states through equal solid looping rates from the separately operating CFBs is important. The cold model has shown that the long term steady dual fluidized bed operation with equal solid flow rates from the cone valves can be easily achieved. Aim of the experiments was to validate if the design of the DFB test plant can fulfill the required operational boundary conditions. In cold model only the boundary conditions related to the hydrodynamics such as riser velocity, riser inventory, riser entrainment flux and looping rates through cone valve are tested. The results from cold model are scaled to test plant using scaling ratios and compared with the required operational boundary conditions. Both CFB's operate satisfactorily in the required velocity range, the required inventory in the carbonator is easily obtained through the application of wide bottom design. The riser entrainment rates from the carbonator are found satisfactory. The wide bottom's influence on the entrainment flux is less.

Regenerator entrainment rates are found to be lower than the required, therefore the maximum looping rates are limited. The effect of air staging in the regenerator is found to be the major reason for the limitation of entrainment rates. To counter the influence of air staging regenerator with conical bottom is suggested, having smaller diameter at the bottom and diameter gradually increasing axially. It is also found that the length of the section above exit has a significant influence on the entrainment flux.

Increasing height decreases entrainment rates therefore riser height above exit should be kept as minimum as possible.

The cone valve throughput with the preliminary design was limited, therefore the use of loop seals with an increased weir height is suggested. This suggestion tested in cold model shows that with increase in weir height of the loop seal the cone valve throughput is improved.

The effect of parameter variation is studied in order to characterize the DFB system. The influence of increment in total solid inventory, riser velocity and cone valve opening are investigated to observe the changes in riser pressure profile and cone valve flow rate. It is observed that the additional solid inventory goes to the bottom of both risers primarily to the carbonator. The increment in riser velocity can cause inventory transfer from one CFB to other, while increment of cone valve opening in both CFB does not cause significant change in pressure profile of both CFB's. Changes in the solid inventory, riser velocity and cone valve opening cause change in cone valve flows, change in the cone valve flow due to the velocity change and total solid inventory change is hard to predict. On the contrary change caused due to cone valve opening is more predictable and reliable.

The results from the cold model shows a satisfactory design of a DFB system for calcium looping process. Certain limitations are highlighted, which can be overcome by the suggested modifications.

5. Hydrodynamic studies of cold model of 200 kW$_{th}$ CFB-BFB test plant for SER process.

The sorption-enhanced reforming (SER) process is a promising subtype of the gasification process through which hydrogen rich product gas is generated. Previous lab scale results at University of Stuttgart has inspired to investigate the process at a higher scale but in a set up suitable for the industry. The 200 kW$_{th}$ test plant is also designed to demonstrate SER process in SER mode set-up, the set-up is described earlier in section 3.2. It consists of a BFB-CFB type DFB system where BFB is a gasifier and CFB is a combustor and the solid looping will be carried out with the help of an L-valve (see Figure 16). This chapter will focus on the hydrodynamic studies carried out on the cold model of the SER mode test plant set-up and will show that the planned set-up is suitable for the SER process. The work presented in this chapter is published in a peer reviewed journal [184].

5.1. Objectives of the hydrodynamic studies

The usefulness of the cold model studies is already discussed in depth in this work. The objectives of the hydrodynamic studies of SER mode cold model could be drawn parallel to CaL mode cold model, i.e. to achieve
   a. Long term hydrodynamic steady DFB operation
   b. Achieving operational boundary conditions for the SER process
   c. Investigate suitability of the BFB reactor as a gasifier.
The long term steady DFB operation is vital to the operation and demonstration of the SER process. However, BFB-CFB type DFB are more commonly used DFB systems and there is certain degree of assurance about feasibility of long term operation. This assurance is mainly due to experience from previous work at University of Stuttgart [71,72] and also by learning from other DFB systems reported from TU Wien [136]. But for the novelties brought in the design like the use of L-valve and the gasifier loop seal, it will be interesting to test the long term operation of the SER mode DFB system.

Similar to operational boundary conditions mentioned for CaL process in section 4.2, boundary conditions are also set for the SER mode. But unlike CaL process, the SER process is more complex and involves a significant number of parameters. Describing a detailed relationship between the design parameters and process boundary conditions for the SER process is not intended in the scope of this thesis. The main process boundary conditions defined for SER process are particle residence time and superficial velocities in gasifier and regenerator. The particle residence time in gasifier ($\acute{\tau}_{R\,Ga}$) is defined as the ratio of bed mass of gasifier ($\acute{M}_{Ga}$) to the solid looping

rate. In SER mode the solid flow rate generated by the L-valve is none other than the solid looping rate ($\acute{G}_{L_{LV}}$). Thus residence time ($\acute{\tau}_{R\,Ga}$) as per Eq. (42) is

$$\acute{\tau}_{R\,Ga} = \frac{\acute{M}_{Ga}}{\acute{G}_{L_{LV}}} \tag{42}$$

The particle residence time indicates how long the particle will reside in the gasifier, this parameter is very significant because kinetics of steam gasification in SER process is a slow process due to low temperature of gasification (600-700°C). The superficial velocities in the gasifier bed and combustor are defined by the regime requirement and thermal firing capacity of the regenerator. Considering all these aspects the process boundary conditions are mentioned in Table 14, the operational boundary conditions for the SER process for 200 kW$_{th}$ test plant are derived from these process boundary conditions.

Table 14 – Simplified process boundary conditions of the test plant for SER mode operation

Parameter	Symbol	Unit	Value
Gasifier residence time	$\acute{\tau}_{R\,Ga}$	min	4-8
Gasifier velocity	$\acute{u}_{0\,Ga}$	m/s	0.4-0.8
Regenerator velocity	$\acute{u}_{0\,Re}$	m/s	4-6

Table 15 shows the boundary conditions for SER mode, derived from the process boundary conditions given in Table 14. As discussed earlier, one of the main concerns in the application of scaling laws to SER mode cold model is the difference in solid to gas density ratio $\left(\frac{\rho_s}{\rho_g}\right)$ (see Eq. (26) page 34). In the case of SER mode this difference is higher compared to the CaL mode. In CaL mode the difference is adjusted using a CO$_2$-Air mixture in the regenerator. In SER mode, if one has to perform the scaled experiments using the same particles, we need substantial quantity of helium in the BFB to adjust the density ratio in the gasifier. To apply the scaling laws to compare cold model and test plant, a simpler approach is followed as described:

i.   The DFB experiments are performed with the steel particles, which fulfil the gas to solid density ratio in gasifier cold model. The scaling ratios for pressure and inventory are only applied to the gasifier and not to the regenerator.

ii.   The regenerator operation (test plant), operational conditions and particles in SER mode are similar as in CaL mode regenerator. Therefore to compare the performance of regenerator for testing boundary conditions in SER mode one can simply use the results from chapter 4 for regenerator and compare for SER mode requirements.

In addition to the operational stability and achieving boundary conditions; an additional aim of the SER mode cold model is to study the suitability of the BFB as a gasifier, the BFB is designed exclusively to work as a gasifier and therefore certain design features considered in the design are described in section 3.2. In order to

validate the functionality of these features, the cold model experiments are a suitable method. To investigate this functionality, two separate approaches are followed.

a. Visual observation of gas solid mixing in the gasifier bed
b. Separate segregation experiments, which enable us to find the mixing behavior of the light fuel particles in the bed.

The segregation experiments are carried out in a separate experimental set up with a different experimental procedure. Since this set up and procedure is peculiar to this chapter, it is described in detail in next section.

Table 15 - Operational boundary conditions of the test plant and cold model for SER mode operation

Parameter	Unit	Gasifier			Regenerator		
		Test plant	Cold model	Scaling ratio	Test plant	Cold model	Scaling ratio
D	m	0.35	0.14	2.5	0.17	0.069	2.5
H	m	6	2.4	2.5	10	4	2.5
T	°C	600-700	20		850-950	20	
ρ_s	kg/m³	2200	7500		1800	7500 5100*	
d_p $d_{p\,50}$	µm	200-500	70-220 110		200-500	70-200 119	
u_{mf}	m/s		0.03			0.02	
ρ_g	kg/m³	0.24-0.3	0.9		0.4	1.18*	
u_0	m/s	0.4 – 0.8	0.26 - 0.52	1.53	4.5 - 6.5	2.6 - 4	1.73*
$G_{S\,Re}$	kg/m²s	-	-	-	8 - 12	13 - 20*	0.61*
G_{Re}	kg/h	-	-	-	1000 - 1500	175 - 265	5.65*
$G_{L_{LV}}$	kg/h	-	-	-	200-900	-	-
Δp_i	mbar	25-60	35-85	0.7	60-80	60-80*	1.05*
M	kg	30-50	8-13	3.9			
θ	h^{-1}	6-18					

*- Use of iron oxide particles for the scaled performance of regenerator

5.2. Set up of segregation experiments

In the SER mode, it is interesting to note that the bed material in the gasifier is received from the top and leaves through the bottom from gasifier loop seal, thus the resultant solid flow direction in the gasifier is downwards. The gasifier bed is comprised of main bed material and char particles. The main bed material which is mainly limestone is heavier than the char which undergoes the gasification reaction. Even though the light char has a tendency to segregate to the upper part of bed, the downward flowing main bed material also may take the light char particles along. To investigate the suitability of the gasifier for SER process, this is an important aspect.

In a separate experimental set up the influence of such downward flowing bed material is studied on the residence time of light and heavy fraction in the bed. This experimental set up is shown in Figure 41. It consists of a simple bubbling fluidized bed (Diameter 70 mm, height 400 mm) having a drain with a ball valve. The bubbling bed has two semicircular slots (at 70 and 140 mm above distributor) to allow flaps inside the bubbling bed as shown in Figure 41. These slots and flaps arrangement is used in the segregation analysis at the end of experiment. The slots are sealed using a cellophane tape during a normal fluidized bed operation. The heavy particles are steel simulating limestone bed and the light particles are limestone simulating char particles. The particles are chosen in such a way that the ratio of density of heavy and light components $\frac{\rho_{S_{heavy}}}{\rho_{s\,light}}$ in test plant gasifier and cold model match or close. Secondly in the cold model, the light and heavy fractions should be able to be easily sieved or separated using magnet. Table 16 shows the densities of the particles used in this experimental set up. In test plant heavy and light fractions are namely CaO and char. In this experimental set up the heavy and light fractions are steel powder and limestone.

The BFB in Figure 41 is loaded with a mixture of light and heavy fraction. At the start normally at the beginning of experiments concentration of light particles is chosen as 5 wt %. The down flow in the bed is generated by opening a valve situated as a drain. The flow rate is controlled by valve opening, and the bed inventory is maintained

Table 16-Particle densities used in the residence time analysis experiments

	Test plant		Cold model	
	Material	Density (kg/m³)	Material	Density (kg/m³)
Heavy fraction	CaO	1800	Steel powder	7500
Light fraction	Char/ Biomass	300-500 [185]	Limestone	1800
Density ratio $\left(\frac{\rho_{S_{heavy}}}{\rho_{s\,light}}\right)$	6 - 3.7		4.2	

constant by continuously adding particle mixture manually. The flow from the drain is collected for a period of one minute and repeated several times (6-10 times). Collected mixture is sieved and weighed separated as heavy and light. The residence time (modified Eq. (42)) for heavy and light fraction is calculated as

$$\tau_{Ri} = \frac{M_i}{G_i} \tag{43}$$

Where M_i is the weight of the component i in BFB bed calculated using input- output mass balance. G_i is the downward solid flow rate of component i measured in kg/hr. Component i is either heavy or light. The residence time ratio (γ) is defined as

$$\gamma = \frac{\tau_{R\,light}}{\tau_{R\,heavy}} \tag{44}$$

The inverse of the Eq. (43) is termed as turnover ratio (θ), which represents how much number of times the bed inventory is replaced by the solid looping rate in a unit time.

$$\theta = \frac{\sum G_i}{\sum M_i} \tag{45}$$

At the end of experiment the fluidization in the bubbling bed is stopped suddenly, this practice is commonly known as bed freezing [186], used commonly in analyzing segregation behavior in fluidized beds. Two flaps are hammered in the frozen or standstill bed in the slots as shown in Figure 41. Thus bed is divided in 3 layers namely top layer, middle layer and bottom layer. The bed is drained separately for 3 separate zones, separated for light and heavy particles and the concentration of the light particles in each section is measured as weight %. The effect on the $\tau_R\,Ratio$ and
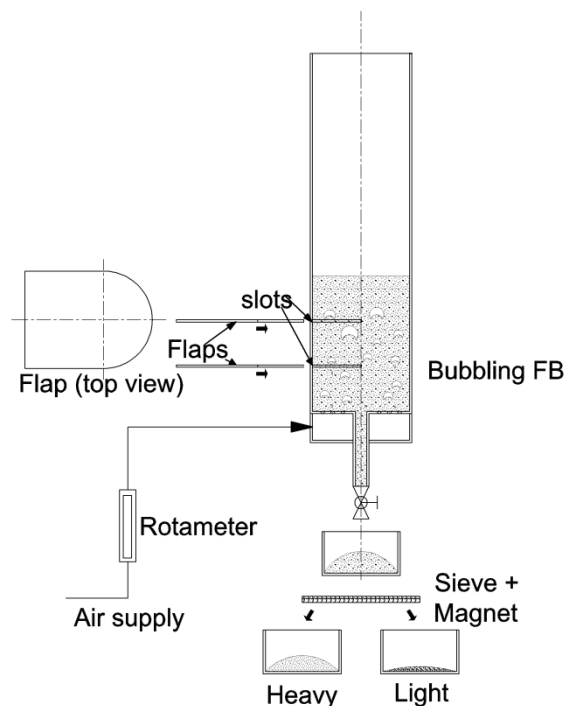

Figure 41 - Experimental setup for segregation and residence time (RT) study

concentration of light particles is analyzed for various bed superficial velocities and turnover ratios.

5.3. Pressure balance analysis

For a SER mode cold model the DFB system is depicted again in Figure 42. In this set up there are two clear distinct pressure balance loops. The first loop is a normal CFB loop in the regenerator as riser-cyclone-standpipe-loop seal-riser-loop-return leg. (follow a-b-c-d-e-f-g-a in Figure 42) The pressure balance for this loop is described in Eq. (37) and the relevant terms are explained thereafter (see page 55).
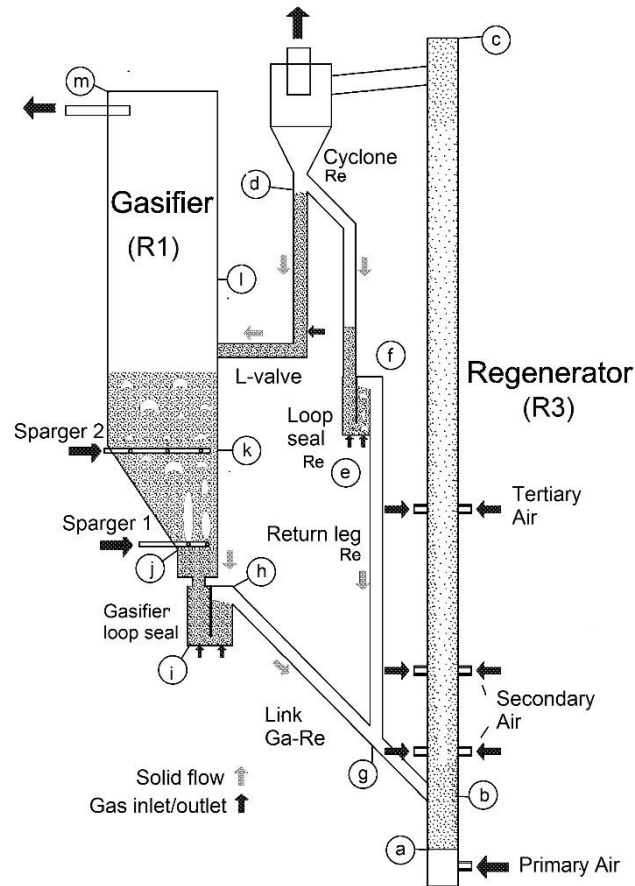
Figure 42- SER mode cold model set up

$$p_{Ga} + \Delta p_{bed\ Ga} + \Delta p_{LS1\ Ga} = \Delta p_{LS2\ Ga} + \Delta p_{riser\ top\ Re} + \Delta p_{cyc\ Re} + p_{Re} \tag{46}$$

The second loop in this DFB system links gasifier and regenerator; this loop can be traced as freeboard (gasifier) – particle bed (gasifier) – gasifier loop seal – riser (regenerator) – cyclone (regenerator) (follow m-l-k-j-i-h-g-a-b-c-d in Figure 42) Pressure balance for this loop can be described as shown in Eq. (46), where p_{Ga} and p_{Re} are the absolute pressure values at the gasifier freeboard and exit of the cyclone of regenerator respectively. $\Delta p_{bed\ Ga}$ is the pressure drop of the bubbling fluidized bed gasifier. This pressure drop is measured above the Sparger 1 of the gasifier till the gasifier freeboard (j-k-l-m Figure 42). $\Delta p_{LS1\ Ga}$ is the pressure drop between the

Sparger 1 of the gasifier and the bottom of the gasifier loop seal (j-i Figure 42); while $\Delta p_{LS2\,Ga}$ is the pressure drop between the bottom of the gasifier loop seal and the entry point of the link between gasifier and regenerator into the regenerator (i-h-g in Figure 42). In the cold model, the CFB and BFB exits are not controlled by a pressure regulating valve therefore the exit pressures of both CFB´s are atmospheric and are equal. However, in the actual test plant exit pressures are controlled using the control valves and have shown an influence on the operation of the DFB system.

5.4. Results and discussion

5.4.1. Suitability of BFB as a gasifier

5.4.1.1.   Solid movement in gasifier

As mentioned earlier, one of the main objectives of the cold model tests is to study the suitability of the BFB as a potential gasifier. The requirements of the suitable gasifier are mentioned in section 3.2. The requirements of section 3.2 implicate the gasifier design should provide suitable residence time, suitable gas solid contact and the BFB with some turbulent regime features. Therefore the proposed gasifier has a conical shape. The gas solid movements can be easily observed in the cold model study, Figure 43 shows the sketch of the gasifier bottom in a DFB cold model set up and typical solid movement patterns observed visually during a DFB. The gasifier is fluidized with the help of two spargers: sparger 1 is located near the lower end of
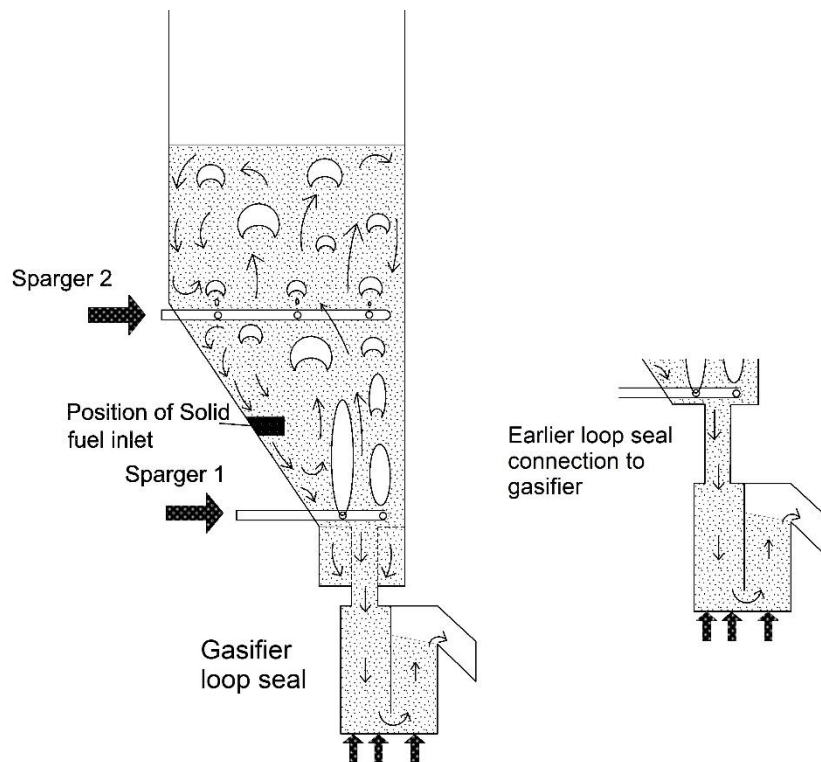

Figure 43 – Solid particles and gas bubbles flow patterns in Gasifier

conical section and sparger 2 is located near the bottom of cylindrical section of the gasifier. The conical section is eccentrically shaped with a slope of 50°. When the gasifier is fluidized through spargers, the part of fluidized bed directly above the Sparger 1 experiences higher velocity than average bed superficial velocity, due to the smaller cross sectional area in this zone, while the part of fluidized bed adjacent to the slant part experiences lower velocity than the average bed superficial velocity. This velocity difference within the fluidized bed drives a distinct solid circulation pattern within the fluidized bed demonstrated by Kuramoto et al. [170], i.e. solid movement upwards in the high velocity zone above the sparger 1 and solid movement downwards on the slant side of the cone as shown in Figure 43. In the cylindrical section of the bed above sparger 2, the gas velocity resulting from both spargers is uniform and solid movement is a typical BFB solid movement. The solid fuel particles can be introduced on the slant side of the cone, as seen the bed material moves downwards in this zone, and this downward flowing bed material will push the solid fuel also downwards, helping to increase the solid residence time of the fuel in the bed. This approach to design the gasifier was earlier proposed by Foscolo et al. [160]. Foscolo in his cold model study found that the residence time of the light particles (simulating char) is improved by introducing the material on the slant side of the cone. However, contrary to the design of the Foscolo et al. [160], in the present design the part of the char is also expected to enter the gasifier loop seal and travel to regenerator.

The regime below the sparger 1 in the gasifier loop seal is a fixed bed regime. The entrance to the gasifier loop seal is improved over the earlier configuration showed in Figure 43. In the previous version serious dead zones on the slant side and channeling in the middle section of the gasifier are observed. In the revised version which is depicted in Figure 43 no such dead zones and channeling behavior is observed.

5.4.1.2. Segregation behaviour

The effect of downward flow direction of solid particles on the residence time of light particles is shown in Figure 44. The residence time ratio (γ) formulated in Eq. (44) is compared with increasing turnover ratio (θ): ref. Eq.(45). The increasing turnover ratio indicates increased solid looping rate (G_L) for a given bed inventory. Each data point shown in Figure 44 is averaged from multiple readings. The fact that all the values of γ is measured above unity concludes that even if the solids flow downwards in a bubbling bed the residence time of the light fraction is more than the residence time of the heavy fraction, however with increasing θ the residence time of the light fraction in the bed lowers. For a test plant operation, char represents light fraction of the bed, increasing solid looping rate will decrease the overall char residence time in the gasifier
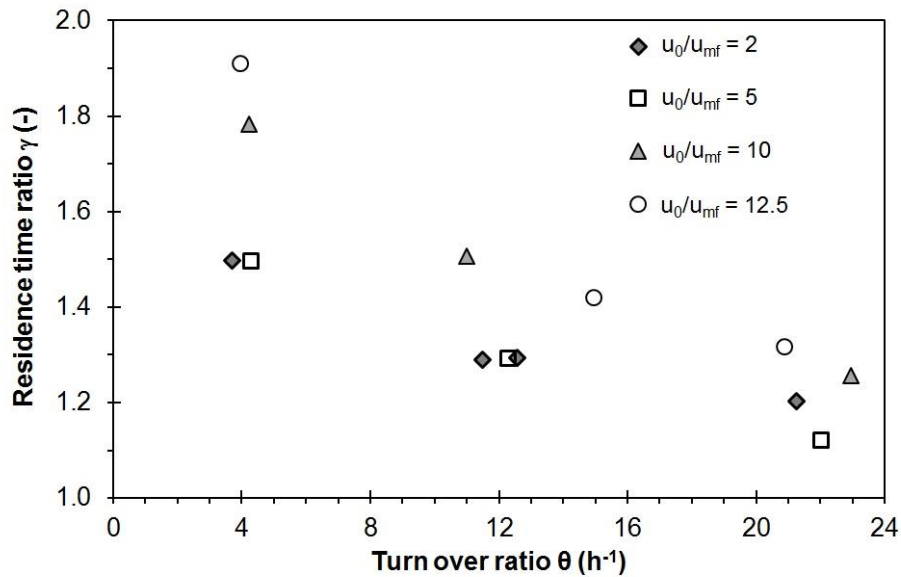
Figure 44 – Residence time ratio (γ) vs turnover ratio (θ) and influence of bed superficial velocity

and increase char flow rate to the regenerator. However, the required θ for the test plant is ranging 6-16 for normal operation and 20 as maximum value. In such a range the residence time for the light particles is observed to be 40% more than residence time of the bed material.

The segregation tendency is studied with the help of the bed freezing method explained earlier in section 5.2. The Figure 45 shows the concentration of the light component in top, middle and bottom layer of the bubbling bed and its variation with the BFB superficial velocity. It is non-dimensionalized by u_{mf}, the u_{mf} is calculated for the major weight fraction of the bed which is a heavy fraction. As observed in Figure 45, the top and middle layer has concentration of the light component more than the concentration at the beginning of experiment. The bottom layer has lower concentration of light component than the beginning of experiment. Therefore it can be concluded that the light particles segregate themselves in the top layers of the bed. An interesting point to note is that the average concentration of light particles from three zones calculated at the end of experiment is higher than the initial concentration. This indicates an accumulation tendency of the light fraction in the bed. Increasing gas velocity (u_0) also enhances the segregation tendency of the light particles as shown in Figure 45. This observation is similar to Shen et al. [146], who suggested that the segregation tendency of light particles enhances with increasing gas velocity in the bed.

The results discussed in section 5.4.1.1 and 5.4.1.2 are summarized. The light particles segregate in the upper region of the bed and residence time for light particles is higher than the main bed material residence time. The gasifier gas-solid flow patterns caused by the conical shaped gasifier design may further improve the residence time. Thus above points indicate that the proposed gasifier design is suitable.
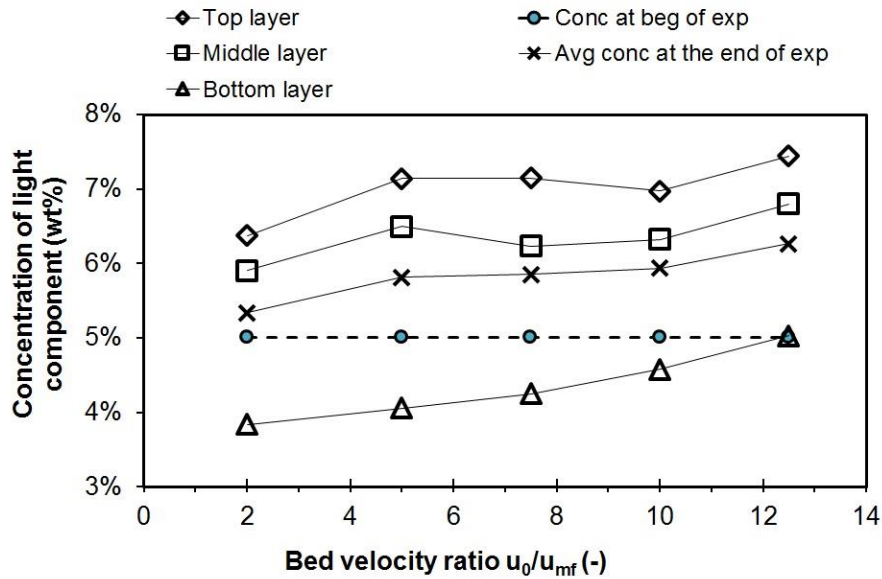
Figure 45 - Segregation tendency of light particles in a BFB with solid exiting from bottom, θ = 12

5.4.2. Dual fluidized bed operation

One of the main aims of the cold model study is to confirm if the DFB in SER mode is able to operate steadily in long term operation. In the SER mode, the DFB is said to be operational when gasifier works in normal BFB conditions, regenerator in a CFB condition and the L-valve and gasifier loop seal is fluidized. The solid flow rate from L-valve should match solid flow rate from gasifier loop seal in order to achieve the dynamic balance of the DFB. In terms of hydrodynamics the DFB is considered stable when the total bed pressure drop in gasifier $\Delta p_{bed\ Ga}$ and regenerator $\Delta p_{riser\ Re}$ remains
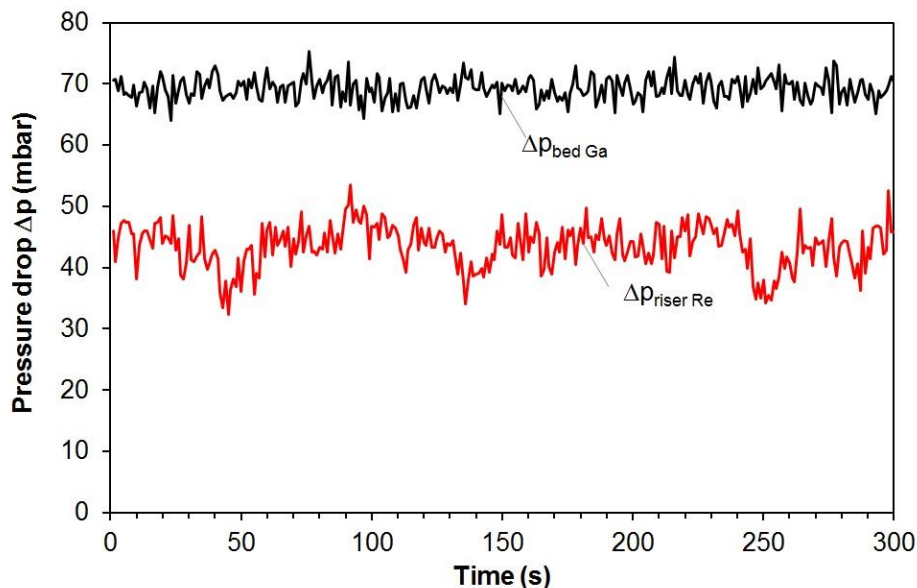

Figure 46 Total pressure drop variation over time in a steady state of a gasifier and a regenerator in DFB coupled operation (Conditions u$_{0\ Re}$= 3.9 m/s u$_{0\ Ga}$=0.3 m/s, M$_{To}$=16.9 kg, particles: steel powder, u$_{0\ Low\ LS}$ = 0.075 m/s, $G_{S_{Re}}$= 25.6 kg/m²s, $G_{L_{LV}}$= 246 kg/h)

constant over a longer period. During cold model operation such dynamic balance is observed. Figure 46 shows the variation of gasifier and regenerator pressure drop over time and one can observe that the pressure drops in both fluidized beds remains constant. The degree of fluctuations indicates the nature of bubbling fluidized bed and circulating fluidized bed in gasifier and regenerator respectively. Such dynamic balance and stable conditions are achieved quickly in cold model operation and have shown that such steady behavior can last for a long time without disturbances. The same has been confirmed during the test plant operation. Therefore this particular DFB system of SER mode is feasible and can be considered for future gasification projects. It can also be considered for the processes which require the use of solid fuels such as chemical looping [141,153] with solid fuels or calcium looping (CaL) [52].

Figure 47 shows the pressure map of the SER mode DFB system in a DFB operation. The pressure profile can be traced to points a to m shown in Figure 42. The pressure profile of the gasifier above the Sparger 1 (j-k-l-m) is a typical pressure profile of a BFB, while below the Sparger 1 (j to i) it is either moving bed profile or a bubbling bed profile. The amount of aeration is the parameter which decides the pressure profile between sparger 1 and gasifier loop seal. This is analyzed in detail in next section. The regenerator pressure profile (a to g) is a typical CFB profile. More details about the regenerator pressure profiles, about the effect of air staging, riser velocity and solid fraction profiles can be referred in section 4.4.2.2 (page no 61) which concludes that the regenerator is able to work satisfactorily as a combustor.

Furthermore, it is necessary to check in the cold model studies if the gasifier can hold enough bed inventory mentioned in Table 15, in order to provide enough residence time for CO$_2$ capture reactions and H$_2$ production. Figure 48 shows the effect
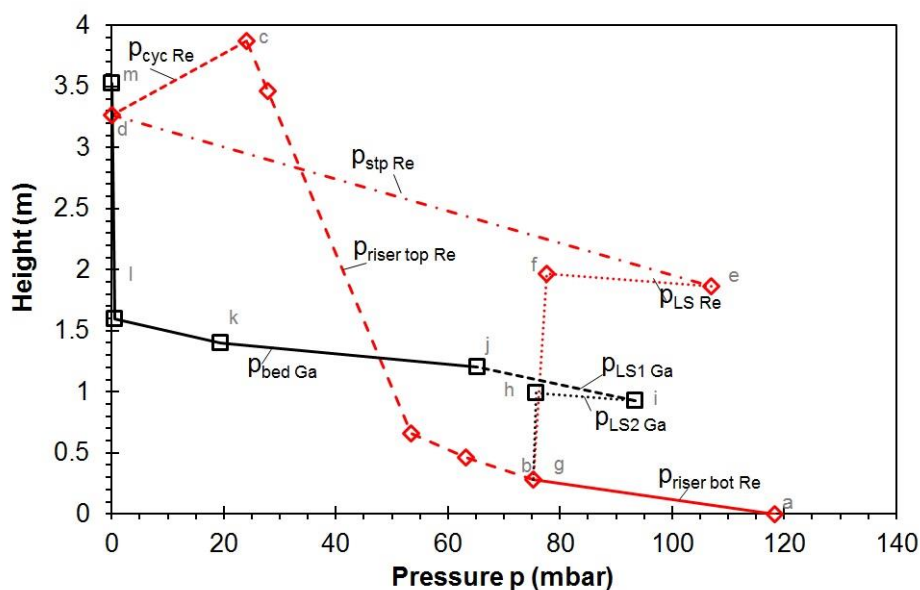

Figure 47 - Pressure profile of a DFB system (Conditions $u_{0\,Re}$= 3.9 m/s $u_{0\,Ga}$=0.3 m/s, M_{To}=20 kg, particles: steel powder, $u_{0\,LS\,Ga}$ = 0.106 m/s, G_s=30.3 kg/m²s, $G_{L_{LV}}$= 245 kg/h)

of addition of M_{To} in a coupled mode. The increment in M_{To} results in increase in pressure drop of both gasifier and regenerator.

The gasifier inventory is calculated using the Eq. (13) neglecting any friction and acceleration pressure drop [71], where $\Delta p_{bed\ Ga}$ is the average pressure drop above the sparger 1 measured by the pressure transducer in a given steady state experiment, M_{Ga} is the cold model inventory in the gasifier, g is gravitational constant and A_{Ga} is the area of gasifier. Although the gasifier area is variable in the conical section, in all experiments the gasifier is always filled much above the conical section. Therefore the conical section inventory is measured once and assumed constant. The remaining inventory is calculated using separate pressure transducers in the cylindrical section of the gasifier. The calculated cold model inventory $\acute{M}_{Ga}$ extrapolated to the test plant using scaling ratio (ref. Table 15) is shown in Figure 48. It clearly shows that the gasifier can easily hold 30 to 50 kg of bed material, as required in Table 15.
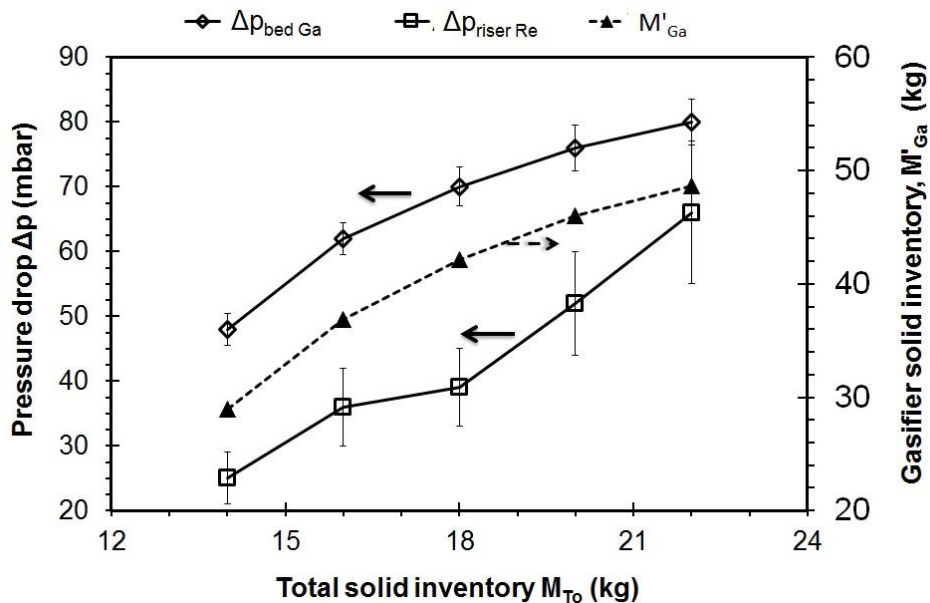
Figure 48 – Influence of the total solid inventory on the pressure drop in the gasifier and regenerator

5.4.3. Regenerator entrainment

The regenerator entrainment flux $(G_{s\ Re})$ against regenerator velocity $(u_{0\ Re})$ in a single loop operation is shown in Figure 49 and corresponding calculated scaled circulation rates $(\acute{G}_{Re})$ in kg/h is shown as secondary axis. Since the regenerator is the same for CaL mode and SER mode, the Figure 49 is same result of Figure 26 but considered in terms of SER mode requirements. Figure 49 shows that the required

Figure 49 – Regenerator entrainment rates with and without air staging, particles - iron oxide

operational boundary limits of riser velocity in the test plant ($\acute{u}_{0\,Re}$= 4.5-6.5 m/s). At lower boundary limit of $u_{0\,Re}$= 2.6 m/s, the entrainment rates are less than the required maximum solid looping rate ($\acute{G}_{L_{LV}}$). Above $u_{0\,Re}$=3 m/s ($\acute{u}_{0\,Re}$=5.2 m/s) the entrainment rates are well above the maximum solid loopi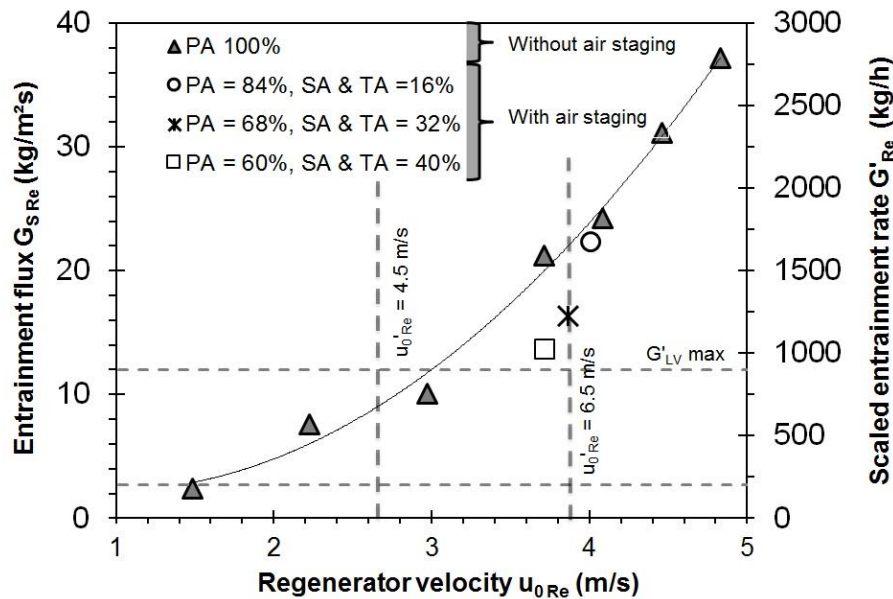ng rate and the required solid looping rates of 200-900 kg/h are easily achievable. Since the riser entrainment rates are higher than the required solid looping rates the use of solid flow control devices such as L-valve is justified.

5.4.4. L-valve performance in a DFB operation

Although L-valves are common in single loop CFB systems to control riser entrainment rates, the coupling of a DFB system with an L-valve is not very common. In this work the L-valve is primarily used as a mechanism to control the solid looping rates in the DFB system, whereas in the other similar DFB systems the solid looping rates are primarily driven by the riser velocity [53,140]. Figure 50 shows the solid flow rate through L-valve against the L-valve aeration used in this study. The measurements are carried out at uniform conditions in gasifier and regenerator. The regenerator entrainment rates were recorded between 440-470 kg/h. The L-valve aeration is represented by $\left(\frac{u_{0\,LV}}{u_{mf}}\right)$, where $u_{0\,LV}$ is superficial gas velocity in the L-valve calculated by gas flow rate to the L-valve: divided by the cross sectional area of the L-valve. The solid flow rate measurement procedure of L-valve is described earlier on page 50. The measured solid flow rates are shown as a flux ($G_{s\,LV}$) as well as actual solid flow rates ($G_{L_{LV}}$). The flux is calculated based on the cross sectional area of the horizontal section of the L-valve. As observed in Figure 50, the increment in L-valve aeration increases the solid flow rate. The L-valve can control the solid looping rate between the two fluidized beds pretty well. An advantageous feature of the L-valve is that, the solid looping rates are independent of the hydrodynamic conditions in the fluidized bed e.g.
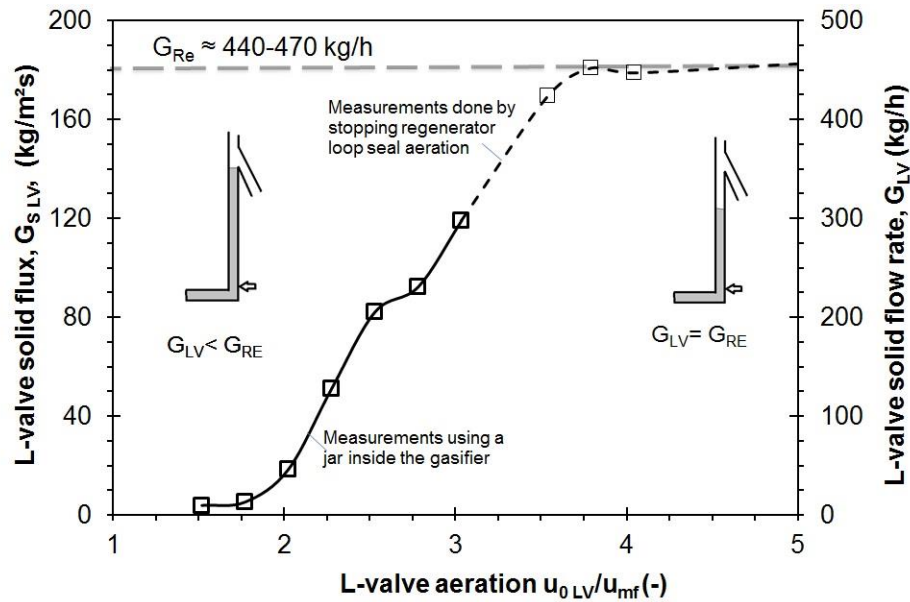
Figure 50- L-valve flow rate variation with L-valve aeration rate in a DFB operation conditions u$_{0\ Re}$= 3.9 m/s, u$_{0\ Ga}$=0.3 m/s, particles: steel powder, u$_{0\ Low\ LS}$ = 0.074 m/s, G$_{S\ Re}$=30-32 kg/m²s, M_{To}= 18 kg

regenerator velocity, total solid inventory or fluidization in gasifier, contrarily the other solid flow controlling options like the cone valve. The solid looping rates are highly influenced by such conditions as discussed in section 4.4.4 (page 66 - 69). Another main feature is that the requirement of aeration gas in the L-valve is very little compared to cone valve or loop seal, therefore in test plant operation the dilution of the product gas resulting from the L-valve gases will be lower compared to cone valve or loop seal. Furthermore, the quantity of the dilution will be known. Therefore, analyzing the process results will be easier. In comparison, dilution resulting from loop seal operation is difficult to predict and quantify. Chapter 6 is dealing with this topic about loop seals.

The values shown as dotted in Figure 50 are measured by stopping the regenerator loop seal aeration with and without L-valve aeration. In these cases the measuring jar placed inside the gasifier was too small to measure these flow rates. The L-valve used in this work is able to control the solid flow only below the regenerator entrainment rates. Once L-valve flow rate equals the regenerator entrainment rates, further aeration did not change the L-valve flow rate. In this scenario the particle height in the vertical arm of the L-valve reduced. Further increment in L-valve aeration reduced the particle height in the L-valve even further (depicted in Figure 50), up to a point L-valve vertical arm becomes a bubbling bed. In this scenario the L-valve practically acts like a loop seal. However, such scenario is undesirable.

5.4.5. Influence of aeration in the gasifier loop seal

An interesting observation of the cold model tests is the effect of aeration in the gasifier loop seal. Figure 51 shows the effect of increase in gasifier loop seal aeration

on the pressure profile in the gasifier. The respective influence on the total pressure drop in the gasifier bed and regenerator is shown in Figure 52. Increase in gasifier loop seal aeration primarily influences the pressure gradient between the gasifier loop seal and the sparger 1 (point j to I in Figure 42). The aeration in the gasifier loop seal is quantified by $u_{0\,LS\,Ga}/u_{mf}$ where $u_{0\,LS\,Ga}$ is the flow rate given to the gasifier loop seal divided by the cross sectional area of the gasifier loop seal. As seen in Figure 51, at low aeration rates e.g. $u_{0\,LS\,Ga}/u_{mf} < 1$, the pressure at the bottom of gasifier loop seal ($\Delta p_{LS1\,Ga}$) is lower than the pressure at sparger 1. With increasing gasifier loop seal aeration, increases the pressure at the bottom of the gasifier loop seal to a point the pressure at the bottom of the gasifier loop seal becomes higher than the pressure at sparger 1. This scenario primarily occurs at condition $u_{0\,LS\,Ga}/u_{mf} > 1$.
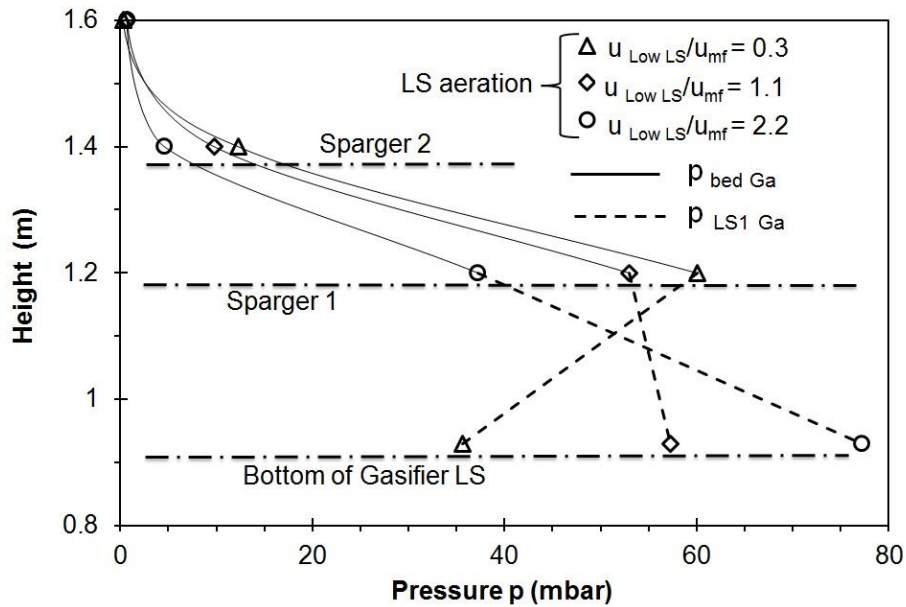
Figure 51 – Effect of loop seal aeration on the pressure profile in DFB operation on the pressure profile in the gasifier and the loop seal

The above explained phenomenon has two major implications on the hydrodynamics of the DFB system. Firstly, a change in the pressure at the bottom of the gasifier loop seal changes pressure drop $\Delta p_{LS1\,Ga}$, which influences pressure drop in the regenerator as per pressure balance equation. To balance the left-hand side of Eq. (46), the right-hand side should also get increased. Therefore, the pressure drop in the regenerator is increased. This relationship is shown clearly in Figure 52. One should note that the increase in $\Delta p_{LS1\,Ga}$ is not due to change in inventory but due to the change in gas solid interaction in moving bed, therefore increase in regenerator pressure drop ($\Delta p_{riser\,Re}$) is brought by the reduction in gasifier bed pressure, indicating an inventory transfer from gasifier to regenerator. This fact is evident in Figure 51 as well as in Figure 52.

Secondly the regime below the sparger 1 is a moving bed/ fixed bed regime and above the sparger 1 it is bubbling-slugging. In a moving bed scenario the pressure drop between the sparger and the loop seal is governed by the Ergun equation [71].

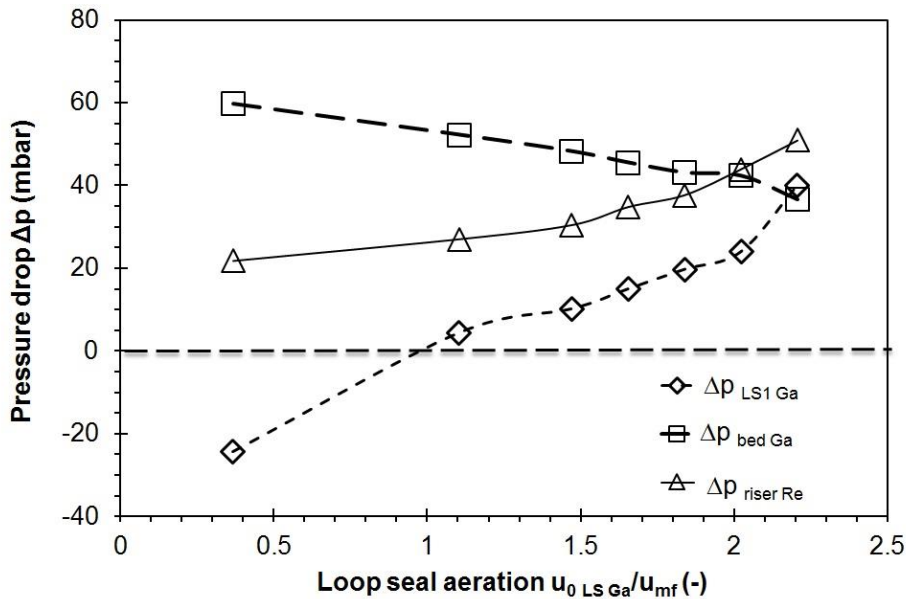**Figure 52 – Pressure drop changes in gasifier, gasifier loop seal and regenerator with increasing loop seal aeration**

Ergun equation suggests that for the negative gradient values indicate below the sparger 1 the gases are flowing downwards, thus a possibility of gas leakage between the two fluidized beds exists.

The aeration in the gasifier loop seal thus offers a tool to control the inventory distribution between the two fluidized beds. Although that low aeration rates, may cause a slight gas leakage, it offers another advantage with a possibility of larger bed inventory in the gasifier while keeping the moderate pressure profile in the regenerator. Thus SER mode DFB set up offers more flexibility in terms of the variation of fuel residence time in the gasifier.

5.5. Summary

A novel DFB system for the gasification of solid fuels is proposed and the scaled cold model experiments are performed in a 2.5 times smaller geometrically similar cold model. The novelty of the DFB system is attributed to the use of an L-valve for controlling solid looping rate and the use of a loop seal connected to the bottom of the gasifier. Solid flow patterns in the BFB gasifier showed the circulation patterns predicted by Kuramoto et al. [170]. The bed material leaves the gasifier from the bottom through a loop seal. Separate experiments with a similar arrangement of solid leaving from the bottom of BFB show that the light particles have a longer residence time (ca. 20% more) than the heavy particles. This happens due to fact that light particles have a tendency to float in a BFB. With increased residence time of char and favorable solid circulation patterns in a gasifier the yield and the quality of the product gas is expected to improve. The DFB system operates in a very stable manner, promising long term test plant operation. The scaled experiments showed that the measured solid inventory

in the gasifier (M_{Ga}) and the measured regenerator entrainment flux ($G_{s\,Re}$) when extrapolated to test plant using scaling ratios meet the required operational boundary condition of the SER process. The entrainment rates from the regenerator are higher than the required solid looping rate. Therefore the use of solid flow control mechanism is necessary. The L-valve is used as a device to control solid looping rates. The L-valve aeration and the solid flow rate through L-valve are proportional. The linear characteristic remains as long as the solid flow rate through L-valve is below the regenerator entrainment rates ($G_{L_{LV}} < G_{Re}$). Above this limit the solid flow rate from L-valve is limited by the regenerator entrainment rates ($G_{L_{LV}} = G_{Re}$). It is found that the gasifier loop seal aeration influences gasifier pressure profile and also plays a role in the inventory distribution between the gasifier and regenerator. At low aeration rates the pressure gradient between the bottom of the gasifier loop seal and the sparger 1 is measured as negative, indicating resultant gas flow downwards from sparger 1 to gasifier loop seal. At higher aeration rates this pressure gradient is measured as positive, indicating an upward gas movement from the gasifier loop seal towards the sparger. With low aeration rates more solid inventory can be allocated to the gasifier.

6. Study of a standpipe and a loop seal function in a CFB system

6.1. Background

Loop seals are widely applied in CFB systems. In almost every DFB facility applied to HTSLC processes, the use of a loop seal has been cited. The use of loop seals in a DFB system is discussed previously in section 2.2.5 and it is learned that the role of a loop seal is not only to transfer solid reactants from one reactor to the other reactor but also to prevent mixing of gases from each other. The mixing of gases between the reactors is the most undesirable thing in HTSLC. Therefore, in a CFB as well as a DFB system, the standpipe-loop seal operation is very important.

Despite of the significance of loop seals and standpipes in CFB or DFB systems, little is known about this vital part. Information in the literature about the design and suitable aeration rates in the literature is found insufficient. Regarding HTSLC processes the loop seal aeration could become a source of dilution for the product gases. Therefore optimizing the loop seal and standpipe design is important for these processes. The occurrence of slugging in the standpipe [44] as well as unsteady loop seal operation [71,72] experienced earlier at 10 kW$_{th}$ plant University of Stuttgart, resulted in breakdown of the entire DFB operation. In the same test plant, during gasification experiments the dilution from the loop seals always caused concerns about the errors in analyzing the data. Therefore in general, there is a need for better understanding of loop seal and standpipe operations. The considerations for standpipe, loop seal design and operation, which this thesis aims to contribute too, are summarized below:

(i)   To study the suitable aeration rates of the loop seal and its influence on the riser operation
(ii)   To study the gas solid flow between the different chambers of the loop seal so as to quantify dilution or leakages in DFB systems due to the loop seal aeration.
(iii)   To understand slugging phenomenon in the standpipe and discuss solutions to prevent such phenomenon.

The work presented in this chapter is partly published in a conference [187].

6.2. Experimental

The experimental setup used in this chapter is the regenerator cold model (R3). Its details are earlier discussed in sections 3.3 and dimensions of the riser standpipe and loop seal are shown in Table 9. However, the particles used in these experiments are ilmenite particles, which have a density of 4400 kg/m³ with a size distribution of 100-200 μm and mean particle size of 143 μm. Ilmenite particles were particles under investigation for the development of chemical looping process [141]. The calculated u_{mf} for these particles using Eq. (11) is 0.029 m/s. The details of the particles are given in Table 17. The experiments are performed with a single loop cold model of reactor R3 (regenerator used in CaL mode), without the application of cone valve or L-valve. The weir height in the loop seal is kept fixed at 150 mm and loop seal is aerated only in the supply chamber. This is done in order to bring simplicity to study the gas flow path in a loop seal.

The experiments are performed with the standard experimental procedure explained for the single loop CFB system earlier in section 3.3.3. The details of the loop seal aeration rate, standpipe height and loop seal regime observations are meticulously recorded. The main parameters varied are the riser velocity and the loop seal aeration. The loop seal aeration is represented in terms of superficial velocity in the loop seal ($u_{0\,LS}$) i.e. total loop seal aeration flow divided by the total cross sectional area of the loop seal. The riser velocity is varied between 2 to 4 m/s while the loop seal aeration is varied between 0.02 to 0.3 m/s.

Table 17 – Details of the particles and the experiments

Property	Unit	value
Particle density	kg/m³	4400
Size distribution	μm	100-200
$d_{p_{50}}$	μm	143
u_{mf}	m/s	0.029
Sphericity φ	-	0.75 [79]
Bulk voidage ε	-	0.51
Riser velocity $u_{0\,Re}$	m/s	2-4
Loop seal aeration $u_{0\,LS}$	m/s	0.02-0.3

6.2.1. Data analysis for gas flow path determination

Understanding the gas and solid flow is the main objective of this chapter. Following steps will explain the data evaluation procedure which is based on the work of Basu & Cheng [132]. These steps are:

- calculation of slip velocity ($U_{sl\ stp}$)
- calculation of gas ($U_{g\ stp}$) and solid velocity ($U_{s\ stp}$) in the standpipe (and)
- calculation of gas flows rates and aeration split (ξ_{su} and ξ_{re})

The slip velocity $U_{sl\ stp}$ is defined earlier in section 2.2.5, as the difference between the gas and solid velocity in the standpipe. It is calculated using the modified Ergun equation shown in Eq. (21) (see page 28) and is related to pressure drop (Δp_{stp}) in the standpipe and the bed height in the standpipe (L_{stp}). The pressure drop through the standpipe and the bed height have been measured for every steady state, thus defining also the pressure gradient $\left(\frac{\Delta p}{dH}\right)_{stp}$ and then $U_{sl\ stp}$. However, this methodology is applied only when the fluidization regime in the standpipe is moving bed. The situations in which this standpipe showed bubbling or slugging mode of fluidization, these steady states are not considered in the $U_{sl\ stp}$ calculations. The areas of standpipe and loop seal vary in this set up, but for simplification the $\left(\frac{\Delta p}{dH}\right)_{stp}$ is assumed to be constant and further calculations of gas and solid velocity are based on the area of standpipe. The real solid down flow velocity ($U_{s\ stp}$) is calculated using the expression in Eq. (47).

$$U_{s\ stp} = \frac{G_{s\ riser}\ A_{riser}}{\rho_s(1 - \varepsilon)A_{stp}} \tag{47}$$

where $G_{s\ riser}$ is the solid entrainment flux generated in the riser. It is measured as described in section 3.3.2. A_{riser} and A_{stp} are the cross-sectional area of the riser and standpipe respectively. The gas velocity ($U_{g\ stp}$) is calculated through Eq. (22) and Eq. (47). For solid flow downward flow is assigned a positive sign while for gases the downward flow is assigned a negative value.

The loop seal aeration flow is split between the loop seal supply chamber and the recycle chamber (refer Figure 9 for the location of supply chamber and recycle chamber). The gas which flows into the supply chamber flows towards the riser cyclone, while gas which flows towards recycle chamber goes to the riser. The aeration split in the supply section (ξ_{su}) is calculated using Eq. (48) and the recycle side (ξ_{re}) given by Eq. (49).

$$\xi_{su} = \frac{U_{g\ stp}\varepsilon\ A_{stp}}{u_{0\ LS}A_{LS}} \tag{48}$$

$$\xi_{re} = 1 - \xi_{su} \tag{49}$$

where $u_{0\ LS}$ is the superficial velocity in the loop seal corresponding to the total cross sectional area of the loop seal (A_{LS}), which includes both supply section and recycle section. The product $u_{0\ LS}.A_{LS}$ is the aeration flow given in the loop seal. The superficial

gas velocity in the standpipe ($u_{g\ stp}$) is calculated as a product of the real gas velocity ($U_{g\ stp}$) and the voidage (ε) shown in Eq. (50).

$$U_{g\ stp}\varepsilon = u_{g\ stp} \tag{50}$$

6.3. Results and discussion

6.3.1. Suitable aeration rates in the loop seal

The magnitude of loop seal aeration plays a very important role in the CFB operation and hydrodynamics of the CFB system. Little has been published about the suitable aeration rates in a CFB or a DFB system. The loop seal aeration in the present experiments is represented by the ratio of superficial velocity in the loop seal to the minimum fluidization velocity $\left(\frac{u_{0\ LS}}{u_{mf}}\right)$, so that the results can be easily compared with other works.

At low aeration rates visual observation shows relatively no movement of the particles. The loop seal becomes functional when $\frac{u_{0\ LS}}{u_{mf}}$> 1, but shows significant particle movement only above $\frac{u_{0\ LS}}{u_{mf}}$> 2. The loop seal aeration works best between 2-5 u_{mf}, at values above 6 u_{mf} the slugging phenomena becomes very obvious. However, for increased total solid inventory in the system the slugging occurs at higher aeration rates. The experimental data from earlier experimental works carried out at University of Stuttgart [34,72,172] is compared. The observed loop seal aeration is found to be consistent with the observation in the present work.

6.3.2. Influence of loop seal aeration on the gas-solid flow in the standpipe

Loop seals in the CFB system are usually not employed as a solid circulation control device but mainly as a solid pass through device [132,179]. However, it is interesting to see the influence of loop seal aeration on the riser entrainment flux. The riser entrainment flux (G_s) and solid velocity in the standpipe ($u_{s\ stp}$) (as secondary axis) is plotted against the loop seal aeration ratio $\left(\frac{u_{0\ LS}}{u_{mf}}\right)$ at two riser velocities and constant total solid inventory (M_{To}) in Figure 53. It is seen that, for a given riser velocity (u_0), the riser entrainment flux (G_s) increases with increase in loop seal aeration. However, this increment is limited till a maximum value is reached. This observation is consistent with several works from Basu et al. [109,132,133]. According to Basu et al. [132], once the highest entrainment flux is achieved, the entrainment flux remains constant for further increment in the loop seal aeration, unless the riser velocity is changed. However, in the present work with further increase in the loop seal aeration, little decrease in the entrainment flux is observed, with slugging in the standpipe. Next section will discuss

this slugging phenomena in detail. Lee et al. [188] have also reported a similar observation. According to Lee et al. the decrease in the entrainment flux is due to the small standpipe diameter and inconsistencies (presumed slugging) observed in the loop seal operation. For low loop seal aeration rates, the loop seal seems to control the solid circulation rates. However, this happens due to low solid suspension in the riser, through which the riser entrainment capacity is limited. Therefore, it is not justified to claim loop seals as a controller of solid circulation rates.
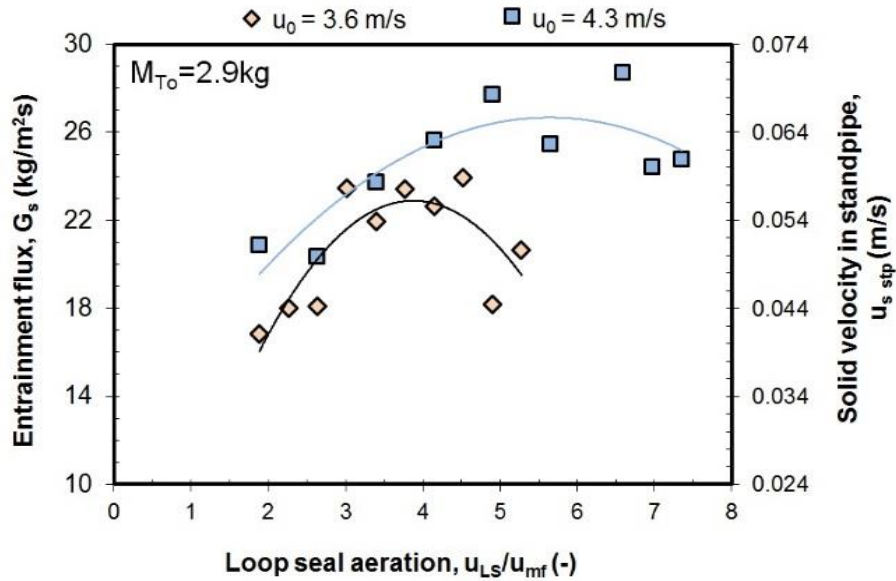

Figure 53 - Effect of loop seal aeration on riser entrainment G_s at two velocities. M_{To}=2.9 kg

The solid velocity ($u_{s\,stp}$) in the standpipe calculated by using values of riser entrainment flux and Eq. (47) is shown as secondary axis. The solid velocity forms the basis of calculation of gas velocity in the standpipe ($u_{g\,stp}$) using Eq. (21),(22) and (50). The voidage considered for the calculation is 0.51. Figure 54 shows the variation in $u_{g\,stp}$ with variation loop seal aeration ratio ($\frac{u_{0\,LS}}{u_{mf}}$). As seen in Figure 54 an increase of $\frac{u_{0\,LS}}{u_{mf}}$ results in an increase of $u_{g\,stp}$ for the riser velocity (u_0) of 3.6 m/s. For higher riser velocity of 4.3 m/s and loop seal aeration ratios $u_{0\,LS}$<5.6u_{mf}, $u_{g\,stp}$ is in the range of -0.02 m/s. When the $u_{g\,stp}$ values are negative, it indicates that the resultant gas flow in the standpipe is moving downwards, that means from the cyclone towards the loop seal. For the lower riser velocity of 3.6 m/s, negative values of $u_{g\,stp}$ are recorded for a very small $\frac{u_{0\,LS}}{u_{mf}}$ range, i.e. $u_{0\,LS}$< 2.6u_{mf}. For a given $\frac{u_{0\,LS}}{u_{mf}}$ value, the gas velocity in the standpipe ($u_{g\,stp}$) is higher at lower velocity (u_0 = 3.6 m/s) than the higher velocity (u_0 = 4.3 m/s). As observed in Figure 53 the higher riser velocity generates higher entrainment flux and thus higher solid velocities ($u_{s\,stp}$) in the standpipe, creating more resistance for the gas travelling upward. However, with increased loop seal aeration
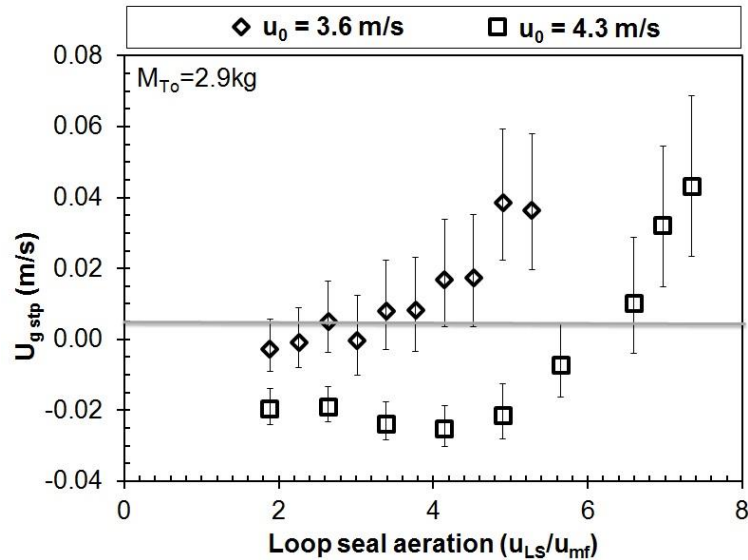
Figure 54 - Effect of loop seal aeration on gas velocity in standpipe (u_g) at different riser velocities u_0, M_{To} =2.9 kg

the $u_{g\ stp}$ gradually increases and becomes positive at 6 u_{mf}. It is also observed that the downward $u_{g\ stp}$ has a limitation of - 0.03 m/s. Basu and Butler [133] also have a similar conclusion about limited value of negative $u_{g\ stp}$.

The aeration split calculated from the values of Figure 54 as per Eq. (48) and (49) is shown in Figure 55. As per Figure 55 aeration split in the supply chamber (ξ_{su}) is calculated between -8% to +6%. This concludes that remaining 94-100% of the aeration gas given to the loop seal is entering the recycle side of the loop seal. In case of negative values of $u_{g\ stp}$, entire loop seal aeration is going towards the recycle side. An additional gas, up to 8% of the total aeration flow coming from the cyclone is also entering the recycle side of the loop seal.

Number of assumptions in the calculation of $u_{g\ stp}$ could raise the concerns about the accuracy of the results. The deviation bars in Figure 54 and Figure 55 show the influence of voidage in the calculations of $u_{g\ stp}$ and aeration split, calculated for lower and higher voidage values of 0.48 and 0.54 respectively. Furthermore, in this work a constant $\left(\frac{\Delta p}{dH}\right)_{stp}$ is assumed for the calculation procedure explained in section 6.2.1, which in reality is not confirmed. If variable, it could also influence the results of $u_{g\ stp}$. Therefore, to find out the exact gas flow pattern would require the use of tracer gases. Johansson et al. [122] reported loop seal aeration flow into the supply side of the loop seal as 2 to 7 % using tracer gases, this is equivalent to the aeration split (supply). Johansson et al. [122] also reported $u_{g\ stp}$ values of -0.05 m/s to + 0.1 m/s. Therefore the results obtained in this work are close to the results of with the data of Johansson et al. [122]. However, due to different experimental set up and experimental conditions compared to present work, results of Johansson et al. [122] cannot be the basis of comparing the results.
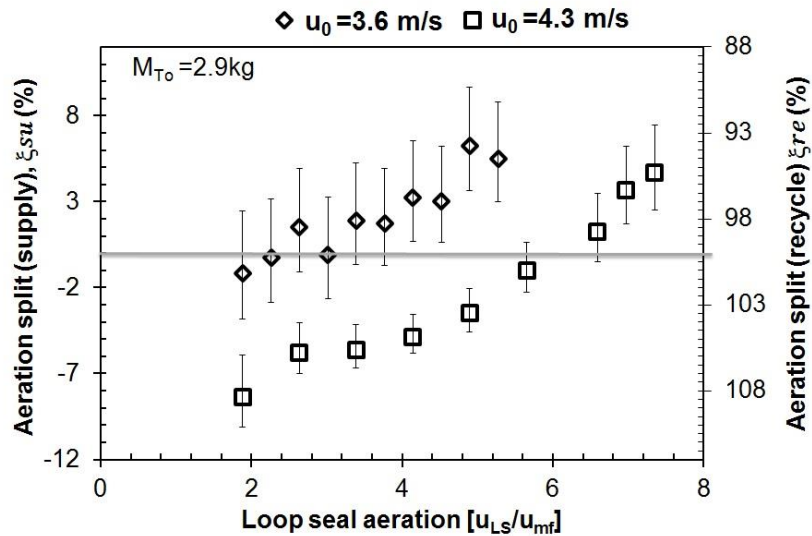
Figure 55- Effect of loop seal aeration on the aeration split in supply and recycle chamber

To summarize, the gas flow especially in the standpipe could be upwards or downwards, depending on the loop seal aeration and the riser entrainment rates. Increasing loop seal increases the gas flow upwards in the standpipe and increasing solid flow increases the tendency of gas flow downwards in the standpipe. Only a small fraction of the loop seal aeration gases enter the standpipe side of the loop seal, rest of the aeration flow goes to the recycle side of the loop seal.

6.4. Fluidization regimes in the standpipe

The gas velocity in the standpipe $u_{g\,stp}$ is primarily influenced by loop seal aeration rate and the riser velocity (u_0) as observed in Figure 54 and Figure 55. At the same time the regimes are also recorded based on visual observation. At low or negative gas velocities the standpipe was in moving bed mode, typically when $u_{g\,stp}<u_{mf}$. At higher aeration rates or when $u_{g\,stp}>u_{mf}$, the bubbles appear in the standpipe. In the small standpipes the gas bubbles are equivalent to a standpipe. This situation is typically referred as slugging. Two types of slugging have been described by Knowlton (ed. Wen) [109].

- type A - round nose slugging
- type B - flat nose slugging.

The type A is similar to normal bubbling bed where bubbles rise up in a particle bed. The difference between BFB and a type A slugging is that a gas bubble is nearly equal to the standpipe diameter in Type A slugging. A typical type B slugging or flat nose slugging is shown in Figure 56 where gas slug completely occupies the cross section and lift the solid chunk above it. The solid downward motion is only possible by raining down as solid streamers or when the solid chunk is broken. According to
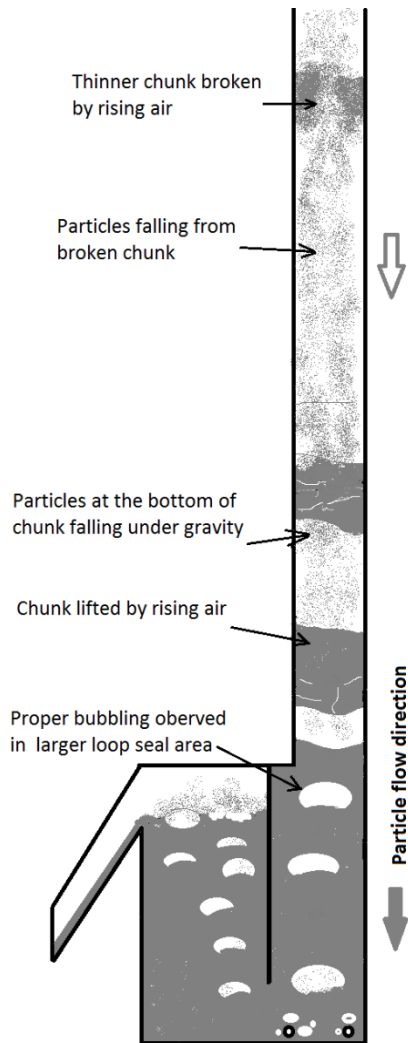
Thinner chunk broken by rising air

Particles falling from broken chunk

Particles at the bottom of chunk falling under gravity

Chunk lifted by rising air

Proper bubbling oberved in larger loop seal area

Particle flow direction

Figure 56 - Slugging in the standpipe

Knowlton (ed. Wen) [109] the type B slugging occurs mainly with cohesive particles and is not a suitable mode for the standpipe to operate. Our experience shows that the type B slugging caused a frequent operational break-down. Typical operational break-down occurred when the slug used to be very thick and solid particles did not rain down in the loop seal steadily. As a result solid particles used to pile up till the cyclone. On the other hand the loop seal becomes empty since it didn't receive particles from cyclone. Then the riser gases entered the loop seal and entrained all the particles in the standpipe out of the CFB, thus ending the CFB operation. Such type B slugging occurred when $u_{g\,stp} > u_{mf}$ at riser velocities of 3.6 and 4.3 m/s and has caused reduction in the entrainment rate (see Figure 53). However in the same experimental set up type A slugging is also occurred when the riser velocity was as low as 2.9 m/s. Comparing the occurrence of type A with type B slugging, the main difference observed is the solid velocity in the standpipe ($u_{s\,stp}$). The $u_{s\,stp}\left(\frac{U_{s\,stp}}{\varepsilon}\right)$ value at $u_0 = 2.9$ m/s is 0.019 m/s.

The values of standpipe solid velocity ($u_{s\,stp}$) from all cold model experiments of this thesis, previous readings including [72] and hot test plant readings are collected compared with the standpipe regimes. From all these results it is consistently observed that type B slugging occurred typically at $u_{s\,stp} > 0.03$ m/s while type A or bubbling occurred at $u_{s\,stp} < 0.025$. Sometimes both types occurred simultaneously, i.e. type B in the standpipe and type A in the loop seal supply side where cross section is larger than the standpipe. This clearly shows the influence of solid velocity on the type of slugging. This fact can be explained as follows: increasing loop seal aeration increases the gas velocity in the standpipe and at lower solid velocity ($u_{s\,stp} < 0.025$ m/s), the particles bed is expandable and allows smooth bubble travel. At higher solid velocities ($u_{s\,stp} > 0.03$ m/s) the particles tend to flow closely packed, at the same time increasing gas velocity in the standpipe tries to expand the bed. This counter acting behavior of gas and solid leads to the type B slugging depicted in Figure 56.

For the calcium looping process, the preferred fluidization mode in the standpipe is bubbling to prevent the calcium particles from sticking together [9]. For large scale facilities, the slugging may not be relevant because the standpipe and loop seals sizes are big enough. However, in small facilities, say up to 1MW$_{th}$ for certain conditions, type A slugging is unavoidable. The above results give suggestions how to prevent standpipe from operating in the type B slugging mode. To avoid type B slugging, it is suggested that $u_{s\,stp}$ in the standpipe is kept lower than 0.025 m/s, which can be achieved either by reducing the riser entrainment or by increasing the standpipe area.

6.5. Summary of loop seal and standpipe studies

The standpipe-loop seal behavior in small scale CFB is studied through variation of the loop seal aeration of the supply chamber. Ilmenite particles are used to perform this study. The standpipe gas velocity and aeration split in the standpipe increases with increasing loop seal aeration. Increasing the solid velocity decreases the gas velocity and aeration split for a given loop seal aeration. An increment in the loop seal aeration increases the riser G_s up to a limit and then decreases due to slugging in the standpipe. The standpipe slugged easily due to its small diameter. However, at solid velocities up to 0.025 m/s round nose slugging occurred while at higher solid velocity i.e. above 0.03 m/s flat nose slugging occurred. For a stable CFB operation flat nose slugging should be avoided. Based on these observations and experiences gained a refined design procedure for loop seal and standpipe is suggested and is described in Annexure C.

7. Friction losses in a CFB riser of 10 kW$_{th}$ carbonator

This chapter presents results of detailed hydrodynamic studies carried out for studying the influence of friction phenomena in the riser. The work presented in this chapter is published in [189].

7.1. Background

For any chemical process, it is necessary to know the actual quantity of compounds reacting in the process. For HTSLC processes the terms such as space time (Eq. (31)) or residence time (Eq. (43)) require the knowledge of solid inventory inside the reactor. Various instruments are employed in reactor technology for the measurement of reacting inventory such as level indicators, pressure indicators, gravimetric instruments or flow instruments depending on the application. In case of fluidized bed reactors, the solid particles are suspended in gas or liquid medium, the quantity of solid particles is mainly estimated from the pressure drop across the reactor, because the weight of the particles causes the pressure drop and solid inventory is calculated from Eq. (13). However, the main disadvantage of this method is the fact that the friction between gas-solid particles, reactor wall and acceleration of the particles are also contributing to the pressure drop. The magnitude of the friction and acceleration pressure drop reported in literature shows a significant variation. The scientific models available in the literature also do not reveal a final solution. Therefore, fluidization engineers commonly follow a simplified approach of neglecting frictional and acceleration pressure drop [96]. In reality, one has to accept that there will be a deviation. Furthermore, the work done regarding the friction and acceleration in a fluidized bed is mostly studied in dilute regions of the CFB risers where very small fraction of the inventory is located. The bottom region of the CFB where most of the solid inventory is located is not well studied from the friction and acceleration aspects. This work will focus on studying the difference between actual solid inventory in the reactor and inventory predicted by the pressure drop. This difference is attributed to the friction and acceleration phenomenon in the CFB system. Furthermore, the conditions close or similar to calcium looping process are used in the study. So the results arising from this study will be helpful in corrections in actual riser inventories to provide efficient scale up of the process.
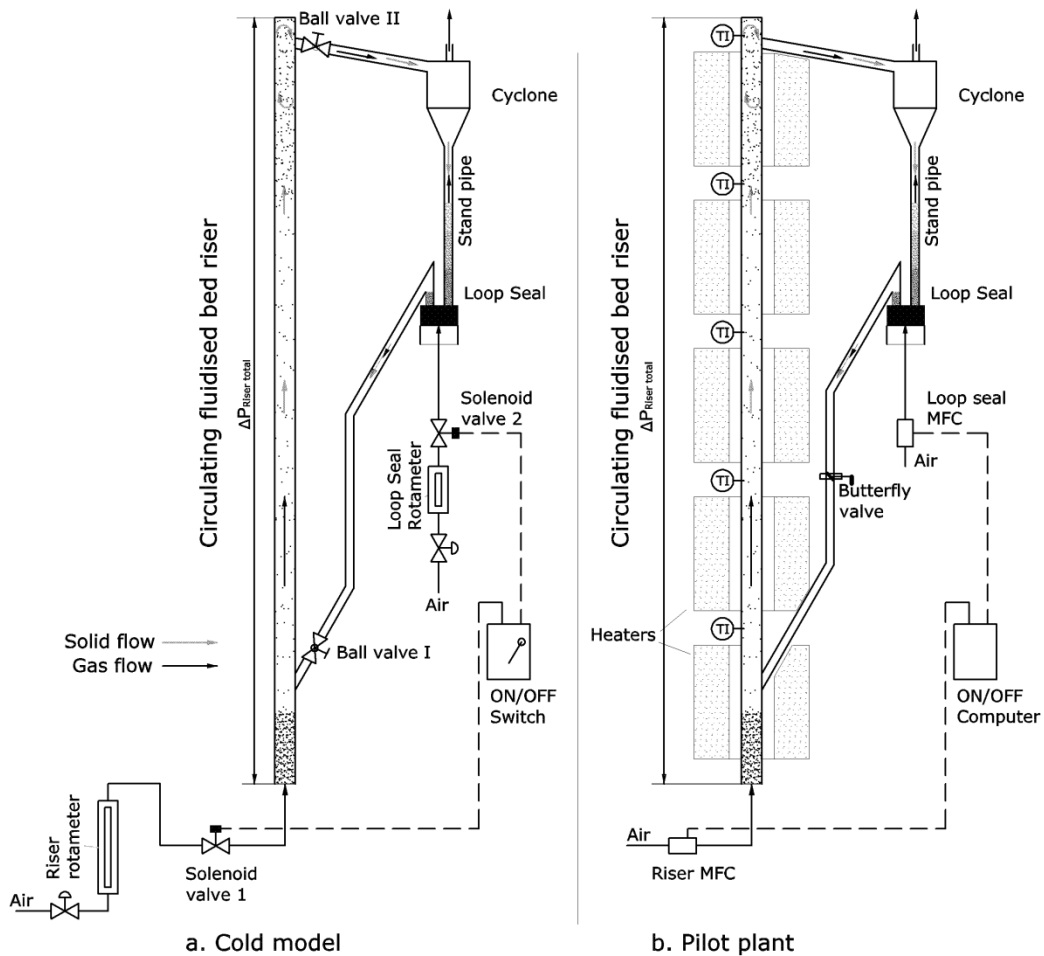
Figure 57 - Experimental set up for estimation of friction and acceleration losses in a small scale CFB

7.2. Experimental setup and procedure

The scope of work in the present study is limited to study the deviation in the calculation of actual inventory in a CFB riser caused by the friction and acceleration pressure drops, especially for the calcium looping process. The experiments are performed in two experimental set ups,

1. The cold model of 10kW$_{th}$ bench scale test plant at University of Stuttgart (cold model) (Figure 57a)
2. The 10 kW$_{th}$ CFB riser at University of Stuttgart. This set up was earlier used for studying CaL process (bench scale test plant). (Figure 57b)

The details of the two experimental set ups are given in Table 18. The cold model is a hydrodynamically scaled cold model of the 10kW$_{th}$ bench scale test plant. The geometric ratio is 1:2.3. The details of the cold model and bench scale test plant are available in previous works such as [71] along with their hydrodynamic studies. Although the cold model and bench scale test plant are dual fluidized bed systems (CFB + BFB coupled with cone valve and loop seals), in the present work only the CFB

105

Table 18 – Experimental conditions used in friction and acceleration losses measurement

	Cold model	bench scale test plant (Hot)	Scaling ratio Cold : Hot
Diameter (mm)	30	71	1:2.33
Height (m)	5.1	12.4	1:2.33
Temperature (°C)	20	630	
Velocity (m/s)	2-4.3	3.5 - 6.1	1:1.53
Particles	Iron oxide 5100 kg/m³ 140 µm.	CaO/CaCO3 1800 kg/m³300-500 µm	

risers are used for the investigation.

The theoretical aspects about the pressure drop in a CFB are covered earlier in chapter 2, section 2.2.3. To summarize, a pressure drop in a CFB riser is caused due to static pressure drop, friction between gas and solid particle, friction between particle and wall and the acceleration of particles. The static pressure drop is the pressure drop caused by the weight of the particles or the solid inventory (M_{riser}) present in the riser. The friction and acceleration pressure drops are mainly the function of friction factor and the velocity formulated in Eq. (17) to Eq. (19).

To estimate frictional pressure drop experimentally, the most common method employed is the quick closing valves method, cited at [115]. Another method is the use of optical fiber probes [116]. In the first method, the solid inventory is trapped inside the riser, weighted and converted to pressure drop using Eq.(13). This calculated pressure drop is compared with the pressure drop measured by instruments. In the optical fiber probe method, the actual solid suspension is measured and converted to pressure drop using Eq.(13). In both methods, the difference between the calculated and measured pressure drop is linked to the friction and acceleration pressure drop as per Eq.(15). In this work the method of quick closing valve is used because it is simple and its implementation is possible in the available experimental set up. Although one should notice that the method of quick closing valves has some limitations, apart from being non-continuous this method cannot reveal separate friction pressure drop and acceleration pressure drop in a riser. Also the extent of the friction and the acceleration pressure drop in the various sections of the riser cannot be measured.

The cold model of 10kW$_{th}$ bench scale test plant is modified with the quick closing valves as follows. As shown in Figure 57a, the primary air flow in the CFB riser and the loop seal aeration is mounted with a solenoid valve 1 and 2 to cut off the air flow to riser and loop seal suddenly. Both the solenoid valves are controlled by a single ON/OFF type electric switch. The ball valves, namely ball valve I and ball valve II are

installed in the return leg inlet into the CFB and after CFB exit to the cyclone respectively as shown in Figure 57a.

Figure 57b shows the modified 10 kW$_{th}$ bench scale test plant. The air supply in the test plant is done via MFCs. The quick closing arrangement in the bench scale test plant is achieved through the mass flow controllers (MFC). The MFC can also stop the air flow into the riser and the loop seal instantaneously via controller in the computer. The manual closing butterfly valve is installed on the return leg, similar to ball valve I of cold model. The valve similar to ball valve II of cold model could not be realized in the test plant due to technical difficulties.

In cold model as well as bench scale test plant the manual operation of the ball valves was preferred over the automatic actuators, because the manual closing action was much faster (less than a second) than the automatic action (automatic actuator required 3 s to close). This swiftness is critical in trapping the riser inventory inside the riser only [115].

The particles used in the cold model are shown in Table 18. The particles are same as used in chapter 5. The particles in the bench scale test plant were a mixture of CaO/CaCO$_3$. The operational velocities and pressure drops selected for the experiments in both cold model and bench scale test plant were in suitable range for calcium looping process and discussed earlier in section 5.2. However, the purpose of the hydrodynamic scaling is only limited to create the similarity in hot and cold conditions.

7.2.1. Procedure

The experimental procedure used is different to the standard experimental procedures explained earlier in section 3.3.3. The cold model and bench scale test plant experiments were carried out as follows. The initial experimental steps are same as those used in single loop CFB experiments explained in section 3.3.3. The total solid inventory was weighed and put into the empty loop seal of the CFB as shown in Figure 57a, and Figure 57b. The riser was operated through primary air and normal loop seal fluidization. The pressure drop in the riser was measured by means of a differential pressure transducer. The average riser pressure drop was adjusted to a desired value in mbar by addition or removal of total solid inventory. The steady state was considered when the pressure drop in the riser remained constant with uniform fluctuations. The pressure drop data was recorded for a period of 10 minutes and then the riser primary air and loop seal aeration was suddenly stopped by means of quick closing valve mechanism. In cold model solenoid valve 1 and 2 and ball valve I and II are closed at the same moment. In bench scale test plant both MFC are stopped at computer command and same time butterfly valve was closed manually. For every experimental condition (i.e. riser velocity and riser total pressure drop) multiple

experimental runs (min 3 runs-max 6 runs) were performed to ensure the reproducibility of the results.

7.2.2. Data analysis

The inventory trapped inside the riser and the return leg are weighed separately and compared with the measured pressure drop. The static pressure drop Δp_{static} for a given experiment is calculated from Eq. (16) as follows, by neglecting the static pressure drop of the gas in the riser.

$$\Delta p_{static} = \int (1 - \varepsilon)\rho_s g dh = \frac{M_{riser}g}{A_{riser}} \tag{51}$$

Where, M_{riser} is the trapped inventory in the riser and A_{riser} is the cross sectional area of the riser. In this study a separate friction and acceleration pressure drop could not be calculated, therefore for simplification reasons both pressure drops are summed up as (Δp_{fr+acc}). Eq. (17), Eq. (18) and Eq. (19) could be simplified into Eq. (52) as

$$\Delta p_{fr} + \Delta p_{acc} = \Delta p_{fr+acc} = \Delta p_{riser} - \frac{M_{riser}g}{A_{riser}} \tag{52}$$

where

$$\Delta p_{fr} = \Delta p_{fr\,g} + \Delta p_{fr\,s} \tag{53}$$

and Δp_{riser} is the time averaged pressure drop measured during the experimental steady state. The fraction of friction and acceleration pressure to the total riser pressure drop measured is represented by ψ, and defined by Eq. (54)

$$\psi = \frac{\Delta p_{fr+acc}}{\Delta p_{riser}} \tag{54}$$

The inventory trapped in the return leg is weighed and the particle height in the standpipe is also measured (only in cold model) during the experiment and after valve closure only for cold model experiments. The inventory trapped in the return leg and the one in the standpipe is later used in the analysis of inventory distribution of CFB system. In bench scale test plant these measurements were not possible.

7.3. Results and discussion

7.3.1. Effect of riser velocity on frictional and acceleration pressure drop (cold model set up)

The riser superficial velocity is one of the main parameters influencing solid distribution in a CFB riser. Friction and acceleration pressure drop equations also show that they are highly influenced by the riser velocity. Figure 58 shows the effect of riser

velocity on the friction and acceleration losses in the cold model set up. In this set of experiments the Δp_{riser} is kept constant around 80 mbar. The inventory trapped in the riser is converted to Δp_{static} using Eq. (51) and Δp_{fr+acc} is calculated using Eq. (52). The values of Δp_{static} and Δp_{fr+acc} shown in Figure 58 are the average values of multiple runs. In Figure 58 it is clear that an increase in riser velocity increases Δp_{fr+acc}. However, it is interesting to note that at low velocities the Δp_{static} measured is more than the Δp_{riser}. Therefore Δp_{fr+acc} values are calculated as negative values. Above 3.3 m/s the Δp_{static} is found to be lower than the Δp_{riser} and continues to decrease with increase in velocity, thus Δp_{fr+acc} are recorded as positive and increase with increase in velocity. From Eq. (16) to (19) it is observed that the friction and acceleration pressure drop is highly dependent on the velocity of gas and particles in the riser. Therefore, the increment in Δp_{fr+acc} can be explained. The % friction and acceleration pressure drop as per Eq. (54) for the above results is calculated between -55 to +70 % of the riser pressure drop.

The "negative" values of Δp_{fr+acc} should not be mistaken as the negative friction. The fluidized bed is a combination of annular and core region. The total pressure drop is defined as a combination of static pressure drop caused by the core and the annular region particles. The particles at the wall (annular region) experience a very low gas velocity zone, below u_{mf} thus the already suspended particles flow downwards or stop fluidizing. Below u_{mf}, the pressure drop caused by the particles is lower than the weight of the particles [9]. At lower velocities, the riser inventory was found more than the one calculated through the observed pressure drop. This phenomenon indicates that the population of such down flowing particles is significant in such small cross section, as in our experiments. The volume fraction of the annular region could be higher than the one of a riser with bigger cross section. A similar phenomena has been
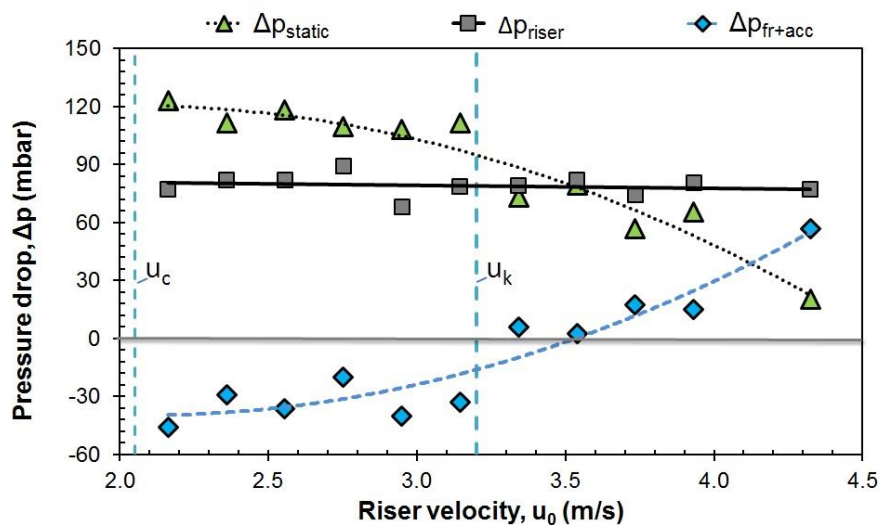

Figure 58 – Variation of static head and the friction - acceleration pressure drop in a CFB riser with the riser velocity

previously reported by Sankar and Smith [190] and Rautiainen et al. [115,117]. According to Rautianen et al. [115] the solid friction factor (f_s) mentioned in Eq. (19) varies with the solid velocity and at low velocity the values are "negative". Rautianen et al. [115] also developed a correlation for friction factor which takes this observation into consideration.

From Figure 58 it is clear that the negative values of Δp_{fr+acc} occur between u_c and u_k while above u_k most of the Δp_{fr+acc} values were reported to be positive. These values of u_c and u_k are calculated using the formulas proposed by Kunii and Levenspiel [79]. These velocities mark the onset and end of transition to the turbulent regime or as per [191] it is the turbulent regime. Since no similar observation could be found in literature, co-relating the turbulent regime and the observed phenomenon is not appropriate. Further investigation is suggested in this issue.

To conclude, friction and acceleration pressure drop show considerable variation. Neglecting this influence could bring significant error in calculating riser inventory in small scale cross section reactor. Without friction and acceleration taken into consideration, at low riser velocities below u_k within transition to turbulent phase the riser inventory could be underestimated and above u_k overestimated.

7.3.2. Effect of total riser pressure drop (cold model)

In previous section the effect of riser velocity on the friction and acceleration losses is shown at constant total pressure drop in the riser. However, it is interesting to see the effect of total pressure drop on the friction and acceleration pressure drop. Figure 59a shows Δp_{fr+acc} subject to variation in Δp_{riser} and riser velocity u_0. The Δp_{riser} selected were ca. 40, 60 and 80 mbar at the velocities of 3.15, 3.5 and 3.9 m/s. The velocities were selected such for providing negative, near zero and positive Δp_{fr+acc}.

As it can be seen, that the Δp_{fr+acc} measured for a velocity of 3.15 m/s is negative for all three Δp_{riser} as observed earlier in Figure 58. For 60 mbar and 80 mbar the values were close in the range of -35 mbar and -40 mbar, while for 40 mbar the value was - 20 mbar. At a riser velocity of 3.5 m/s the Δp_{fr+acc} is also measured as close to zero for the Δp_{riser} of 60 mbar and 80 mbar. However, for 40 mbar Δp_{fr+acc} was measured as 16.5 mbar. For a riser velocity of 3.9 m/s the Δp_{fr+acc} measured is in the range of 16-18 mbar for all three Δp_{riser}, which is very close. In other words, at this velocity the effect of increased Δp_{riser} through addition of total solid inventory had less effect on ΔP_{fr+acc}. Thus comparing Figure 58 and Figure 59a it can be deduced that the riser velocity is the major factor which determines the magnitude of friction and acceleration pressure drop in the riser. The discrepancy of the results of 40 mbar at the velocity of 2.1 and 3.5 m/s could not be yet explained. Figure 59b shows the results of Figure 59a, as ψ defined by Eq. (54). Since ψ represents ΔP_{fr+acc} as a fraction of
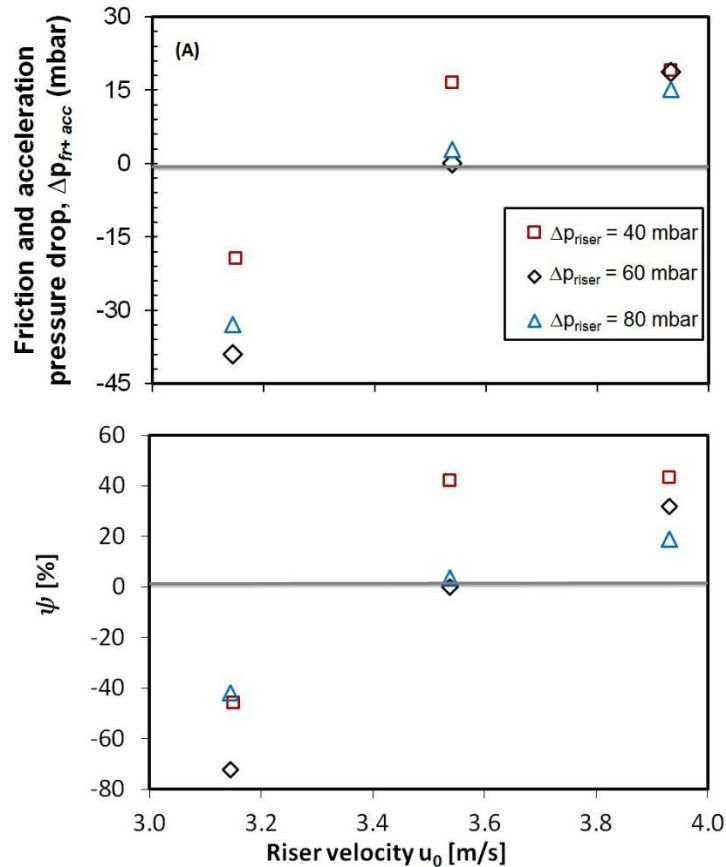
Figure 59: Influence of riser inventory or total riser pressure drop on the friction and acceleration pressure drop

the total pressure drop, and may be useful to compare the other results in literature which are often gives information of frictional pressure drop as a percentage of the total pressure drop [118]. For a riser velocity of 3.9 m/s, it can be seen that increasing Δp_{riser} the ψ decreases. This is explained since the Δp_{fr+acc} nearly remained constant and Δp_{riser} increased. Issangya [121] also observed that for high density CFB risers the contribution of pressure drop due to friction is less compared to low density risers.

7.3.3. Experiments in the bench scale test plant- influence of riser velocity on friction and acceleration pressure drop

The results presented in the previous sections show an interesting phenomenon. However, it is hard to conclude that such phenomenon could occur in the large scale CFB risers. Therefore, similar experiments were performed in the bench scale test plant facility shown in Figure 57b. The facility and the experimental conditions are described in Table 18. These conditions are exact conditions for calcium looping process, except the fluidizing gas was air instead of flue gas in order to avoid carbonation reaction. The riser superficial velocity was the main parameter investigated. Figure 60 shows the static pressure drop (static head) and the friction and acceleration pressure drop. It can be observed that even during the test plant
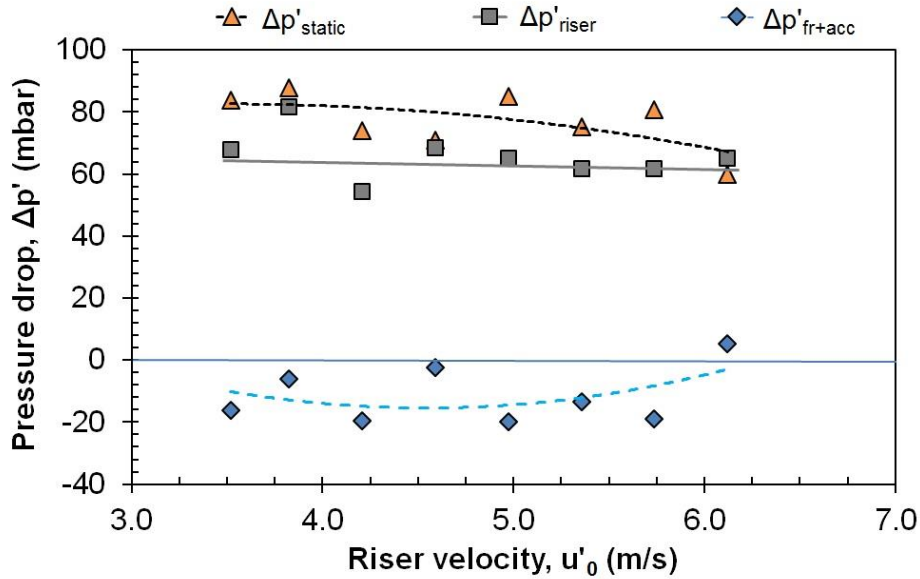
Figure 60 – Influence of riser velocity on the friction and acceleration pressure drop in hot condition in bench scale test plant

experiments the static head was recorded higher than the actual pressure drop. Thus as per Eq. (52) negative values of friction and acceleration pressure drop are obtained. For velocities between 3.5 to 6.1 m/s the Δp_{fr+acc} was calculated to be -20 to +5.3 mbar. The results of Figure 60 are analogues to the results as per Figure 58, if we consider the scaling ratio of velocity (Table 18) except the results at velocity higher than 6.1. The term "analogues" is used here, since the cold model and bench scale test plant showed similar results.

The experiments could not be performed at higher velocity due to facility related limitations. Although, the phenomenon has been repeated in the scaled up facility, it is still audacious to conclude that such behaviour will be observed in larger scale risers also. Contrary, employing similar experimental method or quick closing valve is not suitable for large scale risers. The use of optical fibre probes will be a suitable method.

The space time ($\acute{\tau}_{ca}$) values as per (Eq. (31) to Eq. (34)) are shown in Figure 61 for the results obtained from test plant. The calculations are done assuming a CO_2 inlet concentration of 15 vol% and bed material as pure CaO at 630°C. The actual space time is calculated using the solid inventory of riser captured using quick closing valve method ($\acute{M}_{riser}$) of Figure 60 and estimated space time is calculated using the riser total of Figure 60. As seen in Figure 61, for all cases except at 6.1 m/s the actual space time is higher than the estimated space time. Nevertheless, the suitable velocity range for calcium looping process is also between 4-6 m/s. Therefore, the scientists who rely on the pressure drop values for space time calculations (Eq.(31)) can consider pressure drop values as a conservative approach. Thus, space time values predicted from pressure drop readings will be lower than the real space time values.
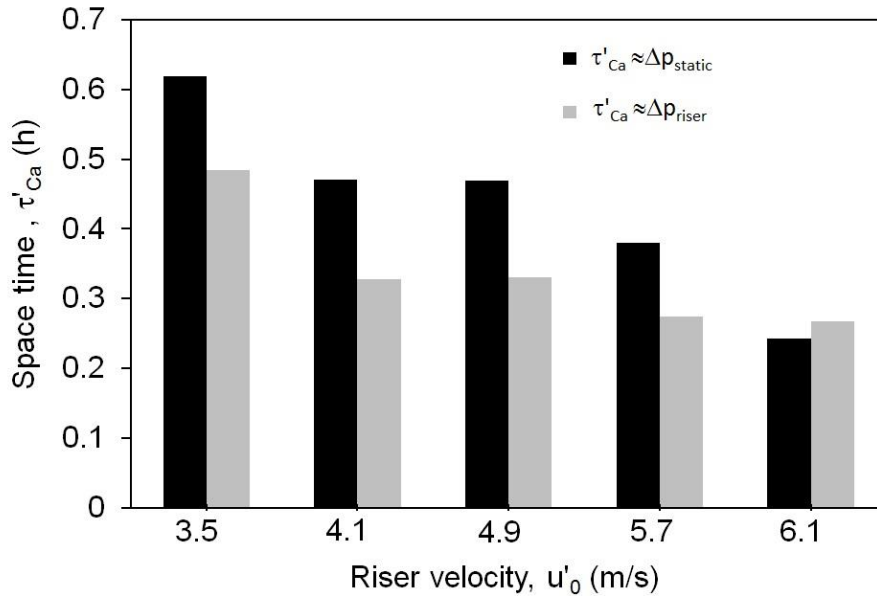
Figure 61 – Comparison of actual space time (Δp_{static}) and estimated space time (Δp_{riser})

7.4. Summary

The deviation of actual riser inventory deviation is studied in terms of combined frictional and acceleration pressure drop. The experiments were carried out in a cold model and in a geometrically scaled test plant in hot conditions. In the cold model the friction and acceleration pressure drop are highly influenced by the riser velocity and increase with the increment in riser superficial velocity. However, at low velocities i.e. between u_c and u_k the static pressure drop was observed being higher than the riser pressure drop. At higher riser velocity, the friction and acceleration pressure drop is positive and increases rapidly with the riser velocity. The range of friction and acceleration pressure drop is found to be between -55 to +70 % of the riser pressure drop. Analogous results were obtained in the test plant (-20 to +5 mbar). The calculation of riser inventory based on the pressure drop is very complex and could lead to error if friction and acceleration terms are not considered with appropriate friction factor models. However, from the test plant results it could be concluded that within the operational velocity range of calcium looping process, the inventory calculated from the pressure drop results can be taken as conservative value.

8. Outlook and future work

The hydrodynamic studies of DFB systems for a 200 kW$_{th}$ test plant are presented in this thesis. Two different DFB schemes are investigated in a cold model, based on the results from the cold model, the test plant is built and respective HTSLC processes namely calcium looping and sorption-enhanced reforming are successfully demonstrated. The DFB system is a very versatile reactor system and has been the most suitable reactor system for HTSLC processes. If the processes are to be commercialized for CO_2 capture or for energy conversion, the DFB systems proposed in the present work can be considered for the scale-up. For large scale commercial calcium looping process the CFB-CFB option is the suitable option and therefore it was considered as a primary option for the investigation in this work. However, recently Dieter et al. [192] also used the Figure 15 (SER mode) schematic for the demonstration of CaL process and concluded that such schematic is also a highly feasible option, as it offers a greater flexibility in terms of handling the quantity of flue gas. Apart from CaL and SER, the investigated DFB schematics can also be applied to the other HTSLC processes such as steam gasification and chemical looping combustion, chemical looping reforming and those processes which are yet to be invented. The author believes that the number of processes based on the principal of HTSLC will continue to grow in the future. At University of Stuttgart, a combination of SER and CaL is currently under the investigation [126]. This process aims at increasing the calorific value of the product gas by the removal of CO_2 from the product gas.

The investigations related to the standpipe and loop seal are done with an aim to improve the DFB system design. However, the outcome of these investigations can be readily applied to simple CFB systems as well. Based on the experience gathered during the span of this thesis, a simple design procedure for the loop seal and standpipe is made and described in the Annex C.

The investigations related to the friction and inventory estimation in a CFB riser have shown that the actual inventory in the riser may be more than the one calculated from the pressure drop. The observation of this phenomenon has opened a need to study the friction phenomenon in the CFB once again. However, these observations were made at very small-scale risers (30 mm cold model and 70 mm test). Therefore, similar experimental investigation at larger scale risers or the computational study is required.

As a matter of future work, the proper hydrodynamic studies should be carried out in the 200 kW$_{th}$ test plant. The hydrodynamic studies at the process conditions are important for the scale up. The influence of reactions happening in the risers (CO_2 absorption in carbonator and CO_2 release in the regenerator) on the riser hydrodynamics will be clear.

Some CaL sorbents or the CLC oxygen carriers may require much higher entrainment flux to support the reactivity or the heat transfer, therefore DFB systems should be designed accordingly. The loop seals in such situations may be inadequate as a solid supply device. Therefore special configurations of the DFB systems should be formulated and tested in the cold model. The cold model should be further carried out to exploit design improvements. The use of internals to improve the gas solid contact in the risers can be studied in the cold model. In addition the influence of obstructions inside the risers such as heat exchanger pipes should be investigated. Another section where the author feels a need to investigate is the cyclone design especially for the calcium looping process. Furthermore, a detailed research on achieving the fine control of the solid looping between the two fluidized beds will be highly appreciated.

Annexes

Annexe A – Definitions and Hydrodynamics of the fluidized bed
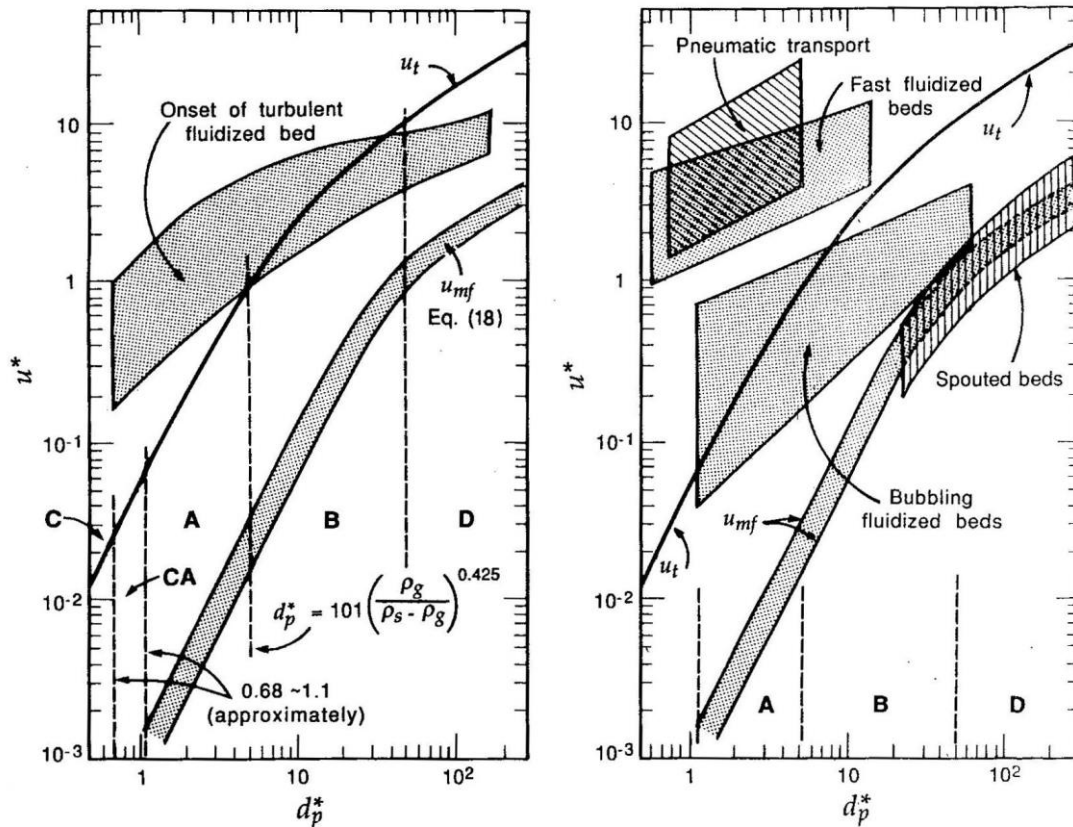
Grace diagram

Figure A 1 - Diagram mapping various regimes proposed by Grace [93]

Extending the work of Reh, Grace [93] presented the following chart for mapping the fluidization regimes: Where u^* and d_p^* are dimensionless velocity number and dimensionless particle number respectively. They are calculated as below

$$u^* = u \left[\frac{\rho_g^2}{\mu(\rho_s - \rho_g)g} \right]^{1/3} \tag{A 1}$$

and

$$d_p^* = d_p \left[\frac{\rho_g(\rho_s - \rho_g)g}{\mu^2} \right]^{1/3} \tag{A 2}$$

Co-relations of some important velocities related to regimes of fluidization

Minimum bubbling velocity: Minimum velocity at which bubbles occur is called minimum bubbling velocity u_{mb}. The u_{mb} is greater than u_{mf} only for very fine (Geldart A) particles. In this case a bubble free fluidization regime between u_{mf} and u_{mb} exists. According to Geldart and Abrahamsen [94]

$$u_{mb} = 33d_p \left(\frac{\rho_g}{\mu}\right)^{0.1} \tag{A 3}$$

Minimum slugging velocity (u_{ms}): Bubbles become larger when the superficial gas velocity is increased further. Slugging occurs when the bubbles grow to sizes comparable to the column diameter. Chapter 6 deals with the topic of slugging in standpipe. For estimating the slugging velocity a correlation is given from Stewart and Davidson [193],

$$u_{ms} = u_{mf} + 0.7\sqrt{gD} \tag{A 4}$$

where D is the diameter of the fluidized bed

Terminal velocity: Terminal velocity is the maximum relative velocity that can be achieved between the moving gas and the solid particles. Theoretically, if the superficial velocity exceeds the terminal velocity for a given particle than the particle will be carried out of the reactor no matter the height of the reactor. Terminal velocity u_t is calculated using the following set of formulas,

$$u_t = u_t^* \left[\frac{\mu(\rho_s - \rho_g)}{\rho_g^2}\right]^{1/3} \tag{A 5}$$

where u_t^* is calculated as,

$$u_t^* = \left[\frac{18}{\left(d_p^*\right)^2} + \frac{2.335 - 1.744\varphi_s}{\left(d_p^*\right)^{0.5}}\right]^{-1} \tag{A 6}$$

here d_p^* is defined from Eq. (A2)

Minimum velocity for turbulent fluidization u_c: The transition to turbulent regime is encountered when the superficial velocity becomes equal to u_c. The u_c is the superficial gas velocity at which the standard deviation of the pressure fluctuations reaches a maximum. Bubble coalescence and break up reach a dynamic balance. If velocity is further increased bubble break up becomes predominant. Bi and Grace [100] came up with a coorelation for this velocity:

$$Re_c = 1.24 \, Ar^{0.45} \tag{A 7}$$

where Re_c is the Reynold number corresponds to u_c same way as in Eq. (11) and Ar is Archimedes number shown as Eq.(12).

The end of the turbulent regime marks the beginning of the fast fluidization regime. The minimum velocity of the fast fluidization regime is defined by u_{se}.

$$Re_{se} = 1.53\ Ar^{0.5} \tag{A 8}$$

where Re_{se} corresponds to u_{se} same way as in Eq. (11).

Classification of particles

The characteristics and behavior of a fluidized bed are strongly dependent on gas and solid properties. By carefully observing the fluidization of all sorts of sizes and solids, Geldart came up with four clearly recognizable kinds of particle behavior. For smallest to larger particles they are as follows:

Group A: aeratable, or materials having a small mean particle size and/ or low particle density (1.4 g/cm³). These solids fluidize easily, with smooth fluidizations at low gas velocities and controlled bubbling with small bubbles at higher gas velocities. FCC catalyst is representative of these solids.

Group B: sand like, or most particles of size 40µm $<d_p$ <500µm and density 1.4 g/cm³ $<\rho_s<$ 4 g/cm³. These solids fluidize well with vigorous bubbling action and bubbles grow large.

Group C: cohesive or very fine powders. Normal fluidization is extremely difficult for these solids because inter particle forces are greater than those resulting from the action
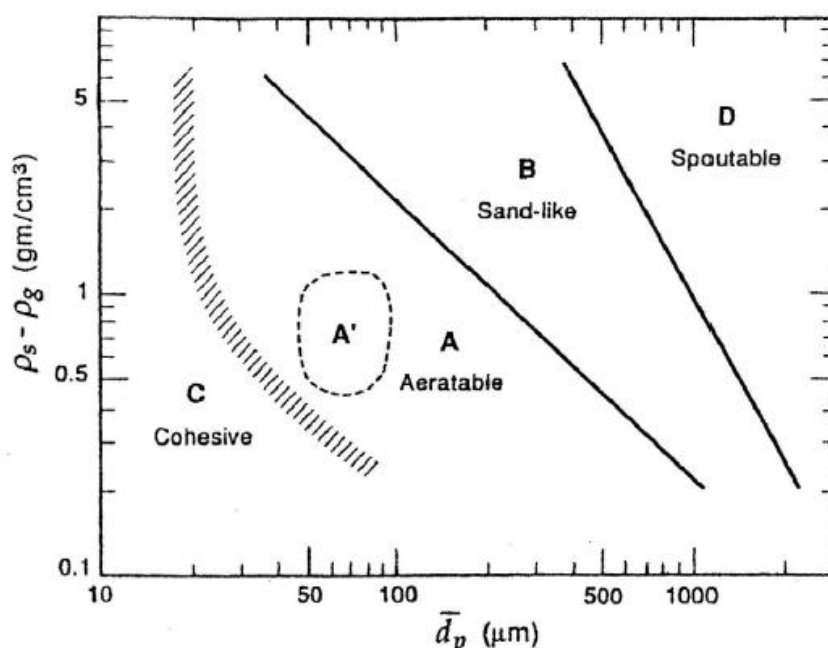

Figure A 2 – Particle classification proposed by Geldart [102]

of gas. They tend to rise as a plug of solids or form channels from the distributor to the bed surface.

Group D: spoutable, or large and/or dense particles. Deep beds of these solids are difficult to fluidize. They give large exploding bubbles or severe channeling, or spouting behavior if the gas distribution is uneven.

Annexe B – Details of the experimental set up

Following information can be found in this annexe

- Pictures of the cold model
- Process flow diagram of the experimental set up
- List of rotameters
- Particle properties and particle size distribution of the particles used in chapter 4 and 5
- 3 D views of the CaL mode and SER mode 200 kW$_{th}$ test plant

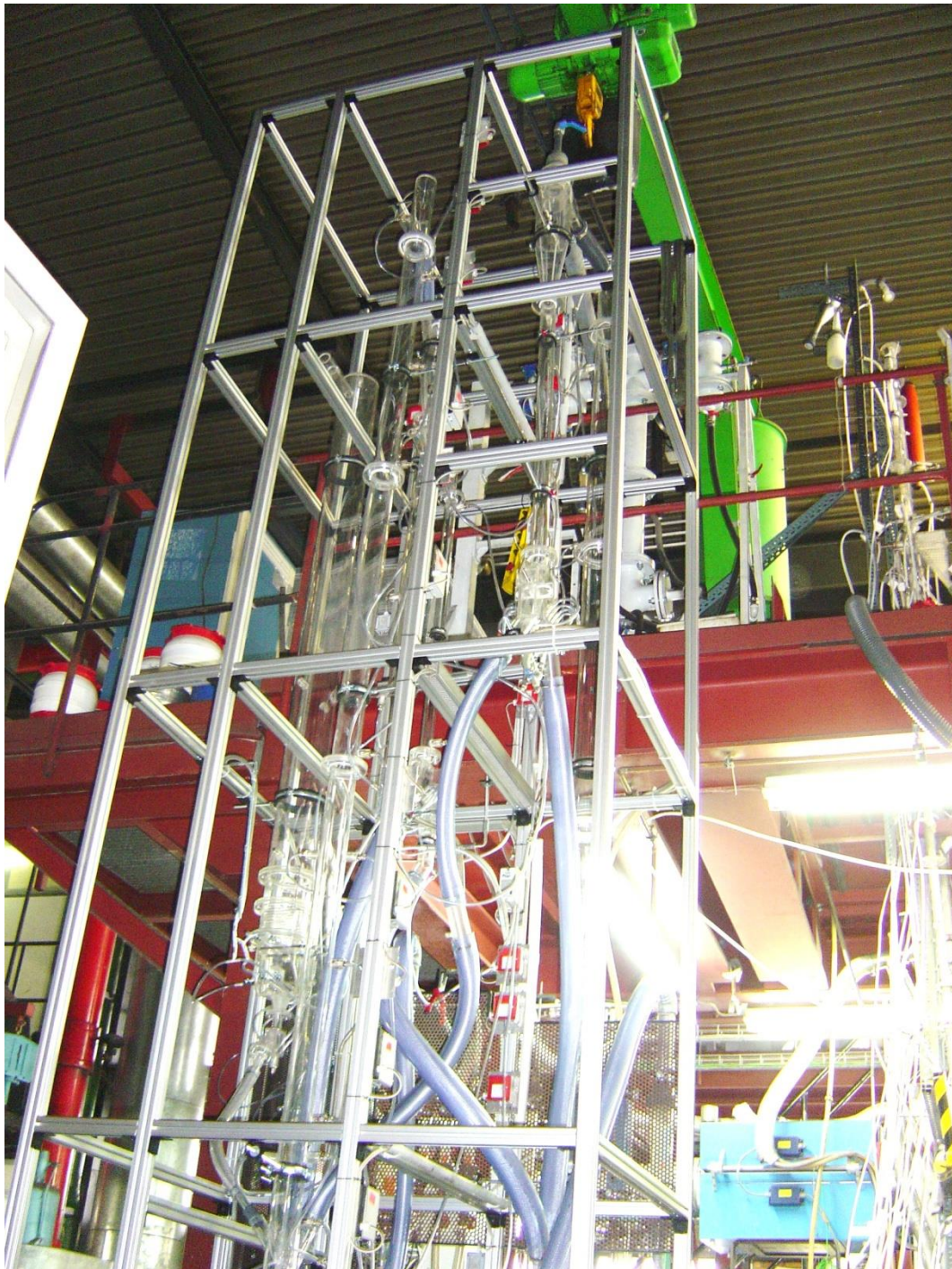**Figure A 3 – Side view of the cold model**

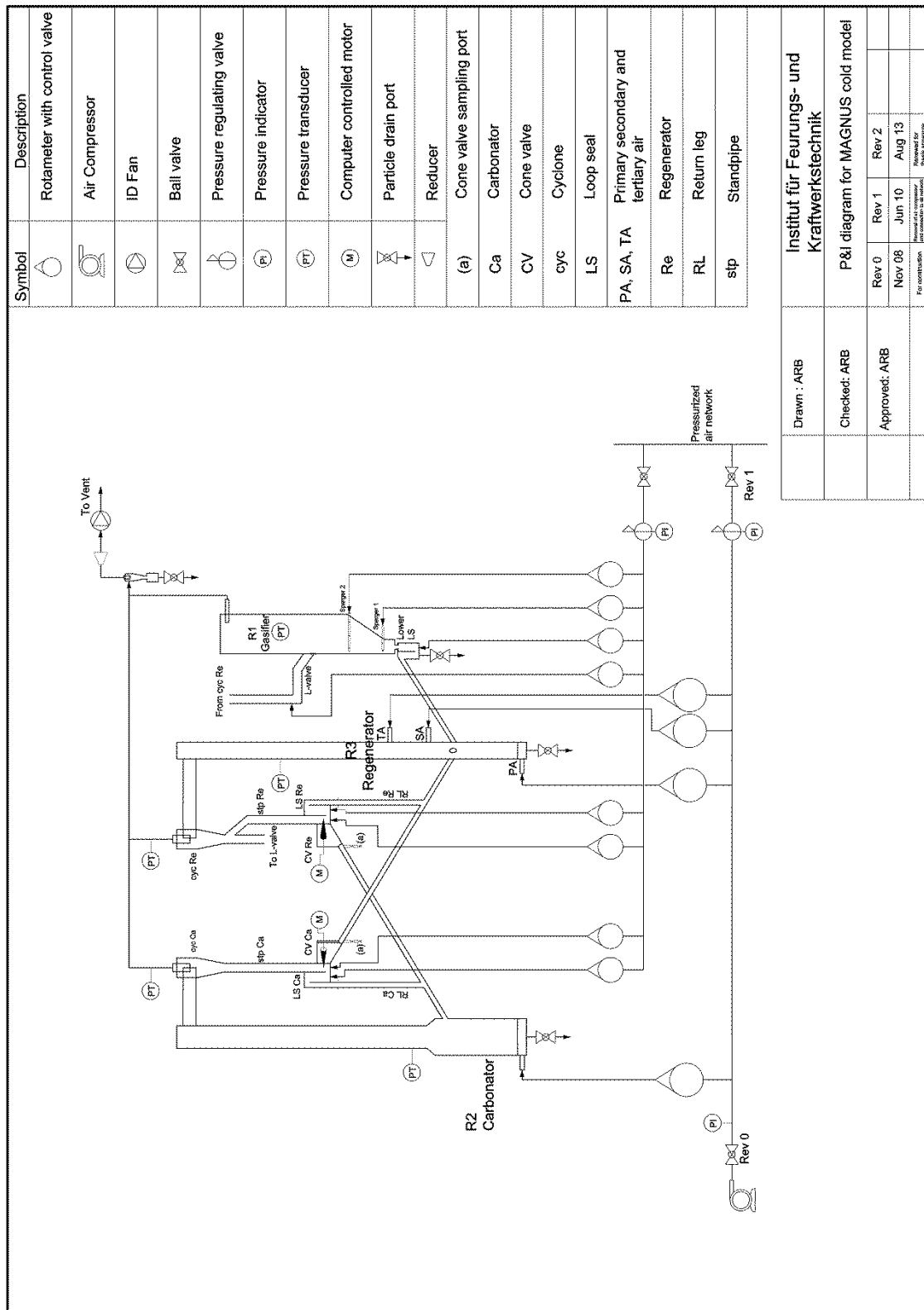**Figure A 4: Front view of the cold model installation**

Figure A 5 – Piping and instrumentation diagram of the cold model used in this thesis

Table A1 : List of Rotameters (Air flow requirements in cold model)

Sr. No	Description	Range
	R1	
1	Upper Sparger	3-30 Nm³/h
2	Lower sparger	3-30 Nm³/h
3	Bottom loop seal	4-50 l/min
4	L-valve	1-10 l/min
	R2	
5	Primary air	22-190 Nm³/h
6	Loop seal supply chamber	2-6 Nm³/h
7	Loop seal recycle chamber	2-6 Nm³/h
	R3	
8	Primary air	10-70 Nm³/h
9	Secondary air	3-24 Nm³/h
10	Tertiary air	3-24 Nm³/h
11	Loop seal supply chamber	4-50 l/min
12	Loop seal recycle chamber	4-50 l/min

The solids used for the fluid hydrodynamic analysis were characterized for the determination of the mean particle diameter, voidage and density of each material. The results are presented in Table A2, Figure A 6 and Figure A 7 show the particle size distribution of iron oxide and steel respectively.
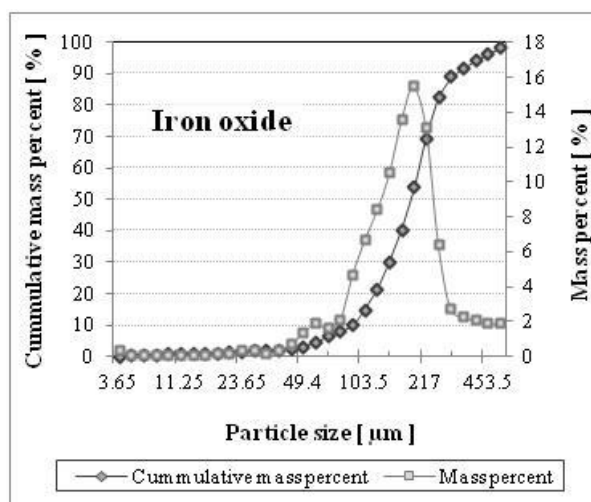
Figure A 6 : Iron oxide particle size distribution
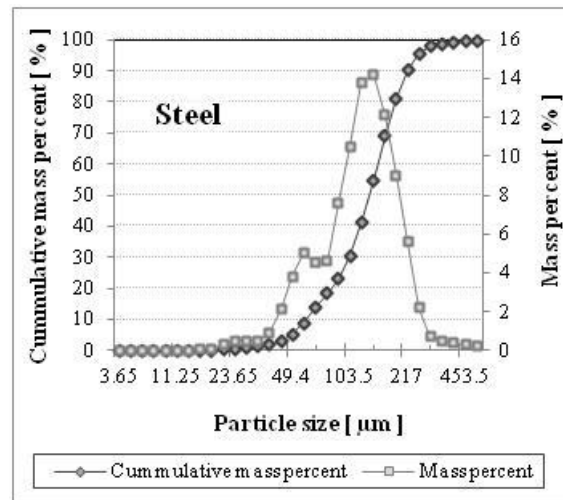
Figure A 7: Steel particle size distribution

Table A2: Properties of the fluidized material

	Mean particle diameter [μm]	Bulk density [kg/m³]	Voidage [–]
Steel	~ 127	3368	0.55
Iron oxide	~ 169	2200	0.54

Figure A 8 : 3D view of the CaL mode test plant

Figure A 9: 3D View of the SER mode test plant [66]

Figure A 10 : Final view of the regenerator with the suggested improvements

    a.   **The hopper shaped bottom**

    b.   **The loop seal with deeper weir height**

Annexe C– Design procedure of loop seal and standpipe for small scale FB and DFB facilities

The standpipe and loop seal arrangement is widely used in the circulating fluidized bed and dual fluidized bed systems. 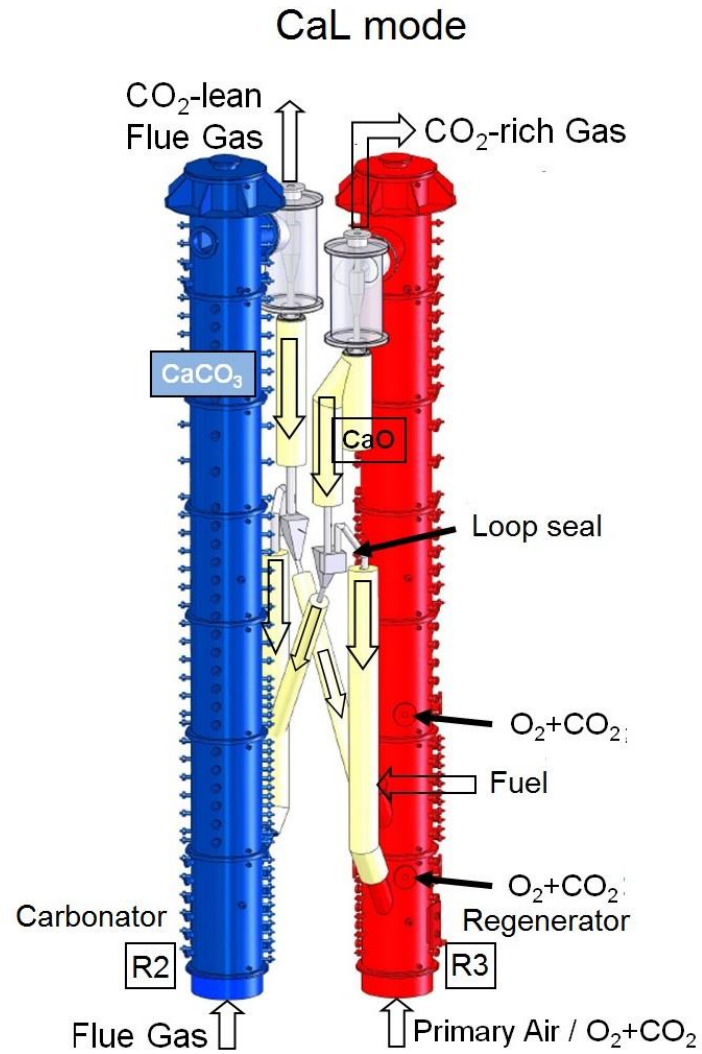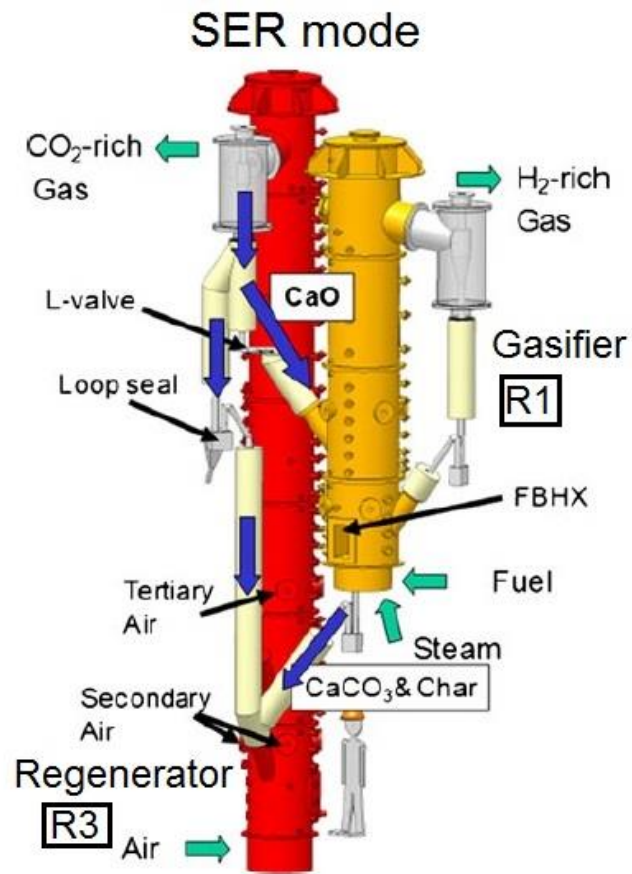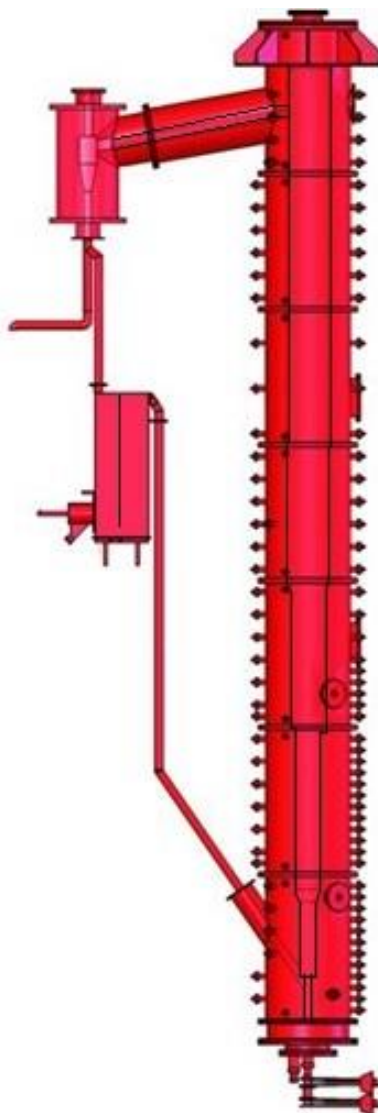It is a very important part of the system and could be considered as a heart of the system as it circulates the solid particles back into the riser. Due to absence of any moving parts it is very robust and maintenance free. However if falsely designed, the loop seal and standpipe could become a bottle neck and can lead to severe problems in the entire fluidized bed operation. Although loop seal and standpipes are considered important but very less information is available in the literature about the design of a loopseal, except some guidelines mentioned by Basu [9]. This annex will try to provide some more guidelines regarding a loop seal design. The information provided in this section is a result of the experience collected in the span of this thesis.

The standpipe and loop seal design can be divided in the following sections

- The sizing of the standpipe and loop seal
- Determination of the aeration requirement in the loop seal
- Detailing of the standpipe and loop seal
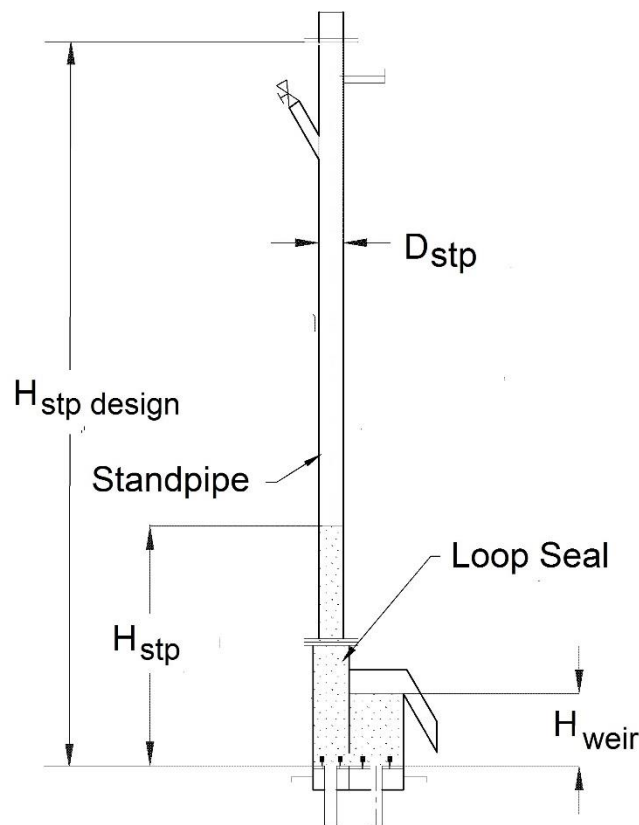

Figure A 11 – A typical standpipe and loop seal arrangement

The sizing of the standpipe and the loop seal is a complex process and sizing every component is dependent on the different physical principal. Below the list of

sizing to be done is given for a loop seal and standpipe system and their respective influencing factor.

	Part	Influenced from
1	Standpipe height	Riser and cyclone pressure drop
2	Standpipe diameter	Solid downflow velocity and circulation rate
3	Loop seal dimensions	Standpipe size
4	Loop seal aperture	Solid circulation rate and particle size
5	Loop seal weir height	Pressure fluctuations in the riser

The standpipe height is primarily influenced from the pressure drop in the riser and the cyclone. From Eq. (28) of the pressure balance it is clear that the standpipe must provide enough pressure drop in order to keep the system in the balance. The pressure drop is generated via the particle bed height and the loop seal aeration. The detailed relationship is shown in chapter 7. Furthermore, three types of regimes are identified namely the bubbling regime, moving bed regime and dilute flow regime. The bubbling regime pressure drop can be easily calculated from the Eq. (13). The moving bed pressure drop can be calculated from modified Ergun equation as per Eq. (21). However moving bed regime pressure drop is difficult to estimate. Dilute regime primarily occupies the volume between the cyclone bottom and the top of the particle bed, where particles fell freely under the gravity influence. Here the pressure drop contribution is accepted as null. Weather the particle bed in the standpipe is under bubbling bed or moving bed, is dependent on the aeration rate and the solid downflow rate in the standpipe.

From pressure balance

$$\Delta p_{stp} = \Delta p_{LS} + \Delta p_{\,riser\,top} + \Delta p_{cyc}$$

(A 9)

Adapting Eq. (13) for a bubbling standpipe

$$(1 - \varepsilon_b)\rho_s g H_{stp} = \Delta p_{LS} + \Delta p_{\,riser\,top} + \Delta p_{cyc}$$ (A 10)

where ε_b is the voidage in bubbling fluidized bed condition, we achieve

$$H_{stp} = \left(\frac{\Delta p_{LS} + \Delta p_{\,riser\,top} + \Delta p_{cyc}}{(1 - \varepsilon_b)\rho_s g} \right)$$ (A 11)

However, for a moving bed regime the standpipe particle height is difficult to estimate from available co-relations, more investigation is required in this regard. Author suggests a safety factor of 2 (for fine particles) and 3 (for coarse particles) which will provide sufficient standpipe height.

$$H_{stp\,design} = (2\,to\,3)H_{stp}$$ (A 12)

Sizing standpipe diameter is dependent on the solid downflow velocity. As we have studied in the chapter 7 the choosing of higher downflow velocity leads to the operational problems like slugging in the standpipe and therefore may cause the shut down of the fluidized bed operation. As suggested in the chapter 7 the design solid down flow velocity ($U_{S_{stp}design}$) can be taken as 0.025 m/s and then using the expected solid circulation rates and the information about the particle density; the standpipe diameter can be sized.

$$A_{stp\ design} = \frac{\pi}{4} * D^2_{stp\ design} = \frac{G_{riser}}{U_{S_{stp}design}\rho_{S_{bulk}}} \tag{A 13}$$

For small scale designs the minimum diameter for the standpipe should be selected as 50 mm. Less than this size would anyway cause severe slugging problems.

The guidelines about loop seal sizing and sizing of the loop seal aperture are well described in Basu [9]. The same guidelines can be used.

Basu [9] proposed following guidelines

$L_{1\ LS} = 2.5\ D_{stp}$ and $L_{2\ LS} = 1.25\ D_{stp}$

where $L_{1\ LS}$ and $L_{2\ LS}$ are the length and width of the loop seal. However, author would like to suggest a following improvement to Basu`s guidelines. The recycle chamber of the loop seal receives gas from recycle chamber as well as supply chamber (see Section 7.3). Therefore larger cross section in the recycle chamber would help lower the slugging tendency in the recycle chamber, therefore

$L_{1\ LS} = 3.25\ D_{stp}$

of which, 1.25 D_{stp} of length should be allocated to the supply chamber of the loop seal and 2 D_{stp} length should be allocated to recycle chamber of the loop seal.

The sizing of the loop seal weir height is hardly mentioned in the literature. The author proposes a practical approach to size the weir height. During the experiments of section 4.5.3, (i.e. influence of loop seal depth on the cone valve performance), it was found that the loop seals with lower weir height are prone to dysfunction when risers showed high fluctuation tendency. During the high pressure fluctuation or pressure jerk, the gases from the riser were observed to enter the standpipe from the weir side of the loop seal. In this situation the gas quantity was enough to cause the fast fluidization of the particles in the standpipe and entire standpipe inventory was lost to second cyclone. It caused the complete fluidized bed operation to come to stand still. The loop seals with higher weir height proved to be more stable. The main reason behind this phenomenon is the lack of particle bed height in the standpipe. As observed in Figure 37 increasing the weir height increases the particle height in the standpipe.

Subsequently pressure seal of the loop seal improves. Particle height in the recycle side of the loop seal also provides an extra barrier against the fluctuating riser.

Section 4.4.2.3 shows the relationship between the riser fluctuation and the riser velocity. At low velocities the riser fluctuations are more while at higher they are stable. If designer knows the riser velocity and then from the knowledge of fluctuations $\frac{\sigma(\Delta p_{riser})}{\Delta p_{riser}}$ one can decide the weir height of the loop seal.

The recycle section of the loop seal always in bubbling conditions therefore

$$H_{weir\ design} = \frac{\sigma(\Delta p_{riser})}{\Delta p_{riser}} \frac{\Delta p_{\ riser}}{(1 - \varepsilon_b)\rho_s g} \tag{A 14}$$

for example the $\frac{\sigma(\Delta p_{riser})}{\Delta p_{riser}}$ for a given riser velocity is around 30% and if the riser needs to operate at 100 mbar. For this situation the loop seal must provide a barrier of 30 mbar. The weir height is designed for a 30 mbar pressure drop.

The loop seal aeration requirements are also less mentioned in the literature. Lack of this information caused obstacles in selection of the suitable range for gas supply instruments. However after a brief literature search number of studies have shown loop seal aeration [132–134,194,195]. Collecting all the information and the observations from chapter 7, it can be concluded that the optimum range of loop seal aeration is between 2 to 8 u_{mf}. More aeration would result in excess gas in the supply side and standpipe, therefore causing unnecessary slugging and resistance to solid downflow. Therefore, from the known area of the loop seal the required quantity of aeration can be found out.

The author did the experiments on the loop seal with the aeration only in the supply side of the loop seal. However a common practice followed normally, is the aeration in both sections of the loop seal. The recycle side of the loop seal is normally fluidized at bubbling fluidized bed conditions (2-3 u_{mf}) and the remaining aeration is provided in the supply side of the loop seal. Thus

$$\dot{V}_{LS} = A_{LS} * u_{0\ LS} \tag{A 15}$$

where $u_{0\ LS}$ is 2-3 u_{mf}, the above calculation, a suitable range for the flow instrument for the loop seal can be selected.
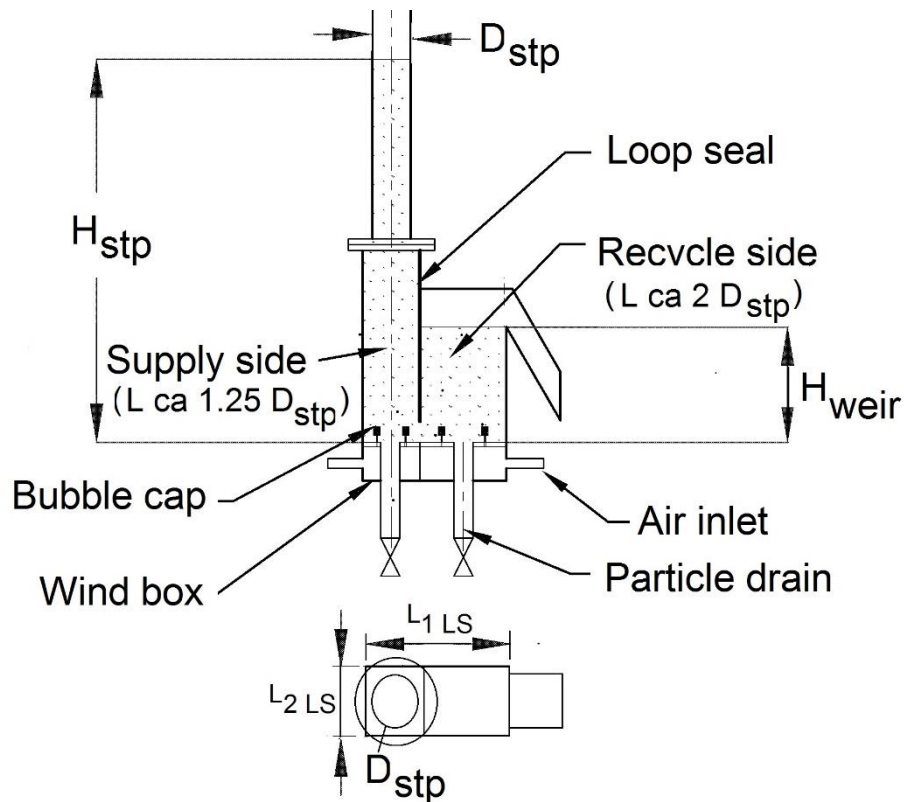
Figure A 12 – Details to be considered in the loop seal design

The standpipe is relatively simple part and just consists of a pipe. As shown in Figure A 11, the standpipe should be equipped with a particle feeding port and a pressure measuring port.

The detailing of the loop seal is critical. Figure A 12 shows the further details of the loop seal. The air supply should be given in the wind box and preferably separate in separate sections of the loop seal. The bubble caps are necessary to distribute air evenly inside the loop seal and prevent particle falling inside the wind box. The sizing of the distributor and bubble caps can be referred in detail elsewhere. The particle drain is necessary. It is a perfect location to take the solid sample and position to empty the CFB system.

Bibliography

[1]   E.G. Beck, 180 Years of atmospheric CO2 gas analysis by chemical methods, Energy Environ. 2007 (n.d.) 259–282.

[2]   CO2 Now- CO2 Home, (2012). http://co2now.org/.

[3]   J.H.P. Seinfeld, Spyros N., Atmospheric chemistry and physics: from air pollution to climate change, Wiley Subscription Services, Inc., A Wiley Company, 2006.

[4]   S. Solomon, G.-K. Plattner, R. Knutti, P. Friedlingstein, Irreversible climate change due to carbon dioxide emissions., Proc. Natl. Acad. Sci. U. S. A. 106 (2009) 1704–9. doi:10.1073/pnas.0812721106.

[5]   P. Canziani M.L., Impacts, Adaptations and Vulnerability. Intergovernmental panel on climate change (IPCC), Cambridge press, 2007.

[6]   BP Energy Outlook 2030, 2011.

[7]   N.H. Florin, P.S. Fennell, Carbon capture technology : future fossil fuel use and mitigating climate change, Grantham Inst. Clim. Chang. (2010) 1–20.

[8]   E.J. Anthony, Solid Looping Cycles: A New Technology for Coal Conversion, Ind. Eng. Chem. Res. 47 (2008) 1747–1754. doi:10.1021/ie071310u.

[9]   P. Basu, Combustion and Gasification in Fluidized Beds, Taylor & Francis Group, Halifax, Nova Scotia, 2006.

[10]   W. Lewis, E. Gilliland, M. Sweeney, Gasification of carbon, Chem. Eng. Prog. 47 (1951) 251–256.

[11]   A. Sánchez-Biezma, L. Diaz, J. López, B. Arias, J. Paniagua, D. Zárraga, et al., La Pereda CO2: a 1.7 MW pilot to test post-combustion CO2 capture with CaO, in: 21st Int. Conf. Fluid. Bed Combust., Naples (Italy), 2012: pp. 365–372.

[12]   G.T. Rochelle, Amine Scrubbing for CO 2 Capture, Science (80-.). 325 (2009) 1652. doi:10.1126/science.1176731.

[13]   D.W. Sturgeon, E.D. Cameron, F.D. Fitzgerald, C. McGhie, Demonstration of the Doosan Power Systems 40MWt OxyCoal^{TM} combustion system, Energy Procedia. 4 (2011) 933–940. doi:10.1016/j.egypro.2011.01.139.

[14]   J.C. Abanades, E.J. Anthony, J. Wang, J.E. Oakey, Fluidized Bed Combustion Systems Integrating CO2 Capture with CaO, Environ. Sci. Technol. 39 (2005) 2861–2866. doi:10.1021/es0496221.

[15]   I. Vorrias, K. Atsonios, A. Nikolopoulos, N. Nikolopoulos, P. Grammelis, E. Kakaras, Calcium looping for CO2 capture from a lignite fired power plant, Fuel. 113 (2013) 826–836. doi:http://dx.doi.org/10.1016/j.fuel.2012.12.087.

[16]   J.C. Abanades, G. Grasa, M. Alonso, N. Rodriguez, E.J. Anthony, L.M. Romeo, Cost Structure of a Postcombustion CO2 Capture System Using CaO, Environ. Sci. Technol. 41 (2007) 5523–5527. doi:10.1021/es070099a.

[17]   C. Hawthorne, M. Trossmann, P. Galindo Cifre, a. Schuster, G. Scheffknecht, Simulation of the carbonate looping power cycle, Energy Procedia. 1 (2009) 1387–1394. doi:10.1016/j.egypro.2009.01.182.

[18]   J. Ströhle, A. Lasheras, A. Galloy, B. Epple, Simulation of the Carbonate Looping Process for Post-Combustion CO_2 Capture from a Coal-Fired Power Plant, Chem. Eng. Technol. 32 (2009) 435–442. doi:10.1002/ceat.200800569.

[19]   A. Lasheras, J. Ströhle, A. Galloy, B. Epple, Carbonate looping process simulation using a 1D fluidized bed model for the carbonator, Int. J. Greenh. Gas Control. 5 (2011) 686–693.

[20]   I. Martínez, R. Murillo, G. Grasa, J.C. Abanades, Integration of a Ca Looping System for CO 2 Capture in Existing Power Plants, AIChE J. 57 (2011) 2599–2607. doi:10.1002/aic12461.

[21]   L.M. Romeo, J.C. Abanades, J.M. Escosa, J. Paño, A. Giménez, A. Sánchez-Biezma, et al., Oxyfuel carbonation/calcination cycle for low cost CO_2 capture in existing power plants, Energy Convers. Manag. 49 (2008) 2809–2814. http://www.sciencedirect.com/science/article/pii/S0196890408001179.

[22]   L.M. Romeo, Y. Lara, P. Lisbona, A. Martínez, Economical assessment of competitive enhanced limestones for CO_2 capture cycles in power plants, Fuel Process. Technol. 90 (2009) 803–811. doi:http://dx.doi.org/10.1016/j.fuproc.2009.03.014.

[23]   L.M. Romeo, Y. Lara, P. Lisbona, J.M. Escosa, Optimizing make-up flow in a CO_2 capture system using CaO, Chem. Eng. J. 147 (2009) 252–258. doi:http://dx.doi.org/10.1016/j.cej.2008.07.010.

[24]   J.-M. Amann, M. Kanniche, C. Bouallou, Natural gas combined cycle power plant modified into an O_2/CO_2 cycle for CO_2 capture, Energy Convers. Manag. 50 (2009) 510–521. doi:http://dx.doi.org/10.1016/j.enconman.2008.11.012.

[25]   M. Anheden, G. Svedberg, Exergy analysis of chemical-looping combustion systems, Energy Convers. Manag. 39 (1998) 1967–1980. doi:10.1016/S0196-8904(98)00052-1.

[26]   V. Kempkes, A. Kather, Thermodynamic analysis of a base case coal-fired Chemical Looping Combustion power plant, in: Second Int. Conf. Energy Process Eng., Frankfurt (M), Germany, 2011.

[27]   N. Poboß, A. Schuster, G. Scheffknecht, Machbarkeitsstudie für das Carbonate Looping verfahren zur CO2 Abscheidung aus Kraftwerksabgasen, 2008.

[28]   F.H. Smyth, L.H. Adams, The system, Calcium oxide- Carbon dioxide, J. Am. Chem. Soc. 45 (1923) 1167–1184. doi:10.1021/ja01658a009.

[29]   T. Shimizu, T. Hirama, H. Hosoda, K. Kitano, M. Inagaki, K. Tejima, A Twin Fluid-Bed Reactor for Removal of CO_2 from Combustion Processes, Chem. Eng. Res. Des. 77 (1999) 62–68.

[30]   J.C. Abanades, The maximum capture efficiency of CO_2 using a carbonation/calcination cycle of $CaO/CaCO_3$, Chem. Eng. J. 90 (2002) 303–306. doi:http://dx.doi.org/10.1016/S1385-8947(02)00126-2.

[31]   S.K. Bhatia, D.D. Perlmutter, Effect of the product layer on the kinetics of the CO_2-lime reaction, AIChE J. 29 (1983) 79–86. doi:10.1002/aic.690290111.

[32]   D. Alvarez, M. Peña, A.G. Borrego, Behavior of Different Calcium-Based Sorbents in a Calcination/Carbonation Cycle for CO_2 Capture, Energy & Fuels. 21 (2007) 1534–1542. doi:10.1021/ef060573i.

[33]   G.S. Grasa, J.C. Abanades, CO_2 Capture Capacity of CaO in Long Series of Carbonation/Calcination

Cycles, Ind. Eng. Chem. Res. 45 (2006) 8846–8851. doi:10.1021/ie0606946.

[34]   A. Charitos, N. Rodríguez, C. Hawthorne, M. Zieba, B. Arias, G. Kopanakis, et al., Experimental Validation of the Calcium Looping CO 2 Capture Process with Two Circulating Fluidized Bed Carbonator Reactors, Ind. Eng. Chem. Res. 50 (2011) 9685–9695.

[35]   N. Rodriguez, M. Alonso, G. Grasa, J.C. Abanades, Heat requirements in a calciner of CaCO3 integrated in a CO2 capture system using CaO, Chem. Eng. J. 138 (2008) 148–154. doi:http://dx.doi.org/10.1016/j.cej.2007.06.005.

[36]   J. Blamey, E.J. Anthony, J. Wang, P.S. Fennell, The calcium looping cycle for large-scale CO2 capture, Prog. Energy Combust. Sci. 36 (2010) 260–279. doi:10.1016/j.pecs.2009.10.001.

[37]   R.W. Hughes, D. Lu, E.J. Anthony, Y. Wu, Improved Long-Term Conversion of Limestone-Derived Sorbents for In Situ Capture of CO2 in a Fluidized Bed Combustor, Ind. Eng. Chem. Res. 43 (2004) 5529–5539. doi:10.1021/ie034260b.

[38]   W. Wang, S. Ramkumar, S. Li, D. Wong, M. Iyer, B.B. Sakadjian, et al., Subpilot Demonstration of the Carbonation−Calcination Reaction (CCR) Process: High-Temperature CO2 and Sulfur Capture from Coal-Fired Power Plants, Ind. Eng. Chem. Res. 49 (2010) 5094–5101. doi:10.1021/ie901509k.

[39]   C.C. Dean, J. Blamey, N.H. Florin, M.J. Al-Jeboori, P.S. Fennell, The calcium looping cycle for CO2 capture from power generation, cement manufacture and hydrogen production, Chem. Eng. Res. Des. 89 (2011) 836–855. http://www.sciencedirect.com/science/article/pii/S0263876210003047.

[40]   S. Sivalingam, S. Gleis, H. Spliethoff, C. Hawthorne, A. Charitos, G. Scheffknecht, Analysis and Comparison of Reactivity and CO[sub 2] Capture Capacity of Fresh Calcium-Based Sorbents and Samples From a Lab-Scale Dual Fluidized Bed Calcium Looping Facility, J. Eng. Gas Turbines Power. 133 (2011) 71705. doi:10.1115/1.4002683.

[41]   N.H. Florin, A.T. Harris, Enhanced hydrogen production from biomass with in situ carbon dioxide capture using calcium oxide sorbents, Chem. Eng. Sci. 63 (2008) 287–316. doi:10.1016/j.ces.2007.09.011.

[42]   D.Y. Lu, R.W. Hughes, E.J. Anthony, Ca-based sorbent looping combustion for CO 2 capture in pilot-scale dual fluidized beds, Fuel Process. Technol. 89 (2008) 1386–1395. doi:10.1016/j.fuproc.2008.06.011.

[43]   A. Charitos, C. Hawthorne, A.R. Bidwe, S. Sivalingam, A. Schuster, H. Spliethoff, et al., Parametric investigation of the calcium looping process for CO2 capture in a 10kWth dual fluidized bed, Int. J. Greenh. Gas Control. 4 (2010) 776–784. doi:10.1016/j.ijggc.2010.04.009.

[44]   A. Charitos, Experimental Characterization of the Ca-looping Process for CO2 Capture, Universität Stuttgart, 2013.

[45]   G. Duelli, I. Papandreou, A.R. Bidwe, V. Stack Lara, H. Dieter, G. Scheffknecht, Calcium Looping Process for CO2 capture: Experimental characterization of the regenerator operation under oxy-fuel conditions, in a 10kWth dual fluidized bed facility., in: CCT, Tsaloniki, Greece, 2013.

[46]   D. Alvarez, J.C. Abanades, Determination of the Critical Product Layer Thickness in the Reaction of CaO with CO2, Ind. Eng. Chem. Res. 44 (2005) 5608–5615.

[47]   M. Alonso, N. Rodríguez, B. González, G. Grasa, R. Murillo, J.C. Abanades, Carbon dioxide capture from combustion flue gases with a calcium oxide chemical loop. Experimental results and process development, Int. J. Greenh. Gas Control. 4 (2010) 167–173. http://www.sciencedirect.com/science/article/pii/S1750583609001145.

[48]   A. Charitos, C. Hawthorne, A.R. Bidwe, H. Holz, T. Pfeifer, A. Schulze, et al., Parametric study on the CO2 capture efficiency of the carbonate looping process in a 10 kWth dual fluidized bed, in: 20 Th Int. Conf. Fluid. Bed Combust., Xian, China, 2008.

[49]   F. Fang, Z. Li, N. Cai, Continuous CO2 Capture from Flue Gases Using a Dual Fluidized Bed Reactor with Calcium-Based Sorbent, Ind. Eng. Chem. Res. 48 (2009) 11140–11147. doi:10.1021/ie901128r.

[50]   S. Plötz, A. Bayrak, A. Galloy, J. Kremer, M. Orth, M. Wieczorek, et al., First carbonate looping experiments with a 1 mwth test facility consisting of two interconnected CFBs, in: 21st Int. Conf. Fluid. Bed Combust., Naples (Italy), 2012: pp. 421–428.

[51]   C. Hawthorne, H. Dieter, Bidwe, A. Schuster, G. Scheffknecht, S. Unterberger, et al., CO2 capture with CaO in a 200 kWth dual fluidized bed pilot plant, Energy Procedia. 4 (2011) 441–448. doi:10.1016/j.egypro.2011.01.073.

[52]   H. Dieter, C. Hawthorne, A.R. Bidwe, M. Zieba, G. Scheffknecht, The 200 kWth dual fluidized bed calcium looping pilot plant for efficient CO2 capture: plant operating experiences and results, in: 21st Int. Conf. Fluid. Bed Combust., Naples (Italy), 2012: pp. 397–404.

[53]   H. Hofbauer, Scale Up of Fluidized Bed Gasifiers from Laboratory Scale to Commercial Plants : Steam Gasification of Solid Biomass in a Dual Fluidized Bed System, in: F. Winter (Ed.), 19th Int. Conf. Fluid. Bed Combust., Vienna/ Austria, 2006.

[54]   S. Wu, J. Gu, L. Li, Y. Wu, J. Gao, The Reactivity and Kinetics of Yanzhou Coal Chars from Elevated Pyrolysis Temperatures During Gasification in Steam at 900–1200°C, Process Saf. Environ. Prot. 84 (2006) 420–428. doi:http://dx.doi.org/10.1205/psep06031.

[55]   G.P. Curran, C.E. Fink, G. Everett, CO2 Acceptor Gasification Process, in: Fuel Gasif., American Chemical Society, 1967: pp. 141–165. doi:doi:10.1021/ba-1967-0069.ch010.

[56]   M. Mahishi, D. Goswami, An experimental study of hydrogen production by gasification of biomass in the presence of a CO2CO2 sorbent, Int. J. Hydrogen Energy. 32 (2007) 2803–2808. doi:10.1016/j.ijhydene.2007.03.030.

[57]   S. Lin, M. Harada, Y. Suzuki, H. Hatano, Continuous experiment regarding hydrogen production by coal/CaO reaction with steam (I) gas products, Fuel. 83 (2004) 869–874. doi:http://dx.doi.org/10.1016/j.fuel.2003.10.030.

[58]   C. Pfeifer, B. Puchner, H. Hofbauer, In-Situ CO 2 -Absorption in a Dual Fluidized Bed Biomass Steam Gasifier to Produce a Hydrogen Rich Syngas, Int. J. Chem. React. Eng. 5 (2007) 1–13.

[59]   N. Poboss, K. Swiecki, A. Charitos, C. Hawthorne, M. Zieba, G. Scheffknecht, Experimental investigation of the absorption enhanced reforming of biomass in a 20 kWth dual fluidized bed system, Int. J. Thermodyn. 15 (2012) 53–59. doi:10.5541/ijot.321.

[60]   J. Corella, J.M. Toledo, G. Molina, A review on dual fluidized-bed biomass gasifiers, Ind. Eng. Chem. Res. 46 (2007) 6831–6839.

[61]   J. Corella, J.M. Toledo, G. Molina, Biomass gasification with pure steam in fluidised bed : 12 variables that affect the effectiveness of the biomass gasifier, Int. J. Oil, Gas Coal Technol. 1 (2008) 194–207.

[62]   G. Soukup, C. Pfeifer, A. Kreuzeder, H. Hofbauer, In Situ CO2 Capture in a Dual Fluidized Bed Biomass Steam Gasifier – Bed Material and Fuel Variation, Chem. Eng. Technol. 32 (2009) 348–354. http://dx.doi.org/10.1002/ceat.200800559.

[63]   N. Poboss, K. Swiecki, A. Charitos, C. Hawthorne, M. Zieba, G. Scheffknecht, Experimental investigation of the absorption enhanced reforming of biomass in a 20 kW th dual fluidized bed system, in: 23rd ECOS Concerence, Lausanne, Switzerland, 2010.

[64]   C. Pfeifer, S. Koppatz, H. Hofbauer, Steam gasification of various feedstocks at a dual fluidised bed gasifier: Impacts of operation conditions and bed materials, Biomass Convers. Biorefinery. 1 (2011) 39–53. doi:10.1007/s13399-011-0007-1.

[65]   N. Poboss, M. Zieba, G. Scheffknecht, Experimental investigation of affecting parameters on the gasification of biomass fuels in a 20 kWth dual fluidized bed, in: ICPS 7, Leipzig, 2010.

[66]   C. Hawthorne, N. Poboss, H. Dieter, A. Gredinger, M. Zieba, G. Scheffknecht, Operation and results of a 200-kWth dual fluidized bed pilot plant gasifier with adsorption-enhanced reforming, Biomass Convers. Biorefinery. 2 (2012) 217–227. doi:10.1007/s13399-012-0053-3.

[67]   B. Acharya, P. Basu, A. Dutta, Circulating fluidized bed based calcium looping gasification of biomass for hydrogen enriched gas production, in: 21st Int. Conferance Fluid. Bed Combust., Naples (Italy), 2012: pp. 736–743.

[68]   C. Pfeifer, B. Puchner, H. Hofbauer, Comparison of dual fluidized bed steam gasification of biomass with and without selective transport of CO2, Chem. Eng. Sci. 64 (2009) 5073–5083. http://www.sciencedirect.com/science/article/pii/S00092509005600.

[69]   S. Koppatz, C. Pfeifer, R. Rauch, H. Hofbauer, T. Marquard-Moellenstedt, M. Specht, H2 rich product gas by steam gasification of biomass with in situ CO2 absorption in a dual fluidized bed system of 8 MW fuel input, Fuel Process. Technol. 90 (2009) 914–921. http://www.sciencedirect.com/science/article/pii/S0378382009000708.

[70]   A. Nikolopoulos, N. Nikolopoulos, A. Charitos, P. Grammelis, E. Kakaras, A.R. Bidwe, et al., Numerical investigation and experimental validation of an isothermal CFD model developed for a CFB carbonator ., in: 21st Int. Conf. Fluid. Bed Combust., Naples (Italy), 2012: pp. 1042–1049.

[71]   A. Charitos, C. Hawthorne, A.R. Bidwe, L. Korovesis, A. Schuster, G. Scheffknecht, Hydrodynamic analysis of a 10kWth Calcium Looping Dual Fluidized Bed for post-combustion CO2 capture, Powder Technol. 200 (2010) 117–127. doi:10.1016/j.powtec.2010.02.012.

[72]   A.R. Bidwe, Scaled Cold Model Investigation Of a Dual Fluidised Bed System For The Post-combustion, University of Stuttgart, 2007. doi:2873.

[73]   L.R. Glicksman, Scaling Relationships for fluidized beds, Chem. Eng. Sci. 39 (1984) 1373–1379.

[74]   L.R. Glicksman, Scaling relationships for fluidized beds, Chem. Eng. Sci. 43 (1988) 1419–1421.

[75]   L.R. Glicksman, M. Hyre, P.A. Farrell, Dynamic Similarity in fluidization, Int. J. Multiph. Flow. 20 (1994) 331–386.

[76]   M. Horio, A. Nonaka, Y. Sawa, I. Muchi, A new similarity rule for fluidized bed scale-up, AIChE J. 32 (1986) 1466–1482. http://dx.doi.org/10.1002/aic.690320908.

[77]   F. Winkler, Verfahren zum Herstellen von Wasserglas, DE 437 970, 1922.

[78]   Y. Chen, Evolution of FCC – past present and future – and the challenges of operating a high-temperature CFB system, in: T.M. Knowlton (Ed.), 10 Th Int. Conf. Circ. Fluid. Bed Technol. Fluid. Technoloy-(CFB - 10), Sun River, Oregon USA, 2011: pp. 58–85.

[79]   D. Kunii, O. Levenspeil, Fluidization engineering, 2 nd, Butterworth-Heinemann, 1991.

[80]   G.P. van der Laan, Kinetics , Selectivity and Scale Up of the Fischer-Tropsch Synthesis, University of Groningen, Netherland, 1999.

[81]   S. Kavidass, G.L. Anderson, G.S. Norton, Why Build a Circulating Fluidized Bed Boiler to Generate Steam and Electric Power, in: POWER-GEN Asia 2000, Bangkok, Thailand, 2000: pp. 1–7.

[82]   P. Basu, Combustion of coal in circulating fluidized-bed boilers: a review, Chem. Eng. Sci. 54 (1999) 5547–5557. doi:10.1016/S0009-2509(99)00285-7.

[83]   F. Winter, Formation and Reduction of Pollutants in CFBC : From Heavy Metals , Particulates , Alkali , NOx , N2O , SOx , HCl, in: G. Yue, H. Zhang, Z. Luo (Eds.), 20 Th Int. Conf. Fluid. Bed Combust., Tsinghua University Press, Beijing and Springer, Xian, China, 2009: pp. 43–48.

[84]   ALSTOM- A World Leader in Power Solutions for Enhanced Profitability, (2001).

[85]   A. Hotta, Foster wheelrs solutions for large scale CFB boiler technology : Features and operational performance of Łagisza 460 MWe CFB boiler, in: 20 Th Int. Conf. Fluid. Bed Combust., Tsinghua University Press, Beijing and Springer, Xian, China, 2009: pp. 59–70.

[86]   Z. Fan, A. Roberson, S. Goidich, 800 MWe Circulating Fluidized Bed Boiler with 1300 ° F Supercritical Steam, in: 33rd Int. Tech. Conf. Coal Util. Fuel Syst., Clearwater, Florida USA, 2008.

[87]   G.X. Yue, H.R. Yang, J.F. Lu, H. Zhang, Latest development of CFB boilers in china, in: G. Yue, H. Zhang, C. Zhao, Z. Luo (Eds.), 20 Th Int. Conf. Fluid. Bed Combust., Tsinghua University Press, Beijing and Springer, Xian, China, 2009: pp. 3–12.

[88]   Outotec, Alumina and aluminium technologies Proven technologies for the aluminium industry, (2011).

[89]   J. Baeyens, P. Cuvelier, D. Geldart, The development, design and operation of a fluidized limestone calciner, Zement- Kalk- Gips. (1989).

[90]   F. Niu, J. Haslam, R. Rajewski, B. Subramaniam, A fluidized-bed coating technology using near-critical carbon dioxide as fluidizing and drying medium, J. Supercrit. Fluids. 66 (2012) 315–320. doi:10.1016/j.supflu.2011.11.007.

[91]   W.R.W. Daud, Fluidized Bed Dryers — Recent Advances, Adv. Powder Technol. 19 (2008) 403–418. doi:10.1016/S0921-8831(08)60909-7.

[92]   L. Mörl, S. Heinrich, M. Peglow, Fluidized Bed Spray Granulation, in: A.D. Salman, M.J. Hounstow, J.P.K. Seville (Eds.), Granulation, Elsevier B.V., 2007: pp. 21–188.

[93]   J.R. Grace, Fluidized bed hydrodynamics, in: G. Hestroni (Ed.), Handb. Multiph. Syst., Hemishpere, Washigton D.C., 1982.

[94]   A.R. Abrahamsen, D. Geldart, Behaviour of gas-fluidized beds of fine powders part I. Homogeneous expansion, Powder Technol. 26 (1980) 35–46. http://www.sciencedirect.com/science/article/pii/0032591080850054.

[95]   R.K. Singh, G.K. Roy, Prediction of minimum bubbling velocity, fluidization index and range of particulate fluidization for gas–solid fluidization in cylindrical and non-cylindrical beds, Powder Technol. 159 (2005)

168–172. http://www.sciencedirect.com/science/article/pii/S0032591005003669.

[96]   J. Yerushalmi, N.T. Cankurt, Further studies of the regimes of fluidization, Powder Technol. 24 (1979) 187–205. http://www.sciencedirect.com/science/article/pii/0032591079870369.

[97]   H. Bi, L.-S. Fan, Existence of turbulent regime in gas-solid fluidization, AIChE J. 38 (1992) 297–301. doi:10.1002/aic.690380216.

[98]   Z. Jesse, Circulating turbulent fluidization—A new fluidization regime or just a transitional phenomenon, Particuology. 8 (2010) 640–644. http://www.sciencedirect.com/science/article/pii/S167420011000146X.

[99]   L. Reh, Fluidized bed processing, Chem. Eng. Prog. 67 (1971) 58–63.

[100]   H.T. Bi, J.R. Grace, Flow regime diagrams for gas-solid fluidization and upward transport, Int. J. Multiph. Flow. 21 (1995) 1229–1236. doi:http://dx.doi.org/10.1016/0301-9322(95)00037-X.

[101]   C.A. Perez-Pulido, Application of Hydrodynamic and Kinetic Models to Design a CaO-based Circulating Fluidized Bed CO2 Dry Scrubber for the Post-Combustion Capture of Carbon Dioxide from Flue Gas, in: IVD, Univ. Stuttgart Master Thesis No 2872, 2008.

[102]   D. Geldart, The effect of particle size and size distribution on the behaviour of gas-fluidised beds, Powder Technol. 6 (1972) 201–215. doi:http://dx.doi.org/10.1016/0032-5910(72)83014-6.

[103]   J.R. Grace, T.M. Knowlton, J. Werther, Lecture notes - Fluidization, Engineering conferances international, 2011.

[104]   W. Namkung, S.W. Kim, S.D. Kim, Flow regimes and axial pressure profiles in a circulating fluidized bed, Chem. Eng. J. 72 (1999) 245–252.

[105]   S. Malcus, G. Chaplin, T. Pugsley, The hydrodynamics of the high-density bottom zone in a CFB riser analyzed by means of electrical capacitance tomography (ECT), Chem. Eng. Sci. 55 (2000) 4129–4138. doi:10.1016/S0009-2509(00)00083-X.

[106]   H. Zhu, J. Zhu, Characterization of fluidization behavior in the bottom region of CFB risers, Chem. Eng. J. 141 (2008) 169–179. doi:10.1016/j.cej.2007.12.015.

[107]   Pugsley. Tod S., F. Berruti, A predictive hydrodynamic model for circulating fluidized bed risers, Powder Technol. 89 (1996) 57–69.

[108]   S. Gupta, Evaluation of the gas–solid suspension density in CFB risers with exit effects, Powder Technol. 108 (2000) 21–31. doi:10.1016/S0032-5910(99)00199-0.

[109]   W.-C. Yang, Handbook of fluidization and fluid-particle systems, Marcel Dekker Inc., 2003.

[110]   A. Gungor, N. Eskin, Hydrodynamic modeling of a circulating fluidized bed, Powder Technol. 172 (2007) 1–13. doi:http://dx.doi.org/10.1016/j.powtec.2006.10.035.

[111]   P. Kaushal, Modelling of the fast fluidized combustion reactor of a dual fluidized bed biomass gasificaition system, TU Wien, 2006.

[112]   R.W. Breault, V.K. Mathur, High-velocity fluidized-bed hydrodynamic modeling. 1. Fundamental studies of pressure drop, Ind. Eng. Chem. Res. 28 (1989) 684–688. doi:10.1021/ie00090a006.

[113]   R.W. Breault, V.K. Mathur, High-velocity fluidized-bed hydrodynamic modeling. 2. Circulating bed pressure drop modeling, Ind. Eng. Chem. Res. 28 (1989) 688–693. doi:10.1021/ie00090a007.

[114]   C. Zhu, J. You, An energy-based model of gas–solid transport in a riser, Powder Technol. 175 (2007) 33–42. doi:10.1016/j.powtec.2006.12.022.

[115]   A. Rautiainen, G. Stewart, V. Poikolainen, P. Sarkomaa, An experimental study of vertical pneumatic conveying, Powder Technol. 104 (1999) 139–150.

[116]   W.H. and J.Z. Qi, Xiaobo, Friction between co-current upward gas – solid flow and column wall, Asia-Pacific J. Chem. Eng. 3 (2008) 307–319. doi:10.1002/apj.

[117]   A. Rautiainen, P. Sarkomaa, Solids friction factors in upward, lean gas-solids flows, Powder Technol. 95 (1998) 25–35. doi:10.1016/S0032-5910(97)03312-3.

[118]   U. Arena, A. Cammarota, L. Pistone, High velocity fluidization behaviour of solids ina laboratory scale circulating bed, in: 1st Int. Conf. Circ. Fluid. Bed Technol., 1986: pp. 119–125.

[119]   E.-U. Hartge, Y. Li, J. Werther, Analysis of the local structure of the two phase flow in a fast fluidized bed, in: 1st Int. Conf. Circ. Fluid. Bed Technol., 1986: pp. 153–161.

[120]   W.P.M. Van Swaaij, C. Buurman, J.W. van Bruegel, Shear stresses on the wall of a dense gas—solids riser, Chem. Eng. Sci. 25 (1970) 1818–1820.

[121]   A.S. Issangya, Flow dynamics in high density circulating fluidized beds, The University of British Columbia, Canada, 1998.

[122]   E. Johansson, A. Lyngfelt, T. Mattisson, F. Johnsson, Gas leakage measurements in a cold model of an interconnected fluidized bed for chemical-looping combustion, Powder Technol. 134 (2003) 210–217. doi:10.1016/S0032-5910(03)00125-6.

[123]   X.T. Bi, X. Liu, High density and high solids flux CFB risers for steam gasification of solids fuels, Fuel Process. Technol. 91 (2010) 915–920. doi:10.1016/j.fuproc.2009.12.011.

[124]   C. Fushimi, G. Guan, M. Ishizuka, Y. Nakamura, A. Tsutsumi, Y. Suzuki, et al., High-flux triple bed circulating fluidized bed (TBCFB) gasifier for exergy recuperative IGCC/IGFC, in: T.M. Knowlton (Ed.), Proc. Tenth Intenational Conferance Circ. Fluid. Beds Fluid. Technol. CFB 10, 2011: pp. 193–200.

[125]   G. Guan, C. Fushimi, M. Ikeda, Y. Nakamura, A. Tsutsumi, T. Suda, et al., Flow behaviors in a high solid flux circulating fluidized bed composed of a riser , a downer and a bubbling fluidized bed, in: Fluid. XIII, Engineering conferances international, Gyeong-ju, Korea, 2011.

[126]   N. Armbrust, A.R. Bidwe, Cold Model Investigation of a Triple Fluidized Bed Gasification Process for Production of Hydrogen Rich Syngas from Biomass, in: 11th Int. Conf. Fluid. Bed Technol., 2014.

[127]   A. Abad, J. Adánez, F. García-Labiano, L.F. de Diego, P. Gayán, J. Celaya, Mapping of the range of operational conditions for Cu-, Fe-, and Ni-based oxygen carriers in chemical-looping combustion, Chem. Eng. Sci. 62 (2007) 533–549. doi:10.1016/j.ces.2006.09.019.

[128]   J.-S. Kim, R. Tachino, A. Tsutsumi, Effects of solids feeder and riser exit configuration on establishing high density circulating fluidized beds, Powder Technol. 187 (2008) 37–45. doi:10.1016/j.powtec.2008.01.002.

[129]   K. Smolders, J. Baeyens, The operation of L-valves to control standpipe flow, Adv. Powder Technol. 6 (1995) 163–176. doi:10.1016/S0921-8831(08)60525-7.

[130]   U. Arena, C.B. Langeli, A. Cammarota, L-valve behaviour with solids of different size and density, Powder Technol. 98 (1998) 231–240.

[131]   D. Geldart, P. Jones, Geldart & Jones L -valve 1991.pdf, Powder Technol. 67 (1991) 163–174.

[132]   L. Cheng, P. Basu, Effect of pressure on loop seal operation for a pressurized circulating fluidized bed, Powder Technol. 103 (1999) 203–211. doi:10.1016/S0032-5910(99)00018-2.

[133]   P. Basu, J. Butler, Studies on the operation of loop-seal in circulating fluidized bed boilers, Appl. Energy. 86 (2009) 1723–1731. doi:10.1016/j.apenergy.2008.11.024.

[134]   S.W. Kim, W. Namkung, S.D. Kim, Solids flow characteristics in loop-seal of a circulating fluidized bed, Korean J. Chem. Eng. 16 (1999) 82–88. doi:10.1007/BF02699009.

[135]   M. Orth, J. Ströhle, B. Epple, Design and operation of a coal-fired 1 MWth chemical looping pilot plant, in: 2nd Int. Conf. Chem. Looping, Darmstadt, Germany, 2012.

[136]   T. Pröll, P. Kolbitsch, J. Bolhàr-Nordenkampf, H. Hofbauer, A novel dual circulating fluidized bed system for chemical looping processes, AIChE J. 55 (2009) 3255–3266. http://dx.doi.org/10.1002/aic.11934.

[137]   Y.D. Kim, B.J. Kim, J.H. Moon, W. Yang, U. Do Lee, C. Won, et al., Test of a pilot scale biomass gasifier based on a dual fluidized bed system, in: 21st Int. Conf. Fluid. Bed Combust., Naples (Italy), 2012: pp. 775–780.

[138]   N. Berguerand, A. Lyngfelt, Design and operation of a 10kWth chemical-looping combustor for solid fuels – Testing with South African coal, 2008. doi:10.1016/j.fuel.2008.03.008.

[139]   B. Arstad, R. Blom, E. Bakken, I. Dahl, J.P. Jakobsen, P. Røkke, Sorption-enhanced methane steam reforming in a circulating fluidized bed reactor system, Energy Procedia. 1 (2009) 715–720.

[140]   T. Pröll, K. Rupanovits, P. Kolbitsch, J. Bolhàr-Nordenkampf, H. Hofbauer, Cold Flow Model Study on a Dual Circulating Fluidized Bed (DCFB) System for Chemical Looping Processes, Chem. Eng. Technol. 32 (2009) 418–424. http://dx.doi.org/10.1002/ceat.200800521.

[141]   A.R. Bidwe, F. Mayer, C. Hawthorne, A. Charitos, A. Schuster, G. Scheffknecht, Use of ilmenite as an oxygen carrier in chemical looping combustion-batch and continuous dual fluidized bed investigation, Energy Procedia. 4 (2011) 433–440. doi:10.1016/j.egypro.2011.01.072.

[142]   A. Thon, M. Kramp, E.-U. Hartge, S. Heinrich, J. Werther, Operational experience with a coupled fluidized bed system for chemical looping combustion of solid fuels, in: 2nd Int. Conf. Chem. Looping, Darmstadt, Germany, 2012.

[143]   P. Markström, A. Lyngfelt, C. Linderholm, Chemical looping combustion ina a 100 kW unit for solid fuels, in: 21st Int. Conferance Fluid. Bed Combust., Naples (Italy), 2012: pp. 285–292.

[144]   Facilities at CSIC Zaragoza, (n.d.). http://www.icb.csic.es/index.php?id=147&L=1.

[145]   T. Sozinho, W. Pelletant, H. Stainton, F. Guillou, T. Gauthier, Main results of the 10 kW th pilot plant operation, in: B. Epple (Ed.), 2nd Int. Conf. Chem. Looping, Darmstadt, Germany, 2012: pp. 26–28.

[146]   L. Shen, J. Xiao, F. Niklasson, F. Johnsson, Biomass mixing in a fluidized bed biomass gasifier for hydrogen production, Chem. Eng. Sci. 62 (2007) 636–643.

[147]   Q. Wang, Z. Luo, M. Fang, M. Ni, K. Cen, Development of a new external heat exchanger for a circulating fluidized bed boiler, Chem. Eng. Process. 42 (2003) 327–335.

[148]   J.F. Davidson, D.R.M. Jones, The flow of particles from a fluidized bed through an orifice, Rheol. Acta. 4 (1965) 180–192.

[149]   M. Yazdanpanah, A. Hoteit, A. Forret, T. Gauthier, U.H. Poincaré, Gas tracer study in a non mechanical L-valve, in: T.M. Knowlton (Ed.), Proc. Tenth Intenational Conferance Circ. Fluid. Beds Fluid. Technol. CFB 10, 2011: pp. 98–105.

[150]   M.K. Karmakar, A.B. Datta, Hydrodynamics of a dual fluidized bed gasifier, Adv. Powder Technol. 21 (2010) 521–528.

[151]   H.-J. Ryu, Y.-C. Park, S.-H. Jo, M.-H. Park, Development of novel two-interconnected fluidized bed system, Korean J. Chem. Eng. 25 (2009) 1178–1183. doi:10.1007/s11814-008-0194-z.

[152]   A. Bischi, Ø. Langørgen, J.-X. Morin, J. Bakken, M. Ghorbaniyan, M. Bysveen, et al., Hydrodynamic viability of chemical looping processes by means of cold flow model investigation, Appl. Energy. 97 (2012) 201–216.

[153]   T. Pröll, K. Mayer, J. Bolhàr-Nordenkampf, P. Kolbitsch, T. Mattisson, A. Lyngfelt, et al., Natural minerals as oxygen carriers for chemical looping combustion in a dual circulating fluidized bed system, Energy Procedia. 1 (2009) 27–34. http://www.sciencedirect.com/science/article/pii/S1876610209000071.

[154]   D.C. Guío-Pérez, G. Tondl, W. Höltl, T. Pröll, H. Hofbauer, Cold Flow Model Study of an Oxyfuel Combustion Pilot Plant, Chem. Eng. Technol. 34 (2011) 2091–2098. http://dx.doi.org/10.1002/ceat.201100160.

[155]   L.R. Glicksman, M. Hyre, K. Woloshun, Simplified scaling relationships for fluidized beds, Powder Technol. 77 (1993) 177–199. doi:10.1016/0032-5910(93)80055-F.

[156]   R. Kehlenbeck, Scaling of a 500 kWth pilot plant with integrated circulating fluidized bed for the generation of a hydrogen-rich gas from biomass steam gasification and fluid dynamic investigations of a cold model, TU Wien, 2000.

[157]   J.M. Matsen, Scale-up of fluidized bed processes: Principle and practice, Powder Technol. 88 (1996) 237–244. http://www.sciencedirect.com/science/article/pii/S0032591096031269.

[158]   R. Kehlenbeck, J. Yates, R. Di Felice, H. Hofbauer, R. Rauch, Novel scaling parameter for circulating fluidized beds, AIChE J. 47 (2001) 582–589. http://dx.doi.org/10.1002/aic.690470308.

[159]   U. Lee, I. Choi, J. Song, W. Yang, Y. Kim, Y. Choi, Hydrodynamics of dual fluidized bed systems with internal mixing channels between circulating and bubbling fluidized bed reactors, in: Proc. Tenth Intenational Conferance Circ. Fluid. Beds Fluid. Technol. CFB 10, 2011: pp. 114–120.

[160]   P.U. Foscolo, A. Germanà, N. Jand, S. Rapagnà, Design and cold model testing of a biomass gasifier consisting of two interconnected fluidized beds, Powder Technol. 173 (2007) 179–188. http://www.sciencedirect.com/science/article/pii/S0032591007000186.

[161]   A. Bischi, Chemical looping reactor system design, Norwegian University of Science and Technology - Trondheim, 2012.

[162]   A. Thon, M. Kramp, E.U. Hartge, S. Heinrich, J. Werther, Coupled fluidized bed system for chemical -

looping combustion : Cold model investigation of the operational behaviour, in: 21st Int. Conferance Fluid. Bed Combust., Naples (Italy), 2012: pp. 293–300.

[163]   Y. Cao, S.P. Sit, W. Pan, The development of 10-KW Chemical Looping Combustion Technology in ICSET , WKU, in: B. Epple (Ed.), 2nd Int. Conf. Chem. Looping, Darmstadt, Germany, 2012: pp. 26–28.

[164]   G.A. Ryabov, O.M. Folomeyev, D.A. Sankin, K. V Khaneyev, Cold flow model study on interconnected fluidized bed reactors for multi-generation systems and chemical looping processes, in: T.M. Knowlton (Ed.), Proc. Tenth Intenational Conferance Circ. Fluid. Beds Fluid. Technol. CFB 10, 2011: pp. 169–176.

[165]   M.M. Yazdanpanah, a. Forret, T. Gauthier, a. Delebarre, An experimental investigation of L-valve operation in an interconnected circulating fluidized bed system, Powder Technol. 221 (2012) 236–244. doi:10.1016/j.powtec.2012.01.007.

[166]   S. Rifflart, A. Hoteit, M.M. Yazdanpanah, W. Pelletant, K. Surla, Construction and operation of a 10 kW CLC unit with circulation configuration enabling independent solid flow control, Energy Procedia. 4 (2011) 333–340. doi:10.1016/j.egypro.2011.01.059.

[167]   N. Rodríguez, M. Alonso, J.C. Abanades, A. Charitos, C. Hawthorne, G. Scheffknecht, et al., Comparison of experimental results from three dual fluidized bed test facilities capturing CO2 with CaO, Energy Procedia. 4 (2011) 393–401. doi:10.1016/j.egypro.2011.01.067.

[168]   L.E. Ersoy, M.R. Golriz, M. Koksal, F. Hamdullahpur, Circulating fluidized bed hydrodynamics with air staging: an experimental study, Powder Technol. 145 (2004) 25–33. doi:10.1016/j.powtec.2004.05.008.

[169]   R. Kehlenbeck, J.G. Yates, R. Di Felice, H. Hofbauer, R. Rauch, Particle Residence Time and Particle Mixing in a Scaled Internal Circulating Fluidized Bed, Ind. Eng. Chem. Res. 41 (2002) 2637–2645. doi:10.1021/ie010513u.

[170]   M. Kuramoto, D. Kunii, T. Furusawa, Flow of dense fluidized particles through an opening in a circulation system, Powder Technol. 47 (1986) 141–149. http://www.sciencedirect.com/science/article/pii/0032591086801103.

[171]   I. Boukis, P. Grammelis, S. Bezergianni, A. Bridgwater, CFB air-blown flash pyrolysis. Part I: Engineering design and cold model performance, Fuel. 86 (2007) 1372–1386. doi:10.1016/j.fuel.2006.11.002.

[172]   L. Korovesis, Parametric analysis of the hydrodynamics of a Dual Fluidized Bed system for post-combustion capture of CO2 through a scaled cold model, University of Stuttgart, 2009.

[173]   R.H. Perry, D.W. Green, eds., Perry's Chemical Engineering Handbook, 7th ed., McGraw-Hill, 1997.

[174]   A. Nikolopoulus, Hydrodynamic study and design of solid circulation devices and configurations for dual fluidised bed system for CO2 capture, University of Stuttgart, 2006.

[175]   M. Louge, Experimental techniques, in: J.R. Grace, T.M. Knowlton, A.A. Avidan (Eds.), Circ. Fluid. Beds, Springer, n.d.

[176]   A.R. Bidwe, C. Hawthorne, H. Dieter, M.A.M. Dominguez, M. Zieba, G. Scheffknecht, Cold model hydrodynamic studies of a 200 kWth dual fluidized bed pilot plant of calcium looping process for CO2 Capture, Powder Technol. 253 (2014) 116–128. doi:http://dx.doi.org/10.1016/j.powtec.2013.10.043.

[177]   A.R. Bidwe, M.A.M. Dominguez, C. Hawthorne, H. Dieter, Cold Model Investigation of a High Temperature looping Process in a Dual Circulating Fluidized Bed System, in: T. Knowlton (Ed.), Proc. Tenth Intenational Conferance Circ. Fluid. Beds Fluid. Technol. CFB 10, Sun River, Oregon USA, 2011: pp. 137–144.

[178]   C. Hawthorne, A. Charitos, C.A. Perez-Pulido, Z. Bing, G. Scheffknecht, Design of a dual fluidised bed system for the post combustion removal of CO2 using CaO. Part I: CFB carbonator reactor model, in: J. Werther (Ed.), CFB 9, Hamburg, Germany, 2008.

[179]   L. Cheng, P. Basu, K. Cen, Solids Circulation Rate Prediction in a Pressurized Loop-Seal, Ind. Eng. Chem. Res. 76 (1998) 761–763. doi:10.1205/026387698525342.

[180]   S.W. Kim, S.D. Kim, D.H. Lee, Pressure Balance Model for Circulating Fluidized Beds with a Loop-seal, Ind. Eng. Chem. Res. 41 (2002) 4949–4956. doi:10.1021/ie0202571.

[181]   J. Zhu, Circulating turbulent fluidization—A new fluidization regime or just a transitional phenomenon, Particuology. 8 (2010) 640–644. doi:10.1016/j.partic.2010.08.008.

[182]   G. Schwab, Inbetriebnahme und Erprobung einer 200 kWth Pilotanlage zur CO 2 - Abscheidung mit dem Calcium-Looping Verfahren Commissioning and testing, IFK-University of Stuttgart, Studienarbeit Nr. 3013, 2010.

[183]   U. Lackermeier, J. Werther, Flow phenomena in the exit zone of a circulating fluidized bed, Chem. Eng. Process. Process Intensif. 41 (2002) 771–783. http://www.sciencedirect.com/science/article/pii/S0255270102000089.

[184]   A.R. Bidwe, C. Hawthorne, X. Yu, H. Dieter, G. Scheffknecht, Cold model study of a dual fluidized bed system for the gasification of solid fuels, Fuel. 127 (2014) 151–160. doi:http://dx.doi.org/10.1016/j.fuel.2013.12.020.

[185]   M. Gupta, J. Yang, C. Roy, Density of softwood bark and softwood char: procedural calibration and measurement by water soaking and kerosene immersion method, Fuel. 81 (2002) 1379–1384. http://www.sciencedirect.com/science/article/pii/S0016236102000431.

[186]   B. Formisani, G. De Cristofaro, R. Girimonte, A fundamental approach to the phenomenology of fluidization of size segregating binary mixtures of solids, Chem. Eng. Sci. 56 (2001) 109–119.

[187]   A.R. Bidwe, A. Charitos, H. Dieter, A. Wei, M. Zieba, A Study of Standpipe and Loop Seal Behaviour in a Circulating Fluidized Bed for Geldart B Particles, in: T. Knowlton (Ed.), Proc. Tenth Int. Conferance Circ. Fluid. Beds Fluid. Technol. CFB 10, Sun River, Oregon USA, 2011: pp. 641–648.

[188]   H. Lee, Y. Lee, S.-S. Park, H.-J. Chae, S.-Y. Jeong, D. Lee, Hydrodynamic characteristics of cold-bed circulating fluidized beds for the methanol to olefins process, Korean J. Chem. Eng. 27 (2010) 1328–1332. http://dx.doi.org/10.1007/s11814-010-0187-6.

[189]   A.R. Bidwe, G. Varela (Duelli), H. Dieter, G. Scheffknecht, Experimental study of the effect of friction phenomenon on the differences between actual and calculated inventory in small scale CFB riser, Particuology. 21 (2015) 41–47. doi:doi:10.1016/j.partic.2014.12.002.

[190]   S.R. Sankar, T.N. Smith, Slip velocities in pneumatic transport part II, Powder Technol. 47 (1986) 179–194. doi:http://dx.doi.org/10.1016/0032-5910(86)80114-0.

[191]   K. Smolders, Gas fluidized beds operating at high velocities: a critical review of occurring regimes, Powder Technol. 119 (2001) 269–291. doi:10.1016/S0032-5910(01)00267-4.

[192]   H. Dieter, A.R. Bidwe, G. Varela (Duelli), A. Charitos, C. Hawthorne, G. Scheffknecht, Development of the Calcium Looping CO2 capture technology from Lab to Pilot Scale at IFK, University of Stuttgart, Fuel. 127 (2013) 23–37.

[193]   P.S.B. Stewart, J.F. Davidson, Slug flow in fluidised beds, Powder Technol. 1 (1967) 61–80.

145

doi:http://dx.doi.org/10.1016/0032-5910(67)80014-7.

[194]   X. Yao, H. Yang, H. Zhang, C. Zhou, Q. Liu, G. Yue, Gas−Solid Flow Behavior in the Standpipe of a Circulating Fluidized Bed with a Loop Seal, Energy & Fuels. 25 (2010) 246–250. doi:10.1021/ef1011897.

[195]   R. Solimene, R. Chirone, P. Bareschino, P. Salatino, Hydrodynamics of a loop-seal operated in a circulating fluidized bed : influence of the operating conditions on gas and solid flow patterns, in: T.M. Knowlton (Ed.), Proc. Tenth Intenational Conferance Circ. Fluid. Beds Fluid. Technol. CFB 10, 2011: pp. 145–152.

[196]   J.R. Van Ommen, N. Ellis, Fluidization Gas-Solid Fluidized Bed, 2010.